Web-based GIS Modelling of Building-integrated Solar Photovoltaic System for the City of Cape Town

Adedayo Kelvin Adeleke

December 2018

Web-based GIS Modelling of Building-integrated Solar Photovoltaic System for the City of Cape Town

By: Adedayo Kelvin Adeleke

Thesis Presented for the Degree of

DOCTOR OF PHILOSOPHY

In the Geomatics Division

School of Architecture Planning and Geomatics

Faculty of Engineering and the Built Environment

UNIVERSITY OF CAPE TOWN

December, 2018

Supervisor: Associate Professor Julian Smit

DECLARATION

I, Adedayo Adeleke, hereby declare that the work on which this thesis is based is my original work (except where acknowledgements indicate otherwise) and that neither the whole work nor any part of it has been, is being, or is to be submitted for another degree in this or any other university. I authorize the University to reproduce for the purpose of research either the whole or any portion of the contents in any manner whatsoever.

Signature:… 

Date: 09/10/2018

ACKNOWLEDGEMENTS

Firstly, my immense gratitude goes to my maker, the eternal God for the abundance of his loving-kindness and benevolence towards me. He has sustained me and given me the grace to complete this study.

I would like to express the deepest appreciation to my supervisor, Associate Professor Julian Smit, for the guidance and countless opportunities granted to me while my study lasted. Also, I appreciate all the academic and support staffs of the Geomatics division of School of Architecture, Planning and Geomatics for all the support during the period of this program.

Likewise, I would like to extend my sincere gratitude to the University of Cape Town through the postgraduate funding office for providing the “International Student Scholarship” and also the National Research Foundation for providing the “NRF Innovation Doctoral Scholarship” that provided funds and grants towards the completion of this study.

Finally, I would like to express my profound appreciation to the family of Adeleke for their relentless support and encouragement.

ABSTRACT

Population increase in African cities have made it hard to reduce their ecological footprint and attain self-sustainability. This made the United Nations to put forward the seventeen sustainable development goals. Three of these goals centre on provision of clean energy and reduction of reliance on fossil fuels. It is therefore important for cities in Africa to chart a path of attaining sustainability. Consequently, the city of Cape Town is leading the drive for a greener city and self-sustainability in energy. Solar energy, which is regarded as a clean and renewable source of energy, makes it possible to generate electricity by using photovoltaics technology. However, the problem of creating awareness as to the potentials of building-integrated solar photovoltaic system persists. The study is aimed at using remote sensing and Geographic Information Systems (GIS) techniques in creating awareness about the potentials of building rooftops for solar photovoltaics installations in an urban setting. In achieving this, Light Detection and Ranging (LiDAR) data and aerial imagery are sourced from City of Cape Town municipality to serve as the primary data input. Four phases of analysis are involved: (1) extraction of whole building roof outline and its roof planes, using the integration of LiDAR-derived products and aerial imagery, in order to determine the surface area of the roof planes. This is achieved by developing a unique two-in-one, object-based classification rulesets; (2) estimating and validating the global solar radiation incidence on each roof plane, using a LiDAR-derived elevation model in a python script utilizing the GRASS script library; (3) evaluating the solar photovoltaic potential of each roof plane, using inputs from two previous phases to create a solar photovoltaic potential database; and (4) deploying the solution online to create awareness, by utilizing JavaScript and Hypertext Mark-up Language (HTML) to implement a map mashup, which incorporates tile map and table services. This results in a web-based solution, which can be queried to retrieve information about the solar photovoltaic potential of a building roof. From the results generated and the system developed, it becomes possible to remotely and sufficiently evaluate buildings in the city for solar photovoltaic potentials, designs and installations. Thereby reducing reliance on the fossil fuel generated electricity and improving the self-sustainability of the city.

TABLE OF CONTENTS

LIST OF TABLES

LIST OF FIGURES

LIST OF ACRONYMS

ALS	Airborne Laser System
CO_2	Carbon dioxide
DEADP	Department of Environmental Affairs and Development Planning (Western Cape, South Africa)
DEM	Digital Elevation Model
DME	Department of Minerals and Energy (South Africa)
DSM	Digital Surface Models
DTI	Department of Trade and Industry (South Africa)
DTM	Digital Terrain Model
GHG	Greenhouse Gas
GIS	Geographic Information System
GSD	Ground Sampling Distance
HTML	Hypertext Mark-up Language
HVAC	Heating, Vent and Air Conditioning
IDW	Inverse Distance Weighting
IEA	International Energy Agency
IRP	Integrated Resource Plan
LiDAR	Light Detection and Ranging
MCE	Multi-criteria Evaluation
MRS	Multi-resolution Segmentation
nDSM	Normalized Digital Surface Model

NDVI	Normalized Difference Vegetation Index
NERSA	National Energy Regulator of South Africa
NN	Natural neighbours
REFIT	Renewable Energy Feed-in Tariff
REPA	Renewable Energy Purchasing Agency
S.A. DoE	South African Department of Energy
SBO	Single Buyer Office
SSEG	Small Scale Embedded Generation
TIN	Triangulated Irregular Network
TSA	Trend Surface Analysis
TTA	Training and Test Area
UN	United Nations
USA	United States of America
VHR	Very high resolution

CHAPTER 1
INTRODUCTION

Sustainability and reduction of ecological footprint in urban areas are increasingly becoming difficult to achieve, since greater proportion of the world's population now resides in cities and urban areas (UN Department of Economic and Social Affairs, 2013). Three of United Nation's seventeen sustainable development goals centre on provision of clean energy and reduction of reliance on fossil fuels, which are the main cause of greenhouse gases (UN General Assembly, 2015). It is therefore pertinent for cities in Africa to chart a path of attaining sustainability in terms of energy and climate, as its' continual survival depends on it.

In most part of Africa, solar energy from the sun, known to be one of the largest source of renewable and sustainable energy, has the technical potential to generate energy, which often exceeds the prevailing total primary energy consumption of such areas, when evaluated (De Vries, Van Vuuren & Hoogwijk, 2007). The viability of solar energy was recently made obvious by its implementation in powering an aircraft (Solar Impulse 2): for the first time in history, an aircraft was able to fly day and night, even for longer periods of time, up to 100 hours, without using fuel (O'Callaghan, 2015). Also, solar energy is now being considered more in urban areas, as solar power is becoming cheaper than coal in some part of the world. It is projected that solar energy would likely become the cheapest energy option in less than a decade (Shankleman & Martin, 2017).

This chapter presents an insight into how a city in Africa could achieve sustainability in terms of harnessing solar energy using remote sensing and Geographic Information Systems (GIS) techniques. An overview and background is initially provided, beyond this, the objectives, scope of the research and the thesis structure is laid out.

1.1 Background

Globally, the demand for electricity has increased by 40% between the year 2000 and 2010, despite a small downturn in 2009, caused by the global economic crisis (IEA, 2012). It is anticipated that the demand for electricity will continue to grow faster than

the demand for any other form of energy over the projected period, viz. until 2050. However, the rate of growth differs in the policy-based scenarios used in projecting energy demand, depending on the nature of government policies relating to carbon dioxide (CO_2) emissions, energy efficiency and energy security (IEA, 2012). According to Inglesi-Lotz and Pouris (2012), countries around the world are facing a challenge of finding and investing in various sources of sustainable energy, which means their attitude and approach towards energy usage will have to align with their social, environmental and economic targets.

Likewise, both developed and emerging countries face similar energy and environmental challenges. South Africa, being among the developing countries, is no exception. South Africa's steady economic growth, coupled with an increasing focus on industrialization and a mass electrification program that is to make power accessible deep within rural areas, has brought about a steep increase in the demand for energy. As a matter of fact, South Africa's energy demand is projected to be twice the current levels by 2030 (SA GCIS, 2013). Over the past two decades, however, the country has not made any significant investments in the energy sector. The capacity that was created in the 1980s was sufficient to carry the country through to the early 2000s. However, economic growth, fuelled by the commodity boom, has now surpassed the existing power supply. This has therefore placed the country in a situation in which the demand for electricity continues to grow within a supply-constrained environment. The massive electrification program, which started in the 1990s, and the on-going rapid industrialization of the country have also put a huge strain on the use of fossil-based energy sources (SA GCIS, 2012).

According to Krupa and Burch (2011), in South Africa and other parts of Africa, it is anticipated that renewable energy generation will offer the capacity to fight efficiently against the rising risk of climate change. In many areas of sub-Saharan Africa, it is already apparent that climate change is threatening to derail the improvements in their living standards, realized over the last few decades, by increasing extreme weather conditions, rising sea levels, droughts, and reducing crop yields, among other damaging effects (Krupa & Burch, 2011). South Africa, as a so-called "non-annex 1 developing country", is ranked among the top 20 countries measured by absolute carbon dioxide (CO_2) emissions. The vast majority of South Africa's CO_2 emissions (about 80%) are produced by the electricity sector, the metals industry and the

transport sector. The electricity sector's total reliance on low-cost fossil fuels-based electricity generation is one of the main reasons for the carbon-intensive nature of the economy (SA DNT, 2010).

South Africa, of recent (2013 - 2015) has experience power outages more frequently than ever before. The state-owned power utility, Eskom, rolled out different stages of load shedding in order to ration the insufficient supply of electricity. Various reasons were given by Eskom to support its decision to resort to load shedding. Among them were planned maintenance of generating plants during winter. Load shedding is regarded as a last resort to balance electricity supply and usage, and only implemented when other options have been exhausted. Other options, according to Eskom, include voluntary and contract-based options with specific large consumers to reduce their demand on the national grid and the use of the gas or hydroelectric power to supplement the main supply from coal-fired plants (Eskom, 2015b). South Africa had previously suffered widespread rolling blackouts in 2008, when factories and mines were forced to shut down, thereby costing the economy billions of dollars (eNCA, 2015). Currently, the country has managed to overcome the challenges of power outages it faced recently, with the completion of the three of six units Medupi coal power plant (Eskom, 2017). However, this addition is not a sustainable nor clean energy source. Likewise, political tension and instability in the state-owned power utility company management, coupled with delay in approving coal contract for supply of coal by the parliament's standing committee on public accounts, could translate to shortage in electricity production and could result in load shedding eventually (Dentlinger, 2017).

South Africa is fortunate to have abundant solar resources, which could be tapped to reduce the over-dependence on coal-based generating plants and as well to mitigate greenhouse emissions from the use of fossil fuels (Krupa & Burch, 2011). According to Pegels (2010), the electricity sector of South Africa is facing three major problems. Firstly, an undersupply of electricity has resulted in a narrow reserve margin and consequently in power shortages. As the demand for electricity is expected to double within the next 15 years, the pressure to increase the electricity supply and/or to reduce the demand is enormous. Secondly, Eskom estimates it will need a large sum of money, about ZAR 300 billion over the next decade, for the extension of current power infrastructure (Pegels, 2010). Thirdly, the South African economy has a high

emission intensity, especially in the electricity sector, which results in widespread environmental damage.

Due to the history of cheap and abundant electricity in South Africa, most areas of the Western Cape, particularly Cape Town, have been wasteful in terms of energy management (City of Cape Town, 2014). This non-sustainable pattern of living, according to the municipality, has exacerbated the energy shortage, and prompted an urgent call for improvements in energy efficiency and diversification of energy supply in order to improve the city's energy security. The carbon footprint of Cape Town city is generally lower than the average for the entire country, but quite high when compared with other developing cities with similar economies. This is because most of the electricity consumed in the city is derived from national coal-based power generating plants. The city's electricity consumption accounts for about 64% of its carbon footprint (City of Cape Town, 2014).

According to the City of Cape Town (2014), the electricity consumed in the city gradually increased between 2001 and 2007 in response to an increasing population and growing economy. It touched a high of about 12,250 GWh in 2007. Subsequently, there has been a decline year after year, reaching 10,556 GWh in 2010. The downward trend continued through 2011, with the total annual electricity consumption at 10,488 GWh and declining further to 10,200 GWh in 2013.

Despite this downward trend in electricity consumption pattern in the City of Cape Town, and despite the fact that Koeberg nuclear power station is close by, the city still could not meet the demand for electricity from its residents. The nuclear power plant has an installed capacity of 1800 MW and averages about 13,668 GWh annually over last three years running at 83.1% efficiency (Eskom, 2015a). The electricity generated at Koeberg is fed directly into the national grid, therefore neither the City of Cape Town nor Western Cape Province have any control over the source of electricity they purchase from the grid (City of Cape Town, 2011).

Achieving sustainability for a city like Cape Town would therefore require investment in renewable energy sources like solar and efficiency in use of electricity (UN Department of Economic and Social Affairs, 2013). The city had set out an energy action plan to achieve 10% renewable and cleaner energy target by 2020 (Trollip, Ward & Walsh, 2011). Furthermore, the city plans to attain 120MW of installed

building-integrated solar photovoltaic system by year 2020 (City of Cape Town, 2015a). According to Euston-Brown et al. (2015), the commercial (44%) and residential (37%) sectors top the city's electricity consumption (see Figure 1.1). Leading by example, the city has committed to improve its energy efficiency and manage energy consumption for its operations in order to reduce the city's environmental impact (Western Cape Government, 2015).

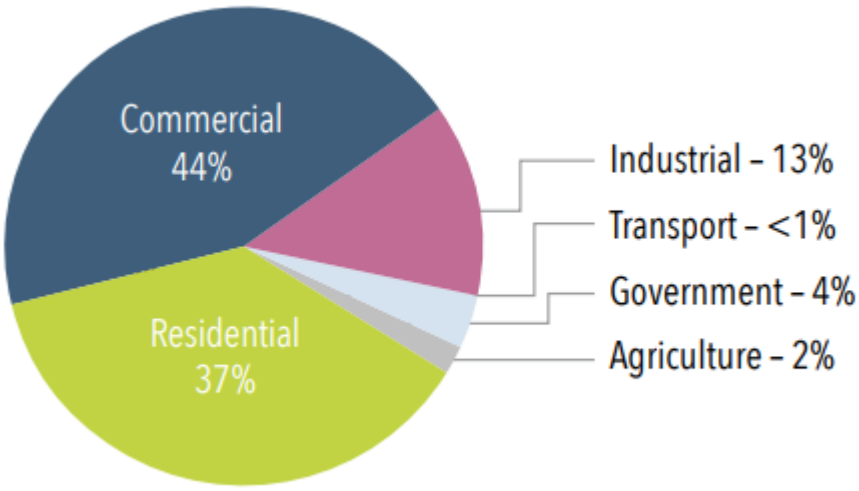

Figure 0.1.1: Electricity consumption by sector, Cape Town, 2012. Source: (Euston-Brown et al., 2015).

1.2 Problem Statement

The latter part of the background to this study above highlighted the City of Cape Town's drive for a greener city and self-sufficiency in terms of energy sustainability. However, the problem of creating awareness as to the potentials of building-integrated solar photovoltaic system persists. Some business parks and shopping malls (Black River Park and V&A Waterfront) have recently invested into building-integrated solar photovoltaic system and it seems others are waiting for the success of these pioneers before embracing the system. Solar energy is one of the most environmentally friendly sources for generating electricity by means of photovoltaic systems, and it offers a viable and expedient means of generating electricity within a short period of time. Nevertheless, there are a few impediments to the extensive deployment of solar photovoltaic systems. The most prominent among these are generation potential and the high capital cost of initial set-up. Hence, the location, design and yield of building-

integrated photovoltaic systems have to be well thought-out before their deployment. There is therefore a need for the development web-based solar photovoltaic potential calculator, which can provide visual-aided information about the potential, location and design of building-integrated solar photovoltaic system for the entire city. This tool would eventually help in creating the awareness about the solar photovoltaic potential and as well provide solutions to the common impediments plaguing the extensive deployment of solar photovoltaic systems.

1.3 Aim and Objectives

This research is aimed at using remote sensing and GIS techniques in creating an online tool, which could be deployed in evaluating and assessing the potentials, designs and installations of building-integrated solar photovoltaic systems.

In achieving the aim stated above and confirming the hypothesis earlier stated, the following objectives will be pursued:

- To identify a suitable and effective spatial data analysis method of building roof extraction and roof plane segmentation using an integration of aerial imagery and LiDAR data.
- To identify a suitable solar radiation model that provides a good estimate of global solar radiation of the study area.
- To estimate the solar photovoltaic potential of building roofs using the inputs from building roof extraction and estimates of global solar radiation.
- To build an interactive tool capable of evaluating and assessing the potentials, designs and installations of building-integrated solar photovoltaic systems at a municipal scale.

1.4 Research Questions

In the process of creating awareness about the potentials of building-integrated solar photovoltaic system, this study will seek to provide answers to the following questions;

- Which spatial data analysis method is suitable to effectively extract building roof outline together with each roof plane comprising the whole building roof?

- How can the global solar radiation over a building be efficiently estimated and validated?
- How can solar photovoltaic potentials be estimated, using building roof data and solar radiation database?
- How can a solar photovoltaic estimation tool be enhanced to become a web-based system, which will provided an efficient solution for building-integrated solar photovoltaic systems modelling, simulation and estimation?

1.5 Significance of Research

The ability to remotely access and analyse building roofs contributes a lot in urban planning, as information about building roof slope, orientation, height and area (span and surface) have found usefulness in areas such as city infrastructural development planning, suitability analysis, disaster/risk management and public safety, building roof modelling, visualization and simulation (Wang, Lodha & Helmbold, 2006). Particularly, of importance to this research is the suitability analysis, visualization and simulation. The output of this research would not only provide awareness in terms of building-integrated solar photovoltaic system potentials, but the information about the roof geometry could also be utilised in other sectors of urban planning such as in rainwater harvesting decision, roof deformation monitoring and building roof inventory generation at municipal scale. All the areas highlighted above combine to contribute to the attainment of sustainability for a city or an urban area.

Therefore, in achieving the aim of this research, the research design would be contributing to the advancement of research, by designing and implementing a unique two-in-one building roof structure detection algorithm to extract whole building roof outlines and roof planes. The study would also provide a validated high-resolution GIS-based solar radiation database for the study area. Lastly, a web-based solar photovoltaic potential calculator is designed for the entire city.

1.6 Scope of Research

The City of Cape Town municipality was selected to validate the above stated objectives. Very high resolution (VHR) imagery with ground sampling distance (GSD) of 8cm and LiDAR data with about 60cm average point spacing will be utilised as the primary data. A method will be developed to extract whole building roof outline and roof planes using the integration of these primary data. Global solar radiation incident over these roof will be estimated and validated, while the solar photovoltaic potential for each building roof will be determined using outputs from the preceding stages. Only residential and commercial building rooftops within the suburbs or formal settlements will be considered in this study.

1.7 Thesis Outline

Having presented the background and purpose of the study in the foregoing sections, the rest of the thesis is structured as follows: Chapter 2 reviews all the relevant earlier research studies on the need to adopt renewable energy instead of the traditional fossil fuels because of their impact on the environment. The government's view to adopting renewable energy is reviewed, and instances and methods of how solar energy can be modelled and evaluated are presented.

Chapter 3 elaborates on the various spatial data analysis methods involved in extracting the building roofs, estimating their global solar radiation amount and calculating the solar photovoltaic potential of these roofs. Suitable and feasible methodologies are integrated and adopted, and a selection of systems is briefly introduced in this chapter. It also presents an overview of the study area, and the data acquisition methods and the source of the data used in achieving the aims of this study. It also describes the process of data verification, integration and pre-processing in preparation for the core analysis.

Chapter 4 gives details of each stage of analysis performed and discusses the result generated from each of these analyses and their implications. Chapter 5 presents the conclusions and recommendations, based on the analysis performed in Chapter 4.

CHAPTER 2
LITERATURE REVIEW

The previous chapter provides an introduction and background to the study. This is elaborated upon in this chapter, with a detailed insight into previous studies that have been carried out in areas related to this research and that are relevant to this study. Climate change and sustainable energy are discussed in Section 2.1 under sustainable development. The renewable energy potential of South Africa and government policies are reviewed in Section 2.2, while the application of geographic information system (GIS) to renewable energy is discussed in Section 2.3. Section 2.4 gives a brief of the solar energy and key factors affecting its wider use and Section 2.5 focuses on solar photovoltaics. The four phases involved in creating a web-based system for solar photovoltaic potential of a building roof will be discussed in Section 2.7 as “building roof detection and extraction”, in Section 2.8 as “modelling solar radiation” and in Section 2.9 as “evaluating solar photovoltaic potential”. Section 2.10 gives an insight into factors affecting solar photovoltaic potential while Section 2.11 looks at the web mapping. Finally, a concluding summary to the works reviewed is presented in Section 2.13.

2.1 Sustainable Development

The United Nations (UN) drafted seventeen sustainable development goals, themed agenda 2030, it came into effect on 1st of January 2016. The sustainable development goals are designed to complement and overtake the earlier millennium development goals (UN General Assembly, 2015). Some of the goals related to this study include taking urgent actions to curtail climate change and impact, ensuring access to affordable and sustainable energy, making cities and urban areas sustainable and resilient, among others. These can be further summarized under the two subsequent sub-headings.

2.1.1 Climate Change

Over the past five decades, greenhouse gases concentration in the atmosphere has increased by about 30% and fossil fuel based energy generation and consumption accounts for two thirds of this concentration (UNDP, 2016). According to Orndonez et al. (2010), increasing awareness about the negative impacts of fossil fuels and their related environmental hazards will have a direct influence on how energy challenges are dealt with in the future. Climate change, as a serious global problem, consequently requires an intensive international response, in addition to national efforts to minimize greenhouse gas (GHG) emissions. In response to this situation, the United Nations (UN) in 1997 established a framework, which became known as the Kyoto Protocol. This is an international agreement that classifies each country according to their level of industrialization, and it also requires certain countries to reduce their GHG emissions by setting internationally binding targets (UNFCCC, 1998).

Pegels (2010), argued that South Africa is already being affected by global climate change and that these effects may likely intensify in the coming decades. This stems from CO_2 emitted as a result of electricity production, which accounts for about 80% of total GHG emissions in South Africa. The high emission intensity is attributed to the use of coal (72%) as the primary energy source in electricity production (see Figure 2.1).

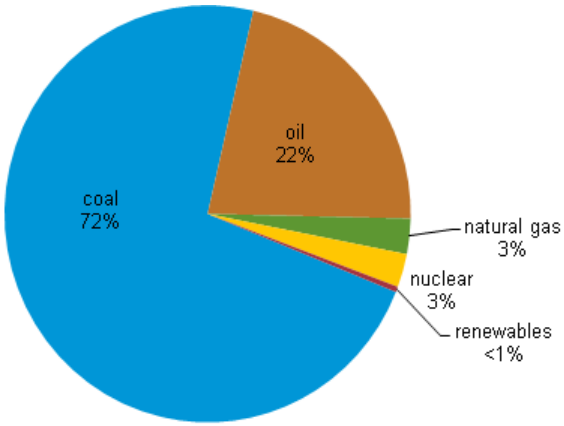

Figure 2.1: Total primary energy consumption in South Africa, 2012. Source: (Hulsey, 2014).

According to Krupa and Burch (2011), the climate change being experienced in many part of sub-Saharan threatening the improvements, which have been experienced in those countries' living standards over the last decades, as a result of increase in

extreme weather conditions, rising sea levels and crop yield reductions amongst others. It is anticipated that a shift to renewable energy generation in most African countries and cities will increase their capacity to fight efficiently against the rising risk of climate change and its impacts (Krupa & Burch, 2011).

2.1.2 Sustainable Energy

As mention above, the energy sector contributes significantly to the concentration of greenhouse gases in the atmosphere. Therefore, it is important that clean and sustainable energy options are pursued (UNDP, 2016). It has been identified that production and distribution of renewable energy can contribute significantly to the economic development of any country, since energy is central to its sustainable development (UN Department of Economic and Social Affairs, 2013). Other countries can take a cue from Germany's Energiewende (energy revolution). Germany is in the fore front of energy revolution, as the country strife to hit a target of about 80 % contribution from renewable energy before 2050, thereby reducing greenhouse gas emissions by about 80 % (Nield, 2016). The current contribution of renewable energy to total electricity generation in Germany stands at 37.1 % (Burger, 2017). Renewable energy, for few days in May 2016 supplied more than 90 % of Germanys' power demand (Shankleman, 2017).

According to World Economic Forum (2017), Germany is currently the world's fourth largest economy. The country was able to increase its energy security by embracing renewable energy, which has helped in cutting down on energy imports, about two thirds of Germany's energy are imported, costing about 90 billion euros in 2013 (Morris & Pehnt, 2016). This energy transition has positively impacted Germany's local economy, as it has stimulated technology innovation, created more jobs and helped the country positioned itself as pioneer exporter of green technologies (Morris & Pehnt, 2016). Likewise, renewable energy has boosted the income of German farmers as they now generate more profit from sale of renewable energy than their actual crop yields. Farms in the state of Bravaria is home to about 465,000 solar photovoltaics panels, having a technical capacity (10,400 MW) equal to about ten nuclear reactors (Hockenos, 2014). If each country would look introspectively, there would be some kind of renewable energy potential it could maximize to improve its energy security.

South Africa's renewable energy potential and government's policies concerning it are discussed below.

2.2 Renewable Energy in South Africa

Pegels (2010) is of the view that promoting renewable energy technologies could offer a viable solution to the electricity supply challenge and the problem of GHG emission levels in South Africa. However, little progress has been made in deploying renewable energy despite the presence of a high resource potential in the country. This is evident from the series of policies formulated from different White Papers, which have been published since the start of the democratic dispensation in 1994. Krupa and Burch (2011) noted that South Africa possesses a significant amount of renewable energy resources, and that, several previous studies have shown that solar and wind energy in particular have meaningful output capacity over comparatively small areas.

According to the annual government publication (South African Yearbook), most areas in South Africa average more than 2,500 hours of sunshine per year, while average daily solar radiation levels range between 4.5 kWh/m^2 and 6.5 kWh/m^2 in a day. The southern part of African and other regions of Africa are well endowed with the sunshine all year round. The annual 24-hour global solar radiation average is about 220 W/m^2 for South Africa compared with about 150 W/m^2 for parts of the USA, and about 100 W/m^2 for Europe. Without a doubt, the solar resources available in South Africa are one of the highest in the world. Moreover, it is readily accessible all over the country and lends itself to a number of potential uses (SA GCIS, 2013).

Renewable energy sources in the year 2016 account for about 5% of the country's total installed capacity, increasing from less than 1% in 2012. As at of September 2016, the Renewable Independent Power Procurement Program under the coordination of Independent Power Producer (IPP) office has procured 6376 MW electricity capacity, out of which 2738 MW is connected and operational (NERSA, 2016).

2.2.1 Government Policies

As highlighted earlier, the generation and distribution of energy is pivotal to the economy of any country. South Africa is heavily dependent on its large-scale and energy-intensive coal mining industry (US EIA, 2014b). The necessity to alleviating the harmful environmental impacts of fossil fuel consumption has led to a surge in grid-connected renewable energy production around the globe, including in South Africa. In addition, the instability of fuel costs and the improvement of national energy security have brought about similar growth over the past two decades (Sebitosi & Pillay, 2008).

The post-election period after 1994 in South Africa saw policy makers changing their priorities. Every single aspect of social and economic policy in South Africa was re-examined, reformed and redrafted. The new government identified energy issues as critical for the economic development of the country, demonstrating a commitment to providing affordable and sustainable energy for small businesses, disadvantaged households, small farms, schools, clinics, and a wide range of other community establishments, in rural as well as urban areas. The government drafted a White paper on Energy policy in 1998 titled “White Paper on the Energy Policy of the Republic of South Africa”. It provided a formal framework for the energy sector to operate within the broad national strategy for reconstruction and development (SA DME, 1998).

South Africa hosted the World Summit on Sustainable Development in 2002. The country is fortunate to be endowed with an abundance of renewable energy sources, and thus, in 2003, the government, through the Department of Minerals and Energy (DME) prepared a White Paper on Renewable Energy, to ensure that these abundant renewable energy sources are used optimally. The government consequently set a target that 10,000 GWh from renewable energy sources would be contributing to final energy consumption by 2013. This renewable energy, mainly from biomass, wind, solar and small-scale hydro, was meant to be utilised for power generation and non-electric technologies such as solar water heating and biofuels. This target translates to approximately 4% (1,667 MW) of the projected electricity demand for 2013, which amounts to 41,539 MW (SA DME, 2003). However, the set target was not met, and it has since been overtaken by another target set, which was set in the Integrated Resource Plan (IRP) for electricity of 2010 (SA DoE, 2010).

The South African Department of Energy (SA DoE) intends to use the IRP to determine the long-term electricity demands of the country; the plan also sets out the details of how this demand would be met, by considering generating capacity, type timing and cost. It also serves as input to other planning functions, such as economic development, environmental and social policy. In doing this, the DoE aims to achieve a balance between an affordable price for electricity, which will support a globally competitive and efficient economy and the need to meet the desired emissions targets, in line with global commitments. It is worth noting that the IRP is a 20-year electricity capacity plan spanning several decades, from 2010 to 2030 (SA DoE, 2010).

According to Pegels (2010), in 2009, about 73 countries had formulated renewable energy policy targets, and not less than 64 had specific support schemes in place. One of the most common and very effective policy instruments used in supporting renewable energy deployment are the feed-in tariffs. These are designed to guarantee the producer's fixed tariffs for power generated from renewable energy source over a certain period, usually 10 – 20 years. These feed-in-tariffs have helped played a significant role in improving solar energy deployment in countries leading in solar energy market growth, especially Italy and Germany (Timilsina, Kurdgelashvili & Narbel, 2012).

The National Energy Regulator of South Africa (NERSA) introduced a Renewable Energy Feed-in Tariff (REFIT) program at the end of 2007 to regulate electricity tariffs under its authority in the country. The program necessitates the creation of the Renewable Energy Purchasing Agency (REPA), which is the Single Buyer Office (SBO) of the national electric utility company Eskom, authorized to purchase renewable energy from licensed generators at stipulated prices. The stipulated prices are then envisaged to act as incentives to renewable energy developers and investors by mitigating the financial risk and offering market certainty. The REFIT program was commissioned in March 2009, and was intended to help the government meet its target of 10,000 GWh renewable energy by 2013. Likewise, it was aimed at promoting competitiveness within the renewable energy industry in the medium and long term. Key objectives set out to be achieved by the REFIT program include (Curren et al., 2009):

- Creating an enabling environment for renewable energy power generation

- Creating an active mechanism to reflect market, political and economic developments
- Providing access to the grid and a commitment to purchase the power generated
- Promoting critical mass investment in renewable energy and providing a base for a self-sustaining market.
- Providing a level playing field for investors and developers
- Creating a fail-safe pricing for electricity generated from renewables for a determined period of time, providing a steady income stream and sufficient return on investment

Likewise, the Renewable Independent Power Procurement Program (REIPPP) was established in November 2010 by the DoE to procure electrical energy generated from renewable sources by the private sector (NERSA, 2016). This sector has managed to attract about 194 billion Rand from inception and over 25% of this is from foreign direct investment, this has helped in stimulating the growth of local renewable energy technology in the country (Bronkhorst, Raw & Mulcahy, 2017).

At the provincial level, the Western Cape government has realized the need to develop a more sustainable energy sector, moving away from the traditional reliance on fossil fuels. This prompted the drafting of the "White Paper on Sustainable Energy for the Western Cape" in September 2010. Prior to this, there had been a series of policies formulated over a period of time; these include the "Draft Integrated Energy Plan of Action" in 2007, the "Sustainable Energy Strategy and Program of Action" in 2007, and the "Sustainable Development Implementation Plan" of 2008. Targets set by the White Paper of 2010 include 15% of the electricity consumed in the province to be sourced from renewable sources by 2014, a reduction in final energy demand of 15% by 2014, and a reduction in carbon emissions of 14% by 2014, using the 2004 emission level as benchmark. These targets were to be met through the objectives of the White Paper, which include promoting "the implementation of renewable energy and energy efficiency through technology and behavioural change" (DEADP, 2010).

Likewise, the City of Cape Town took some steps in addressing the city's energy-related challenges. In 2010, an all-inclusive "Energy and Climate Change Action Plan" was adopted by the city council. This action plan was designed to link the energy and

climate sector to the city's developmental strategy. The plan was utilised in organizing a range of forty program sectors, which consists of over 120 projects altogether. The objectives of the city's action plan include a 10% reduction in electricity consumption in the city by 2012, a 10% reduction in carbon emission by 2014 and a 10% addition from renewable energy sources to the electricity supply mix by 2020 (City of Cape Town, 2014).

In pursuit of meeting the target of a 10% addition from renewable energy by the year 2020, the City of Cape Town in September 2014 signed its first commercial agreement to buy back surplus electricity from consumers (Botes, 2014). The scheme is referred to as Small Scale Embedded Generation (SSEG). According to the City of Cape Town (2015b), SSEG refers to power generation from solar photovoltaic systems or small wind turbines that generates less than 1 MVA. These generating sources could be located on residential or commercial sites and most of the electricity generated is consumed by the owner; however, when the generation surpasses consumption, "a limited amount of power is allowed to flow in reverse from the consumer onto the utility grid" (City of Cape Town, 2015c). A guideline, which is regularly updated, has been provided by the municipality for the interested public to consult. However, the buy-back rate, which is currently pegged at 49.72c/kWh, is far lower than the rate at which the consumer/generator will buy the electricity back from the municipality when needed (City of Cape Town, 2015c).

With the formulation of these polices, the government, at various levels, have shown significant commitments in increasing the contribution of renewable energy to the final energy consumption. With the renewable energy potentials and government policies already highlighted, it is important to review how GIS can be applied in tapping these enormous potentials, as the use of GIS technologies now play a dominant role in measuring renewable energy quantities and in locating suitable and potential sites for renewable energy projects.

2.3 GIS Applications in Renewable Energy

According to Amador et al. (2005), the use of GIS plays a leading role in analysing renewable energy, as it approaches the issue by integrating of all the possibilities.

Early spatial analyses in renewable energy were mainly hampered by a lack of tools to correlate different types of information (Rialhe, 1996). Voivontas et al. (1998) solved the problem of identification and estimation of renewable energy sources by evaluating the spatial distribution of energy supply in a region and combining this with the energy demand profile. Using MAPINFO Professional software, they developed a Decision Support System to evaluate the geographical distribution of wind energy in the Crete region of Greece, thereby creating a new framework for parties involved in energy planning. Highlighting the importance of GIS, Voivontas et al. (1998) pointed out that the main advantages of using GIS technology included its flexibility in handling data on different levels of spatial analysis and its ability to highlight spatial correlations between datasets.

Sorensen and Meibom (1999) too created a general tool for systems modelling, assessment and planning using GIS. Energy use and supply per unit area of the land were considered, and mismatches entailing needs for energy trade and energy exchange facilities establishment were directly identified. Similarly, Baban and Parry (2001) applied GIS to locate suitable sites for wind energy development in Lancashire, United Kingdom. Information from questionnaires and various literature were used to compile the criteria utilised in locating the suitable sites.

Subsequently, GIS has been applied in many tasks involving renewable energy, especially in mapping and measuring the quantity and location of renewable energy sources, as well as in determining suitable sites for renewable energy developments (Ramachandra & Shruthi, 2007; Ramírez-Rosado et al., 2008; Simao, Densham & Haklay, 2009; Brewer et al., 2015; Sadeghi & Karim, 2017). However, Resch et al. (2014), highlighted that some of the major challenges of early studies on GIS applications in renewable energy to include the non-consideration of topographic or geographic relationships of energy systems developed, lack of vital data and wide range of disparity in data formats and structures utilized, thereby making system integration difficult to achieve. This study is hinged on the solar energy as the renewable energy source, therefore, it is now brought into focus in the next section.

2.4 Solar Energy

The sun is the main source of energy on the earth, providing the basis for photosynthesis and permitting the flow of air and water (Dubayar & Rich, 1996). Solar energy can be received or harvested from the sun's light rays hitting the earth, which is generally referred to as solar radiation or insolation (US EIA, 2014a). Solar energy can be harvested for either heat generation or electricity generation. According to Knier (2002), solar radiation can be harnessed and converted to electricity using the photovoltaic cells, which absorbs photons and then release electrons, which can be captured in the form of an electric current.

Key issues affecting the wider use of solar energy include strong spatial and temporal variations in solar radiation forms. This is influenced by various factors, such as basic patterns of seasonal and daily variations, as well as daily variations caused by astronomic factors are strongly modified by the changing atmospheric conditions, such as water vapour, ozone, clouds and aerosols. These patterns become more intense at local levels because of varying local conditions, such as temperature and sky-view obstructions, among others (Hofierka & Kaňuk, 2009).

Solangi et al. (2011), highlighting the benefits of solar energy concerning sustainable development, listed several environmental advantages of solar energy relative to other energy sources:

- No emissions of GHGs
- No depletion and release of liquid or solid waste products
- Reduction in numbers of transmission lines and pylons
- Increase in regional or municipal energy independence
- Acceleration of rural electrification
- Diversification and energy security of energy supply

2.4.1 Spatial and Temporal Variations

According to Suri and Hofierka (2004), the interaction of solar radiation with the surface of the earth and the atmosphere is influenced mainly by three sets of factors, which could be spatial or temporal:

1. Atmospheric conditions: e.g. clouds, air molecules, ozone, CO_2, solid and liquid particles
2. Geometry of the Earth: e.g. rotation, revolution, latitude, declination and solar hour angle
3. Terrain: e.g. elevation, orientation (aspect), surface inclination and shadows.

Solar radiation reaching the earth's surface is fairly consistent at about 1,367 kW/m^2. However, the amount of radiation actually reaching a particular rooftop varies due to factors, such as spatial and temporal variations (Kodysh et al., 2013). Spatial and temporal variations refer to variations of solar radiation in time and space. The atmosphere has a strong effect on the amount of solar radiation available at any particular point on earth surface. Spatial and temporal variation are mostly influenced by clouds, since these reflect a substantial part of the incident solar radiation (Bojanowski, 2013). The photovoltaics technology, as stated already, is used to harvest electricity for the sun, this system is further discussed in the following section.

2.5 Solar Photovoltaic Systems

The Bells Lab invented solar photovoltaic cells in the United States of America (USA) in 1954. Starting from the late 1950s, solar photovoltaic technology has been put to use in space satellites to generate electricity, thus keeping the satellites in orbit throughout their lifetime (Hoogwijk, 2004). The photovoltaic technology converts solar radiant energy, which is contained in light quanta into electric energy when the light reflects on a semiconductor material. This causes electron excitation, which enhances conductivity. The two main types of photovoltaic on the market are crystalline silicon-based photovoltaic cells (which could be single-crystalline or multi-crystalline) and thin film PV cells (Sorensen, 2000).

A photovoltaic cell is the smallest basic device designed to generate electricity when exposed to sunlight, while a photovoltaic module is the smallest unit of assembled and interconnected photovoltaic cells. According to the Department of Trade and Industry (Great Britain Dept. for BERR & DTI Sustainable Energy Programme, 2006), these modules are manufactured and combined in different sizes according to industry specifications to form photovoltaic panels and arrays of panels. Recent trends in solar

photovoltaic development has seen increase in favouritism for solar tiles (solar shingles), in lieu of panels. Advantages presented by solar tiles include aesthetic, insulation and space maximization, this allows all part of the roof to be filled with photovoltaic cell (Mo, 2015).

The solar photovoltaic market continues grow with the total global operating capacity reaching 100 GW in 2012. Most European countries now have more solar photovoltaic installed capacity than wind and other renewable energy sources (REN21, 2013). Such rapid growth in the solar energy market can be attributed to various factors, such as the high volatility of fossil fuel prices and the increased global campaigns against the use of GHGs due to their negative environmental impacts. It has been established that solar energy possessed abundant resource potential that far exceeds the entire world energy demand. Ironically, the percentage contribution of solar energy to the global energy supply mix is still small despite this potential and despite recent rapid market growth (Timilsina, Kurdgelashvili & Narbel, 2012).

According to Timilsina et al. (2012), solar energy as a carbon-free energy resource is been projected to take a leading role in meeting future energy demands. Figure 2.2 shows the photovoltaic installed capacity per capital of various countries around the world in 2011. South Africa and India have the smallest installed capacity compared to other developed countries, which can be attributed to the initial capital costs that are still a major barrier to the widespread adoption of solar photovoltaic technology, particularly in developing countries.

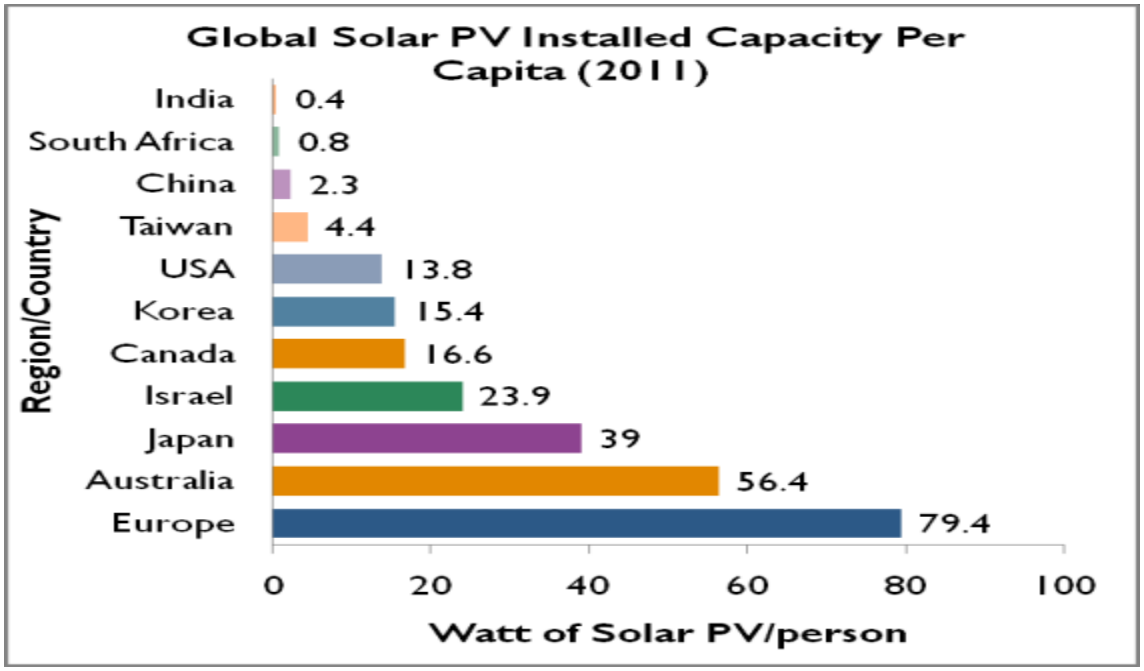

Figure 2.2: Solar photovoltaic installed capacity per capita for 2011. Source: Adapted from EPIA/Greenpeace (2011).

However, with or without political commitments, the long-term growth of solar energy is forecast to increase in capacity rapidly to about 1,845 GW by 2030, from around 40 GW in 2010. This forecast is based on the assumption that the present market supports are sustained, and that supplementary market support mechanisms will be put in place (EPIA, 2011). Similarly, a study conducted in 2008 by the International Energy Agency (IEA) based on two scenarios in which solar energy expansion are separated on the basis of global CO_2 emission reductions shows that solar photovoltaic global capacity is expected to rise from 11 GW in 2009 to 600 GW by 2050 for the first scenario. This first scenario involves restricting global CO_2 emissions at the 2005 level. In terms of the second scenario, global CO_2 emissions are reduced by 50% from the 2005 level, which will result in the installed capacity of solar PV exceeding 1,100 GW by 2050 (IEA, 2008).

The deployment of solar photovoltaics worldwide has continued to exceed the projections from various leading renewable energy agencies, thereby requiring the projections to be revised upwards each year a new report is issued (Brown et al., 2017). According to REN21 (2017), solar photovoltaic sets new record as the star performer by accounting for about 47% of the total newly installed renewable energy capacity in 2016. With solar prices falling rapidly across the globe, South Africa

emerged the leader for new installed capacity in Africa for the year 2016 with 0.5 GW installed (REN21, 2017). As a result of falling prices and new business models, more projects of varying sizes are springing up across the country (REN21, 2017). This has thus pushed the demand for information about solar photovoltaic potential estimates. This vacuum is quickly being filled with remote sensing and GIS technologies, by providing techniques to how such estimates can be derived.

Using a combination of remote sensing and GIS techniques, three main phases are involved in estimating the solar photovoltaic potential of building roofs. The first phase involves extracting the building roof outline in order to determine the roof area; the second phase involves calculating the amount of total solar radiation incident upon such roof; and lastly, the third phase involves estimating the solar photovoltaic potential, using the outputs from the two previous phases. However, a key requirement, in terms of input to the first and second phase is the LiDAR data processing and DEM generation, these are discussed in the following section.

2.6 LiDAR Data Processing

The processing of the LiDAR data can occurr in two stages: the first stage involves the classification of the LiDAR points, while the second stage generates the DSM and the nDSM from the classified LiDAR data, as discussed below.

2.6.1 LiDAR Points Classification

The classification of ground and non-ground points is the initial step in getting the raw LiDAR data ready for use in extracting building rooftops or estimating solar radiation (Morgan & Tempfli, 2000; Zhang et al., 2003; Kim & Shan, 2011). It involves separating ground and non-ground points. This can be achieved by using a height threshold to separate the ground points from non-ground points, using:

$$(T_h = H_g + X_m) \quad (2.1)$$

Where T_h denotes height threshold, H_g is the ground height and X_m is the offset in meters to separate ground and non-ground points. The ground height can be determined from an existing DTM (Awrangjeb, Zhang & Fraser, 2013). In instances, where there is no DTM, ground-filtering algorithms are employed to separate ground

points from non-ground points (Sithole & Vosselman, 2004). These filtering algorithms could be interpolation-based, slope-based or morphological (Liu, 2008).

In generating the ground height from the DTM, different offset values were adopted by various authors to distinguish between ground and non-ground points. Rottensteiner et al. (2004) and Awrangjeb et al. (2013) used 2.5m as their threshold, while Li et al. (2013) used 2m, and Awrangjeb and Fraser (2013) used 1m. Care should, however, be taken when choosing the offset threshold so as not to classify some low building points as part of the ground points. The intensity of the LiDAR returns can also be used in separating ground points from non-ground points by analysing the skewness and kurtosis of the LiDAR intensity (Yunfei et al., 2008).

The LiDAR point classification process can be automated, and this can be achieved by using the point cloud processing tools available in some Geomatics propriety software. For the purposes of this study, the LiDAR data utilised has been pre-classified into ground class and non-ground class by the vendor using LiDAR processing software. The non-ground points can be further classified by using the first and the last returns (Kim & Shan, 2011). This can be helpful in separating buildings from vegetation and generating height normalized points, by computing the height of each point relative to the ground point. The height normalized points can then be used directly to generate a normalized DSM, without having to subtract the DTM from the DSM. The lasheight tool from LAStools software can be employed to classify the LiDAR points by using the heights attribute. This functions by computing the height of each LiDAR point above the ground. Since the LiDAR data has been previously ground-classified, the ground points can then be triangulated to construct a ground triangulated irregular network (TIN). The elevation of each point is then computed with reference to the ground TIN.

2.6.2 Digital elevation model generation

The DEM as used in this study refers to all the elevation models, including the DTM, DSM and the nDSM. The DTM refers to elevation model showing the terrain only, while the DSM refers to the elevation model showing both the terrain and the features on the terrain. In creating an elevation model, important factors to be considered include the model type, the interpolation type and the resolution. These factors can be

adjusted to suit the intended purpose of the DEM and to achieve high-quality elevation models, which the LiDAR data avails. Different model types include the TIN, the regular grid and the contour line model (Ramirez, 2006). The regular square grid model is of most importance to this study. It uses a matrix structure to store the topological relationships between the data points, and each grid cell stores a single elevation value (Liu, 2008). Elevation values assigned to each cell are acquired by means of interpolation between neighbouring or surrounding points, depending on the type of interpolation adopted.

Interpolation can be described as the process by which values of variables are predicted within unmeasured locations, based on recorded or measured values at other areas within the same area of interest (Burrough & McDonnell, 2011). According to Childs (2004), interpolation is founded on the principle of spatial autocorrelation and/or spatial dependence, thus measuring the degree of dependence between near and distant entities. The interpolation technique is always utilised in terrain modelling to determine height values in areas where measurements are not available, by using the established heights of surrounding or neighbouring points. Interpolation becomes an important aspect of terrain modelling, since terrain surfaces are known to be continuous and terrain heights are highly correlative (Liu, 2008). Interpolation methods can be classified as either deterministic, such as Trend Surface Analysis (TSA), Inverse Distance Weighting (IDW), Natural Neighbours (NN), etc., or as stochastic (Geostatistical), such as krigging and cokrigging (Myers, 1994; Luo, Taylor & Parker, 2008). Deterministic interpolation generates surfaces based on mathematical expressions and measured points, while Geostatistical interpolators make use of statistics to generate surfaces, especially where some measure of certainty of prediction is required (Childs, 2004).

Each method of interpolation makes use of a different technique in assigning the output cell values; identifying the most suitable interpolation method to adopt depends on the distribution of sample points and the phenomenon being investigated (Childs, 2004). For the purpose of generating elevation models in this study, the binning technique of interpolation was adopted. Binning is not a real method of interpolation; rather it is an approach to speed up the rate of interpolation, while preserving the quality of the interpolation (Blaha & Paksoy, 2006). Binning basically averages the elevation values of points that fall within a grid cell, and assigns this value to the grid

cell. However, due to the non-uniform spacing of LiDAR point clouds and sizes of the grid cell (resolution), which may be adopted, there may be some cells with no data in the output grid (Blaha & Paksoy, 2006). This setback can be avoided, notwithstanding the irregular LiDAR points spacing or the specified grid cell size, by adopting a void fill method alongside the binning process, so as to assign elevation value to cells that do not contain any LiDAR point (ESRI, 2013). The Binning process could either be serial or parallelized (Blaha & Paksoy, 2006).

Typically, any of the deterministic interpolation methods could be used as the void fill interpolator. However, (ESRI, 2013) recommends the NN interpolation method (Sibson, 1980) for the sake of quality. The NN interpolator performs generally well with irregularly spaced and scattered points, as it uses an equation similar to that used in inverse distance weighting (IDW) (Childs, 2004). NN interpolation adopts a weighted average system based on the Voronoi diagram to determine both the weight to be assigned to each sample and the set of neighbours to select, based on their adjacency (Ledoux & Gold, 2005).

The last option to be considered is the resolution of the output raster expressed in grid cell size. The quality of a DEM is mostly measured or rated by this spatial resolution, which is controlled or determined by the data used in creating the DEM (Anderson et al., 2006). Spatial resolution, as pertaining to DEMs, refers to its grid cell size, expressed as a ground distance; the smaller the grid cell size, the higher the resolution of the DEM raster (Liu, 2008). Arriving at the optimal grid cell size is often a central problem in DEM generation (Liu, 2008). This could result in a situation, where a high-resolution DEM is imposing an unnecessarily heavy computational burden during processing. However, some applications do require the DEM to be of same resolution as another raster, especially if both are to be integrated during processing. This is evident in this study, where the DSM is required to have the same high resolution as the aerial imagery for the extraction of building roofs. In the case of solar radiation modelling, the spatial resolution could, however, be compromised to save computation time and computer memory allocation.

2.7 Detection and Extraction of Building Roofs

The detection and extraction of relevant features from remotely sensed data is fast becoming important in various fields of application, such as city planning, homeland security, disaster management, real estate industry and electricity utility among others (Cheng et al., 2008). The accurate extraction of the roof structure from a LiDAR data and/or aerial imagery is vital in estimating the rooftop solar photovoltaic potential of an area or region. However, 100% successful automatic extraction of buildings or rooftops is still an unachievable goal, as a result of scene complexity, incomplete cue extraction and sensor dependency (Sohn & Dowman, 2007). Building or rooftop detection techniques can be categorized into three groups, namely extraction from imagery, extraction from LiDAR data, or integration of imagery and LiDAR data (Lee, Lee & Lee, 2008).

According to Vu et al. (2009), the introduction of LiDAR indeed offered a favourable alternative for improving the level of automation in building detection and extraction, as compared to image-based extraction. However, some authors have identified various issues with object extraction using the LiDAR data alone. Awrangjeb et al. (Awrangjeb, Ravanbakhsh & Fraser, 2010) conclude that LiDAR usually provides more accurate height information but less accurate boundary lines, and that some regions in LiDAR data do possess null values as a result of the self-occlusion of a building or if water is present. Likewise, Cheng et al. (2008) found that it was hard to obtain a detailed and geometrically accurate boundary using only LiDAR point could.

In the following sub-sections, extraction of rooftop from imagery (Section 2.7.1) and from LiDAR data (Section 2.7.2), as well as from the combination of LiDAR data and imagery (Section 2.7.3) are discussed.

2.7.1 Extraction from Imagery

The earliest form of automatic extraction of man-made objects, such as rooftops, buildings and roads from urban scenes involved the use of aerial imagery. It has now become a topic of growing interest for remote sensing and photogrammetry professionals (Peng & Liu, 2005). Using stereopairs of high-resolution aerial imageries, objects are segmented into tiny pieces, and various forms of classification

algorithms are used to filter out unwanted objects or to extract desired object (rooftops), as the case may be (Baillard & Maıtre, 1999).

Cord et al. (2001) utilised aerial image stereopairs in a hierarchical approach to detect buildings in a complex image scene. Realizing dense and accurate height information is the key to building detection, and thus an efficient stereo matching scheme was designed to derive a dense digital elevation model (DEM). A global scene classification based on height data in the DEM was employed after image segmentation to classify height 'blobs', detected as either building or vegetation, by analysing their local surface normal dispersion. However, the automatic extraction of building from aerial imageries only has proven to be challenging, time-intensive and labour-intensive. According to Mayer (1999), the approaches provided are far from suitable in practice for imageries of diverse characteristics and difficult components. Another technique of extraction from imagery was demonstrated by Yuan (2016), by leveraging on thematic building footprints layers and 0.3 m resolution aerial imagery of entire Washington D.C. area to extract building rooftops using convolution networks.

2.7.2 Extraction of Objects from LiDAR

Extraction of objects from LiDAR data is fast becoming popular. Several countries, states and municipal departments, as well as private organizations, now use high-resolution LiDAR data for countless environmental, urban planning and cadastral mapping projects (Kodysh et al., 2013). The use of LiDAR data has provided faster and automated means of extracting rooftops, buildings or any other objects. A common approach in the literature is to classify or filter the LiDAR point cloud into ground and non-ground points; the non-ground points are further classified, using factors such as number of returns, return intensity and height thresholds to filter out unwanted objects (Kim & Shan, 2011). According to Hill et al. (2000), LiDAR points now offers an accurate and cheaper alternative to conventional technologies for creating DEMs in the form of digital terrain models (DTM) and digital surface models (DSM) at vertical accuracies of about 15 cm to 10 cm. These DSMs and DTMs then serve as a major input for the extraction of building roofs.

According to Zhang et al. (2006), the region growing algorithm based on a plane fitting method is often used to separate building points from its neighbours, mostly vegetation

and ground points. The algorithm functions by finding neighbouring points, which meet a specified height threshold, and fitting these into the defined plane; these points are then segmented into smaller patches. The patches are evaluated, using factors such as area, slope and roughness, to eliminate vegetation patches. Other patches, which meet the specified thresholds set for the building class are then classified as building points. Once the building points have been correctly classified, the next step in deriving an outline of the building roof using this approach is to connect the boundary points around each rooftop. This can be achieved by further processing the building classified points to construct a 2D Delaunay triangulation network, which detects the polygonal boundary. However, the resulting initial footprint is often noisy, since LiDAR points are irregularly spaced (He, Zhang & Fraser, 2014).

Deriving an accurate footprint from a complex and noisy polygon, according to Zhang et al. (2006), is quite challenging. Nevertheless, the raw footprint can be enhanced by generalization, and applying a least squares model to smoothen the edges (Sampath & Shan, 2004). Another method for generalizing footprint edges is the Douglas-Peucker algorithm, which generalizes edges by joining the start and end points initially, then repeatedly picking a point that is left having the largest distance to the edge until a set distance threshold is attained (Zhang, Yan & Chen, 2006). Zhang et al. (2006) applied a series of algorithms to extract building roof boundaries automatically using LiDAR data only. The raw LiDAR data was first filtered into ground and non-ground points using a progressive morphological filter. It was noted that the progressive morphological filter best suits coastal urban areas with a gentle slope, a type of terrain that applies to the study area. A region-growing algorithm based on the plane fitting technique was then used to detect building points from other non-ground points. The final stages of extracting the building footprint involved joining the boundary points around each building object detected earlier to obtain an initial building footprint. The initial footprints generated with jagged edges were then smoothed using a boundary generalization algorithm to obtain the final building boundary.

Other approaches employed in extracting building roofs using LiDAR data only were demonstrated by Lafarge et al. (2008), Kim and Shan (2011), amongst others. Buildings were automatically extracted from DEMs based on object approach by using a marked point process to derive a rough approximation of the building footprint by means of rectangles. The rough rectangular footprints were then regularized by fusing

and improving the connection between nearby rectangles and detected roof boundaries (Lafarge et al., 2008). The level set approach was utilised by Kim and Shan (2011) to extract building roofs. The normal vector on each of the LiDAR points of the building was determined, while analysing the local planarity at each point to exclude non-planar points on the roof edges. An initial level set function, represented as surfaces, was defined to enclose all building points. Segmentation was carried out by minimizing the energy function formulated as a multiphase level set, while roof boundaries were extracted by intersecting adjacent roofline segments, which connect based on their topological relationships, as inferred from the segmentation result. More recent approaches in utilizing LiDAR data (also referred to as Airborne Laser Scanner data) to extract building now have benchmarked dataset and results to compare results with in other to achieve better accuracies(Tomljenovic, Tiede & Blaschke, 2016; Jarząbek-Rychard & Maas, 2017).

2.7.3 Integration of Imagery and LiDAR

The integration of LiDAR with imagery provides complementary benefits in extracting features, especially building rooftops, as each technique compensates for the shortcomings of the other (Awrangjeb, Ravanbakhsh & Fraser, 2010). The combination of LiDAR and imagery to extract building roofs offers increased options, such as the use of height, spectral and intensity information. The imagery referred to in this approach can either be aerial imagery or satellite imagery. It is of the utmost importance that the LiDAR and imagery data were acquired around the same time. Moreover, the elevation model to be generated from the LiDAR data and the aerial imagery should have the same or a similar spatial resolution and to be co-registered. This is essential to avoid a ‘saw-tooth’ distortion between the imagery and the DSM (Trimble, 2010).

Various authors have used different combinations of such options in their extraction processes as explained below. These processes can be further differentiated into “Edge Detection and Extraction” and “Rule-based Classification”. Both approaches make use of elevation models derived from LiDAR data. In both cases, the raw LiDAR data is passed through pre-processing or classification. The desired end product is a normalized digital surface model (nDSM) from the interpolation of the LiDAR points.

Edge detection involves using algorithms to locate discontinuities in intensity values within an image scene. Edge detectors function by searching for areas within an image scene, where brightness changes swiftly within a short distance (Li et al., 2013). A commonly used edge extraction algorithm is the “Canny” edge detector, which detects edges by first smoothing the image using Gaussian convolution, before then applying a 2 dimensional first derivative to determine the gradient magnitude and direction in both the horizontal and the vertical direction (Canny, 1986). Thereafter, the next step is to apply non-maximal suppression processes to the gradient image, and finally, an edge tracking process controlled by two thresholds is employed to detect the object’s edges (Li et al., 2013).

This same edge tracing algorithm was also employed by Awrangjeb et al. (2010) and Awrangjeb et al. (2013), to detect building roof outlines. Since their interest is on extracting building footprints alone, building objects were separated by generating ground and above-the-ground masks. This is then used in conjunction with the Normalized Difference Vegetation Index (NDVI) to remove vegetation objects from non-ground objects, leaving only the initial building objects (Awrangjeb, Ravanbakhsh & Fraser, 2010). The edge tracing algorithm can now be utilised on the aerial imagery, using the initial building position mask generated from the previous step to obtain the edges of the building objects. However, some small line segments that are not part of the building still exist, and these were removed using a 3m threshold. Detected corners and edge endpoints that are not properly aligned are fixed by using a least square straight-line fitting technique (Awrangjeb, Ravanbakhsh & Fraser, 2010).

In another approach, described by Awrangjeb et al. (2013), building roof edges are identified by first applying the “Canny” edge detector to the grey-scale version of the image. The resultant lines are then classified into various classes, such as ground, roof edge, roof ridge and tree, using the ground mask image, texture information from entropy and NDVI information. Similarly, Sohn et al. (2007) first identify features that are above a specified height threshold above ground level, before using the NDVI and other spectral information to detect buildings. To extract the final building roof boundaries, sharp edges of building were detected and polygons were matched to these edges.

Following a similar approach, DongHyuk et al. (2008) also combined information from LiDAR data and imagery to extract building boundaries. The initial building region was extracted from the height information provided by the LiDAR data; thereafter, this was improved upon by enhancing the initial boundary using the colour information obtained from the aerial imagery. Edge matching and close loop construction was applied in post-processing to obtain the final building boundaries. Adopting the object-oriented rule-based classification approach, Demir et al. (2008) integrated LiDAR and imagery data by comparing four different methods of extracting building boundaries. The first method used a comparison of DSM and DTM in combination with NDVI analysis; the second method was based on supervised multispectral classification complemented by the height information extracted from the LiDAR data. The third method utilised the voids in LiDAR-derived DTM and NDVI classification, while the fourth method centred on the analysis of the DSM's vertical density.

The combination of DSMs and intensity raster derived from LiDAR with orthoimage was used as input by Uzar and Yastikli (2013) to enable them to extract building boundaries automatically. Using object-oriented image analysis, a combination of segmentation techniques, including contrast split, chessboard and multi-resolution segmentation was employed to segment the input images into smaller homogeneous objects. The rule-based classification was then applied in hierarchical order, starting with the classification of vegetation, followed by classification of the ground class, and finally, classification of the building class. Intensity rasters coupled with morphological operations were used to improve the accuracy of classifying the building objects.

For the purposes of this study and given the type of data available for the study area, the integration of LiDAR data with aerial imagery using rule-based classification is considered adequate to extract the building roof outlines. Rule-based classification can be said to comprise the combination of pixel and object-based classification. Rule-based classification involves exploring features of interest in an image scene with a view to determining various characteristics that can be used to separate or extract them from other features in the image.

Various algorithms are utilised in detecting the feature of interest, depending on the software employed. Both features of interest and non-interest are then assigned to the appropriate classes created for them, as soon as they are detected. Rule-based

classification systems are particularly important when ancillary data are to be incorporated in image classification, which becomes difficult for a typical classification technique to implement (Lawrence & Wright, 2001). Major steps involved in rule-based classification include segmentation and classification.

Segmentation is the process of splitting an image into smaller homogenous pieces based on variations in the pixel grey values, texture or other supplementary data (Jinmei & Guoyu, 2011). The outcome of a segmentation process is determined by parameters such as thresholds and seeds, depending on the application used and the data employed. Therefore, a few trials might be required before the substantive parameters can be identified and adopted (Bouziani, Goita & He, 2010). Seed or seed pixel in image segmentation refers to the starting point or location from which a desired action originates (Baatz & Schäpe, 2000; Muñoz Pujol, 2003). While threshold refers to the critical value within a set of values, which determines the point at which an action or process takes effect on a particular value or set of values (Tobias & Seara, 2002). The most basic and simplest form of segmentation is called thresholding (Muñoz Pujol, 2003).

Other segmentation algorithms can be sufficiently classified as region-based and boundary-based (Carleer, Debeir & Wolff, 2005). The region-based algorithms attempt to segregate image areas that are similar, using a specified set of attributes; examples include region growing, split and merge methods, etc. (Muñoz Pujol, 2003). The boundary-based algorithms detect image object edges using discontinuity properties within an image scene; examples include watershed segmentation and optimal edge detector (Carleer, Debeir & Wolff, 2005). A combination of the methods of segmentation is recommended, as it is difficult to get satisfactory results using only ones of these methods (Muñoz Pujol, 2003).

Considering segmentation algorithms available within the eCognition developer software used; they include chessboard, multi-resolution, quadtree, and contrast split, amongst others; the multi-resolution segmentation (MRS) algorithm is more popular and commonly used (Zuo, Chen & Zhang, 2014). The MRS algorithms was used in this study to detect building roofs for extraction. The chessboard segmentation algorithm splits an image scene into specified grid (square) tile size, creating image

objects, these are then classified based on rules set to form desired image object (Definiens, 2007).

The MRS algorithm was developed by Baatz and Schäpe (2000); it is a technique involving multi-scale image segmentation based on region merging. The algorithm begins with each pixel in the image scene creating one image object or region. At each level, a pair of the image object may be merged, using a merging decision threshold based on local homogeneity criteria, to merge the objects into a larger image object (Baatz & Schäpe, 2000). Basic parameters that affect the MRS algorithm are image layer weight, scale parameter, smoothness and compactness (Definiens, 2007). The image layer weight parameter is used to specify the extent to which an image layer will be participating in the segmentation process; the higher the weight assigned to a particular layer, the more of its information will be required in the segmentation process (Definiens, 2007). An image layer refers to image bands representing different parts of the electromagnetic spectrum, or they may be other layers, such as slope, DSM layer, etc. The scale parameter is used to manipulate the size of image objects by defining the maximum allowed heterogeneity for the output image objects. This depends on the homogeneity criteria, which include colour, smoothness and compactness, of which the colour criterion is the most important when seeking to create meaningful objects, while the shape criteria (smoothness and compactness) are helpful in avoiding fractured image object output (Definiens, 2007).

Based on the segmented homogeneous pieces, or primitives, various characteristics or attributes of the desired object(s), such as colour, shape, texture, area and height in the image scene are explored, using various fuzzy logic operators. Threshold setting plays an important role in classification, as this determines how objects are allocated to different classes; the application of fuzzy logic operators on segmented object primitives using the definitive thresholds is referred to as the rule-sets application (Uzar & Yastikli, 2013). The moment that objects of interest are detected after applying these rule-sets, a command is given to assign such homogenous pieces into the appropriately labelled class. Common cues used in detecting buildings include height, texture, rectangular fit, elliptic fit, area and compactness amongst others (Jabari & Zhang, 2013). The first level of classification does not usually produce the desired result. Therefore, a post-classification process might be required before the final classification can be accepted.

Once the building roofs have been successfully extracted, the next step in the evaluating the solar photovoltaic potential of the building roofs is to model the solar radiation over the roof to obtain an estimate, this process is discussed in the following section.

2.8 Modelling Solar Radiation

It is important to understand how much solar radiation is reaching the earth surface, as so many human and even plant activities depend on it (Fu & Rich, 2000). Solar radiation can be described as the amount of solar energy incident upon the earth's surface. The actual amount of solar radiation available on a roof surface is the single most important factor that affects electricity generation from solar photovoltaic panels (Carl, 2014). The radiation, which originates from the sun, is modified as it travels through the atmosphere; it is also affected by the topography and the nature of surface features (ESRI, 2012b). Solar radiation comprises three components, namely, direct beams from the sun, diffused beam, and ground reflected radiation (Perez et al., 1987). The direct beam travels unimpeded in a direct line from the sun, the diffuse radiation is scattered, as it comes in contact with atmospheric elements, such as dust and clouds, and the reflected radiation bounces off the surface of the intercepting feature (see Figure 2.3). The combination of the direct, diffuse and reflected radiation is referred to as the global or total solar radiation (ESRI, 2012b).

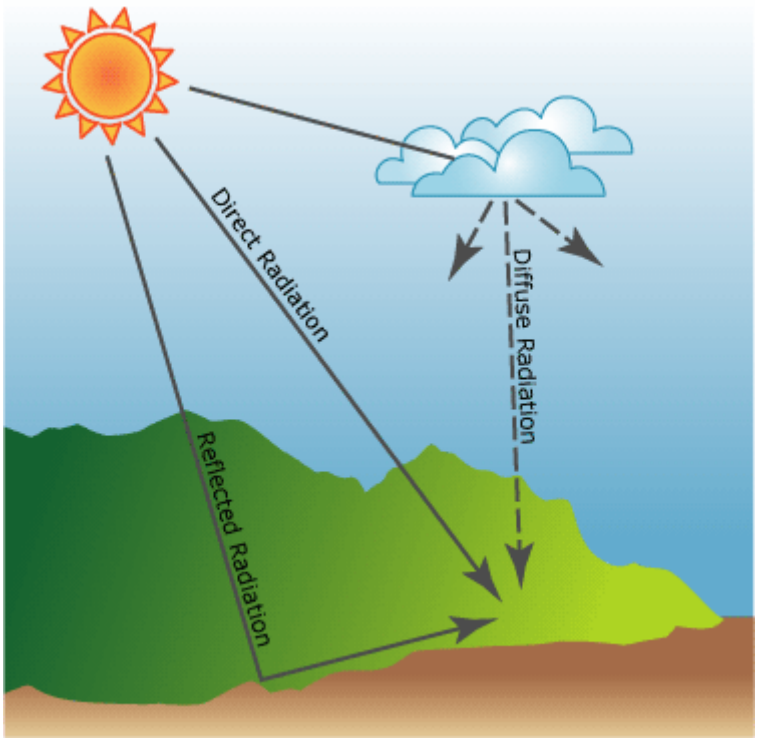

Figure 2.3: Components of incoming solar radiation. Source: ESRI ArcGIS Online Resources (2012b).

There are three techniques of generating spatially continuous irradiance values for any surface. These three techniques do have some areas of correlation, but there is a distinction about the source of data and/or the techniques used. The three categorization is given as follows;

- Ground meteorological station data based solar radiation models
- Meteorological satellite data based solar radiation models
- GIS-based solar radiation models

Each of these categories listed above has its strength and weakness. The ground weather stations have the capability to directly or indirectly measure accurate solar radiation at its location per time, but to derive a continuous irradiation values for areas off the weather station, mean historical data and different interpolation techniques are used. Apart from errors that could arise from the interpolation technique, this model lacks adequate modelling of terrain or surface characteristics during the interpolation. Terrain characteristics are one of the determinant factor in how solar radiation interacts with the landscape (Hofierka & Suri, 2002).

In some locations where there are no ground meteorological stations, satellite-derived weather data can be used to model solar radiation estimates. It provides a better

estimate of solar radiation data at any location more than 25km from the closest ground weather station (Dean et al., 2009). However, it uses the same concept as that of ground-based station model in deriving a continuous irradiation values. Also, these models are characterized by low resolution at around 10km grid (Dean et al., 2009). According to Hofierka and Suri (2002), satellite-derived solar data processing provides less accurate values in comparison to ground-measured data. It is however, advantageous when large areal coverage is required at temporal resolution of 0.5 – 12 hours (Hofierka & Suri, 2002). Solar radiation modelling in GIS is further presented below.

2.8.1 GIS-based Solar Radiation Modelling

Solar radiation models integrated within the GIS provides an efficient and accurate means of estimating solar radiation over any surface. Using these models, surface characteristics such as slope, orientation and shadow are efficiently modelled and considered in providing radiation estimates (Dean et al., 2009). According to Dean et al. (2009), incorporating surface characteristics is one of the most accurate means of modelling the rooftop solar potentials. Solar radiation models incorporated within the GIS environment functions by first modelling the available extra-terrestrial radiation by considering the earth's geometry, rotation and revolution. This can be calculated precisely using astronomic expressions (2009). The second factor involves modelling the atmospheric attenuation caused by clouds, gases, solid and liquid particles. This is often the common source of error in GIS-based models, as its modelling is quite complex because of its dynamic nature and can therefore, be modelled to only a certain level of accuracy (Kodysh et al., 2013). The third factor considered is the terrain or surface characteristics, this can be modelled accurately using a surface model. The resolution of the surface model thereby has a significant effect on the radiation estimate. Therefore, care must be taken to ensure that the resolution of the digital surface model (DSM) used in the estimation of solar radiation accurately reflects the distinctive attributes of the surface of interest, such as aspect, slope and adjacent features (Hofierka & Suri, 2002).

Some of these models were developed using numerical simulation, analytical and statistical approaches such as Tymvious et al. (2005). Other models have also been developed using GIS; they include SolarFlux by Dubayar and Rich (1996), for ArcInfo

GIS, the SRAD model by Wilson and Gallant (1998), the ESRI Solar Analyst by Fu and Rich (2000) and the r.sun model in GRASS GIS by Hofierka and Suri (2002) among others. The integration of solar radiation models into GIS has helped to circumvent the intricacy of incorporating GIS functions into mathematical models (Šúri & Hofierka, 2004). The GIS integrated model is an efficient and accurate means of estimating solar radiation over vast areas, while the effects of local terrain are considered (Wiginton, Nguyen & Pearce, 2010). These models have been applied by various authors in determining the solar photovoltaic potential of different regions of the world.

The most important input used in calculating global solar radiation using the GIS-based models is the DEM. Therefore, it can be inferred that the accuracy of the input DEM directly affects the accuracy of the solar radiation or insolation calculation. Care must be taken, however, to ensure that the resolution of the DEM used in the estimation of solar radiation accurately reflects the distinctive attributes of the roof, such as aspect, slope and adjacent features (Kodysh et al., 2013). Processes involved in generating a DEM from raw LiDAR data has already been discussed in the Section 2.6.2. The various solar radiation models differ from each other in their treatment of the diffuse component of solar radiation – this is the key difference between them. The diffuse component is often the prime source of estimation error, as it depends on climate and local terrain conditions (Šúri & Hofierka, 2004).

From the foregoing, it is evident that estimation of solar radiation for building-integrated solar photovoltaic systems, using the GIS-based solar radiation model, provides a better estimate compared to the other two methods. This has been demonstrated by some studies such as Hofierka and Suri (2002), Dean et al., (2009), Camargo et al., (2015), amongst others. However, none of such studies was carried out in Africa, this study would therefore attempt use the GIS-based model in this study and validate it. The estimation of solar radiation will be discussed below, with the first two sections looking at the two most prominent GIS-based models available, namely, Solar Analyst in ArcGIS and r.sun in GRASS GIS, and the third section looking at the comparison between Solar Analyst and r.sun model.

2.8.2 Modelling in ArcGIS

Solar radiation is modelled in ArcGIS using the Solar Analyst, which is now called the 'Solar Radiation Toolset' under the Spatial Analyst extension (ESRI, 2012b). It has the capability of calculating solar radiation for point locations as well as for entire geographic areas. The estimation of solar radiation is achieved following these four steps:

- Calculation of an upward looking hemispherical viewshed based on local surface relief
- Overlay of the above viewshed on a sunmap to calculate direct radiation
- Overlay of the viewshed on skymap to calculate diffuse radiation
- Reiterating the process for a specified location or area of interest to produce an insolation map

The key calculations in each step are discussed below (ESRI, 2012b).

Viewshed Calculation

Solar radiation over a particular surface is greatly affected by the topography and surrounding features of an area, because the amount of visible sky above a point or area determines the access of such area to solar radiation. The viewshed for a particular point or area thus provides a raster representation of a portion of the sky, visible or obstructed, as viewed from that location in an upward manner. A viewshed is calculated by searching and determining the horizon angle to the object that might be obstructing the sky from a location of interest (ESRI, 2012b).

The horizon angles are then interpolated for other unsearched directions and converted to the hemispherical coordinated system. Each cell of the viewshed raster is finally assigned a value, denoting either that the sky is visible at that location or that it is obstructed. This is illustrated in Figure 2.4(b), with the grey area depicting the obstructed region and the remaining area being visible to the sky.

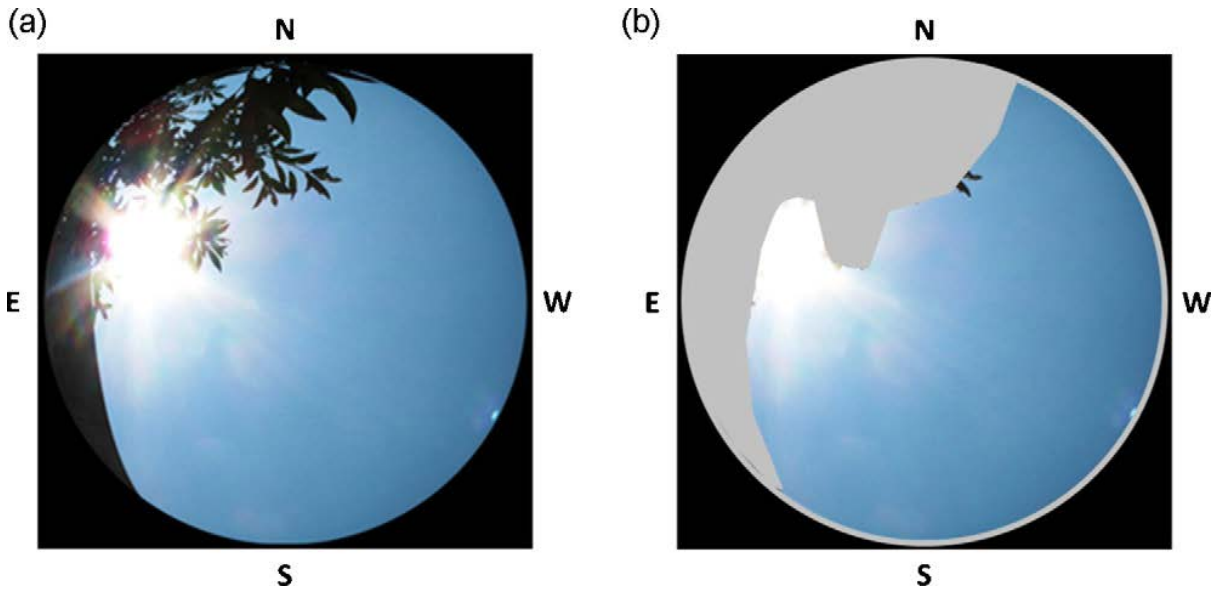

Figure 2.4: (a) Hemispherical image captured by an upward looking camera; (b) Overlay of viewshed raster on the hemispherical image. Source: (Kodysh et al., 2013)).

Sunmap Calculation

The sunmap is used to calculate the direct solar radiation from each sky direction by overlaying the viewshed created earlier on the sunmap. It is a raster map that shows the track of the sun, as it moves from sunrise to sunset of a specified day or time. The sunmap is calculated using standard astronomical formulae based on the latitude of the study area and time configuration supplied as parameters (ESRI, 2012b). Figure 2.5 shows the sunmap calculated for a specified time range, viz. December 22 to June 22 (winter solstice to summer solstice), however, this is peculiar to areas in the Northern hemisphere. Each colour box denotes the sun sector, viz. the position that the sun occupies, using a 30-minute daily interval and a monthly interval for the year.

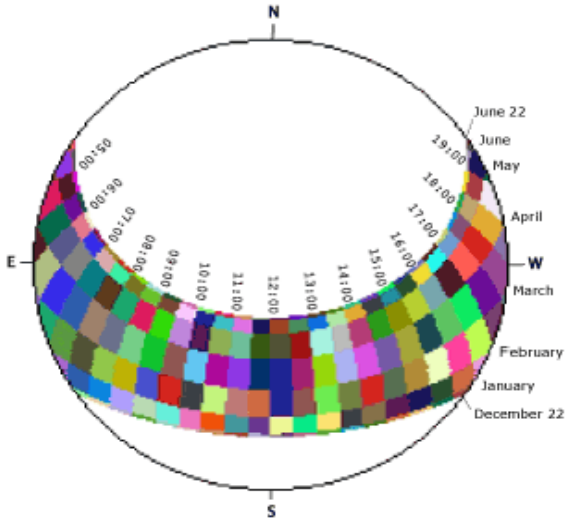

Figure 2.5: Sunmap for December 22 – June 22. Source: ESRI ArcGIS Online Resources (2012b).

Skymap Calculation

The skymap is utilised in estimating the amount of diffuse solar radiation over a specified location. The skymap is created by dividing the entire sky into a series of sectors, which are defined by the zenith and azimuth angle of the particular location. Each of the divided sky sectors are then assigned a unique value to identify whether this corresponds to the calculated centroid zenith and azimuth angles (Fu & Rich, 2000). Figure 2.6 shows a skymap divided into 8 zenith division by 16 azimuth divisions, each colour denotes a single sky sector from which the diffuse radiation originates.

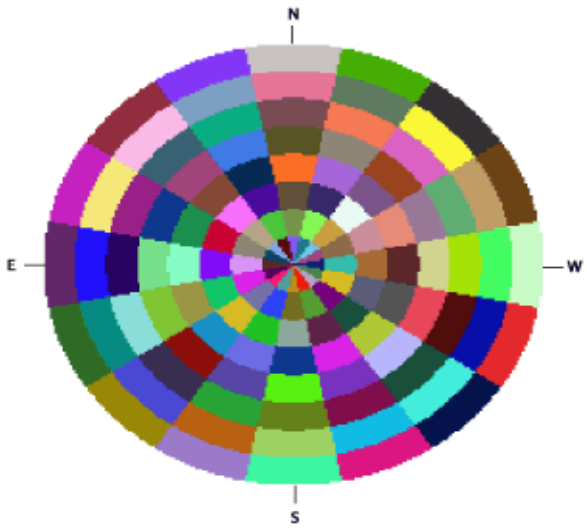

Figure 2.6: Skymap with sectors defined by 8 zenith by 16 azimuth divisions. Source: ESRI ArcGIS Online Resources (2012b).

Insolation Calculation

This is the final set of calculations involved in estimating the global solar radiation of any location of interest. Firstly, the viewshed raster is overlaid on the sunmap and skymap (see Figure 2.7), so as to determine the unobstructed portion of sky area (gap fraction). This is achieved by dividing the number of unobstructed cells by the total number of cells in that sector (Fu & Rich, 2000).

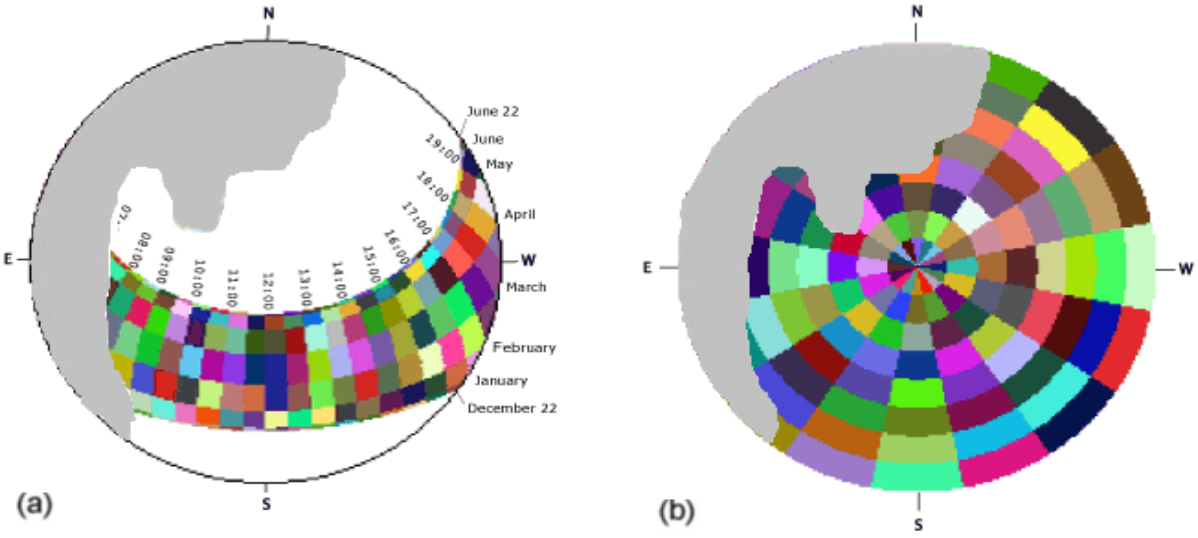

Figure 2.7: Overlay of viewshed with sunmap and skymap. Source: Adapted from ESRI ArcGIS Online Resources (2012b), Kodysh et al. (2013).

The total direct solar radiation of a particular location is given as the sum of the direct insolation from all unobstructed sunmap sectors. This is calculated based on the gap fraction from an overlay of the viewshed with the sunmap, atmospheric attenuation, the sun position from sunmap calculation and the ground receiving surface orientation of the location (Fu & Rich, 2000):

$$Dir_{total} = \sum Dir_{\theta,\alpha} \qquad (2.2)$$

Where ($Dir_{\theta,\alpha}$) is the direct solar radiation for each sunmap sector.

Similarly, the total diffuse solar radiation for a location is calculated as the sum of all diffuse solar radiations at each skymap sector:

$$Dif_{total} = \sum Dif_{\theta,\alpha} \qquad (2.3)$$

Where ($Dif_{\theta,\alpha}$) is the diffuse radiation for each skymap sector.

Finally, the global solar radiation is obtained by calculating the sum of total direct radiation and the total diffuse radiation given as (Fu & Rich, 2000):

$$G_{sr} = Dir_{total} + Dif_{total} \quad (2.4)$$

Brito et al. (2012) used the ArcGIS Solar Radiation Tool to calculate the photovoltaic potential of a Lisbon suburb, considering only rooftops with a slope less than 45^0. Also, Kodysh et al. (2013) utilised the Solar Radiation toolset in ArcGIS to estimate the solar potential of multiple rooftops in Knox County, Tennessee, USA. After the pre-processing steps of deriving the DSM from the raw LiDAR data, the DSM was further refined to remove any undesirable features that could add to the computation time of the solar radiation calculation. This was achieved by creating a buffer of 25m around each building; all features that fall with this buffer zone were retained in the final DSM, while others were discarded. The area-based model of the Solar Radiation toolset was then utilised in estimating the monthly solar intensity values of each rooftop. Recent applications of the ArcGIS Solar radiation in modelling solar radiation over building roofs in the town of Miraflores de la Sierra in Madrid, Spain. The modelling took into consideration features around each building by developing additional equation, however, the equation could not be implemented across board, because of intensive computational time (Martín, Domínguez & Amador, 2015).

2.8.3 Modelling in GRASS GIS

The r.sun model is implemented in the GRASS GIS, which is an open source software. It functions in two modes: Mode 1 calculates the solar irradiance of an area or point for an instant of time (in seconds), and generates raster maps of the selected components, such as beam, diffuse and reflected radiation. Mode 2 computes the daily sum of solar irradiance and the duration of beam irradiation in minutes from the integration of irradiance values calculated for a specified time step, ranging from sunrise to sunset (Hofierka & Suri, 2002).

It has the capability of calculating both the clear-sky irradiance as well as the overcast values, provided the clear-sky index is defined. Obstructions to the clear sky by nearby terrain features can be modelled by using an optional shadowing parameter. These shadows can be modelled separately using the r.horizon module, which further speeds up the calculations for large and high-resolution raster input (Hofierka et al., 2014).

Data inputs required to run the model include elevation above sea level in the form of the DEM, slope and aspect derived from the DEM, and time specification; all of these are compulsory. Other optional inputs are the parameters that are either computed internally, using the supplied mandatory inputs, or they can be specified manually to fit each user's specifications. Such parameters include the clear-sky, ground albedo, Linke turbidity, time step-up and sampling distance for raster cell visibility (Hofierka & Suri, 2002).

The r.sun model was successfully implemented in building a solar database for the assessment of photovoltaic systems in Central and Eastern Europe, covering ten European Union candidate countries, viz. Slovenia, Slovakia, Romania, Poland, Lithuania, Latvia, Hungary, Estonia, Czech Republic and Bulgaria. In achieving this, the clear-sky global irradiation on horizontal surfaces was computed first, followed by the calculation and spatial interpolation of the clear-sky index, coupled with the generation of raster maps of the total irradiation on horizontal surfaces. The last step involved computing the beam and diffuse components of the overcast total irradiation together with raster maps of global irradiation on inclined surfaces (Šúri, Huld & Dunlop, 2005).

Subsequently, this model has been used by others in estimating the potential of solar photovoltaic installations. Nguyen and Pearce used it in parts of Ontario, Canada, whereas Alvarez et al. (2011) used it in the south-central region of Chile, to estimate monthly global solar radiation. Nguyen and Pearce (2010) used the r.sun model in the open source GRASS GIS to estimate the potential photovoltaic yield in parts of Ontario, Canada. They divided this method into three stages, namely, pre-simulation, simulation, and post-simulation. The pre-simulation stage involved gathering and processing input data, such as DEMs, slope and aspect maps, land-use classification maps, etc. The outputs generated from the pre-simulation stage served as inputs for the second stage. The simulation stage involved running the r.sun model tool itself; the second mode, which calculates the sums of monthly solar irradiance for a specified year, was chosen. The final stage, post-simulation, involved using the multi-criteria evaluation (MCE) and analytic hierarchy process capabilities available in GIS to select optimal sites for the study area.

2.8.4 Comparison between Solar Analyst and r.sun

The two solar radiation models discussed above utilize the same topographical information, such as slope, aspect and shadow from the input DEM in estimating the solar insolation of any desired surface or feature. However, different approaches and assumptions were followed in arriving at the global solar radiation value (Ruiz-Arias et al., 2009). Some of these differences are discussed below under the headings of reflected radiation and atmospheric attenuation.

Reflected Radiation

Solar Analyst assumes that the reflected radiation component of the total solar radiation constitutes an insignificant portion of the total radiation. However, there are exceptions for an area that is surrounded by high reflectivity surfaces. Therefore, direct radiation, which is the largest component of total solar radiation, and diffuse radiation, which is the second largest, were used in calculating the total solar radiation (ESRI, 2012b).

In contrast, the r.sun model accounts for the ground reflected radiation component of the global solar radiation. According to Suri and Hofierka (2004), the estimation of clear-sky reflected radiation for inclined surfaces relies on an isotropic assumption, and is calculated as proportional to the total radiation (the sum of direct and diffuse radiation) to the mean ground albedo and to the fraction of the ground viewed by an inclined surface.

Atmospheric Attenuation

The Solar Analyst model accounts for atmospheric attenuation by means of direct atmospheric transmissivity under the uniform diffuse model and the standard overcast diffuse model. It utilizes a geometric approach, which divides the entire sky into smaller sectors, defined by their zenith and azimuth coordinates (Ruiz-Arias et al., 2009). The r.sun model, accounts for atmospheric attenuation under conditions of sunlit, potentially sunlit and shadowed surfaces, using the Linke atmospheric turbidity coefficient (Šúri & Hofierka, 2004).

Irrefutably, it is worth noting that Solar Analyst offers a vast advantage over the r.sun model in flexibility and user friendliness (Fu & Rich, 2000). However, the r.sun model

has been extensively tested and found to present more advantages over the popular Solar Analyst and other GIS-based models (Ruiz-Arias et al., 2009; Jakubiec & Reinhart, 2012; Camargo et al., 2015). Some of the advantages delivered by the r.sun model include providing better estimates, accounting for reflected radiation and speed, it takes significant hours to calculate the solar radiation estimate from large DEM raster files, using Solar Analyst, compared to the few minutes taken by the r.sun model, especially if the shadowing factor has been modelled previously using the r.horizon tool. Another major advantage is its open source implementation, which creates an opportunity for convenient scripting and modifications (Hofierka & Suri, 2002).

Considering the differences in approach to solar radiation estimation, the r.sun model in GRASS GIS open-source software presents overreaching advantages over the Solar Analyst in estimating the solar radiation for the study area. These advantages are highlighted below.

According to Suri and Hofierka (2002), Solar Analyst in ArcGIS is not flexible enough for modelling the atmospheric attenuation and diffuse components of the global solar radiation because it only allows settings for the available parameters of the nearest weather stations or just representative values. Also, it is only suitable for fine-scale studies (smaller areas), thereby limiting its usefulness for larger areas. The features presented in the r.sun model eliminate the shortcomings identified with Solar Analyst, and in addition, its open-source deployment makes it more accessible for improvements (Hofierka & Suri, 2002).

Similarly, a comparative analysis of four (4) solar radiation models carried out by Ruiz-Arias et al. (2009) shows the r.sun model in GRASS GIS to be the most sensitive to the spatial resolution of DEM used and significantly faster in processing time, compared to Solar Analyst in ArcGIS, SRAD and Solei-32 models. The reliability of Solar Analyst also decreases in autumn and winter, whereas the performance of r.sun and Solei-32 remains quite stable throughout the year. Although all the compared models underestimate the amount of solar radiation when compared with the solar radiation estimate derived from data from the observed ground station, the r.sun models gave the closest estimate. The clear-sky solar radiation estimation model as applied in the r.sun tool of GRASS GIS software thus represented an improvement, based on a previous study undertaken for the development of the European Solar

Radiation Atlas (Greif, 2000; Rigollier, Bauer & Wald, 2000; Page, Albuisson & Wald, 2001). Having considered the factors leading to the choice of the r.sun model in GRASS GIS to model the global solar radiation, the techniques used in arriving at the global solar radiation estimate is discussed below.

2.8.5 Clear-sky Solar Radiation

The sum of the beam (direct), diffuse and reflected radiation component in clear-sky conditions are used by the r.sun model to estimate the global solar radiation of an area (Hofierka & Suri, 2002). The basic equations used in estimating these three components are presented as follows:

Beam (direct) radiation

The beam radiation component is estimated by modelling the extra-terrestrial irradiance, denoted as G_o. The extra-terrestrial irradiance is essentially the solar constant (I_o), known to be 1,367 $W.m^{-2}$ (Rigollier, Bauer & Wald, 2000; Rigollier, Bauer & Wald, 2000), but due to the sun-to-earth distance, which varies marginally across the year, a correction factor (ε) is applied to the extra-terrestrial irradiance:

$$G_o = I_o \varepsilon \qquad (2.5)$$

Where $\varepsilon = 1 + 0.03344 \cos (j' - 0.048869)$, and $j' = 2\pi j/365.25$, and j is any day of the year from 1 to 365. The beam irradiance normal to the solar (B_{oc}) is diminished by the clear atmosphere and calculated as:

$$B_{oc} = G_o \exp \{-0.8662 T_{LK} m \delta_R(m)\} \qquad (2.6)$$

The expression ($-0.8662T_{LK}$) refers to the air mass 2 Linke atmospheric turbidity factor and the parameter (m) represents the relative optical air mass (Šúri & Hofierka, 2004). Therefore, the beam irradiance on a horizontal surface denoted as B_{hc} in $W.m^{-2}$ is calculated as:

$$B_{hc} = B_{oc} \sin h_o \qquad (2.7)$$

Where h_o is the solar altitude angle

The beam irradiance on an inclined surface denoted as B_{ic} ($W.m^{-2}$) is now calculated as:

$$B_{ic} = B_{oc} \sin \delta_{exp} \quad (2.8)$$

Or

$$B_{ic} = B_{hc} \sin \delta_{exp} / \sin h_o \quad (2.9)$$

Where δ_{exp} is the solar incidence angle between the sun and the inclined surface (Hofierka & Suri, 2002).

Diffuse radiation

The diffuse radiation depends largely on the Linke turbidity factor for any solar altitude (Rigollier, Bauer & Wald, 2000). Likewise, the diffuse radiation increases as the turbidity increases, while the beam irradiance decreases (Hofierka & Suri, 2002). However, the diffuse irradiance may fall, as turbidity increases at much lower solar altitudes, due to a high loss of radiative energy in the atmosphere, especially along long paths (Rigollier, Bauer & Wald, 2000). Therefore, the diffuse irradiance on a horizontal surface (D_{hc} [$W.m^{-2}$]) is estimated as the product of extra-terrestrial irradiance (G_o), diffuse solar elevation function (F_d) and a diffuse transmission function (T_n), which depends entirely on the Linke turbidity factor (T_{LK}) (Hofierka & Suri, 2002).

$$D_{hc} = G_o F_d(h_o) T_n(T_{LK}) \quad (2.10)$$

The diffuse solar elevation (F_d) function is expressed as:

$$F_d(h_o) = A_1 + A_2 \sin h_o + A_3 \sin^2 h_o \quad (2.11)$$

While the diffuse transmission function $\{T_n(T_{LK})\}$ is evaluated using the following expression:

$$T_n(T_{LK}) = -0.015843 + 0.030543\, T_{LK} + 0.0003797\, T_{LK}^2 \quad (2.12)$$

The model used in estimating the diffuse irradiance on an inclined surface (D_{ic} [$W.m^{-2}$]) under a clear sky differentiates between sunlit, potentially sunlit and shadowed surfaces (Hofierka & Suri, 2002).

For sunlit inclined surfaces, if $h_o >= 0.1$ (in radians):

$$D_{ic} = D_{hc} \{F(\gamma_N) (1 - K_b) + K_b \sin \delta_{exp}/\sin h_o\} \quad (2.13)$$

If $h_o <= 0.1$

$$D_{ic} = D_{hc} \{F(\gamma_N) (1 - K_b) + K_b \sin \gamma_N \cos A_{LN}/(0.1 -0.008 h_o)\} \quad (2.14)$$

For shadowed surfaces:

$$D_{ic} = D_{hc} F(\gamma_N) \quad (2.15)$$

Reflected radiation

The reflected irradiance of an inclined surface under the clear-sky condition depend on an isotropic assumption. It is estimated as the global horizontal radiation (sum of beam and diffuse irradiance) $G_{hc,}$ which is proportional to the mean ground albedo (ρ_g) and to a fraction of the ground viewed by an inclined surface (r_g (γ_N)) (Hofierka & Suri, 2002).

$$R_i = \rho_g G_{hc} r_g (\gamma_N) \quad (2.16)$$

Where r_g (γ_N) = (1 – cos γ_N)/2 and $G_{hc} = B_{hc} + D_{hc}$

Having considered the extraction of building roof and solar radiation modelling, the next step involved in estimating the solar photovoltaic potential of a building roof is to combine the output from the extraction of building roof planes and the estimation of solar radiation with other factors, which will be discussed in the following section.

2.9 Evaluating Solar Photovoltaic Potential

Aguayo (2013) argued that two important conditions had to be fulfilled in defining suitable areas for solar photovoltaic installations. The first condition concerns the size of usable roof area, which must be large enough to hold a solar panel; the second condition involves the high efficiency of the roof portion in retrieving solar insolation. Jakubiec and Reinhart (2012) too emphasized these two conditions as crucial in calculating the solar photovoltaic potential of a building roof.

Apart from these two important components, other parameters considered in evaluating the solar photovoltaic potential include panel efficiency, shading, orientation, tilt or slope and, often, the losses encountered during conversion from

direct current to alternating current (Carl, 2014). All the aforementioned factors and parameters can be grouped into three classes, viz. geographic potential, physical potential and energy exploitation as shown in Table 2.1.

Table 2.1: Solar photovoltaic parameter grouping. Source: Adapted from Bergamasco and Asinari, (2011).

Geographic Potential	**Physical Potential**	**Energy Exploitation**
Roof Surface Area	Total Solar Radiation	Panel Efficiency
Availability	Climate	Roof Slope & Orientation
Roof Topology	Shadowing	Conversion Losses

In modelling the solar photovoltaic potential of a certain area, various simulation tools have been developed; while some complement the GIS-based solar radiation models, others use the regional interpolated solar radiation map (Carl, 2014). Each of these tools or methods follows the same principles in estimating the solar photovoltaic potential, the only difference being the type and source of data for the parameters utilised. Another broad difference in the methods of calculating the solar photovoltaic potential involves using the sampling and extrapolation technique as carried out by Wiginton et al. (2010), Carl (2014) and others, while the other method involves calculating the solar photovoltaic potential for each building roof in the study area, following the methods proposed by Aguayo (2013), Bergamasco and Asinari (2011), Brito et al. (2012) and others.

Wiginton et al. (2010) used a five-step procedure in their analysis to determine rooftop photovoltaic potential in a part of Ontario, Canada. The first step involved dividing the region of study into smaller geographical units, using the administrative boundary of the region's census subdivisions. This level of sub-division was adopted, because it readily provided data such as land area and population, which were available from the census information database. The second step involved sampling ten census subdivisions out of more than 100 census subdivisions, to obtain representative roof areas. The Feature Analyst tool was then employed to extract rooftop boundaries from

these sampling sub-divisions using DRAPE orthophotos as input. The next step involved extrapolating the sampled information to the entire region to derive an estimate for the total roof area. Step four comprised the analysis to determine the useful or available roof area for solar photovoltaic deployment, while the last step involved using the previously generated parameters to estimate total power and energy output for south-eastern Ontario.

Similarly, the sampling and extrapolation technique was utilised by Carl (2014) to calculate the solar photovoltaic potential of residential rooftops in Kailua-Kona, Hawaii. To start with, a few sample rooftops, selected using the stratified random parcel selection technique, were digitized from the Bing map aerial imagery. Thereafter, the LiDAR tiles of areas, where the sample buildings existed, were selected as inputs to estimate terrain parameters and calculate the incoming solar radiation. Some spatial analysis was then carried out to capture the information from the solar radiation, slope and aspect analysis and to merge this with the digitized roof layer. In doing this, a raster to point analysis was first performed, followed by spatial join and clipping to transfer the point values as attributes to the roof area layer. The final stage involved exporting the final attribute table to Microsoft Excel for statistical analysis for extrapolation and calculation of the solar photovoltaic potential for the entire area.

Conversely, Aguayo (2013) estimated the solar photovoltaic potential of a suitable area in part of San Francisco, California, by considering each rooftop in the study area. The building rooftops were extracted using three decision tree models and the solar radiation was modelled using the ArcGIS Solar Analyst. The solar potential of each suitable area was estimated using equations adapted from Bergamasco and Asinari (2011) and Chaudhari et al. (2004). Parameters considered in calculating the solar photovoltaic potential include panel coverage and efficiency of the photovoltaic module, which ranges from 8% to 18%, depending on the photovoltaic module type. The efficiency of thin film modules averages at 8% and 12% for poly-crystalline, while that of mono-crystalline averages at 15% (Wiginton, Nguyen & Pearce, 2010; Jo & Otanicar, 2011). Other factors considered in arriving at the photovoltaic potential estimate are the atmospheric efficiency and the installation efficiency or performance ratio.

Having reviewed the processes involved in evaluating the solar potential of building rooftops in the foregoing section, factors that affect the solar photovoltaic potential of building roofs are discussed below.

2.10 Factors Affecting Solar Photovoltaic Potential

There are various factors that affect the estimation of the solar photovoltaic potential of a building roof. While some are peculiar to the calculation of solar radiation, others are associated with the building roof characteristics. The factors peculiar to the process of estimating the solar radiation were covered in Section 2.4.1 under spatial and temporal variation. Consequently, the factors discussed hereunder are peculiar to the building roof, and they are generally referred to as the surface effects. These include, shading (Section 2.9.1), slope (Section 2.9.2) and orientation or aspect (Section 2.9.3).

2.10.1 Shading

Shading of a building roof manifests in the form of obstruction of the roof by elevated features that are in proximity to the building roof. Such features could be natural, such as trees or mountains, or man-made, such as taller buildings, masts, billboards or chimneys. The output production of solar photovoltaic systems is sensitive to shading, as shading on even a small area of the photovoltaic panel affects the output of the entire array, even when other parts of the panel are exposed to the sun (Tooke, 2013). It is, therefore, a best practice approach to avoid any form of shading as much as possible when installing solar photovoltaic panels. Shading is accounted for in the estimation of solar radiation by modelling it in GIS, using the hemispherical viewshed modelling. Various algorithms have been designed by GIS vendors, such as the popular Viewshed tool in the Spatial Analyst extension of ESRI's ArcGIS (Fu & Rich, 2000). Similarly, the r.horizon tool was made available in the open source GRASS GIS to model shading during the estimation of solar radiation (Šúri, Huld & Dunlop, 2005).

2.10.2 Slope

The tilt angle of the solar photovoltaic panel is a major factor in determining how much energy can be harvested from the roof. This is most often dependent on the slope or

type of roof. The angle at which the solar photovoltaic panel is tilted to maximize the harvest of solar radiation is referred to as the optimal tilt, and it varies depending on the latitude and the time of year. Incident sun rays are nearly vertical during the summer period of the year, and thus a small slope angle for installed solar panels will better maximize solar radiation at this period. In winter, however, the incident rays are nearly horizontal, thus requiring a larger slope angle to optimize solar harvest. It is, therefore, recommended to achieve a mean tilt angle for a fixed solar panel, which will maximize the yearly solar harvest (Aguayo, 2013). As observed from previous available studies, the acceptable slope angle for a solar photovoltaic module or panel ranges from 0^0 to 45^0 with installation on a flat roof representing a 0^0 slope. Slopes greater than 45^0 are mostly excluded, as they are considered to be a near vertical surface (Jakubiec & Reinhart, 2012).

2.10.3 Orientation (Aspect)

Orientation is another vital factor that determines the amount of solar radiation that an array of solar photovoltaic panels can harvest. Orientation or aspect is the indication of the geographic direction, in which a sloping surface is facing; it can also be referred to as the slope direction (ESRI, 2012a). South-facing roofs planes are known to have the highest capacity to harvest solar radiation for houses in the northern hemisphere, and north-facing roofs planes in case of houses in the southern hemisphere. It has now become a standard practice to install solar photovoltaic panels on the section of the building roof facing south or north, depending on the hemisphere in which the building is located (Nguyen et al., 2012). Orientation is often measured in degrees from zero (0) to three hundred and sixty (360), with zero degree (0^0) due north, as in the case for ArcGIS. In the GRASS GIS software, however, zero degree (0^0) is due east and measured clockwise. Using the aspect map, which is calculated from the elevation model, segments of the building roof facing north can be extracted or defined to form an area of the roof, where the solar energy can be best optimized in the southern hemisphere.

Since the desirable output of this study is to provide a web-based system where people can access to retrieve vital information about solar photovoltaic potentials, it is important to review web mapping and how it relates to web-based solar photovoltaic systems. This is now presented in the section below.

2.11 Web Mapping

Web mapping and web-GIS or web-based GIS are quite synonymous, for majority of the years since the invention of GIS, access and interaction with digital geographic information has been limited to desktop computers alone, thereby making it hard for people without access to such computers or the programs to view or interact with GIS outputs (Quinn & Dutton, 2017). Web mapping presents an efficient and effective way of communicating map information to greater number of people, technical or non-technical, and there are two major classifications of web mapping applications viz. static web maps and interactive or dynamic web maps (Mitchell, 2008). Static web maps were common in the early days of web mapping, some web mapping applications still exist in static mode, however, it has evolved to interactive web mapping and distributed web mapping services (Li, Dragićević & Veenendaal, 2011).

Advancements in web mapping can be attributed to inventions in the field of web computing technology, standards and specifications (Li, Dragićević & Veenendaal, 2011). Although, the traditional client-server technology still act as the foundation and plays a vital role, newer web technologies starting with web 2.0 and others like Asynchronous JavaScript and XML (AJAX) has evolved, relying on this foundation, to improve user's interactive experience (Li, Dragićević & Veenendaal, 2011). Others include Really Simple Syndication (RSS), Services Oriented Access Protocol (SOAP), etc. Since the computing model in the client-server technology is dominantly software-defined, with either side operating mostly on different software platform. A communication mechanism between client and server are therefore facilitated by defined set of standards such as Application Program Interfaces (APIs) and Remote Procedure Calls (RPC) (Karnatak, 2012). These have promoted map mashups, by allowing developers and web map users combine map data from different sources and formats to customize their web-GIS services (Li, Dragićević & Veenendaal, 2011). Popular among web map APIs and JavaScript based include Google Maps APIs, OpenLayers, Leaflet, MapBox API, ArcGIS APIs and Bing Maps API. While some are open source, others are proprietary and all have its pros and cons. The Google Maps APIs is the most popular, having a comprehensive API documentation, highest number of users and new features being added continuously (Wagner, 2015).

To further explore the capabilities of web-GIS, the Rich Internet Application (RIA) technology was developed, having the features of desktop applications and embracing the “rich client” idea (O'Rourke, 2004). The RIA was developed with the intention of giving the client-side more role to play, thereby reducing remote calls to the server-side functions and in turn adding richness to the users’ interactive experience (Johansson, 2011). The RIA technology can be broadly classified into two viz. the plugin-based RIA (Silverlight, Adobe Flash/Flex and JavaFX) and JavaScript/AJAX-based such as HTML5 (Li, Xiong & Ou, 2011). The plugin-based RIAs run applications in their own run-time environment, using a browser plugin and makes available an integrated development environment (IDE) with extended functionality like debugging, libraries and frameworks (Johansson, 2011). The JavaScript-based RIAs on the other hand run directly in the browser environment, the functionality of a JavaScript-based RIA depends solely on range of operations provided by the web browser, as each browser offers diverse support (Johansson, 2011).

Having looked at the rapid development of web-based GIS systems, made possible by advancements in web technology, the next sub section discusses existing web-based solar photovoltaic systems, it being a type of customized web GIS services.

2.11.1 Web-based Solar Photovoltaic Systems

There are various existing web-based solar photovoltaic (PV) tools, while some were developed for regional coverage (SolarGIS by Suri and Cebecauer (2010), PV-GIS by Suri et al., (2005) and PVWatts by National Renewable Energy Laboratory (NREL)), others were developed for smaller extents or at municipal level. Also, these existing web-based tools can be categorized based on their type of solar radiation model data utilised. Web-based solar PV tools, which bases its solar radiation estimate on historical ground meteorological station data include, PVWatts, while the SolarGIS tool uses satellite-derived data. The PV-GIS solar radiation database was developed using a GIS-based solar radiation model.

Another variation that exist between these web-based tools is the spatial resolution of the solar radiation resources. Most of the web-based solar PV tools based on ground or satellite-derived solar radiation modelling have a coarse spatial resolution varying between 1km to 40km (Šúri, Huld & Dunlop, 2005; Suri et al., 2012). The PVWatts has

a 40km resolution solar resource data (Šúri & Cebecauer, 2010), while SolarGIS has a spatial resolution of up to 80m (Hill et al., 2000). However, the spatial resolution of the web-based solar PV tools using GIS-based solar radiation models is a factor of the DEM used in the solar radiation modelling. This varies, depending on area of coverage and source of the DEM. DEMs derived from LiDAR data are known to be of very high resolution (Dean et al., 2009).

Other area of variation between existing web-based solar PV tools can be summarized as differences in their site selection, planning, design and visualization of solar PV systems. This has been evaluated by few studies showing how each web-based tool differs in type of inputs required, different solutions available and how results are viewed and disseminated (Dean et al., 2009; Lalwani, Kothari & Singh, 2010). This seems to be the area of competition amongst the web-based solar PV tool developers, with propriety developers competing to add more functionalities and sophistication. However, the open-source tools provide the basic platform and output with less sophistication. It can thus be inferred that various web-based solar PV tool developer opted for different solar radiation models due to factors such as, availability of climatologic data for the area of interest and the vastness of the area of interest. These in turn determine the resolution of the ensuing solar radiation database utilised and eventually, the accuracy of the solar PV estimate or calculation. It can be further said that there is a trade-off between the resolution of the solar radiation database and the coverage area.

2.12 From desktop to web-based system

Most of the recent web mapping applications fancy the JavaScript/AJAX-based RIA as implemented in HTML5 by Leaflet, MapBox API, Google Maps API, etc. over the plugin-based RIA (Microsoft Silverlight, Adobe Flash). HTML5-based RIAs are academically more acceptable as it has open standards unlike the plugin-based Silverlight/Flash, which is enterprise-based and therefore regarded as a closed technology (Johansson, 2011). The JavaScript/HTML5-based RIA is therefore adopted in the study to develop the web-based solar photovoltaic system.

Web mapping applications that adopt the JavaScript/AJAX-based RIA also rely on service-oriented architecture like SOAP, REST and JSON to receive map data from different distributive web services. For instance, image/map tiling used in most web mapping application is made possible by dividing the base image or map into smaller grid tiles for different zoom level or scale. The web map user specifies an area to view and a request is sent using the SOAP or REST to fetch map images from one or various map server. The image tiles are then loaded onto the map grid asynchronously using AJAX techniques (Johansson, 2011). New set of image tile are displayed when the map user pans or zooms in and out changing the scale of the map, as various image tiles for different view scale has already been cached.

The Google Maps JavaScript API and Fusion Tables REST API are chosen to customize the web-based solar photovoltaic system, as they offer comparative advantages over other web mapping applications in term of comprehensive API documentation, oblique-view for three-dimensional feel in selected area where such data exists, ability to query map attributes spatially amongst others. The Google Maps JavaScript API and Fusion Tables REST API are web-based APIs. They are also RESTful APIs, because it is based on Representational State Transfer (REST) style of web service architecture. These are further explained in the sub-sections below.

2.12.1 Web APIs and RESTful web services

APIs provides a platform for software programs to communicate with each other, this becomes necessary in web services because server-side software or programming languages are often different from that on the client side. Web APIs are defined interfaces, which enable controlled communications via HTTP between client and server. Applications on the server side are often enterprise, therefore, controls are set up on the server side to determine the level of exposure to data and services by clients. In essence, web APIs are designed to provide a framework for large number of users (clients) to access server resources for integration and customisation without compromising the server-side applications and data (see Figure 2.8). HTTP requests are sent using a Uniform Resource Identifier (URI) by clients and responses from the server are usually in the format of XML and JSON (Chauhan, 2016). Web APIs are implemented using web services such as REST.

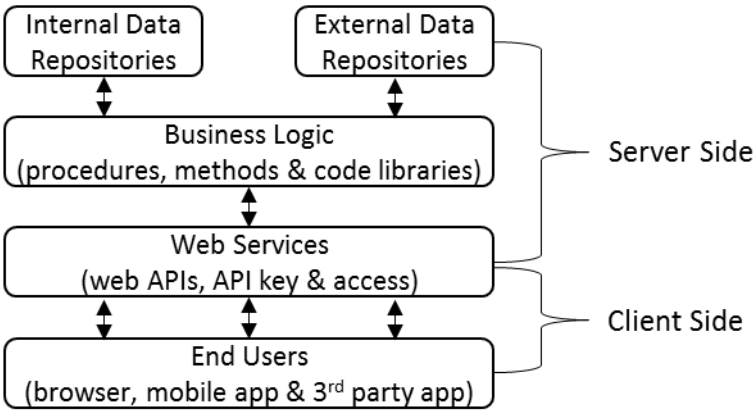

Figure 2.8: Web services and API architecture. Source: Adapted from Miller (2014).

REST is a specification of web services and a type of service-oriented architecture. It serves as preferable alternative to SOAP and JSON because of its ease of use (Barry, 2017). It provides a set of constraints to the interaction between service consumer and service provider via the Hypertext Transfer Protocol (HTTP) verbs such as PUT, GET, POST or DELETE. The constraints include it being a client-server architectural style, stateless, uniform interface, cached, layered system amongst others (Fielding, 2000). Requests made to the service provider using REST would return a response in either XML, HTML, JSON, KML and other formats (see Figure 2.9).

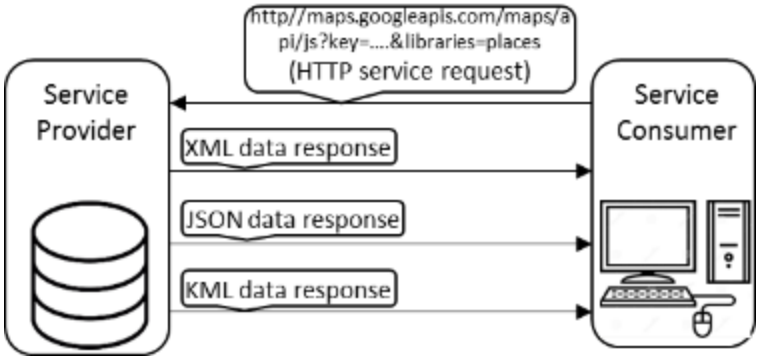

Figure 2.9: Data request and response using REST. Source: Adapted from Barry (2017).

2.12.2 Google APIs

The processes described above explain the techniques required by the client to send requests to and receive response from the backend server in a web mapping environment. The Google web services such as Google Maps APIs and Fusion Tables REST API does not fully comply with the Open Geospatial Consortium (OGC) standards, just like other web map APIs. However, the Google Maps JavaScript API

and the Fusion Tables REST API as adopted in this study can be classified under Web Map Tile Service (WMTS) and Table Joining Service (TJS) of the OGC respectively. The OGC was set up to promote interoperability within technology provider and users in the geospatial industry, as no individual technology provider can set the universal standard. The standards are created to reduce difficulties in sharing data and reusing data, so as to reduce cost and obtain better information content, while increasing the data value (OGC, 2017). Since the output of the analysis carried out in this study is not targeted to only GIS end-users, but mostly, the general public, for information dissemination, the Google web services are therefore considered adequate for this purpose. These web services as adopted are further explained as follows.

Google Maps APIs as a WMTS

Map tiling service was borne out of the efforts to develop performance-oriented and scalable services for distributing cartographic maps and imagery online (Masó, Pomakis & Julià, 2010). The backend application server feeds map to clients asynchronously using tiled images that have fixed (predefined) scale, resolution and content. This method is complementary to Web Mapping Service (WMS), but presents a faster approach to disseminating maps and imagery to client (Masó, Pomakis & Julià, 2010). The client makes a request through a Uniform Resource Locator (URL), specifying a tile layer (street, satellite, terrain, hybrid, etc.), zoom level (scale) and the tile coordinates. Most tile map services have similar structure of how the map/image tiles are stored and requested, however, difference exist in how equivalent tiles are indexed. Google map tiles are indexed using x and y coordinates, with the origin at the north-west corner. The “x” increases eastward while the “y” increases southward. A location on the google map is uniquely referenced by a world coordinate, tile coordinate and pixel coordinate. This is achieved through the API converting its latitude and longitude to a “world” coordinate initially, then its pixel coordinate is determined using a formula (pixelCoordinate = worldCoordinate * $2^{zoomLevel}$) (Google Maps, 2017). At zoom level zero (0) the world is represented on a tile of 256 by 256 pixels, with the origin at the north-west corner and possible world coordinate being (0 – 256) in “x” direction and (0 – 256) in the “y” direction(Google Maps, 2017). For each zoom level, the number of containing tile increases by a multiple of four (4) i.e. at zoom level 1, the earth is divided into four (4) tiles while there would be sixteen (16) tiles at

zoom level 2 (Google Maps, 2017). This relationship makes it possible to reference a point on different zoom levels.

The map tile service is made available through the API or public libraries in JavaScript, Python and others. The API also provides the interface through which the web map can be customised or “mashed-up”. It allows the client to overlay (publish) other desired layers on the base map tiles. The published map layers are anchored to layer control, which can be switched on or off, thereby making the web map interactive.

Fusion Tables REST API as a TJS

Without doubt, an average standard database now has some kind of geographic identifier field/column, this could be in form of postal codes or area code (NRCAN, 2015). A table joining service provides an interface to publish and share tabular data that has a geographic identifier for the purpose of data manipulations, geospatial analyses, spatial/attribute queries and mapping (Schut, 2010). The table can then be accessed and joined to a geospatial dataset, provided they have a common field (primary key). TJS is complementary to other mapping services like WMS and WFS (Web Feature Service), as they have a lot in common. The OGC provided some reasons in their standards’ document why this service was established as a stand-alone and not added to either the WMS or WFS. Amongst reasons cited include, a great deal of complexity, if added to WFS 1.1, it serves a specific group of users with specialized needs that are not often shared with users of WFS, thereby adding unnecessary complexity and no value to either of the groups (Schut, 2010).

Google’s Fusion Tables REST API provides an interface, through which clients can use simple HTTP requests to programmatically perform operations such as create, update, insert, query or delete on a published tabular data (Google Developers, 2016). Google fusion table allows data in different formats like KML, CSV, XLS, etc. to be uploaded. Table structure and metadata in these formats are then represented as JSON data structure through the API, while requests sent using the HTTP yield a response in either JSON or CSV data format (Google Developers, 2016). The tabular data can then be explored using SQL statements for visualization through chart and maps depending on the data types in the published table, also data filtering and aggregation are possible within the table or the table could be joined to other tables from different user (Gonzalez et al., 2010).

Client-side visualization of the published tabular data is a major strength of Google fusion table, as it is fully integrated into the Google Maps JavaScript API using the “FusionTablesLayer” object (Google Developers, 2016). Layers for map resulting from queries to the tables goes through three processes on the server side. The first process (Front end dispatcher) converts the SQL/HTTP request to a representation the system understands and forwards it to the second process (Query processing module), this creates a query plan (Gonzalez et al., 2010). The query plan is then executed in the third process (Backend plan execution) (Gonzalez et al., 2010). The combination of these two services (Google Maps JavaScript API and the Fusion Tables REST API), therefore, makes it possible transfer the outputs from desktop GIS and remote sensing analysis to the web for basic interaction and information extraction.

2.13 Chapter Summary

From the foregoing discussion and review of the relevant literature, it is evident that different levels of government are indeed willing to reduce the effects of GHG emission on the environment and are committed to developing their energy sector sustainably. The relevant government departments have created an enabling environment by formulating policies to this effect, as summarized in Section 2.2. Section 2.3 looked at application of GIS in renewable energy respectively. While Section 2.4 to Section 2.11 have looked at the possibilities of harnessing solar resources from building rooftops by means of photovoltaic systems, using different approaches, depending on the available data of the study area in question. The reviewed literature serves as the foundation for the methodology used in this study.

CHAPTER 3
METHODOLOGY

Having reviewed several relevant publications on the need to adopt renewable energy in lieu of fossil fuels, methods of extracting and analysing the solar photovoltaic potential of building roofs, it is now important to determine which method or combination of methods will be most suitable to achieve the aim of this research. In deciding which methodology to adopt, various factors were considered, including the availability of data and system selection for the particular study area. In this chapter, therefore, the methods adopted are described in detail. Section 3.1 introduces the chapter and shows the overall flowchart of the methodology adopted for this study, while Section 3.2 sets out the methodologies of each phase and workflows as designed adopted for the study. Section 3.3 highlights the relevant details about the software and hardware that was selected for this study.

3.1 Introduction

Developing a web-based GIS system for evaluating the solar photovoltaic potential of building rooftops involves four major phases of operation. The first phase involves extracting the rooftop outlines and its planes or segments using the integration of LiDAR data with an aerial imagery. In this stage, moreover, the LiDAR data is passed through a series of processes so as to have each component (ground, building, vegetation, etc.) attributed to its class. These classified points are then utilised to generate LiDAR derived products, such as DSMs, slope and aspect maps, which are eventually used in extracting the whole roof outline and the roof planes. These also serve as inputs for the solar radiation analysis.

The second phase uses the outputs from the first stage as inputs to determine the amount of solar radiation available for each roof plane area. Outputs generated in this phase include aspect and mean annual solar radiation estimates that are incident over each roof plane. The third phase combines the information or outputs from the two previous phases to calculate the solar photovoltaic potential of each building roof. The fourth phase transfers the solar photovoltaic analysis and results from desktop location

to web location for easy access by large number of users. This is better conceptualized with an overall flowchart as shown in Figure 3.1.

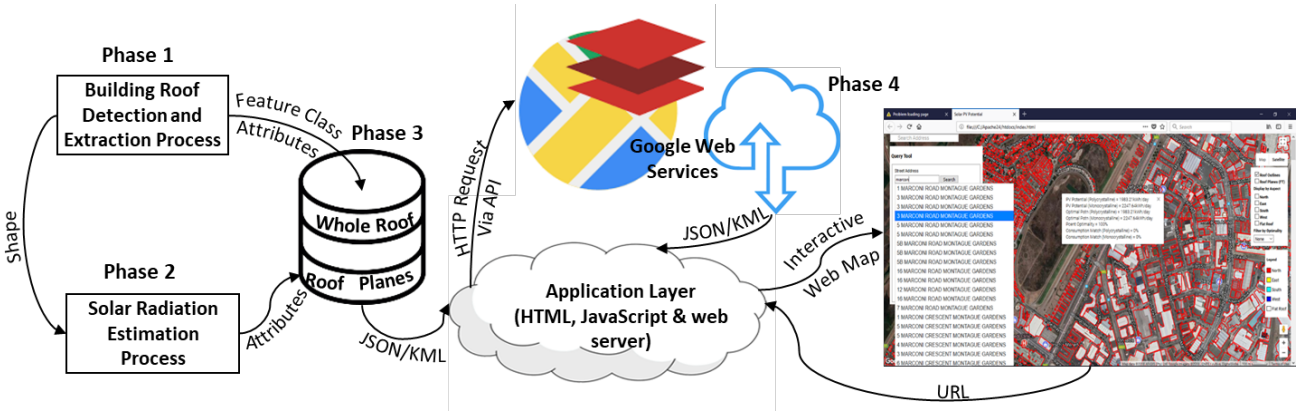

Figure 3.1: Overall flowchart of the methodology

The methods adopted in each phase of the study is further discusses in the following section.

3.2 Research Design

Factors, which influenced the choice of methods adopted for this study include data availability for the study area, system selection and nature of the terrain. The methods adopted in this research design were based on the following assumptions:

- A building roof polygon represents the outline of a building roof, which in most cases is equivalent to the building footprint (Kodysh et al., 2013).
- No significant discrepancy exists in terms of structural development between the LiDAR point data and the aerial imagery, as the datasets were collected within a close timeframe (Nguyen et al., 2012).
- It is possible to fit solar photovoltaic tiles to occupy an entire building roof panel, spaces left are negligible and inconsequential.
- Significant number of building roofs do not have objects hanging on it, therefore, a theoretical photovoltaic potential is calculated for all building roof without factoring the spaces occupied by roof-mounted objects.

In the sub-sections below, the relevant techniques adopted in this study will be presented, namely, the technique employed to generate the DEMs (Section 3.2.1) and the methods used for the extraction of building roof outline and planes (Section 3.2.2),

for estimating the amount of solar radiation (Section 3.2.3), for estimating the solar photovoltaic potential of a particular area (Section 3.2.4) and the approach to deploy the solar photovoltaic potential system to the web (Section 3.2.5).

3.2.1 Generation of DEM

The LiDAR raw data has been pre-classified from source (City of Cape Town) into ground and non-ground class. The subsequent LiDAR data processing required is the normalized height classification to generate height normalized non-ground points. These will be used to generate the nDSM. The LasTool LiDAR processing tool is used in classifying the normalized LiDAR point data as discussed earlier in Section 2.6. The height normalized point can then be interpolated directly to generate a normalized surface model. However, the nDSM is traditionally generated by subtracting the DTM (digital terrain model) from the DSM (digital surface model):

$$nDSM = DSM - DTM \quad (3.1)$$

These two approaches were tested and found to generate similar output, however, the traditional approach takes longer to generate and consumes more data storage. This is evident as it takes more computational time to interpolate two rasters of fine resolution than one.

The binning method of interpolation used in this study was considered adequate to generate the DSMs since the LiDAR data is quite dense (ESRI, 2013). ESRI recommends the mode for binning is set to “Average” for bare earth points when producing a DTM and “Maximum” for biasing the result to higher heights when generating a DSM (ESRI, 2013). To fill the void cells, often prominent when binning is used for interpolation, the Natural Neighbour method of interpolation is recommended for quality by ESRI (ESRI, 2013). The resolution of the DSM raster is determined by specifying the desired resolution as a value for the cell size of the output raster. Floating point raster is considered better suited since the raster DSM will be required for various analytical calculations. The generated DSM or nDSM as the case could be are thereafter used as inputs for other raster surface analysis. A workflow for generating DSM from the LiDAR data using the binning interpolation technique is shown in Figure 3.2.

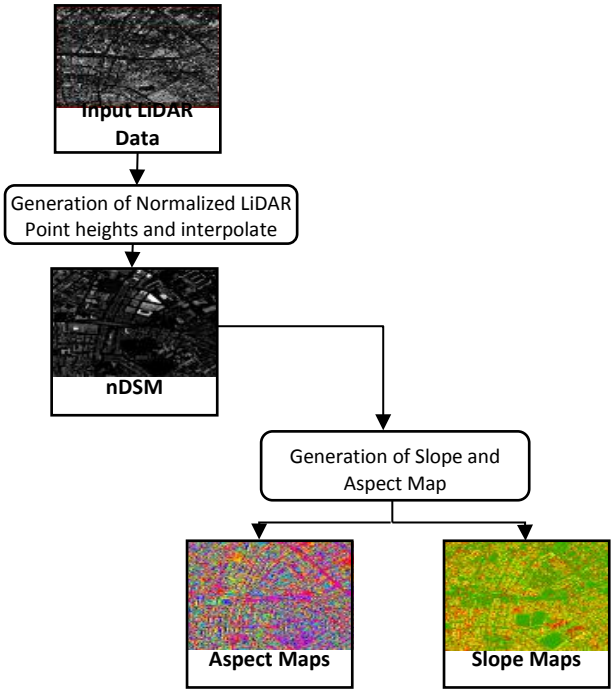

Figure 3.2: Workflow diagram for DEM generation and surface analysis

Using the workflow above, an algorithm is written in Python using the arcpy library to create a single tool, which accepts the LiDAR data as input and generate the nDSM, slope and aspect raster as the output. This algorithm combines the LasTool's lasheight to classify normalized LiDAR point heights, with other arcpy tools such as "CreateLasDataset" and "LasDatasetToRaster_conversion" to generate the nDSM, slope and aspect raster for building roof extraction process. A copy of the Python algorithm is provided in Appendix 1. A similar workflow is used to generate the DSM for solar radiation estimation.

3.2.2 Extraction of Building Roofs

Extracting the whole building roof outline and roof planes is the first major phase of analysis involved in estimating the solar photovoltaic potential of a building. The rule-based classification process offers the possibility of automating the whole extraction process using fuzzy rule-sets. Using such rule-based classification system and incorporating the use of LiDAR-derived data with imagery, a hierarchical object extraction rule-set is designed in eCognition Developer 9 software to detect and extract the building roofs within the scope of this study. An overview of the processes is presented in Figure 3.3(a), while the outlines of the rule-set is given in Figures 3.3(b) and Figure 3.3(c).

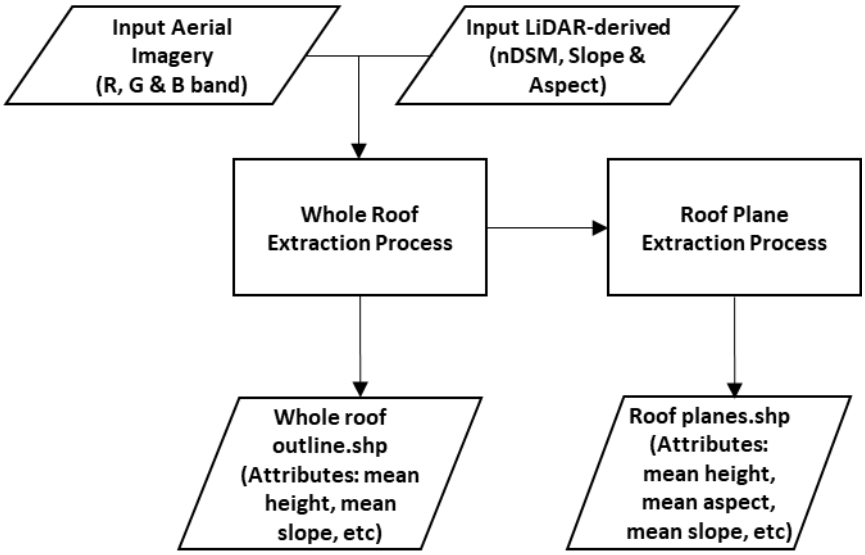

Figure 3.3(a): Input, process and output workflow diagram for extraction of building roofs

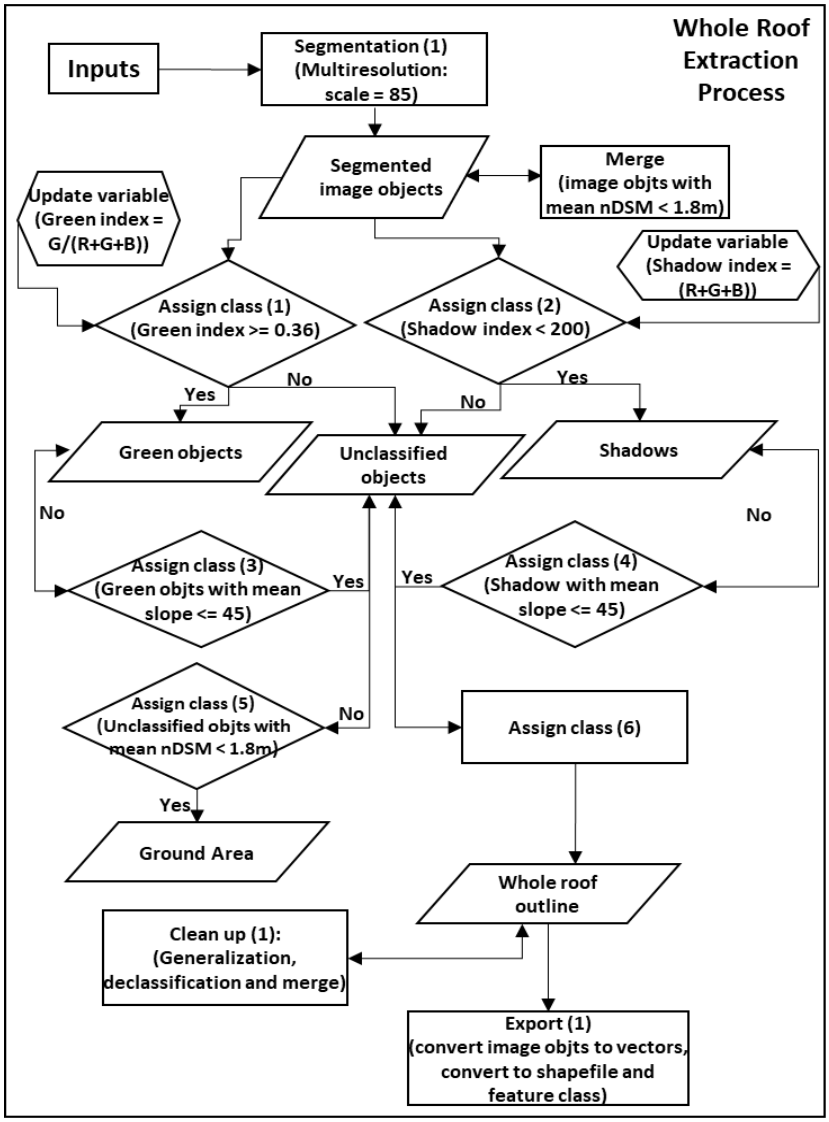

Figure 3.3(b): Workflow diagram for extraction of whole roof outlines

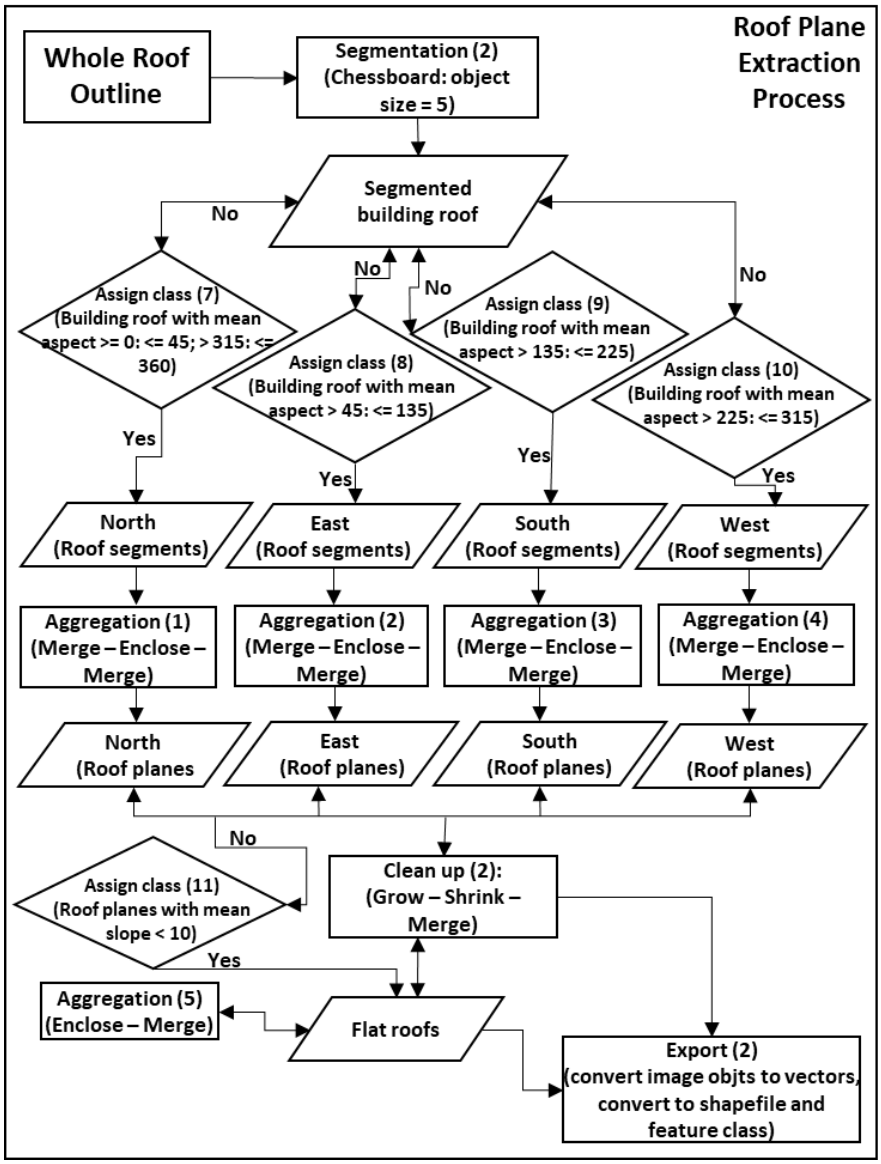

Figure 3.3(c): Workflow diagram for extraction of building roof planes

The detection and extraction of each building roof involves two stages, the first stage detects and extract the whole building roof outline, while the second stage decomposes each building roof into planes. The strategy adopted can be referred to as classification by elimination; objects of non-interest are classified as soon as detected, leaving the desired object as the last object to be classified. The aerial imagery and LiDAR-derived data such as nDSM, slope and aspect raster serve as input in eCognition Developer 9. The first process requires the aerial imagery bands to be segmented using the multiresolution segmentation algorithm (Segmentation 1) to create the initial image object primitives. A scale parameter of 85 was considered adequate for the segmentation, as this captures smaller building objects as a unit and roof planes of bigger building feature as a complete unit of image object. The weight

of the red, green and blue bands are equally set to 1, for full participation in the segmentation process, while the shape and compactness parameters are set to 0.1 and 0.7 respectively. A lower shape and higher compactness parameter ensure image objects of similar colour are not fractured. With a successful segmentation, a merge region process is employed to merge all image objects with heights less 1.8 metres, from interrogating the LiDAR data, image objects with heights less than 1.8m are low-lying objects and vegetation. This cleans up the clutter of image objects leaving only image objects above the ground as object primitives.

With the low-lying image objects eliminated by merging them into a bigger image object, a customised object feature called “green index” is then designed to classify green image objects. The green index adopted in this is obtained by dividing the green band of the aerial imagery with the mean of all the three bands (G / (R + G + B)). This index performs better than the green-red index (G – R / G + R), which is adapted from the NDVI ratio, by replacing the NIR band with the green band. It is able to distinguish better between green objects and similar colour, such as blue-green roofs, when compared with the green-red index. Green objects were found to have an index of 0.36 and above. The closer the index value is to 1, the greener. Green image objects in this study are found to have an index of 0.36 and above. It is worth noting that the index value is based on the bit depth of the input imagery and therefore, not a universal or normalized index value. Using this index, a classification process (Assign class 1) is then added to classify green image objects, which are mostly trees and green building roofs. Using a similar approach another customised object feature is designed to classify (Assign class 2) shadowed areas. A shadow index is obtained by adding the mean of red, green and blue spectral information for each segmented image object (R+G+B). The shadow index identifies dark image objects as objects with index value less than 200, bright image objects have higher values of shadow index beyond 200. Like the green index value, the shadow index value range are also specific to the bit depth of the aerial imagery used in this study. Objects detected with this logic includes shadowed areas as well as very dark building roofs.

The previous classifications (Assign class 1 & 2) misclassify some potential building roofs, since only the spectral properties are utilised. However, tree objects are known to possess high slope value, as a result of varying discontinuity in its branches and sharp difference in elevation to the ground. A fuzzy logic of slope <= 45^0 is therefore

employed in the subsequent classifications (Assign class 3 & 4) to declassify potential building roofs. Since building roof planes with slope greater 45^0 are not suited for solar photovoltaic installations. Subsequently, the merged low-lying objects is classified (Assign class 5) as ground area.

At this stage, all elevated objects, save the building roof have been eliminated. It is then safe to classify (Assign class 6) the remaining unclassified image objects as building roof. The final stage of the whole roof extraction involves refining the building roof into a smoother or more regular building shape. The pixel-based object resizing (shrink and grow) and vector handling algorithms are utilised in this process, the process is further explained in Section 4.2.2. An export process is added to export the building roof polygons as a Shapefile. The building roof object now serves as an input for the second stage, which is the decomposition of the whole building roof outline into roof planes.

The chessboard segmentation algorithm (Segmentation 2) is used to break the whole roof into tiny units, setting the object size to 5 and domain to image object level. Using the aspect values, sets of fuzzy logics (Assign class 7 – 10) are then designed to classify each tiny building roof object into north, east, south or west. In determining what aspect values to use a basic quadrant was draw as shown in Figure 3.4.

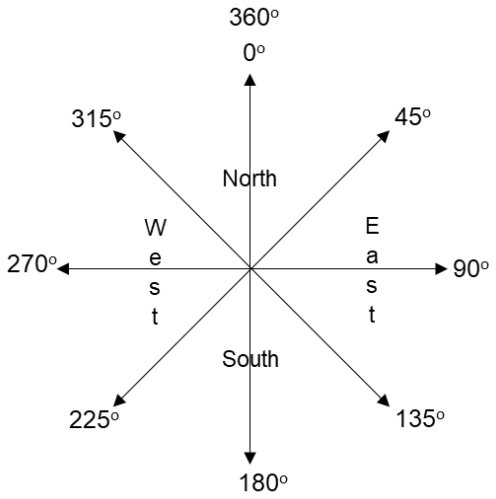

Figure 3.4: Diagram showing cardinal directions and aspect values

The roof segments belonging to north are to be classified (Assign class 7) using “mean aspect >= 0° and <= 45°”; “mean aspect > 315° and <= 360°”. Any building roof segment that does not fulfil this condition is left unclassified. The east roof segments

are classified (Assign class 8) specifying “mean aspect > 45^{o} and <= 135^{o}” as condition to be fulfilled. The south and the west segments are to be classified in a similar way.

The next step involves aggregating (Aggregation 1 – 4) the classified segmented to form a roof plane. Algorithms to be employed includes “merge region” and “find enclosed by class”, the processes are further discussed in Section 4.2.2. This is then carried out on each of the cardinal directions. The last classification process (Assign class 11) detects and classifies roofs that are flat using the slope values. A threshold of mean slope <= 10^{o} is adopted, as flat roof are not perfectly flat, but contains portions gently sloped to drain the roof. Subsequent processes involve cleaning up the classification by smoothing and simplifying the roof plane edges. Finally, the roof planes are exported as Shapefiles and feature classes with attributes such as class name, slope, aspect and height. These attributes are to be utilised for calculating the solar photovoltaic potential of the building eventually.

The next sub-section presents the technique to be used to estimate the global solar radiation.

3.2.3 Estimation of Global Solar Radiation

Estimating the amount of solar radiation is the second phase of analysis in determining the solar photovoltaic potential of a surface. It requires the finest estimates to be utilised in the analysis; this was provided by the r.sun model in the GRASS GIS software. The r.sun model calculates the beam, diffuse and ground reflected radiation for a given day, location, surface and atmospheric condition. It functions in two modes, as discussed earlier in the literature review (see Section 2.8.3). The second mode (Mode 2), which computes the daily sum of solar irradiation [Wh.m^{-2}] was used to compute the global solar radiation in this study.

As inputs, the r.sun model uses the DSM raster, the DSM-based ancillary rasters (slope, aspect, latitude and longitude raster and horizon raster) and day number. Other parameters, such as albedo value, Linke turbidity coefficient and time steps, have default values or can be specify by the user. All the input parameters, as adapted from Hofierka and Suri (2002), are presented in detail in Table 3.1.

Table 3.1: Input parameters for r.sun model. Source: (Hofierka & Suri, 2002).

Parameter Name	Type of Input	Description	Unit	Value Interval
elevation	raster	digital surface model	meters	0 – 8900
aspect	raster	aspect map	decimal degrees	0 – 360
slope	raster	slope map	decimal degrees	0 – 90
lat	raster	latitude raster	decimal degrees	-90 – 90
long	raster	longitude raster	decimal degrees	-180 – 180
horizon_base	raster	horizon or shade raster	decimal degrees	0 – 360
horizon_step	single value	degree interval for horizon computation	dimensionless	0 – 360
linke_value	single value	Linke atmospheric turbidity	dimensionless	0 – 1
albedo_value	single value	ground albedo value	dimensionless	0 – 1
day	single value	day of the year	decimal hours	0 – 366
step	single value	time step for each day	dimensionless	0.01 – 1.0

A workflow diagram for estimating the global solar radiation is shown in Figure 3.5.

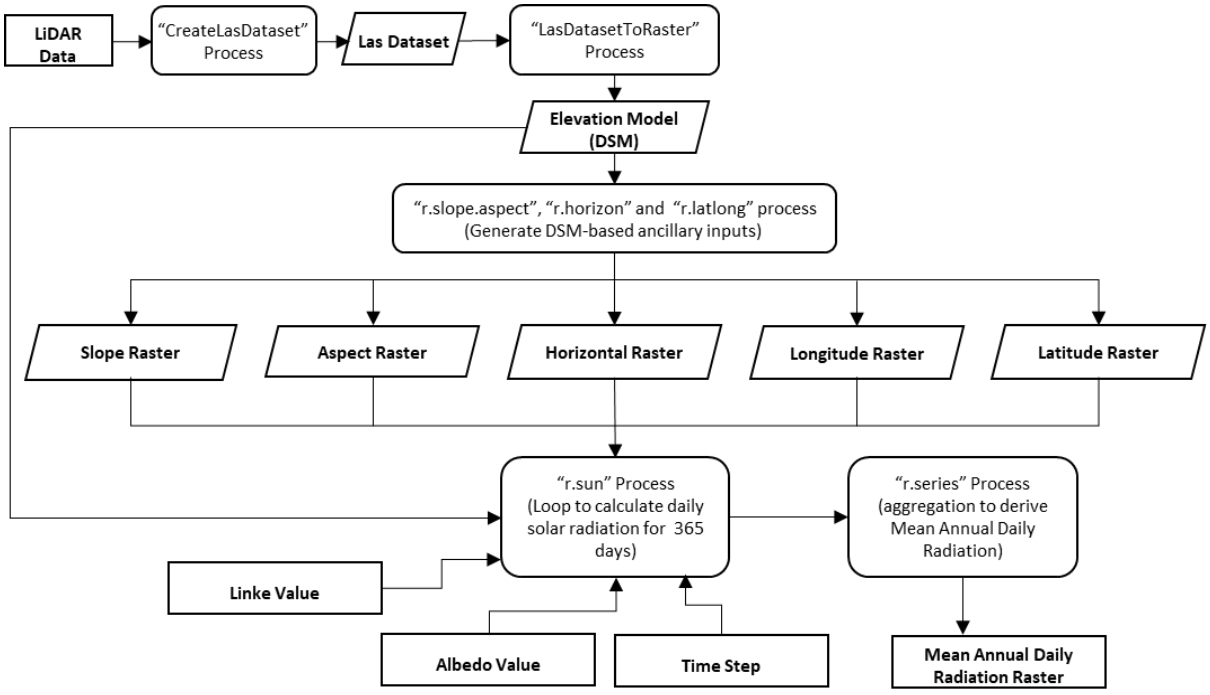

Figure 3.5: Workflow diagram for estimating the global solar radiation

However, the r.sun model does not have the capability of calculating the global solar radiation over a period of time. This is only possible by writing a Python algorithm process to loop the daily calculation over the period of time required, which is a year for the purpose of this study. On completion of the loop, which calculates the daily global solar radiation for the 365 days of the year, another algorithm process is then added to derive the annual mean radiation. This is calculated by adding the daily value for each cell of the 365 days of the year and dividing it by the number of occurrences. This algorithm can be modified to calculate all other required inputs for the estimation of solar radiation, namely, slope, aspect, horizon, latitude and longitude maps; the algorithm requires the DSM as the only input.

In order to achieve algorithm optimization in this study, a single Python algorithm is written, which accepts the LiDAR data as input and returns the calculated mean annual solar radiation. The traditional practice would be to generate the DSM separately, using ArcGIS or GRASS GIS, depending on the resolution desired. The generated DSM then serve as input for the “r.sun” analysis. This algorithm is designed in such a way that it could run on a Python shell or command line, without having to encounter the GRASS GIS software environment and going through the cumbersome setup process. The first step in this phase involves setting up a location where all the outputs would be saved. This is carried out using the GRASS GIS, it involves specifying the projection system, mapset and folder location to store the output.

The next step involves the actual algorithm development, all the required modules are imported, such as “import sys”, “import os”, “import arcpy”, “import grass.script” and others. Lines of codes similar to that used earlier to generate surface models in sub-section 3.6.1 and Appendix 1 is adopted. The LiDAR data flows into “CreateLasDataset” process, then the las dataset goes into “LasDatasetToRaster” to generate the elevation model. The GRASS GIS environment is then set up by specifying paths to the location, mapset and the batch file to execute GRASS GIS via command line. Thereafter, a new mapset is created using the “g.mapset” command. The created mapset would eventually house all files that would be generated during the calculations.

Once the mapset is created, the elevation model, which is an output of the arcpy processes is then imported into the grass module using “r.in.gdal” command. Once

imported successfully, the computation region is set using “g.region” command. All other required inputs, such as the slope, aspect, latitude and longitude map, are generated using the elevation model as input. These are later called up as input for the calculation of global solar radiation. Other inputs, aside from the rasters, are floating integers, such as the Linke turbidity coefficient and the ground albedo value. The mean annual Linke coefficient for the City of Cape Town was obtained from a solar radiation data site, “SoDa”. The values were retrieved by entering the location of the study area, as defined by its latitude and longitude. A mean annual value of 3.2 was retrieved for the City of Cape Town and the default Linke value as provided by “r.sun” tool is 3.0 (SoDa, 2004). The ground albedo value, in contrast, was obtained was obtained from NASA’s atmospheric science data centre. The annual mean retrieved for the study area is 0.18, while the default on the “r.sun” tool is 0.2 (NASA, 2015).

It is important to set these parameters to reflect that of the study area because the default values that comes with the tool are predetermined for European climate condition, as the “r.sun” model is based on the work used for the development of European Solar Radiation Atlas (ESRA) (Šúri & Cebecauer, 2010). The time step for the daily calculation is set to 0.5, which means that, for every 30 minutes in a day an estimate is calculated. These two floating values are inputted during the algorithm scripting to replace the default set by the r.sun tool.

The next step of the algorithm scripting defined a range for the number of days to be calculated. An extra day was added, as the last day would not be calculated, if the exact range was defined. Therefore, a range from 1 to 366 was defined. Using a “for” statement and the “r.sun” command tool, all the required inputs are keyed in, and a series of daily solar radiation estimates are produced. The mean annual estimate is calculated using the “r.series” command, and all the daily estimates generated are fed in using the “g.list” command. The method for the aggregation is set to average, and the “r.out.gdal” command is used to export the final solar radiation raster. A copy of the full Python algorithm is made available in Appendix 2. The Python algorithm is tested by running it on a few samples, and all identified bugs are fixed. The final algorithm is then utilised in estimating the mean annual solar radiation for the entire study area.

The next phase takes into account outputs from building roof extraction and solar radiation calculation in estimating the solar photovoltaic potential. The method adopted for the estimation is presented in the next sub-section.

3.2.4 Estimation of Solar Photovoltaic Potential

The purpose of calculating the solar photovoltaic potential of any rooftop area is to estimate the amount of electricity, which can be produced by mounting photovoltaic panels on such roof space. According to Bergamasco and Asinari (2011), calculating the solar photovoltaic potential entails determining the geographic potential, the physical potential, and the technical potential. The geographic potential refers to the useful roof area that can accommodate the solar photovoltaic panels, the physical potential is the viable solar radiation incident on the roof area, while the technical potential refers to the efficiency of the photovoltaic system.

The first phase in calculating the solar photovoltaic potential for a particular building is to determine the amount of useful area the roof can provide for the installation of photovoltaic panels. This is referred to as the geographic potential. In determining the useful roof area, the space or area occupied by all roof-mounted objects, such as chimneys, HVACs and walls, are usually factored in and deducted from the total roof area (Hofierka & Kaňuk, 2009; Jo & Otanicar, 2011; Aguayo, 2013). However, not all building roof in an area would have objects hanging on it, therefore obtaining a general deduction factor could erode the potential of building roofs without objects hanging on top of it. Likewise, adopting a singular deduction factor across board would be bias, as roof-mounted objects varies in sizes, thereby occupying different roof spaces. This study adopts the true roof area as the useful roof area to compute the photovoltaic potential, individual property owner could then determine the percentage of the roof area occupied by objects on their roof, if any exist, and factor it into the photovoltaic potential calculated for the entire roof space.

Moreover, it can be argued that the roof outline extracted from the integration of LiDAR and aerial imagery actually represents the roof span area, as seen from the top, and not specifically the entire roof area. It should, however, be noted that this argument is peculiar to pitched roofs only. The surface area of a flat roof is essentially the same as its roof span area, as there is no rise or run. This is better illustrated in Figure 3.6.

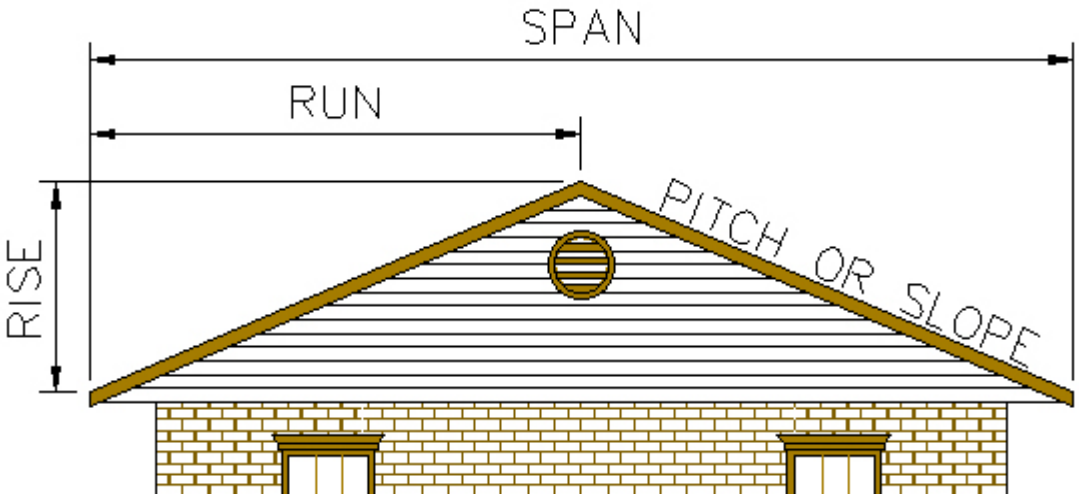

Figure 3.6: Building roof geometry. Source: Roofing Calculator (2015).

Suffice to say, if a pitched roof is flattened to a zero degree slope, its span area will be greater, than when it was still pitched, say at an angle of 35^0. Therefore, it can be said that the initial roof span area obtained from the automatic extraction of building roofs (whole roof outline) underestimates the actual roof area. For the reason highlighted above, and to better estimate the surface area of the building roof, the roof planes were extracted. The surface area of each roof plane can then be calculated taking its slope into consideration. Previous approaches, as highlighted before, adopted the roof span area and factored in areas occupied by roof-mounted objects. An approach (Bottaccioli et al., 2017) that adopted the surface area, effected the surface area on the whole roof outline and not each plane that consist the whole roof structure. These two approaches, in essence under estimate the actual roof surface area. This study, therefore, considered each building roof in terms of its planes (segments), with each roof plane independent of the other. The summation of each roof plane then gives the potential of a single (whole) building roof.

Similarly, it must be considered that solar photovoltaic panels are best optimized for receiving solar radiation at certain orientations, as discussed earlier in the literature review (see Section 2.10.3), typically from south-east to south-west directions for houses in the northern hemisphere, and from north-east to north-west for the southern hemisphere. This means that only about 30% to 80% of the entire roof area could be used optimally for solar photovoltaic panel installation, depending on the orientation of the building roof. Since this study decomposes the whole roof structure into individual planes, it becomes easy to filter out roof planes that are not suitable for solar

photovoltaic installation using its cardinal, topographic or geometric properties. The surface area of the roof plane is therefore denoted as R_{SA}. This is obtained by converting the span area of the roof obtained from the automatic roof extraction process to surface area using the expression given below:

$$R_{SA} = 2D\_Area / Cos\ (slope) \quad (3.2)$$

The second phase involved in estimating the rooftop solar photovoltaic potential is to determine the global solar radiation incident on the particular roof. This is also referred to as the physical potential. The entire annual global solar radiation of an area can be determined by using the adopted method, as discussed already with regard to the estimation of solar radiation (see Section 3.2.3). Obtaining the mean annual global solar radiation for each rooftop, denoted as S_{MR}, entails the following processes:

- The extracted building roof plane shape file is inserted as a mask when estimating the global solar radiation. The output gives the solar radiation estimates within each of the roof plane only.
- There are two ways of extracting the mean of all pixel values that fall within each building roof polygon. The first method involves converting the solar radiation raster to points using the “Raster to Point” tool in the GIS software. Then a spatial join is carried out to join the attributes of the point file to the roof polygon, based on their spatial relationship. The join is done on a one-to-one rule and the merge rule is specified as the mean. The second approach is to use the “Zonal Statistics as Table” tool from the “Zonal” toolset in ArcGIS Spatial Analyst to obtain the mean values of the solar radiation estimate for each building roof polygon. This latter approach was adopted in this study, to obtain the mean annual global solar radiation estimate for each building roof. It was preferred over the first method because it is much faster than using the spatial join, which takes more time for large raster datasets.

The next step involved in estimating the solar photovoltaic potential for each building was to determine the amount of energy exploitation involved in converting the solar energy to electricity. Factors considered here include solar panel efficiency and the performance ratio (conversion coefficients), which take into account sub-factors, such as losses due to temperature and shading, losses due to dust and snow, inverter losses, AC/DC cable losses and other losses. The efficiency of solar panels ranges

from 8% for thin film panels, and 12% to 17% for the crystalline silicon panels (Wiginton, Nguyen & Pearce, 2010; Jo & Otanicar, 2011). The crystalline silicon-based panels are the most prevalent in the market, and monocrystalline panels are the most expensive of the crystalline panels. The solar panel efficiency or solar panel yield, denoted as P_E of 15%, was adopted for this study. The performance ratio or conversion coefficient for a typical roof-mounted mono/polycrystalline panel ranges from 0.75 to 0.77 (Šúri & Hofierka, 2004; Hofierka & Kaňuk, 2009). A performance ratio denoted as P_R of 0.76 as the mean of the range stated above, was adopted for this study.

Combining the three factors stated earlier produces the solar photovoltaic potential for a particular building roof. The formula adopted for this study to estimate the photovoltaic potential denoted as E_{OUT} is given as:

$$E_{OUT} = (R_{SA} * S_{MR} * P_E * P_R) / 1000 \quad (3.3)$$

Where E_{OUT} = Electricity output (kWh)

R_{SA} = Roof surface area (m^2)

S_{MR} = Mean annual solar radiation (Wh/m^2)

P_E = Panel efficiency (%)

P_R = Performance ratio

Now that the solar photovoltaic potential has been estimated using the roof surface area and estimate global solar radiation, the next sub-section gives the details of how the web deployment is designed.

3.2.5 Web-based Solar Photovoltaic System

Upon the completion of the solar photovoltaic estimations, the concluding objective of this study is to develop an interactive web-based system, which can be accessed by various people in order to provide information and solutions to rooftop solar photovoltaic systems. As part of design criteria, it is required that users would be able to click on data-layer features published, in order to retrieve attributes of such features. Likewise, it is required that a query toolbox is designed, with buttons, checkboxes and

radio buttons to interact with attributes of the published data layer, in order to display solar photovoltaic potential per building roof.

Therefore, a four-layered distributed system is designed following after the traditional client-server architecture as depicted in Figure 3.7. Three layers are on the server side, while one layers is on the client side.

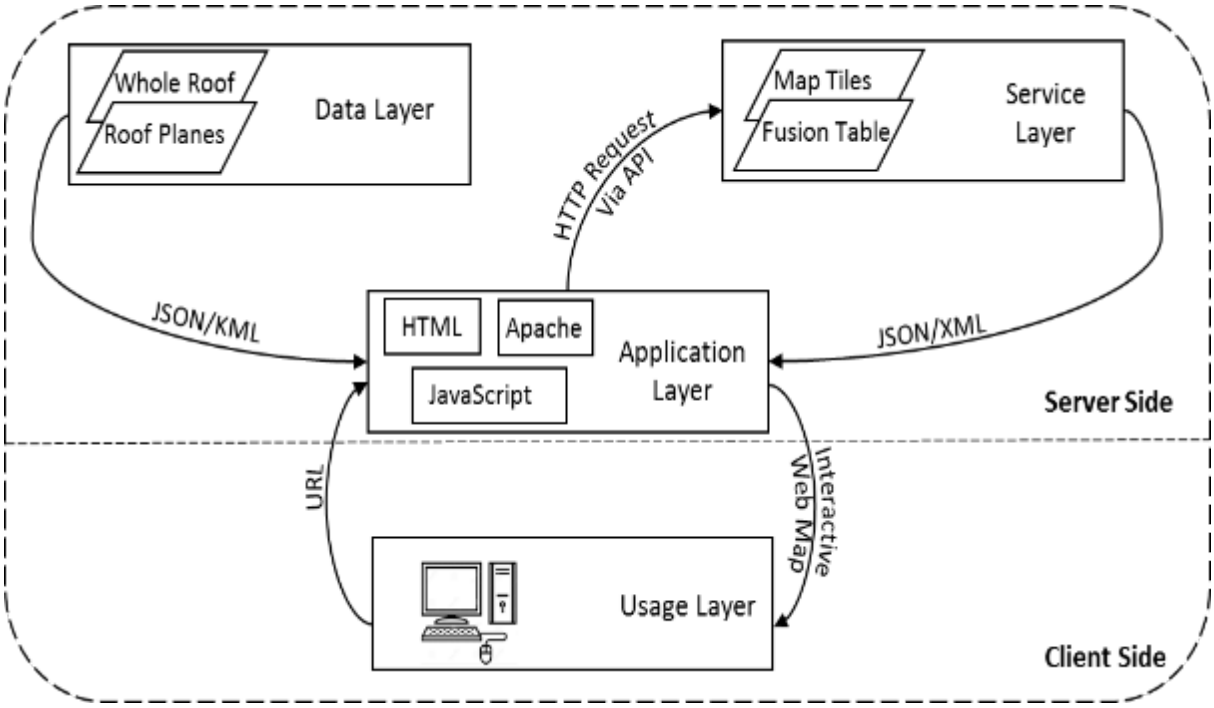

Figure 3.7: Client-server distributed architecture.

The bulk of the processes occurs on the server side and the application layer is the focal point of this side, it takes data from different distributed services and mash-it-up to create a customized web-based system. However, at the design stage, the data layer and the application layer falls on the client (author/system designer) side. The data and application layer transits to the server side upon system deployment and implementation on the web.

An HTML document is written with script tag (<script>) within to house the JavaScript codes used to make calls to the service layer (Google Maps JavaScript API and Fusion Tables REST API). Writing the HTML document, the title, and the styles are given within the header. Likewise, the library links such as jQuery and other JavaScript source code link are declared using the appropriate tag. Within the body of the HTML document, a division is created for the base map (Google map tiles). Other items

housed within the map division include the checkboxes to be used to toggle the published data overlays.

After creating the map division, a function is added to place the map document within this division. The function initializes the map by sending HTTP request to the Google web server and the map document is returned rendered. Map options such as start zoom, centre, bounds, and map type controls are declared within the opened script tag to customize the map. With the successful initialization of the base maps, the next step is to add ancillary tools like the search box, to search and locate addresses on the map. The next step involved scripts to overlay the data layer on the base map created. The whole roof outline and roof planes Shapefiles housed the geometric and attributes features. The solar radiation estimates and solar photovoltaic potential parameters derived from previous phases are already added as attributes. These data layers therefore, forms the database from which solar photovoltaic potential information can be queried and retrieved.

The whole roof outline layer is converted to a JSON data format and added directly as an overlay. While the roof planes layer is converted to KML data format and uploaded to Google fusion table, this is then rendered on the map using the “google.maps.FusionTablesLayer” object. The two layers are the anchored to the checkboxes created to enable toggle on and off. The last stage of the HTML document involved making the web map interactive. This includes making each feature respond to mouse clicks to display information, also an interface is designed to enable feature query, so as to extract and display information. The HTML document is then saved as index.html and ready to be hosted on a web server.

A web server is created on the computer workstation using the Apache HTTP server project. The server is installed by creating a root folder on the workstation “C” drive, the Apache executed file is invoked from the command prompt to start the server and Apache service. Thereafter, the configuration file is edited to reflect the server root, the workstation IP address and the port that the server would listen to. Once the server is correctly set up, the HTML document file and the referenced files are transferred to the document folder of the server. A client from the usage layer can interact with the web-based system by typing the IP/HTTP address on his browser and the index.html page would be returned, which is the interactive web map. A detailed description of

the HTML scripting in provided in Section 4.5.2, while the complete HTML document is provided in Appendix 4

Having looked at various methods and designs adopted for this study, a selection of software and hardware used in executing these methods are presented below.

3.3 System Selection

System selection comprises the selection of tools and assessment methods used to achieve the set goals of a particular study or project. In this case, it refers to the summary of choices of hardware and software employed in developing the methods as discussed previously. The same would be employed in processing the input dataset in analysis in the subsequent chapter to achieve the aim and outputs of this study. The main hardware utilised in this study is the desktop computer workstation, the desktop computer having the following specification:

- Edition: Windows 10
- Processor: Intel(R) Core(TM) 2 DUO CPU E8400 @ 3.00GHz
- RAM: 12GB
- System Type: 64-bit Operating System, x64-based processor

The specifications stated above are not the minimum specifications required to make the system work, but the specifications available for adoption in this study. However, increase in memory and processor speed would enhance speed and seamless handling. The software(s) and programing languages used in analysing the data and presenting the information are presented in Table 3.2.

Table 3.2: System selection.

Software	Manufacturer	Type
Python	Python Software Foundation	Open Source
HTML5	World Wide Web Consortium	Open Source
JavaScript	Netscape	Open Source
Apache 2.4.29	The Apache Software Foundation	Open Source
ArcGIS 10.4	ESRI	Proprietary
eCognition Developer 9	Trimble	Proprietary
ERDAS IMAGINE 2015	Hexagon	Proprietary
GRASS GIS 7.0.1	OSGEO	Open Source
LasTool	rapidlasso GmbH	Open Source
Ms Office 2013	Microsoft	Proprietary

LasTool and ERDAS IMAGINE are employed in LiDAR data pre-processing; the output, which included the classified LiDAR points, is then used as input in Python algorithm to generate the relevant DEMs (e.g. DSM and nDSM). The LiDAR-derived surface models and the aerial imagery are then integrated in eCognition Developer 9 to extract the building roofs (whole and planes), while GRASS GIS 7.0.1 utilise the DSM in estimating the global solar radiation. ArcGIS 10.3 is used in collating the Shapefiles and creating the geodatabase for evaluating the solar photovoltaic potential of the building roofs in the chosen study area. The JavaScript, HTML and Apache tools are utilised in deploying the solution online.

3.4 Study Area and Materials

The area chosen for this study was the City of Cape Town, situated in the southern peninsula of the Western Cape Province in South Africa. Popularly referred to as the "Mother City", it is the oldest city in South Africa. A coastal city covering an area of 2,461km^2 and with a coastline of about 294km (City of Cape Town, 2012), the city lies on the 34th latitude, as do Sydney in the southern hemisphere, and Casablanca and Los Angeles in the northern hemisphere. It has a mild Mediterranean climate, with an

annual average temperature of about 17°C. The average amount of sunshine hour per annum is about 3,100 hours, which compares well with the number of hours of sunshine for Los Angeles (3,300 hours) and far exceeds those of Madrid and Athens (2,900 hours). The average irradiance across the Western Cape Province ranges from 1,500 kW/m^2 per annum in the east to about 2,000 kW/m^2 per annum in the west (DEADP, 2013).

According to UNHABITAT (2014), the City of Cape Town is the tenth most populous city in Africa. Its population has grown by 45.9% from 1996 to 2011, and its current population is estimated to be 3,860,589, which represents an increase of about 100,000 from the 2011 census figure of 3,740,025 (City of Cape Town, 2014). The number of household stood at 1,068,572 as at 2011. Figure 3.8 shows a map of the city.

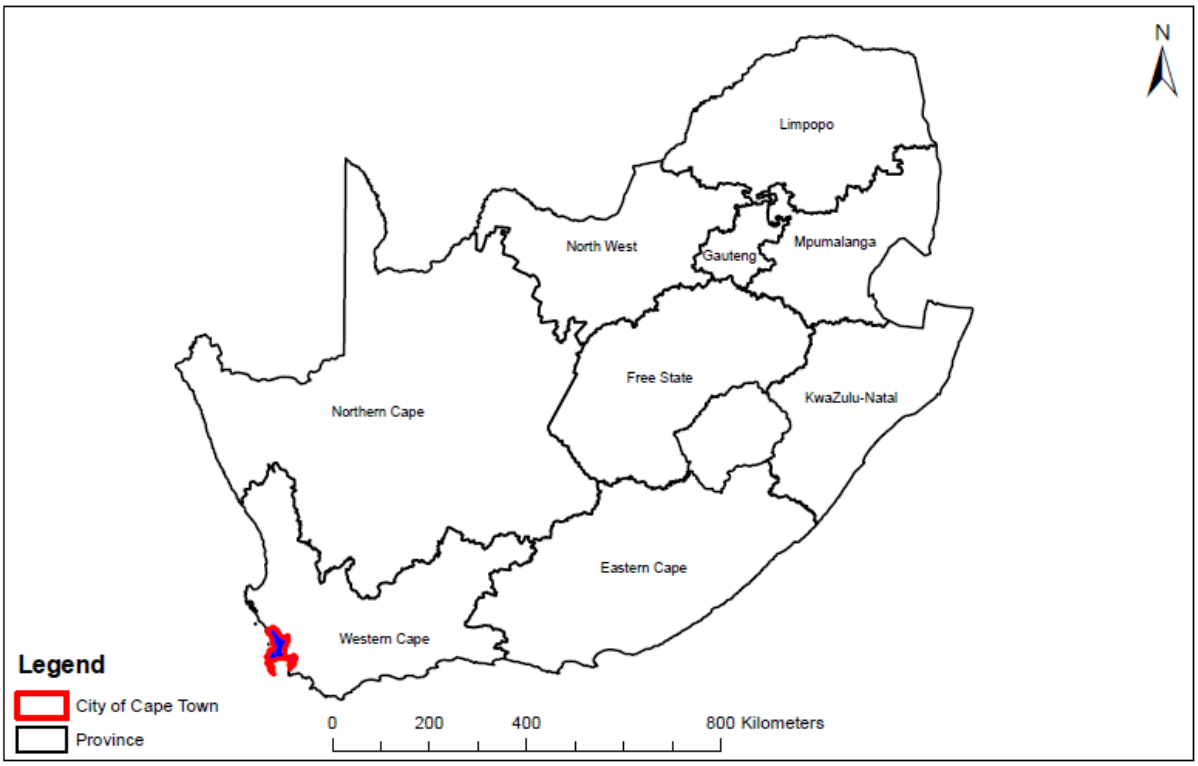

Figure 3.8: Map of the City of Cape Town.

City of Cape Town was considered ideal for this study because the primary input data required for this study, namely, LiDAR data and aerial imagery, are readily available. Some of these datasets were acquired around the same period, moreover, and have a similar high resolution. More importantly, the city is currently grappling with a severe drought crisis as of present. There have been series of campaigns on how to save

water and harvest rain water for use within the household. There have also been series of occasional energy crisis, especially with regards to shortage in electricity supply. The country's sole power generation and distribution company Eskom, has gone from pleading with electricity consumers to reduce electricity usage to threatening them with isolative load shedding, should they fail to yield to the warning. This situation, coupled with the government's policy on GHG emissions, has increased calls for the use of renewable energy sources to supplement the existing fossil fuel based electricity generating sources. Therefore, outputs from this study would go a long way in addressing the aforementioned challenges confronting the municipality.

3.4.1 Data Acquisition

Data acquisition for use in GIS and remote sensing can be broadly divided into two methods, viz. data capture and data transfer. The data capture category is further divided into primary data capture and secondary data capture. The former involves the direct measurement of objects or features, either physically by using land surveying, or remotely by using remote sensing and photogrammetry techniques. Secondary data capture involves using secondary sources to acquire data through scanning and digitizing.

Acquisition of GIS data is not only very time-consuming, but also very expensive, and may consume more than half of available project funds. The best way to avoid both of these pitfalls is to use data already generated by a third party, such as government municipalities, agencies or parastatals. This is the method adopted in the current study.

3.4.2 Data Sources

The quality of data utilised in any analysis depends on the source of such data. Therefore, it is very important to ascertain and verify the source of any data, before it is used in an analysis. This will help in authenticating the currency and level of accuracy of the data about to be utilised. The datasets used in this study were sourced mainly from the City of Cape Town municipality through the Division of Geomatics at the University of Cape Town. The data has been made available to the Division for research and educational purposes by the municipality.

3.4.3 Data Formats

GIS data format are primarily categorized as either vector data or raster data, within each of these categories, there are also different file formats for storing GIS data. The file format is the encoding of the GIS data into a computer file, which can then be read by GIS applications on the computer. Popular among vector GIS data format includes, Shapefile, GML, Spatialite, JSON/GeoJSON, KML, SVG, DXF and others, with Shapefile being the most popular. On the raster side, there is GeoTIFF, JPEG, GIF, IMG, PNG, ESRI Grid, amongst others, of which the GeoTIFF file format is the most widely supported file format.

Some of these data file formats are more associated with GIS desktop applications, while others are used primarily by web-based application. Considering the vector category, the SVG, GML, KML and JSON are predominantly the file format for web-based GIS applications. SVG, GML and KML are based on XML language, while JSON is lightweight and language-independent. The PNG raster data file format is the most widely in internet applications. For the purpose of this study, the Shapefile, GeoJSON and KML data file format were utilised in the vector category, while the GeoTIFF and IMG file format were used for raster analysis.

3.4.4 Data Verification, Integration and Editing

Data verification is the most important aspect of data manipulation, since the output or result of the study is dependent on the quality and validity of the data utilised. Data verification is also a non-negotiable part of the process, once a particular data transfer method has been chosen for analysis. It ensures that the data about to be used meets the requirements and prerequisites for the desired analysis (Congalton, 2009).

The first stage of data verification and integration involved checking the geographic projections of the two main data, namely, the LiDAR data and the aerial imagery. This was carried out in ArcMap 10.3 by checking the properties from the ArcCatalog. The projections of the datasets were found to be in Lo 19 Universal Transverse Mercator and WGS 84 datum. This local projection system is adopted as is for processing purpose, however, for the purpose of interoperability, the final data layers upon completion of the analysis would be transformed to the WGS 84 geographic coordinate reference system, before online deployment. The WGS 84 coordinate system, also

popularly referred to as EPSG 4326 (European Petroleum Survey Group) is a universal and standard coordinate system, thereby informing the decision to adopt this Coordinate Reference System (CRS) for online deployment.

The next stage involved overlaying the LiDAR point cloud on the aerial imagery to check whether the two are adequately co-registered. This is a crucial step, since the two datasets would be integrated in the analysis to extract the building roof outline. This check is carried out using ERDAS IMAGINE 2015; feature edges were visually zoomed into to check whether they aligned with those of the aerial imagery. The registration of the two data had already been done by the data vendor; the process described here is just to verify the registration process.

Further verification involved checking the spatial resolution (the size of the smallest possible feature that can be detected) of the imagery and the point spacing of the LiDAR data. The spatial resolution of the imagery was found to be 8cm, while the average point spacing of the LiDAR point cloud was 60cm. This confirmed that the datasets are of high resolution (high density, in the case of the LiDAR data). The pre-classified raw LiDAR data is also verified by visual inspection. The LiDAR point cloud is overlaid on the aerial imagery and all the unclassified points were switched off, while only the ground points are displayed. Comparing this with the ground areas visible on the aerial imagery confirmed the correct classification of the ground points of the sourced LiDAR data.

With the exception of the primary datasets, other ancillary datasets are also obtained from the City of Cape Town. These include the City boundary Shapefile, the address database and the cadastral parcel Shapefile. The address database is presented as a point Shapefile with addresses as one of its attributes. The address database is verified by overlaying the point Shapefile on the aerial imagery and comparing it with images from Google street view.

3.4.5 LiDAR Data

LiDAR is an acronym for Light Detection and Ranging; it refers to an airborne laser scanning or ground based system. A LiDAR system offers an active remote sensing technology, which emits laser pulses and can be utilised in obtaining 3D topographic data (X, Y, and Z) of natural or man-made features on the earth’s surface. The output

generated from the laser scanning is a set of unstructured points, popularly referred to as a point cloud. The LiDAR system, being an active system, can be used in the daytime or at night, as it has the capability of penetrating tree canopies.

Unlike other remote sensing products, such as aerial or satellite images, LiDAR measurements are not affected by relief displacement and shadows. The airborne laser system (ALS) makes use of Light Detection and Ranging sensors, which are mounted on aircraft. Laser pulses in the visible and near-infrared wavelengths are transmitted in millions from the aircraft-mounted system to the earth's surface. The sensor then records the time taken for each transmitted pulse to reflect back to the sensor, after hitting the features on the ground. The LiDAR sensor uses the time difference between the transmitted and the reflected pulses, coupled with the speed of light, to calculate the distance to each point and subsequently its elevation (Z). A high precision GPS receiver mounted on top of the aircraft concurrently records the geographic location (X, Y) of the measured point. Other ancillary data recorded by the LiDAR sensor includes the intensity of the return pulse(s).

The strength of LiDAR technology lies in its capability to acquire millions of 3D point data in a relatively small amount of time, compared to the traditional land surveying technology, which takes much longer to acquire the same volume of data. Another advantage of the LiDAR system over the land surveying method is that it can easily access areas that might be difficult or completely inaccessible for someone using conventional land-surveying methods. The technical specifications for the LiDAR data utilized in this study is provided in Table 3.3

Table 3.3: Technical specification for the LiDAR data.

Coverage	2,461 km^2
Acquisition Period	2012 - 2014
Point Density	3 points/m^2
Sensor	Trimble Harrier68i (Riegl LMS 680i sensor)

3.4.6 Aerial Imagery

Aerial imagery obtained from aerial photography, processed as ortho-imagery, is one of the most fundamental products of photogrammetry and remote sensing technology. Aerial photography dates back to 1858, when Gaspard Felix Tournachon, a French photographer also known as Nadar, took the first aerial photograph using a tethered balloon (Baumann, 2014).

The sensors used to acquire aerial imagery are referred to as aerial cameras; they are mounted on-board an aircraft. Flight planning is carried out prior to the acquisition of the aerial imagery to determine important factors, such as the number of exposures required to cover an entire project area, the number of flight lines, the scale or the resolution of the output orthoimage, and the flying height, among others. Major factors, which determine the resolution of the aerial imagery, are the flying height of the aircraft used and the specifications of the aerial camera lens. The aerial imagery data utilized in this study is captured using a digital camera, this is then used to produce a very high resolution ortho-imagery in the red, green and blue wavebands. The technical specification of the aerial imagery is provided in Table 3.4.

Table 3.4: Technical specification for the aerial imagery.

Coverage	2,461 km^2
Acquisition Period	2012 - 2014
Resolution	8cm GSD
Sensor	Visonmap A3 RGB (300mm)

3.4.7 Data Grid Tiling

Due to the high point density of the LiDAR data, file sizes are very large. Therefore, to allow for faster and easier processing of the input files, as there are constraints on amount on file size, the computer memory can process without resulting in a system crash. The LiDAR and aerial imagery for the study area are divided into manageable tile grids. A tile size of 1 km^2 (1,000m by 1,000m) is adopted. Using this tile size, the entire City of Cape Town is divided into 2,711 tiles (see Figure 3.9). It is worth noting that not all the tiles are used in the analysis stage, as some tiles covered areas, such

as mountains, farmlands or bare ground; only tiles that contained buildings and that belong to formal settlements are utilised in the analysis.

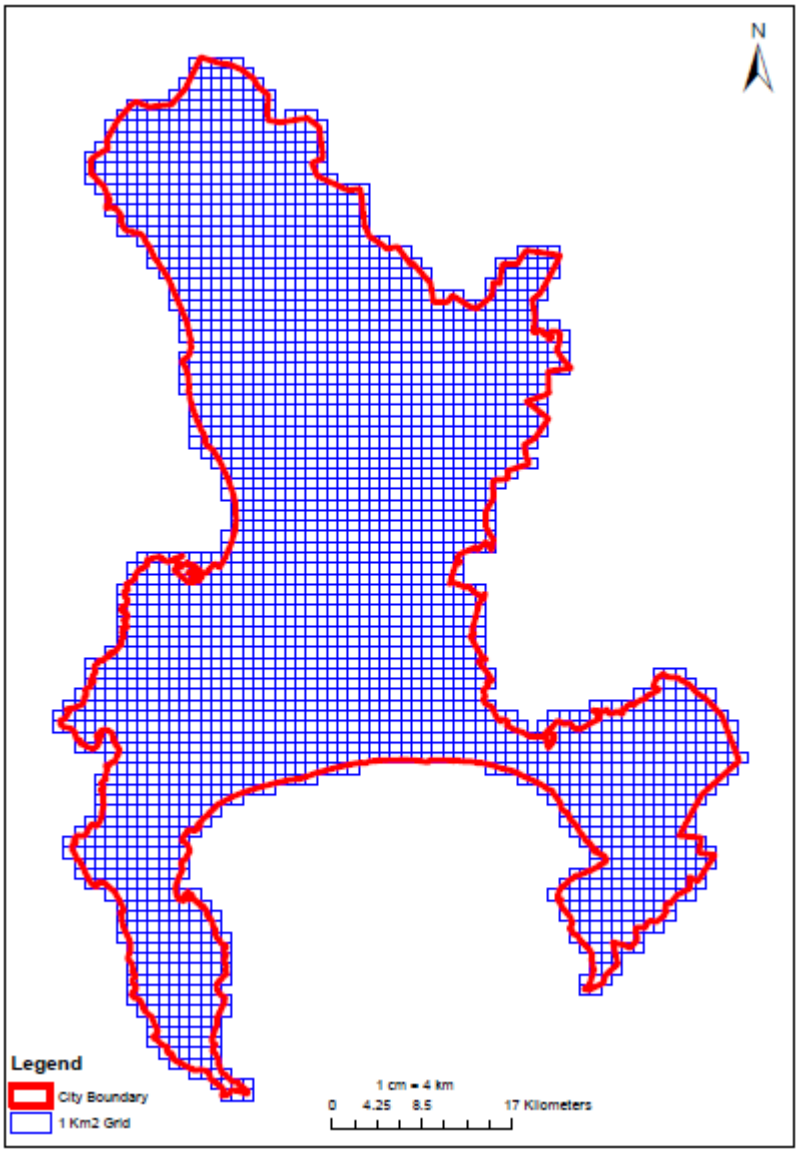

Figure 3.9: Dividing the study area into tiles of smaller workable size

The LiDAR data are divided into 1km^2 tiles using the ERDAS IMAGINE Split and Merge tool. The split schema is drafted in AutoCAD 2016 and converted into a Shapefile using ArcGIS. A file name prefix is required to be provided ("Grid" was chosen for this study), and the tool then makes use of a unique identifier column (01, 02, 03, etc.) from the split schema attribute's table, together with the provided prefix to name each of the new tiled Las files (Grid_01, Grid_02, Grid_03, etc), as shown in Figure 3.10.

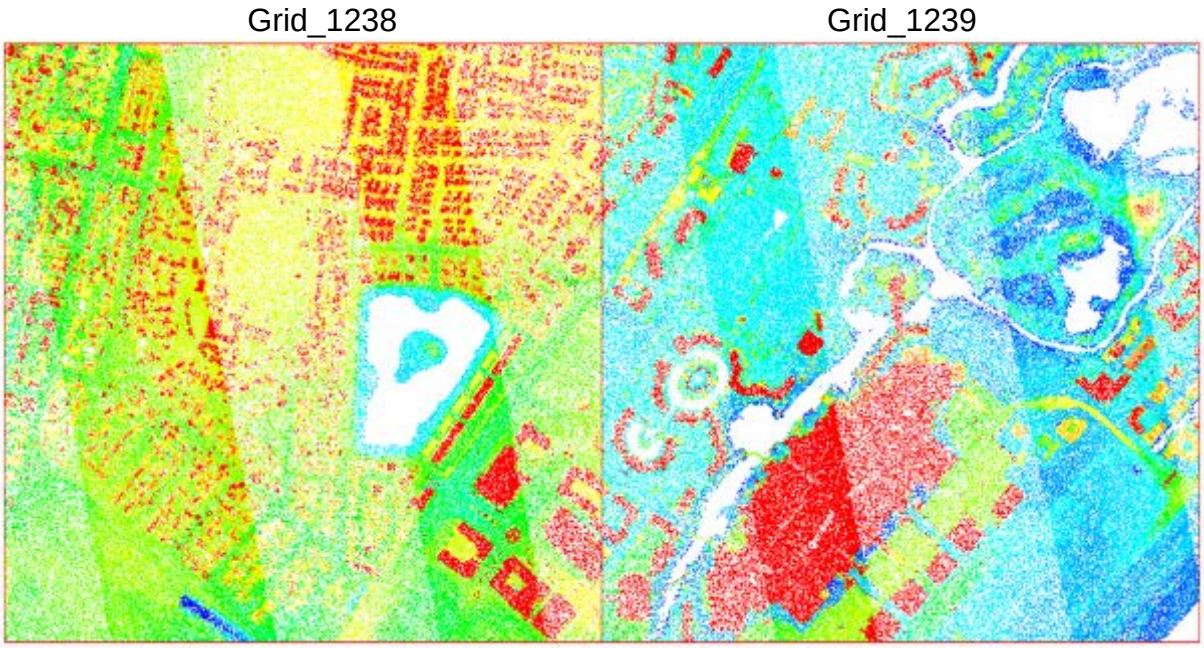

Figure 3.10: LiDAR tiles

A similar process is followed in ArcGIS using the Split Raster tool to break up the mosaicked aerial imagery of City of Cape Town into 1km^2 tiles. The same naming convention used in the LiDAR split is adopted for the sake of easy identification and sorting. Samples of the imagery tile are shown in Figure 3.11.

Figure 3.11: Aerial imagery tiles

3.4.8 Database

A database is a central location where data is stored, managed and manipulated; it also provides the means of retrieving information from it. A GIS database houses data pertaining to the spatial locations and geometry of geographical features, which are stored as areas, lines, points, pixels or TINs. In addition to the geometry of the features, the attributes are recorded as well. A geodatabase is a special type of database or file structure, used primarily to store, query and manipulate spatial data. It records the geometry, spatial reference system, attributes and behavioural rules for the GIS data. Types of geographic datasets that can be stored in a geodatabase include feature classes, attribute tables, network datasets, raster datasets and topologies. A geodatabase could either be a file, personal or an enterprise geodatabase.

In preparation for the analysis, a geodatabase is created in ArcGIS 10.3 for this study. The spatial reference system, Lo 19 Universal Transverse Mercator (WGS 84), is defined to match that of the data to be stored in it. The verified, integrated and edited data that could be stored in the geodatabase are imported into the geodatabase. Dataset classes are created to reflect three phases of the analysis adopted, namely “Roof Polygons”, “Solar Radiation Estimation” and “Solar PV Calculation”. Each dataset and the results from the analysis are stored under matching datasets to ensure that each phase of the analysis is simplified and well organized.

3.5 Chapter Summary

This chapter presented in detail, the methodology upon which the analyses carried out in this study were based. An overview of the entire methodology was provided in Section 3.1, while Section 3.2 looked at the methods designed for each phase of the study. Section 3.3 presented the list of software and hardware utilised in processing the input data, while the study area and materials used in the study was discussed in Section 3.4. The data can now be analysed using the adopted methodologies as described in the next chapter.

CHAPTER 4
RESULTS AND DISCUSSION

The data manipulation and pre-processing described in the preceding chapter prepares the ground for the actual analysis that is required to achieve the aims and objectives of this study. This chapter presents, in detail, the analysis carried out in this study, based on the methodologies that are reviewed and explained in Chapter 3. Section 4.1 of this chapter presents the analysis and results of the preliminary processing common to or required prior to all subsequent stages of the analysis, specifically with regard to the classification of the LiDAR data and the generation of DEMs. Section 4.2 provides the details of the analysis carried out in extracting the building roof outline using relevant rule-sets, while Section 4.3 explains how the global solar radiation is estimated by using the GRASS Python library. Section 4.4 gives some insight into how the solar photovoltaic potential for each building is calculated, and thereafter, Section 4.5 describes the creation of a solar photovoltaic potential database. Section 4.6 describes how the solar photovoltaic database is deployed to the web, while Sections 4.7 and 4.8 summarize the results of the analysis and their application respectively. Samples of results generated from each stage of the analysis are presented after each analysis, and before the discussion of such analysis, for the sake of easy referencing.

4.1 LiDAR Classification and DEM Generation

The LiDAR data provided for this study is already pre-classified into ground and non-ground classes, and was divided up into smaller tile grids for ease of handling and processing, as stated earlier. Two types of DEMs are required for use in this study, namely, the nDSM and the DSM. The nDSM is required as an input for the extraction of building roofs, while the DSM is the main input required for estimating the global solar radiation.

The processes involved in generating the two elevation models differ slightly and are therefore treated separately. The nDSM could be generated by subtracting the DTM from the DSM. It could also be created directly by interpolating a height normalized

LiDAR cloud point. These two methods are assessed during the stage of choosing the most appropriate methodology (see Chapter 3, sub-section 3.6.1) and are found to yield similar results. However, the process of generating the nDSM by interpolating the height normalized points is much faster and required less storage space, and is therefore chosen as the preferred method. The classification of the LiDAR data and the generation of the DEMs is discussed in the following sub-sections.

4.1.1 LiDAR Data Processing

The raw LiDAR points were processed to achieve the height normalized point cloud, using the lasheight tool from “LAStools” toolset for LiDAR processing. The lasheight tool requires the raw LiDAR data “las” file as input. The ground classified points were selected as a reference for constructing the ground TIN, with which the height of all other points was then computed, in respect to these selected ground points. The last step was to select the option of replacing the Z coordinate of points with the calculated height. This process outputs a “las” file containing height normalized LiDAR points, which was then utilised in creating the nDSM. The process was included as a sub-process in the Python algorithm to generate the nDSM.

4.1.2 DEM Generation Analysis

The elevation models are created using various processes contained within the “arcpy” library in Python. The algorithm is designed to read the LiDAR data as the sole input, while the “lasheight” tool is added as a sub-process. The LiDAR data goes into the lasheight model (“arcpy.gp.Model12”) and outputs a height normalized as described in Section 4.1.1. The processed LiDAR then goes into “arcpy.CreateLasDataset_management” process to create a las dataset. The las dataset is then served into the “arcpy.LasDatasetToRaster_conversion” process, this converts the las dataset into a raster using binning method. The value field, which specifies the LiDAR information to be interpolated, is set to “ELEVATION”. The next setting is the interpolation type, which is set to “Binning”; the “MAXIMUM” option for cell assignment type is chosen to assign an elevation value to each cell of the raster. Cells that do not have points within them (void cells) are assigned values using the NN interpolation method. The final output raster settings include setting the data type to floating point and setting resolution (pixel size) to 8cm to match those of the aerial

imagery of the study area; moreover, the NoData value is set to zero. The nDSM raster output now serve as input to calculate the slope and the aspect raster using “arcpy.gp.Slope_sa” and “arcpy.gp.Aspect_sa” process respectively. A copy of the Python algorithm is provided in Appendix 1.

4.1.3 Results

Figures 4.1(a), (b) and (c) show the sample results in respect of the LiDAR-derived products created, using the “lasheight” and “arcpy” in Python algorithm. All the procedures discussed in the analysis stage above are repeated for each of the LiDAR tiles, which contained buildings and within the scope of the study.

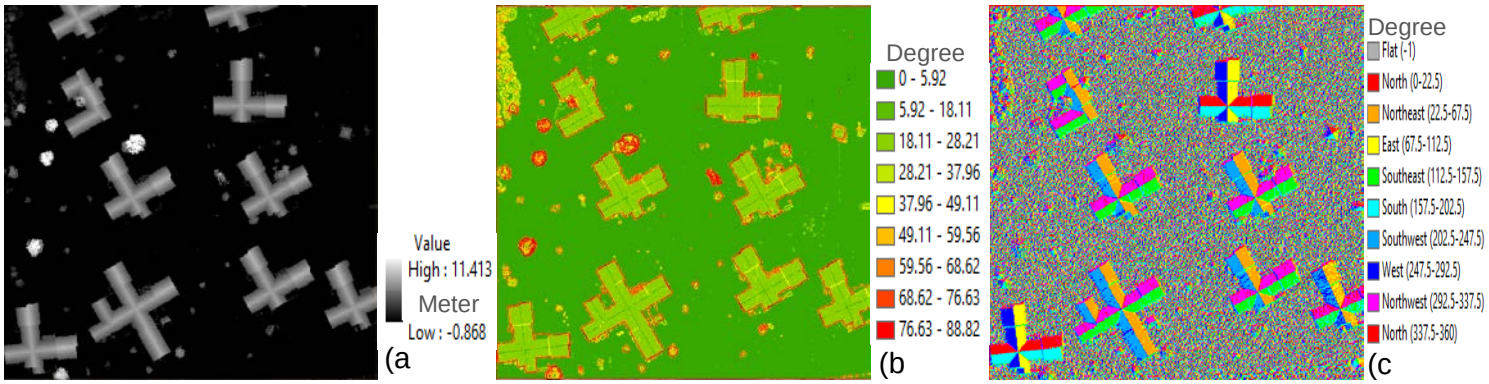

Figure 4.1(a): Normalized digital surface model (nDSM), (b): Slope raster, (c); Aspect raster.

4.1.4 Discussion of LiDAR Processing and DEM Generation

The elevation model generated, as shown in Figure 4.1(a), forms the fundamental input data for the subsequent analysis. This goes a long way in affirming the importance and usefulness of LiDAR data in spatial analysis and surface information generation. The LiDAR data offers a massive collection of 3D points, which can be utilised by various applications in deriving spatial information about a particular area or region.

For instance, based on the sole input of LiDAR data, which has been used to create an elevation model, various surface analysis can be carried out to yield information, such as aspect (Figure 4.1(c)), which determines the orientation or direction a particular surface faces in terms of geographic direction. Other surface information that can be generated from LiDAR-derived DEMs include slope (Figure 4.1(b)),

contour, volume calculation, viewshed, and solar radiation, amongst others. It has also been found to be effective in object detection and extraction, as will be discussed in detail in the subsequent section (see Section 4.2). There are many other areas of application where LiDAR data is very useful, but these are beyond the scope of this study. However, it must be emphasized that investment in LiDAR data acquisition by government establishments or corporate bodies involved in spatial planning is indeed a great asset.

Having discussed LiDAR data processing and generation of DEMs, these outputs are now put to use in the analysis of building roof extraction as presented below.

4.2 Analysis of Building Roof Extraction

The analysis carried out in this study with regards to the extraction of building roofs was carried out using eCognition Developer 9.1 software. The extraction of building roofs forms a vital part of the analysis that is required to estimate the solar photovoltaic potential available to each building. It is, therefore, the first major analysis to be carried out in achieving the aims of this study. There are two stages involved, the first stage detects and extract the whole building roof outline, while the second stage decomposes the whole roof to its consisting planes. The details of this analysis are presented in the following sub-sections, viz. Section 4.2.1 looks at data preparations, while Section 4.2.2 explains how the building roofs are extracted using rule-sets and Section 4.2.3 discusses the results generated from this analysis:

4.2.1 Data Preparation

The data required as input for the analysis include the nDSM, slope, aspect raster generated from the previous analysis, as well as aerial imagery. The eCognition software is launched in the “Rulesets” mode. A new workspace is created, with a name being assigned and a new project being added. Each of the four input data are imported, starting with the aerial imagery, which has three (3) bands. The bands or layers are assigned aliases in order to make each layer identifiable, and to make the resultant rule-sets transferable for subsequent datasets. The same process is repeated for the nDSM, the slope layer and the aspect raster, these all have a single band/layer, unlike the aerial imagery. Therefore, each layer imported was named

according to their aliases, with layer one being assigned “red”, layer two “green”, and layer three “blue”. The fourth layer was named “nDSM”, while layer five and layer six are identified as “slope” and “aspect” respectively. Each of the imported layers is checked to ascertain that they all had the same resolution and extent. The resolution is automatically detected from the imported rasters as 0.08m. The last stage involved setting the “No Data” value to zero for all the imported data layers, as this is necessary for the proper calibration of pixel values, which would be required as threshold values later during the analysis.

4.2.2 Rule-set Development

Before the analysis itself began, the imported data layers are checked using “Edit Image Layer Mixing” tool, so as to ascertain that the correct layers required for the extraction analysis had been imported and correctly named. At this stage, the strategy that would be used in classifying the building roofs is contemplated and explored. This is done using the “Feature View” tools; the object features that are explored included layer values and their geometry. A tool is selected and double-clicked upon, causing the particular operation requested to be computed; the range of values is updated to display and reflect the results of the calculation or operation.

Once the object features had been explored properly, a strategy is adopted to develop the rule-sets: this included creating image object segments from the imagery, assigning the same weight to the red, green and blue bands. This is achieved using the multiresolution segmentation method. Then the segmented image objects are classified starting with the non-desired class and ending with the desired class, in what can be termed classification by elimination. A clean-up process is then applied before exporting the desired object as a Shapefile for further analysis. Series of analysis involved in detecting and extracting the whole roof outline and the decomposition of the whole roof into roof planes are further presented below.

Whole Roof Outline Detection and Extraction

In pursuance of the chosen strategy, the first step is to create image objects, to which the rules-sets are applied in order to classify and extract the desired objects. The multiresolution segmentation algorithm is employed to segment the image scene into image object primitives. The pixel level domain is automatically selected since there

are no image objects yet. Within the settings of the segmentation algorithm, a new level (“L1”) is specified, which would hold the new segmented image objects resulting from the segmentation process. An even weight of one (1) was assigned to the participating layers, which are the red, green and blue bands for full participation. The scale parameter, which defines the size of the resulting image objects is set to 85. This threshold was carefully selected after thorough exploration, the bigger the scale value, the bigger the resultant segmented image objects. The idea is to have smaller building objects as a unit and bigger building objects divided into its roof planes. This is further achieved by setting the “Shape” parameter to 0.1 and the “Compactness” parameter to 0.7, a lower shape and higher compactness parameter ensure image objects of similar colour are not fractured. The number of cycles for the loop is set to 1, the resultant image object segments are displayed below. Figure 4.2(a) shows the image scene as imported into eCognition and Figure 4.2(b) shows the output after segmentation process has been completed.

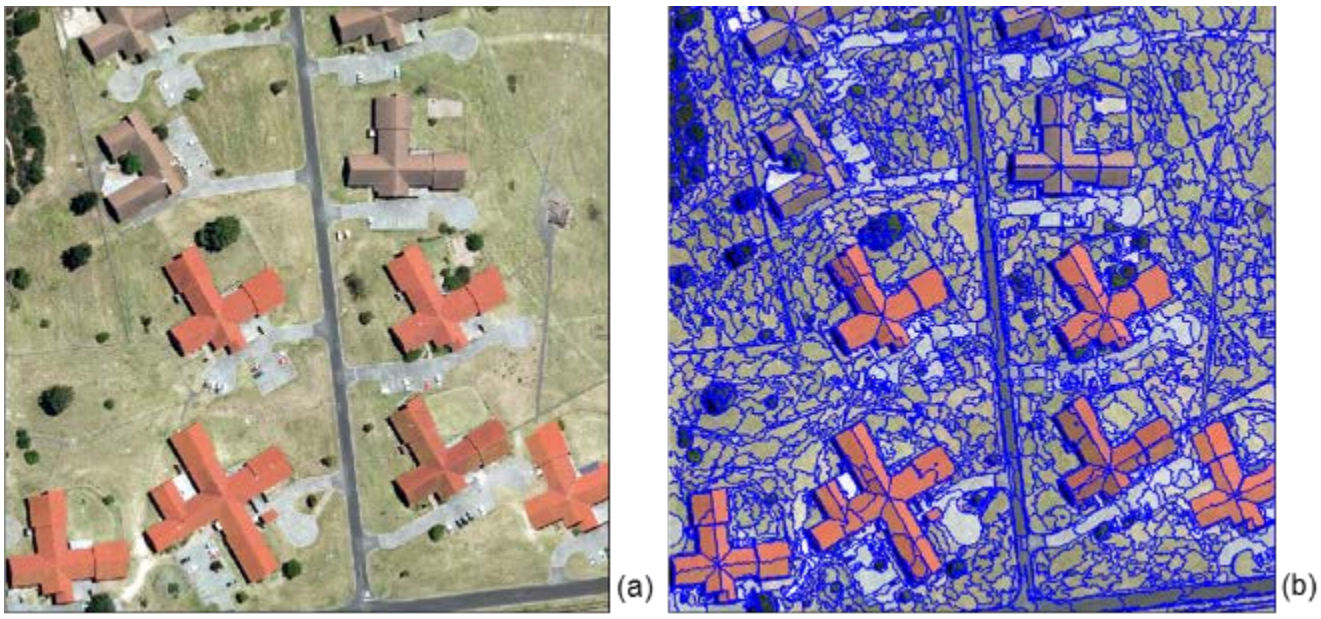

Figure 4.2(a): The aerial imagery before segmentation, (b): The result of multiresolution segmentation.

After the process is executed, the results generated are inspected to see whether the derived segmentation would suffice for the subsequent analysis and classification. It is required that the image object segments containing the building roof does not contain adjoining ground or tree objects. This is the reason why the “Shape” parameter is set to 0.1 and the “Compactness” set to 0.7. With meaningful image object segments resulting from the segmentation process, the next step in developing the rule-set is to

analyse these objects using their properties, with the aim of using these image object properties to classify each image object into its appropriate class. Because the interest is only in the building roofs, the segmentation output is cleaned up by merging areas of lower heights, likely belonging to the ground class. This is achieved by using the “merge region” algorithm. The merge algorithm merges segmented image objects sharing boundary (topology) and fulfilling the set threshold or criteria.

At this stage, the domain, which specifies which level or area an operation is carried out is set to image object level, since the focus is now on the segmented image objects. Within the image object level, the level created in the first segmentation process above is selected and a threshold condition is set using the height information from the nDSM layer. The basic use of “merge region” is to merge image objects that fulfils a set threshold condition and shares topology. The threshold condition (mean nDSM < 1.8) is set to merge all image objects with mean height less than 1.8m and are connected. This threshold is selected as the minimum building height for this study. The resulting image objects are the building roof and other elevated objects retaining the size derived from the specified scale (85) at segmentation, while other objects are merge into a bigger image object, likely belonging to the ground class, highlighted in red (see Figure 4.3).

Figure 4.3: Result of refined segmentation

With the refined segmentation result, the stage is now set for classification of image objects. The green objects are the first object to be eliminated by classifying it, this is

preceded with classifying shadowed areas. A similar strategy is devised to detect and classify these two classes. A green index variable is created using the “update variable” algorithm. The green index is used to identify green objects by exploring their spectral characteristics. The index is constructed by creating a customized feature, the green band is divided by the mean of all the three bands. Using this customized feature, green objects are found to have a minimum index of 0.36. Using similar procedure, another variable is created to detect shadowed areas. The shadow index is calculated by adding the mean of red, green and blue spectral information for each segmented image object (R + G + B). After careful feature exploration, shadow objects are detected having an index of 200 and below. A process flow diagram highlighting the detection and classification of green objects and shadow area is shown in Figure 4.4.

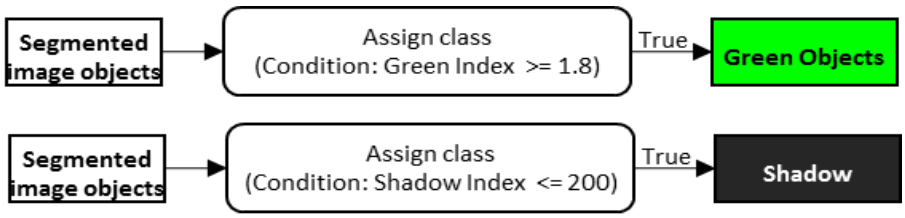

Figure 4.4: Process flow diagram to classify green and shadow objects

Having found thresholds for green and shadow objects by which rules can be set, segmented objects that fulfils these rules or conditions will be assigned to that class, which condition it fulfils. From the algorithm list, “assign class” was chosen, and the condition or rule is specified as “Green Index >= 0.36”. Under the algorithm parameter column, a new class is created called “Green Objects” and a matching colour is assigned to denote it. The process is executed and the resulting classification is previewed as shown in Figure 4.5. Since the index detects any green object, some building roofs that are green are also classified as green object. Therefore, a strategy to declassify the green roofs is required. A similar process is followed to detect shadowed areas using the shadow index. The condition is set as “Shadow Index <= 200” and a class is created named “Shadow” and black colour is assigned to denote it. The resulting classification is shown alongside green objects in Figure 4.5.

Figure 4.5: Result of green and shadow objects classification

To declassify the green roofs, the slope information is utilised. It was discovered that trees have higher slope values compared to roof planes. Moreover, roof planes with slope greater than 45^0 are not suitable for solar photovoltaic installations, as discussed earlier in Section 2.9.2. Therefore, the green objects are merged and a threshold condition set as “Mean slope < 45” is applied to the green objects to declassify the green roofs. Figure 4.6 in comparison with Figure 4.5 shows the “arrowed” green roof declassified.

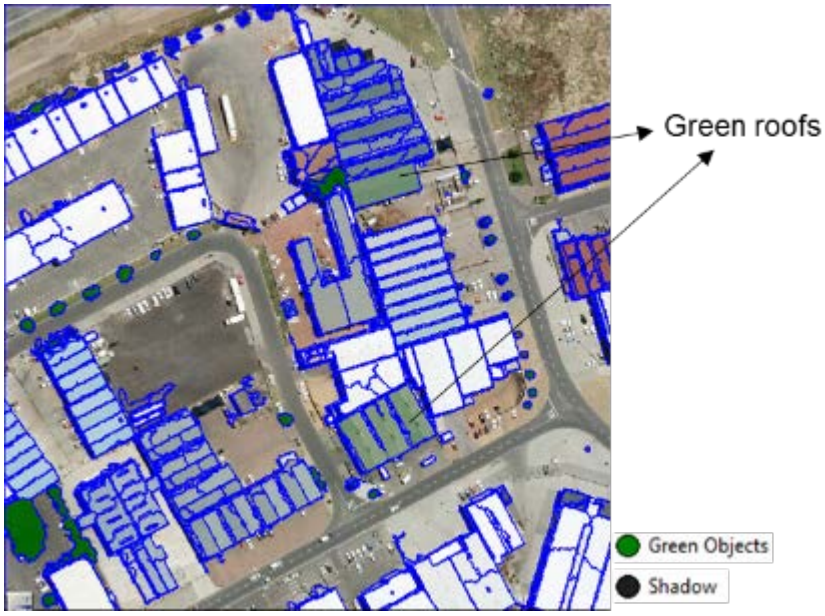

Figure 4.6: Result of green roof declassification

The next object to be eliminated by classifying it, is the ground area, this is already identifiable using the height information from the nDSM raster. Another threshold condition is set on unclassified objects as “Mean nDSM < 1.8”. The class filter dialog tab is used in selecting the class of objects to which a set of rule(s) is applied. A new class is created called “Ground” and an appropriate colour is assigned to denote it. The result of the ground area classification is shown in Figure 4.7.

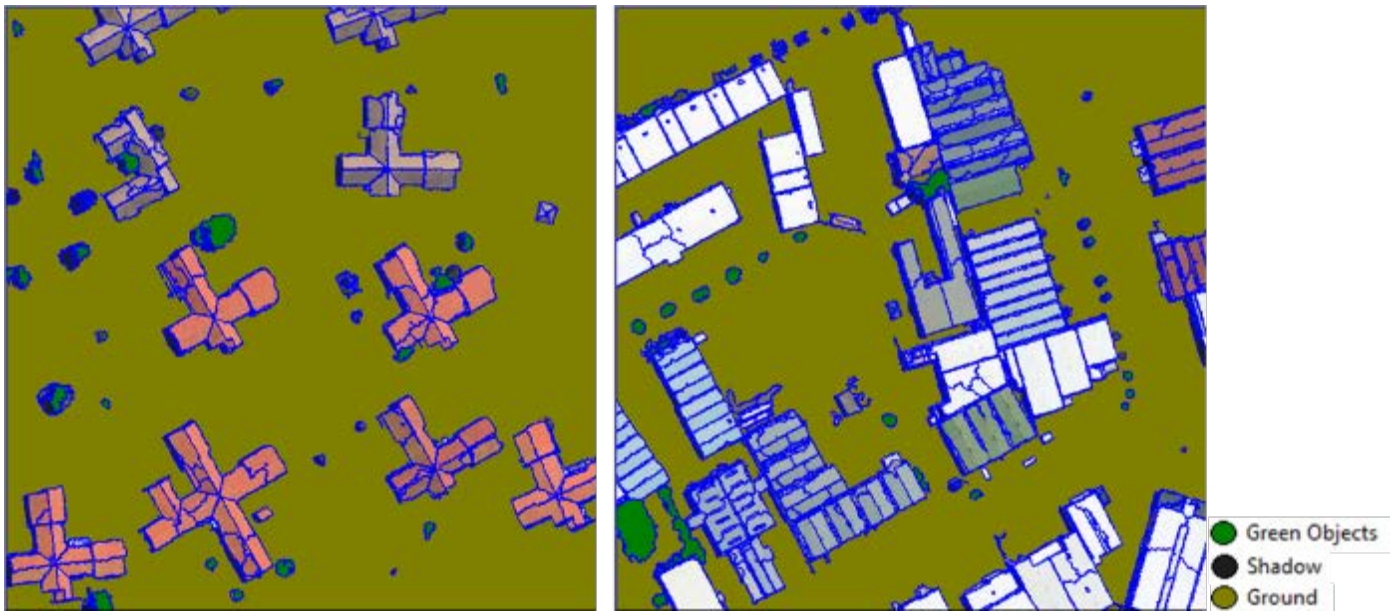

Figure 4.7: Result of ground classification

Using the strategy of classification by elimination, all the undesired objects are successfully detected and classified accordingly. The remaining unclassified image objects are mostly that of building roofs, which made the detection and classification of building roof much easier. Other smaller image objects, which are not building roof objects and did not fulfil any of the rules set earlier are filtered out using area/size threshold. In preparation for classifying the whole building roof object, all the image objects, classified and unclassified are copied to a new image object level called “L2”. This process was deemed necessary, as the previous image object level would serve as a backup, in an instance something goes wrong in subsequent classification analysis.

After creating a new image object level, all the unclassified image objects, which are mostly building roofs are merge, using the “merge region” algorithm. This process merges all smaller building roof image object segments together to form a whole building roof object. A process is then added to classify all unclassified image objects.

The “assign class” algorithm is added, the image object level is set to the new level (L2) and the class of object on which the classifier would be applied is set to “unclassified”. No threshold condition is applied, since the building roof objects are mostly the unclassified image objects remaining. A new class “Building Roofs” is created and an appropriate colour is assigned to it. The classifier process is executed and the result of the classification is shown in Figure 4.8.

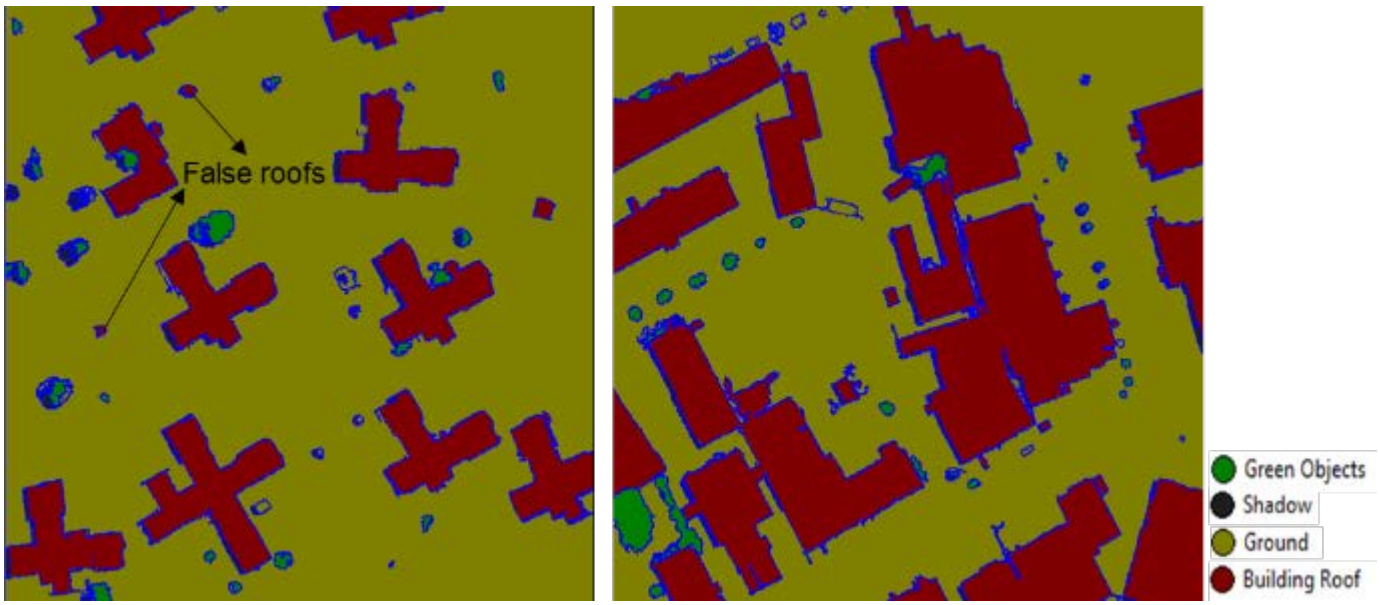

Figure 4.8: Result of building roof classification

Some tiny elevated objects, mostly small tree canopies, which had not fulfilled the green object threshold nor the slope threshold are shown arrowed in the Figure 4.10 as “False roofs”. These image objects have been classified along as building roof, thereby a strategy is required to declassify such wrong classification. As part of the clean-up process, various object reshaping algorithms available within the eCognition software are employed. The first process is designed to remove the misclassifications called false roofs. The “remove object” algorithm is used, it is a fuzzy classifier algorithm that examines candidate objects of a specified class that meets the specified rule or threshold condition(s). It then removes the image object from whatever class it has already been assigned to and merge it with specified target classes. It assigns these candidate objects to the target classes by determining the degree of probability at which each object belongs to the target class using its proximity. The degree of

probability is determined by accessing the neighbouring object largest common border.

The “remove object” algorithm is added as child process; the image object level is set as “L2” and the building roof class is set as the candidate objects. While the target classes are green objects, shadow and ground classes. The rule or threshold condition to be fulfilled by the candidate objects is specified using the area (size) property as “Area < 25 m^2”. This value is considered the size of the smallest building roof allowed for consideration in this study, after careful exploration of the image scene. It is also worth noting that the scope of this study does not cover informal settlements, characterized with smaller roof structures. Other object reshaping tool used in refining the building roof objects includes the “pixel-based object resizing”. This is implemented in two modes, “grow” and “shrink”. This process helps in removing jagged edges around the building roof object. It functions by reducing the peaks and filling up the valleys of the uneven edges. The concluding phase of the whole roof outline detection and extraction involved declassifying all the undesired image objects such as “Green Objects”, “Shadow” and “Ground”. The image objects in these classes are added to a classifier and assigned to “unclassified”. All the unclassified image objects are then merged together using the “merge region” algorithm.

In preparation for the first export and to further simplify the building roof edges, the classified building roof image objects are converted into vector objects using the vector handling tools. Also, by applying the vector handling tools, various processes are carried out in order to create a neat and smooth polygon, describing each building roof. Vector handling processes used included vector smoothing, vector simplification, vector dissolving and vector orthogonalization. The vector orthogonalization generalize vector polygons to orthogonal polygons, to better represent the building roof geometry. The simplification algorithm on the other hand simplifies the vector polygon shape using the Douglas-Peucker algorithm. As part of the attribute to be exported with the building roof, the slope and height (from nDSM layer) feature are added. At this stage, the whole roof detection and extraction process is completed, and the building roof polygons are ready to be exported as Shapefiles for further analysis in ArcGIS software. Figure 4.9 shows samples of the whole roof classification result before been exported as Shapefile to ArcGIS software.

Figure 4.9: Result of whole roof outline detection and extraction

Whole roof decomposition into roof planes

The output from the whole roof detection and extraction as shown in Figure 4.9, now serve as input in generating the building roof planes. In preparation for breaking down the whole building roof into roof planes, a new image object level “L3” is created above the previous level (L2) and the building roof objects are copied to the new level. As stated earlier, the previous level now acts as a back-up, should any problem occur in the next phase of analysis. The first process in classifying the building roof planes involved segmenting the whole building roof into tiny image objects. A chessboard segmentation is applied in the image object domain on the whole building roof objects. An object size of “5” is specified as the resulting image object size, this is deemed sufficient to decompose the whole building roof outline into smaller manipulative size. The resulting segmentation is shown in Figure 4.10(a).

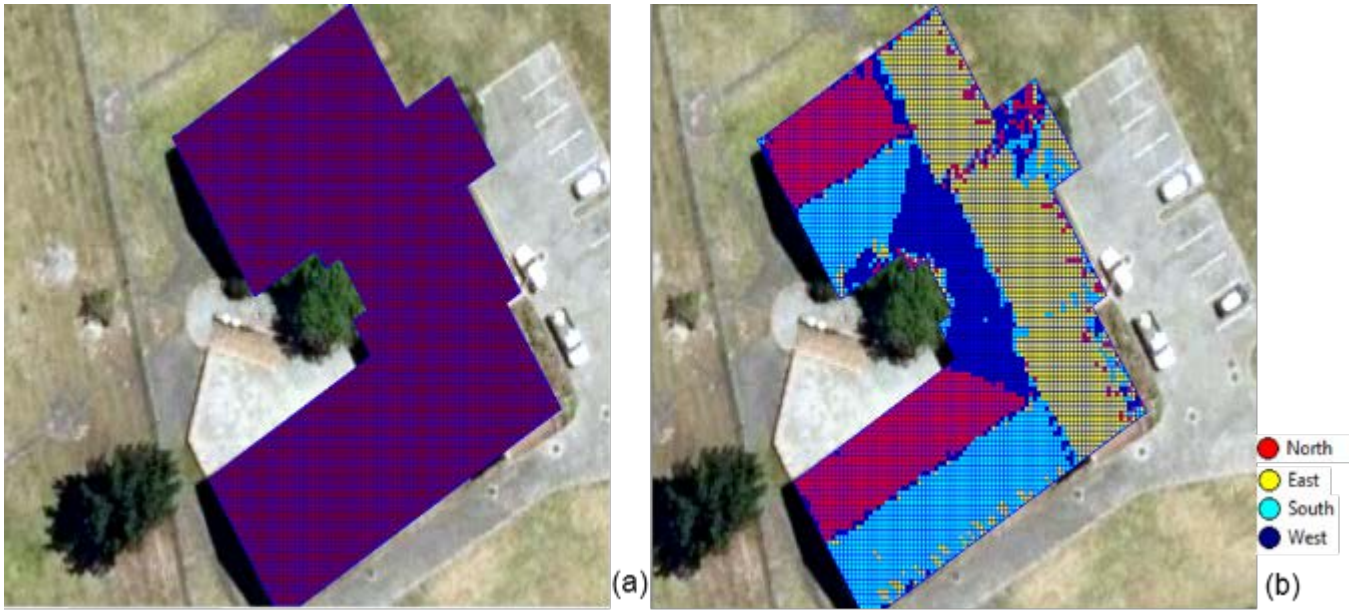

Figure 4.10(a): The segmented building roof, (b): The classified building roof objects.

The tiny building roof objects are then classified into their cardinal directions using the aspect (orientation) values. Each building roof object are evaluated based on its aspect value, derived from the aspect layer and if it fulfils the rules or criteria specified for each of the cardinal direction, it is classified into such. A fuzzy classifier process is designed for each cardinal direction (North, East, South and West). The rule for the north facing planes are set in two fuzzy classifiers because of the nature of its graduation in degrees, north facing roof planes are detected using aspect values from 0^0 to 45^0 and 315^0 to 360^0. The fuzzy classifier is unable to set the two ranges in one process; therefore, each range of aspect are specified in different processes. The first range is set using two threshold conditions viz. “Mean aspect >= 0^0” and “Mean aspect <= 45^0”. Using similar technique, the aspect range for each cardinal direction is specified and a sample result of the classification is shown in Figure 4.10(b).

The next stage in delineating each roof plane involved aggregating common roof plane candidates to form a complete roof plane. This is carried out by merging building roof object that belongs to the same class together. A merge region process is added for each of the four roof plane classes. The class filter is used in defining which class to perform the merge operation on. The result of the merge operation is shown in Figure 4.11.

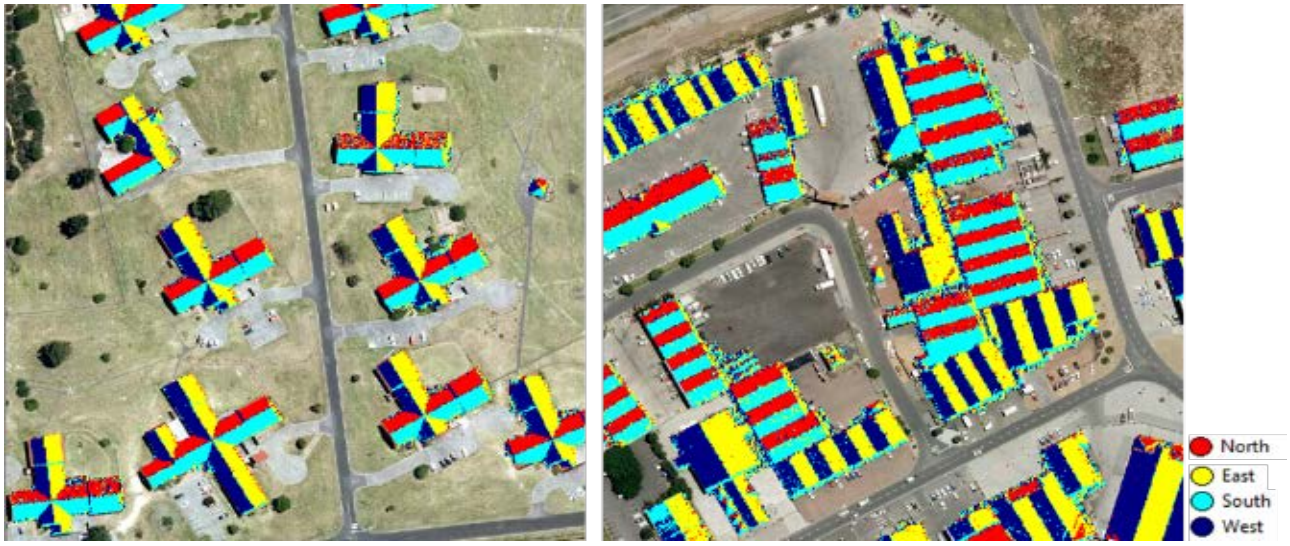

Figure 4.11: Result of building roof objects merged by class

From the results displayed above, there are some speckles of other classes present within the dominant class object. These speckles occur as a result of the configuration of each building or sometimes, the deformity of some roof tiles within each roof plane or section. The “remove object” algorithm is again employed in this situation to remove these tiny building roof objects and merge them with the dominant class object. A “remove object” algorithm is added and the class filter is used to specify all the candidate (speckle) building roof objects of all the four roof plane classes, also the four classes are selected as the target (dominant) class. Using the size criteria again, a threshold condition stated as “Number of pixels <= 1500” is used to detect the speckle building roof objects, then classify and merge such with the closest dominant and appropriate roof plane class. The result of the “remove object” process is shown in Figure 4.12.

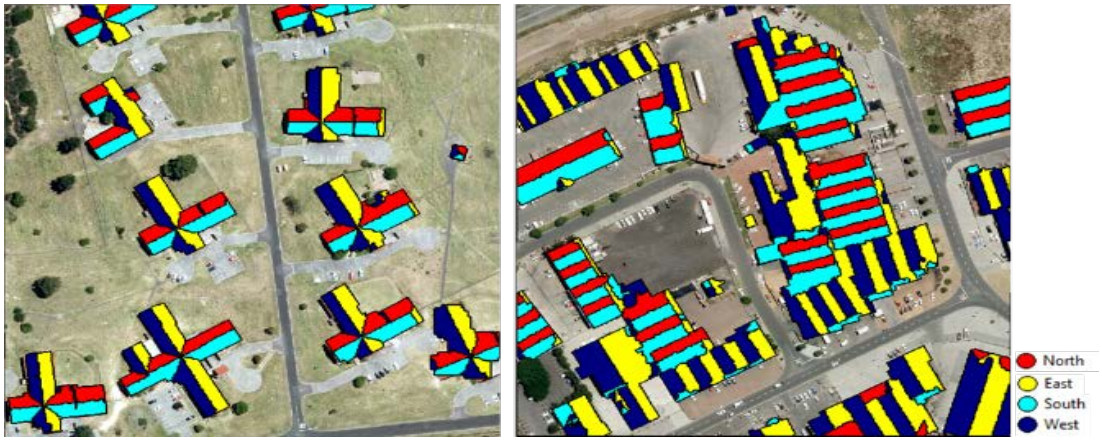

Figure 4.12: Result of building roof objects aggregated into dominant classes

The next stage in the rule-set development is the detection and classification of flat building roofs. The slope values are considered key in identifying flat roof. After careful considerations, it is discovered that roof planes with mean slope less than 10^0 are fairly flat roofs and this is considered the threshold to demarcate the flat roof planes. Therefore, a fuzzy classifier process is added to search for building roof planes that have slope value less than 10^0. The class filter is used to select all the four roof plane classes and the threshold condition is given as “Mean slope < 10”. A new class is created, named “Flat Roof” and an appropriate colour is assigned to it. However, this strategy does not delineate flat building roof completely because of its peculiar nature, as flat roofs are not consistently flat, therefore, creating a diffuse pattern during scanning or sensing. As a result, aspects changes abruptly on fairly flat terrains unlike on sloped terrains. This is better illustrated in Figure 4.13.

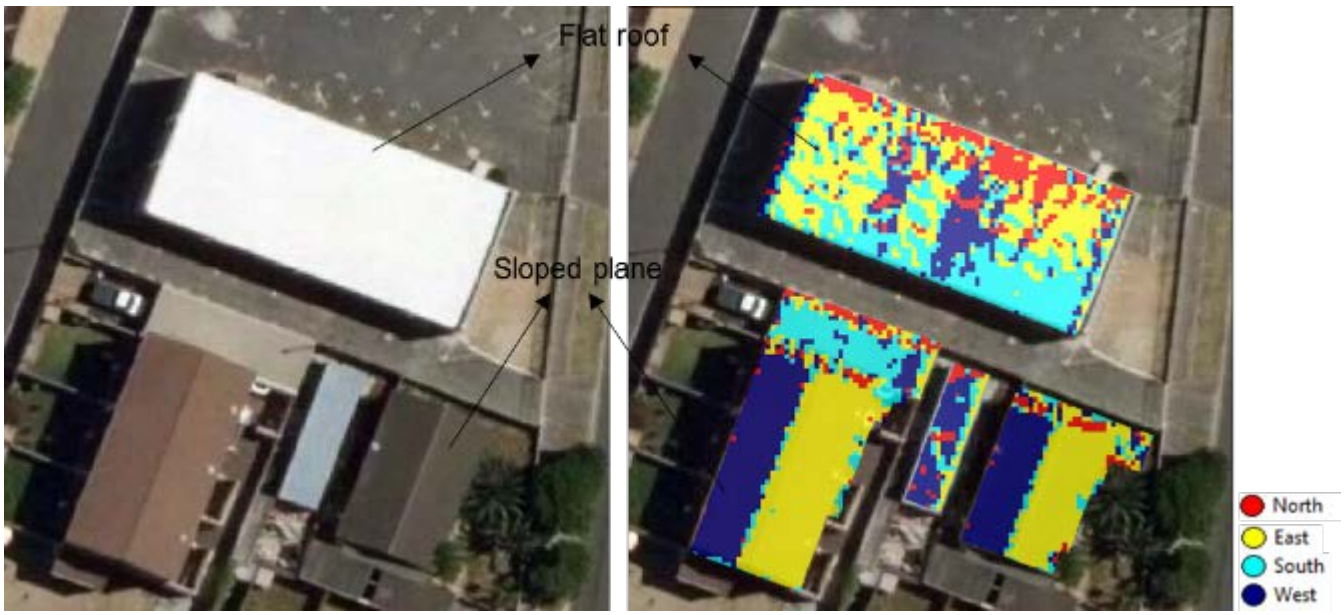

Figure 4.13: Aspect configuration on flat surface vs sloped surface

Therefore, to completely delineate a flat roof structure, some form of aggregation is required. The classification of flat roofs as shown in Figure 4.14 using the slope threshold succeeded in identifying dominant areas on a flat roof structure. Consequently, a strategy is devised to identify roof plane objects that have close proximity to the dominant flat roof objects already classified. Another fuzzy classifier was added and all the four cardinal direction classes are selected using the class filter. Then a rule is set to identify any building roof object in these classes having relative-border index to the flat-roof class objects greater than “0.3”. This process is set to loop

twice and upon completion a “find enclosed by class” process is added to classify any enclosed building roof object as flat roofs. The resulting disjointed flat roof objects are then merged to form a complete flat roof plane. The result of flat roof detection, classification and aggregation is shown in Figure 4.14.

Figure 4.14: Result of flat roof classification and aggregation

The concluding stage of the rule-set development involves cleaning up the roof plane classifications by smoothing its boundaries and exporting it as Shapefile for further processing in ArcGIS. In preparation for the clean-up process, a new image object level is created called “L4” and all the classified roof plane objects are copied to this new level. The “pixel-based object resizing” algorithm is again employed in growing and shrinking the uneven edges. The algorithm is first utilized in “grow” mode, to fill up the deeps of the jagged edges. A box of 7 by 7 pixels is moved around the edges of a specified object and wherever there is an intrusion of the neighbouring object(s) by more than 50 % into a specified object, the intrusion is cut off and used to fill the “deep/valley” on the edge of the specified object. This process is carried out for each class of the building roof planes.

The shrink mode works in a similar manner to the grow mode, but its effect is opposite that of the grow mode. A box of 7 by 7 pixels is moved long an arbitrary straight edge of a specified object and wherever there is a “crowning” of the specified objects “peaks” by the neighbouring object(s) is less than 50 %, the peak part of the object is cut off from the main object. The cut-off objects are then merged to the closest roof plane class object using size threshold in a “remove object” algorithm. The shrink and grow object reshaping process left some disjointed roof plane class objects, these are merged together using the “merge region” algorithm. At this stage the second phase

of the building roof extraction is completed and finally, the roof plane class objects are converted to vector objects using “convert image object to vector object” algorithm. Attribute information such as slope, class name, aspect and height were added to the vector objects and export out of eCognition as a Shapefile. The attribute information would later serve as inputs for the analysis of the solar photovoltaic potentials of each building roof plane. Figure 4.15 shows the output of the whole building roof decomposition into roof planes.

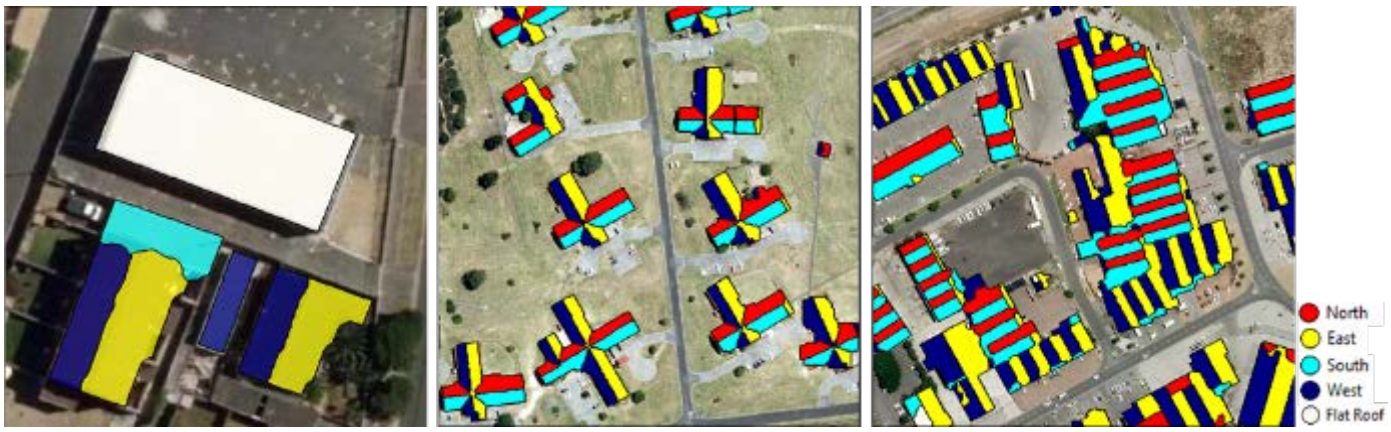

Figure 4.15: Result of roof plane extraction

4.2.3 Discussion of Building Roof Extraction Analysis and Result

The complementary advantages of integrating aerial imagery with ancillary data, such as LiDAR-derived products cannot be overemphasized. The red, green and blue bands of the aerial imagery provide the spectral properties required to meaningfully segment the image scene, as well as identify some objects such as green tree canopies and shadowed area. The slope, height and aspect properties from the LiDAR-derived products help in detecting building roof structures and decomposing it into roof planes. These properties are also exported as attributes of the building roof objects. With the geometry (outline), slope, aspect and height attributes of a building roof structure, it becomes easy to study and investigate it for various purposes, even beyond the primary purpose for which it was intended in this study. Such purposes include, but not limited to determining the rainfall harvesting capacity of a building roof, building roof deformation study and line of sight analysis in urban planning and management.

The essence of the building roof extraction analysis in this study was to generate the surface area of each building roof plane, as this becomes a vital input, required when calculating the solar photovoltaic potential of a building roof. Likewise, the roof plane outline would subsequently be used in defining the extent and boundary area of interest in solar radiation analysis. The whole building roof outline would not have sufficed for the analysis of the solar photovoltaic potential, since it only yields the span area, which is different from the surface area in size. Also, the solar photovoltaic potential is best estimated when each plane of a building roof is evaluated independently of others. From the literature review, it has been established that some planes (sector) of a building roof better harvest the solar radiation than others. With the whole roof structure decomposed into roof planes, it becomes easier to separate building roof planes that poses optimum potential from the ones with general potential.

Once the fuzzy rules developed had been tested and found to be acceptable, their subsequent deployment made the building roof extraction process completely automated and fast. This shows that, much care should be taken in developing the rule-sets in order to achieve the desired result across the board.

Having successfully extracted the whole roof outline and building roof planes, the next analysis to be carried out is the estimation of global solar radiation over the building roofs, and this is presented in the section below.

4.3 Analysis of Global Solar Radiation Estimation

The solar radiation analysis is carried out by using some modules of the open source GRASS GIS software, together with some libraries of ArcGIS in a Python algorithm. It is established (see Section 2.7.4 and Section 3.4) that this tool provides a very good estimate of the global solar radiation, especially over a large area, as is the case in this study. Also, its processing time is much faster than that of ArcGIS's "Solar Radiation" tool. The following sub-sections look at the development of the Python algorithm (Section 4.3.1) and at the processes involved in estimating the global solar radiation (Section 4.3.2), and finally present the analysis and results obtained (Section 4.3.3).

4.3.1 Algorithm Development

In order to avoid alternating between software platforms and to achieve algorithm optimization, a single algorithm is written to accept the LiDAR data as input and produce solar radiation estimate rasters as output. Python libraries from ArcGIS and GRASS are combined to convert the LiDAR data into a DSM and the DSM is fed into the "r.sun" process to generate the solar radiation estimate. The outline of the process involved has already been discussed in Section 3.6.3 and a copy of the Python algorithm is provided in Appendix 2.

The algorithm is designed in such a way that neither ArcGIS nor GRASS GIS software need to be opened before this algorithm can be deployed. However, the algorithm requires that both software are installed on the system on which it will be executed. Also, some set up is required in the GRASS GIS, such as creating a working directory and a location, before it could be initialized. When starting up the GRASS GIS software, it is necessary to define a location for the proposed analysis. A working directory is thus specified and a new folder is created with a coordinate system defined for it, using the projection (.prj) file that is associated with the city building roof extraction Shapefile.

4.3.2 Estimation of Global Solar Radiation

The first few lines of the Python algorithm creates a DSM from the LiDAR data. The DSM now serves as the main input into the solar radiation calculation. The "r.sun" algorithm used to calculate the global solar radiation also requires as ancillary input, slope, aspect, longitude, latitude and horizon rasters, aside the main DSM raster input. Since the DSM raster is the input required to generate the aforementioned ancillary inputs. Therefore, the DSM is fed into the GRASS's "r.slope.aspect" algorithm to generate the slope and aspect raster. Also, the "r.latlong" algorithm computes the location of each cell using the projection system of the DSM raster. Finally, the "r.horizon" algorithm computes the horizon angle raster from the DSM at 30^0 interval.

Alongside the parameters required for computing the global solar radiation, such as Albedo and Linke values, the elevation model (DSM) and all the ancillary rasters are all recalled in the "r.sun" algorithm. The algorithm then computes the global solar radiation for each day of the year at every 30 minutes interval. Once the global solar

radiation estimate for a day is completed, the Python algorithm loops the “r.sun” process to compute the radiation for the subsequent day, until the last day of the year. Each daily estimation is then fed into “r.series” algorithm to compute the mean annual daily estimation. The last stage of the global solar radiation calculation involves exporting the mean daily estimation from the GRASS raster format into a Tagged Image File Format (TIFF).

The Python algorithm is edited each time a new grid is to be executed, since the study area is divided into smaller grid sizes for computational efficiency. The find and replace tool is used in a script editor to edit the grid numbers for the input and output files. A new “mapset” (folder) is created for each analysis, in which all outputs such as DSM, slope, raster, latitude, longitude, horizon and mean solar radiation rasters are stored. Once the input and output files have been correctly edited and labelled, the Python algorithm is launched via the command prompt and the results are stored in the specified directory and mapset. This process is repeated for the number of grid tiles that covered the study area. A subset of the global solar radiation estimation is shown in Figure 4.16.

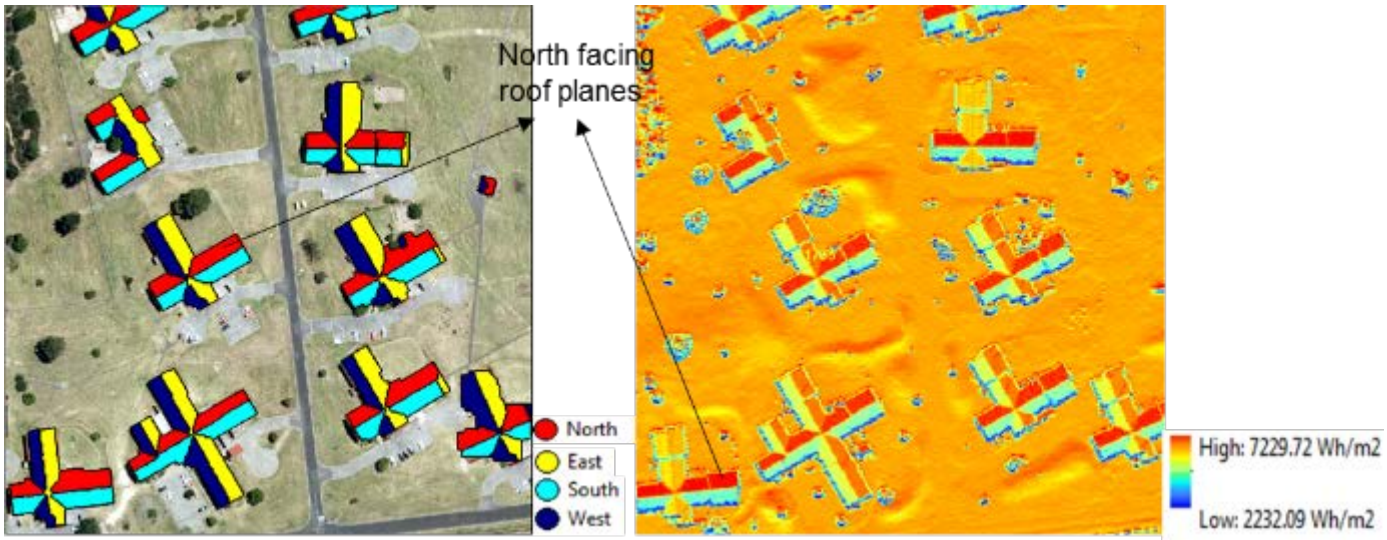

Figure 4.16: Mean annual global solar radiation

4.3.3 Discussion of Global Solar Radiation Analysis and Result

The method employed for estimating the global solar radiation adequately models the orientation of the roof via the aspect map, and the tilt of the surface by using the slope map. Also, the shading factor is modelled by using either the horizon computation or

by flagging the shading option to process the estimate. The shortcomings of having to feed in each input, as required by the r.sun tool, are eliminated by opting for the algorithm development option. In the long run, this helped to save more time, which is critical for online deployment. The aspect and slope maps are two major inputs to the estimation of the global solar radiation. These two inputs provide the required detailed surface characteristics of the building roof, which could not be derived directly from the DSM. As posited in the literature review, the north facing building roof planes in the southern hemisphere receives more solar radiation than other roof plane directions. This is highlighted in Figure 4.13, with north facing roof planes arrowed. The global solar radiation calculated using the GRASS script library algorithms integrated the direct, diffuse and ground reflected solar irradiation between sunrise and sunset for a particular day. The output is given as watt-hour per square meter per day ($Wh/m^2/day$).

The estimate obtained using the r.sun tool is based on a clear-sky solar radiation model. This meant that the solar radiation estimate assumed the sky is clear. This result could, however, be improved upon by applying the clear-sky insolation index correction, which can be obtained from the NASA website. The insolation clearness index value varies from 0 to 1.0. It is defined as the ratio of radiation above the atmosphere to that which reaches the ground surface during clear-sky days (NASA, 2015). Applying the clear-sky index correction to the solar radiation estimate derived from the clear-sky model, as in the case of r.sun in GRASS or Solar Analyst in ArcGIS, would yield the real sky global solar radiation estimate. The correction is applied by multiplying the clear sky solar radiation estimate (G_{hc}) with the clear-sky insolation index (K_c) (Hofierka & Suri, 2002). The clear-sky insolation index over Cape Town area varies from 0.76 in January through 0.71 in June to 0.77 in December for different locations. The average clear-sky insolation index for a year is about 0.75 as obtained from NASA surface meteorological and solar energy data website (NASA, 2015).

$$G_h = G_{hc} K_c \quad (4.1)$$

Another way of obtaining the clear-sky index value was to divide the measured global radiation over a period of time with the calculated clear-sky value of the same period. The measured global radiation value could be obtained from a ground-based meteorological station present within the study area, if available (Suri & Hofierka,

2004). The historical solar radiation data for some weather station within the study area is sourced to compare and validate the values obtained from the method obtained in this study. The details of the validation are provided in Section 4.6. Using the second method of obtaining the clear-sky index value, the measured average radiation of three (3) weather stations are divided with the estimated solar radiation. The average clear-sky index value obtained are 0.75 for the weather station at Constantia, while an average clear-sky index value of 0.72 is obtained for weather stations at Noordhoek and Strand respectively. The average of the clear-sky index for these three weather stations across Cape Town municipality yields 0.73, which is close enough to validate the value obtained from the NASA meteorological and solar energy data website.

The clear-sky insolation index of 0.75 is then adopted, to be applied to the solar radiation estimates gotten from the method used in this study. This value is applied after extracting the clear-sky solar radiation estimates to the attribute table of the building roof planes, in order to obtain the real-sky solar radiation estimate.

Now that the global solar radiation over the building roof has been estimated, the next phase is to analyse the solar photovoltaic potential using the surface area of the extracted building roof planes and their mean annual global radiation estimate. This procedure is discussed in detail in the section below.

4.4 Analysis of Solar Photovoltaic Potential Estimation

Obtaining an estimate for the solar photovoltaic potential of building roofs entails combining information or results from the two previous phases of analysis with the amount of energy that could be exploited while converting the solar energy to electricity. The energy exploitation factors are expressed as constants, while the surface area of the building roof plane and the mean solar radiation values are the variables. Essentially, the attribute table of the extracted building roof polygons is utilised as the workspace to carry out the calculation, thereby functioning as a spreadsheet. For each of the building roof plane evaluated, the solar photovoltaic potential estimate is calculated using the formula adopted during research design. Steps taken in analysing the solar photovoltaic potential of the building roof are presented in the subsequent sub-sections.

4.4.1 Estimation of the Solar Photovoltaic Potential

To obtain the solar photovoltaic estimate, which is the amount of electricity a building roof could generate by harvesting solar radiation, using the photovoltaic panels, each building's roof plane, as extracted from the LiDAR and imagery data, is considered to be the useful roof area. Since the attribute table of the extracted building roof plane already contained some required inputs and it has the capability to carry out basic column arithmetic and statistical operation, it is decided to add the solar radiation estimate and the energy exploitation parameters to the roof plane attribute table. In these phase of the analysis, steps carried out in estimating the solar photovoltaic potential are further explained in the subsequent headings.

Extracting the Solar Radiation Estimate

The first step in this phase involves extracting the global solar radiation estimate for each building roof plane from the cells of the raster output of the solar radiation calculation. In order to achieve this, the "Zonal Statistics as Table" spatial analyst tool in ArcGIS is employed. This tool provided a way of extracting statistical information for a defined zone or area from a set of rasters and presenting this information in a table; this table can then be exported or merged with another table, so as to transfer and integrate the required information. The tool calculates statistics such as sum and mean for values of raster cells that falls within a zone defined by a polygon feature or shape. For the purpose of this study, the zone is defined by the building roof plane shape, while the statistic required is the average of all cell values of the solar radiation raster falling into each roof plane area. Within the "Zonal Statistics as Table" tool, the "OBJECTID" of the roof plane feature class, denoting each roof plane is set as the "Zone field". While the global solar radiation raster is set as the "Input value raster", an output table name is specified and the statistical operation is set to "mean". The resulting statistics table contained information, such as count of all pixels falling into each building roof, and the mean of all the pixel values, which is the output required from this process (see Table 4.1).

Table 4.1: Output table from zonal statistics calculation

Rowid	OBJECTID	COUNT	AREA(m^2)	MEAN(Wh/m^2)
1	1	469	75.040	6068.150
2	2	286	45.760	5501.953
3	3	1486	237.760	5934.169
4	4	161	25.760	5802.981
5	5	144	23.040	5795.046
6	6	390	62.400	5391.246
7	7	4760	761.600	5750.637
8	8	594	95.040	5164.026
9	9	554	88.640	4909.035
10	10	2730	436.800	5665.545
11	11	432	69.120	5456.979
12	12	3715	594.400	5444.493
13	13	620	99.200	5700.660
14	14	3771	603.360	5665.492
15	15	502	80.320	5774.126

The next process is to merge this information or output with other attribute information that is already included in the attribute table of the building roof plane Shapefile. The roof plane attribute table is thus opened and, from the table options menu, browsing to “Joins and Relates”, a join is performed. The “Join attributes from a table” option is selected from the “Join Data” tool, and a primary key field common to both tables (OBJECTID) is set as the join field. For the joining option, the “keep only matching records” option is selected and the join is validated before the final execution of the join process. In the meantime, a new floating data type field is added to the building roof polygon layer and named “Solar_Radiation_Estimate”. This is done before carrying out the join, because creating new fields on a joined table would have caused the table to malfunction. The new field created is meant to contain the mean solar radiation estimate from the subsequently joined zonal statistics table. The values are transferred using the field calculator and, after transferring the values to the “Solar_Radiation_Estimate” field, the join is removed to avoid having unnecessary data on the attributes table.

In other words, to optimize the algorithm process a single tool is created using the model builder that combines the three processes of zonal statistics, creating a new field to house the solar radiation estimate and transferring the estimate value from the zonal statistic table to the new field by a join operation. This tool, therefore, helps

automate the three manual processes, thereby improving on time spent in analysis of the solar photovoltaic potential. This is then deployed for each grid tile processed in the study area. At this stage, the building roof plane layer contained the two vital requirements to compute the solar photovoltaic potential, namely, the roof plane span area and the global solar radiation estimate.

Adding Ancillary Data

The next step in obtaining the solar photovoltaic potential involved adding the energy exploitation parameters and other ancillary data to the attribute table. However, since some of these data are constants and apply to all records of the building roof plane, it is decided that all grids processed be merged together to form a single Shapefile for all building roof planes. The merge tool is employed in order to merge the Shapefile for each processed grid tile. The output yields a single Shapefile for all building roof planes extracted within the study area. The first ancillary data to be added is the corrected solar radiation estimated, by applying the clear-sky insolation index. A new field “Real_Sky_SolRad” is added to the attribute table and using the field calculator, the “Solar_Radiation_Estimate” field is multiplied with “0.75”, which is the average clear-sky insolation index adopted for the study area. The field calculator succeeds in calculating the real-sky solar radiation estimate for all records in the attribute table.

The next step involved obtaining the surface area of each building roof plane by converting the span area of the extracted roof plane in two-dimensional (2D) to three-dimensional (3D). The formula adopted as discussed in the research design stage is to divide the 2D span area with the cosine of the slope angle. The slope angle is already contained in the attribute of the building roof plane as part of export from roof plane extraction process. Therefore, a new field is created and a name “Area_3D” is assigned, with the data type set to float. The field calculator dialog box is used to select the participating field/column and to implement the formula. The cosine function available in the field calculator accepts radian as input, therefore, the slope angle of the roof plane has to be converted to radian first. Using the field calculator, a Python code is written in the pre-logic script code block. The formula is scripted in Python as “!Shape_Area! / math.cos (math.radians (!Mean_slope!))”, where the “Shape_Area” represented the 2D span area. The field calculator computes and populates the surface area for each record in the attribute table.

Subsequently, the energy exploitation parameters are added to the attribute table of the building roof plane. Two new fields are added to the updated table and are named “Panel_Efficiency” and “Performance_Ratio” respectively. The data type for the two new columns are also set to float. The panel efficiency and performance ratio fields are populated using the field calculator with constant values of 0.15 and 0.76 respectively, as determined during the research design (see Section 3.2.4). At this stage, all the information required to estimate the building roof solar photovoltaic potential have been added to the roof plane attribute table.

Calculating Building-integrated Solar Photovoltaic Potential

All the information required to calculate solar photovoltaic potential now available in the building roof plane attribute table include, the surface area of the roof plane, the solar radiation estimate and the energy exploitation parameters. The formula adopted in the research design stage can now be applied in a field calculator to obtain the amount of electricity in kilowatt hour each building roof plane can produce, if it were fitted with polycrystalline solar panels. A new field to house the calculation is added, called “Panel_Potential”. Using the field calculator, the adopted formula is scripted as “(!Area_3D! * !Real_Sky_SolRad! * !Panel_Efficiency! * !Performance_Ratio!) / 1000” in the pre-logic script code block. The division by “1000” is carried out to convert the watt-hour per meter square (Wh/m2) to kilowatt hour (kWh). Other columns could be added, stating the panel efficiency of any solar panel type and a solar photovoltaic potential can be calculated for that solar panel type. A sample result from the attribute is displayed in Table 4.2

Table 4.2: Table showing solar photovoltaic potential estimate for building roof planes

ID	Class	Aspect (°)	nDSM (m)	Slope (°)	P_SolRad (Wh/m^2)	Area_3D (m^2)	Panel_Eff	Perf_Ratio	Real_Sky (Wh/m^2)	P_Potential (kWh)
358	North	61.328	3.455	47.481	6103.592	57.344	0.15	0.76	4577.694	29.925
359	North	32.508	3.551	36.150	6873.717	79.513	0.15	0.76	5155.288	46.730
360	North	104.395	3.304	26.442	6400.811	56.478	0.15	0.76	4800.608	30.909
361	North	99.059	3.025	32.292	6473.778	75.227	0.15	0.76	4855.333	41.639
362	North	226.080	2.624	32.908	6624.835	55.087	0.15	0.76	4968.627	31.203
363	North	265.905	3.148	32.063	6718.124	54.136	0.15	0.76	5038.593	31.096
364	North	316.950	3.594	31.811	6911.717	31.492	0.15	0.76	5183.788	18.610
365	North	223.551	3.642	41.883	5775.182	48.185	0.15	0.76	4331.386	23.793
366	North	78.661	5.883	36.483	6801.604	290.528	0.15	0.76	5101.203	168.953
367	North	78.661	3.808	43.000	6228.447	45.088	0.15	0.76	4671.335	24.011
368	North	105.066	3.040	40.124	5741.847	78.557	0.15	0.76	4306.385	38.566
369	North	73.503	2.902	31.008	6209.147	123.307	0.15	0.76	4656.861	65.462
370	North	125.006	2.724	44.330	5182.906	20.576	0.15	0.76	3887.179	9.118
371	North	89.187	4.273	44.785	6465.531	34.626	0.15	0.76	4849.148	19.141
372	North	144.819	2.505	49.826	4999.640	53.437	0.15	0.76	3749.730	22.843
373	North	301.080	3.515	46.883	6420.753	32.051	0.15	0.76	4815.565	17.595
374	North	111.405	3.153	14.668	5952.673	42.059	0.15	0.76	4464.505	21.406
375	North	289.795	3.586	41.944	6365.683	57.236	0.15	0.76	4774.262	31.151
376	North	90.690	2.908	30.884	6076.321	63.665	0.15	0.76	4557.241	33.076
377	North	153.271	2.335	26.092	6091.218	36.506	0.15	0.76	4568.414	19.013
378	North	126.784	2.592	48.739	5411.361	27.003	0.15	0.76	4058.521	12.493
379	North	132.852	2.639	40.906	5452.412	74.547	0.15	0.76	4089.309	34.752
380	North	83.600	2.657	17.189	5783.726	15.224	0.15	0.76	4337.794	7.528
381	North	157.252	3.057	37.361	5490.829	42.654	0.15	0.76	4118.121	20.025
382	North	69.482	2.757	22.565	6543.783	18.234	0.15	0.76	4907.837	10.202
383	North	111.453	2.895	48.977	4743.889	22.325	0.15	0.76	3557.917	9.055
384	North	137.325	3.273	28.425	5962.158	29.055	0.15	0.76	4471.619	14.811
385	North	68.417	2.848	24.671	6094.319	24.577	0.15	0.76	4570.739	12.806
386	North	168.212	4.004	37.139	6413.339	63.880	0.15	0.76	4810.005	35.028

4.4.2 Creation of Solar Photovoltaic Potential Database

Creating a database provides a basis for the storage and retrieval of desired information. In most instances, information is stored in the database in rows and columns: The column defines a particular field that is common to all entries in the database, and it usually has a title; the title for each field should be brief, concise and correctly define the set of values contained in it. A row presents an occurrence or an instance of a record. Usually, the first item on the row uniquely identifies that particular instance or occurrence of a record.

In preparation for creating the solar photovoltaic potential database, all the processed grids of whole roof outlines are also merged together to form a single Shapefile, so that all the records can be contained in a single attribute table. The database housing the output information about the solar photovoltaic potential of each building roof is contained within the attribute table of the building roof plane Shapefile. This table can be exported for use in other applications, but for the purpose of this study, the information remains as the attributes of the shape of the building roof planes. This will facilitate search and locate queries in any GIS environment. Most of the information with regards to the solar photovoltaic potential of building roofs is already contained in the attribute table.

However, a link is required to establish a connection between the whole roof outlines attribute table and the building roof planes attribute table. Therefore, a key identifier is created in the whole roof outlines attribute table in form of a building identity number. A new field ("Bldg_ID") was added to the whole roof outline table and building identity column is created, increasing from "BD01" upwards, using the field calculator and a Python script code. An overview of the entity relationship between the whole roof outline and the roof plane having one to many is shown in Figure 4.17. Other identifier attributes are also added to the whole roof outline table, these included the street address of each building and the property number (ERF number). In order to achieve this, an address data point Shapefile parcel data Shapefile are firstly sourced from the City of Cape Town municipality. The address point Shapefile is spatially joined to the parcel data, using parameter settings such as "intersect" for the match option and "JOIN_ONE_TO_ONE" for the join operation. The spatial join succeeds in transferring the address profile to the parcel data, which contains the property number. The resultant Shapefile is again spatially joined with the whole roof outline Shapefile, using the same parameter settings as stated earlier. This operation succeeds in joining the address and property number to each whole building roof outline extracted.

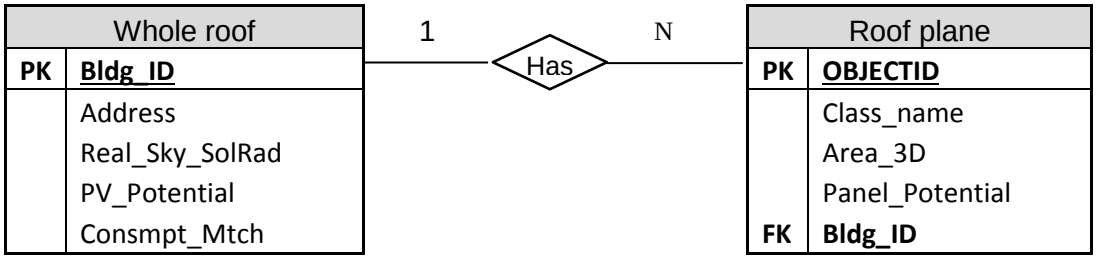

Figure 4.17: Entity relationship diagram showing 1:N relationship between

Using the intersect overlay tool, the whole roof outline is intersected with the building roof plane. The street address and the property number for each building roof plane is therefore joined to the attribute table of the building roof plane, as all building roof planes falling within a whole roof outline acquires its property number and street address. Furthermore, since there is a one to many relationship existing between whole roof outline and the building roof plane, as shown in Figure 4.17, a relationship class is created between the two attribute tables. The relationship is based on the building identity number, with this, if a building is selected in the whole roof outline table, the corresponding building roof planes are automatically filtered and selected, once the “Related Tables” key is triggered. The relationship class definition file is stored in the geodatabase together with the two feature classes.

Using the summarize tool, the sum of solar photovoltaic potential for all building roof planes belonging to each building is summed together and added to the whole roof outline table. The summarize operation creates a table containing the sums, this is then joined to the whole roof attribute table using the building identity number as the joining key. The summed solar photovoltaic potential is then transferred to a field “PV_Potential” created to house the values, thereafter, the summary table joined is removed. The sum of the solar photovoltaic potential for all roof planes of a building roof constitutes the general solar photovoltaic potential. While the optimum solar photovoltaic potential can be calculated as the sum of the solar photovoltaic potential of the north, east, west and flat roof planes, as these directions are better suited to harvest solar photovoltaic in the southern hemisphere, with the north planes having the highest potential. Using summarize tool again, but in this case a query is applied to filter out the south facing planes and selecting only the optimized roof planes. The sum for the solar photovoltaic potential is obtained for the optimized roof planes and the information is added to the whole roof outline table using the same procedure as mentioned earlier.

Further statistical analysis can be carried out to determine the optimal age of a particular building roof. This can be derived by dividing the estimated optimum solar photovoltaic potential by the general estimate of solar photovoltaic potential, and multiplying by 100 to obtain the percentage. This would make it easier to locate buildings that are potentially suitable for solar photovoltaic installations because, the higher the optimal percentage, the more area of the building roof would be available

and the better it would be suited for harvesting solar energy. A new field tagged “Optimal_Percentage” is thereby added to the updated whole roof outline attribute table to compute the optimal percentage. Using the field calculator, an expression stated as “(!Opt_PV_Potential! / !PV_Potential!) * 100” is used to compute the optimal percentage values and displayed in the new field created. Likewise, the percentage contribution of each roof plane to the parent building roof can be obtained, this index would also help in identifying optimal roof planes per building. In this scenario, not only the orientation plays the major factor in determining optimal roof plane, but also the surface area of the roof plane. The percentage contribution is obtained by dividing the solar photovoltaic potential of each roof planes by the potential of the parent building roof and obtaining a percentage of it. An extract of the whole roof outline table, which is linked with the roof plane table via the building identity number is shown in Table 4.3.

Table 4.3: Table showing an extract of the whole roof outline table

Bldg_Id	PROP_NUM	ADDNO	RDNME	RDTYPE	PLANSUBURB	PV_Pont (kWh)	Opt_PV_Pot (kWh)	Opt_Pcent (%)
BD3467	9	22	FIRST	AVENUE	MELKBOSSTRAND	125.740	79.793	63
BD34669	9201	5	HAWK	CRESCENT	FLAMINGO VLEI	255.983	245.148	96
BD34670	9203	9	HAWK	CRESCENT	FLAMINGO VLEI	92.681	60.336	65
BD346681	73552	4	TOPSHAM	ROAD	PLUMSTEAD	115.252	71.105	62
BD346682	71960	15	HONITON	ROAD	PLUMSTEAD	87.801	78.704	90
BD346683	70763	27	DAWLISH	ROAD	PLUMSTEAD	166.648	135.310	81
BD346684	73553	22	WOODGATE	ROAD	PLUMSTEAD	105.928	90.066	85
BD346685	71964	26	CHUDLEIGH	ROAD	PLUMSTEAD	113.154	71.515	63
BD346686	71963	17	HONITON	ROAD	PLUMSTEAD	15.828	15.828	100
BD346687	71962	24	WOODGATE	ROAD	PLUMSTEAD	105.470	94.434	90
BD346688	71963	17	HONITON	ROAD	PLUMSTEAD	113.760	57.947	51
BD346689	71957	32	CHUDLEIGH	ROAD	PLUMSTEAD	381.351	322.828	85
BD346690	70787	28	DAWLISH	ROAD	PLUMSTEAD	63.395	50.282	79
BD346691	71966	26	WOODGATE	ROAD	PLUMSTEAD	123.012	112.762	92

4.4.3 Electricity Consumption Match

The solar photovoltaic analysis would not be complete is there is not comparison between the potential a building roof could generate and the historic electricity consumption of the building under investigation. To complement the solar photovoltaic potential database created above, an additional vital information is required, which helps answer the prominent question, will my building roof be able to generate all the

electricity required by my household? Factors that determines electricity consumption match per household in terms of solar photovoltaic potential include, the surface area of the building roof, the orientation its roof plane faces and the amount of electricity consumed by that particular household. Other factors considered, especially if the system is not grid connected are needs for electricity storage, as some consumption will take place in low or no solar condition (evening and night).

However, potential investors in solar photovoltaic system find it hard to determine the percentage of consumption match. This is due to two major reasons viz, the home owner could not keep track of their average daily or monthly electricity consumption and/or the home owner could not determine the solar photovoltaic potential of their building roof. On a broader basis, solar photovoltaic potential tool developers also have issues providing the consumption match percentage, as municipalities and national power utilities still classify household electricity consumption data as confidential. Therefore, there are no electricity consumption data per household to compare the estimated building-integrated solar photovoltaic potentials against.

For the purpose of this study, electricity consumption data was sourced from University of Cape Town properties and services department for some buildings belonging to the University, which are individually metered. It is worth noting that several attempts were made to obtain the electricity consumption data for the entire study area, but proved abortive, due to the bottleneck in data sharing policies. Two new fields are added to the solar photovoltaic potential database to house the electricity consumption data and the percentage consumption match. The percentage consumption match is obtained by dividing the solar photovoltaic potential calculated with the electricity consumption and obtaining the percentage. An extract on the updated whole roof outline table is shown in Table 4.4.

Table 4.4: Table showing an extract of the updated whole roof outline table

Bldg_Id	PV_Pont (kWh)	Opt_PV_Pot (kWh)	Opt_Pcent (%)	Elect_Consmpt (kWh)	Consmpt_Mtch (%)
BD202530	454.762	415.337	91	105.590	431
BD202539	1354.076	681.557	50	3438.080	39
BD202541	1247.892	719.307	58	3566.110	35
BD202542	1980.793	1480.071	75	1982.690	100
BD202557	983.789	800.153	81	138.720	709
BD202580	2680.776	2359.591	88	2581.060	104
BD202582	919.723	830.721	90	1057.670	87
BD202601	628.746	455.037	72	670.440	94
BD202602	1994.470	1604.988	80	3981.100	50
BD202603	1329.249	1125.291	85	2047.160	65
BD202608	780.087	679.739	87	719.970	108
BD202615	1204.955	1123.572	93	1069.620	113

4.4.4 Discussion of Solar Photovoltaic Potential Analysis and Results

Factors considered in determining the solar photovoltaic potential of a building roof could be broadly classified into three categories, namely, geographical potential, physical potential and the technical potential. The main elements in each of these categories are evaluated to arrive at an estimate of the solar photovoltaic potential for each roof plane and consequently, the whole building roof. Such elements include the roof plane surface area (geographical), the global solar radiation incident upon the roof plane (physical), the efficiency of the solar panel adopted, and the performance ratio (technical). The estimate of the general solar photovoltaic potential is derived by using the surface area of all building roof planes, as extracted from the LiDAR-derived data and the aerial imagery. The optimum estimate is obtained by considering only the sections of the roof where the solar energy could best be harvested.

Identifying the optimal locations for the siting of solar panels is of paramount importance to homeowners, businesses and government departments, as this indicates the area where solar energy can best be harnessed and maximized. The major factor considered in determining the optimum zone is the direction that each segment of the roof is facing. This has been determined already, using the aspect (orientation) information. A further statistical computation that could further determine the potential of each building roof is the optimality percentage. This would help in

determining how suitable each building might be for solar photovoltaic installations. More importantly, the consumption match percentage would also assist in determining the suitability of buildings for solar photovoltaic system. From Table 4.4, buildings with percentage consumption match less than 50% are high-rise buildings, bringing to focus that high-rise buildings do not have enough roof surface area to match the electricity consumption of number of floors contained in it. Access to this information will guide individuals or corporate bodies interested in installing solar photovoltaic systems about the potential offered by their building roofs and which part or section(s) of that roof are best suited for solar panel installations.

The beauty of any analysis or process, especially in the GIS context, is how easily the information presented can be retrieved. A GIS analysis that generates a result but with no clear means of retrieving or accessing the information by the targeted user, amounts to a waste of time and resources. Consequently, each component of the address data, viz. house number, road name, road type and suburb area are available in separate fields, so as to make querying and filtering easy. Likewise, the property/ERF number was added to facilitate search and locate. The solar photovoltaic potential database created from the analyses carried out in this study provides a means of data storage that users can search and from which useful information pertaining to the deployment of solar photovoltaic systems on a building roof can be retrieved. At this stage, the solar photovoltaic potential database can be deployed for use in related GIS desktop analysis, while it is almost ready for web deployment. The process and analysis involved in deploying the solution online is discussed in the subsequent section.

4.5 Web Development

The bulk of analysis in the web development phase occur in the application layer as stated in the research design. The application layer will therefore be the main focus of the analysis under this phase. The previous analysis carried out in the preceding three phases serve as the data layer under the web development phase. Within the application layer, the processes involved are discussed below under the following headings.

4.5.1 Data Layer Preparation

The data to be deployed to the customised web-based system are the database created upon the completion of the solar photovoltaic potential calculation and analysis. However, the data has to be cleaned up and formatted for optimal utilization in the application layer and subsequently for deployment to the web. Two basic database files emerged from the solar photovoltaic potential analysis, which include the whole roof Shapefile and the roof plane Shapefile. The decimal places of number fields were rounded off to two, so as to avoid lengthy display when the information is required for display on the web. The whole roof Shapefile is then converted to a JSON file format, as this is the format that the tile service provider understands and accepts as input. While the roof plane Shapefile is converted to the KML file format, as this is the format required for tables to be uploaded to the table joining service adopted. The KML file is then uploaded to the table web service and a table identity is generated, which would be used to reference and link the table. With the data cleaned and formatted, it can now be used in the application layer, in preparation for deployment to the web-based system.

4.5.2 Web System Design

The HTML script serve as the background algorithm, which connects and combines the data layer together with the service layer to deliver the web-based solar photovoltaic potential system. An overview of the system architecture is represented in Figure 4.18.

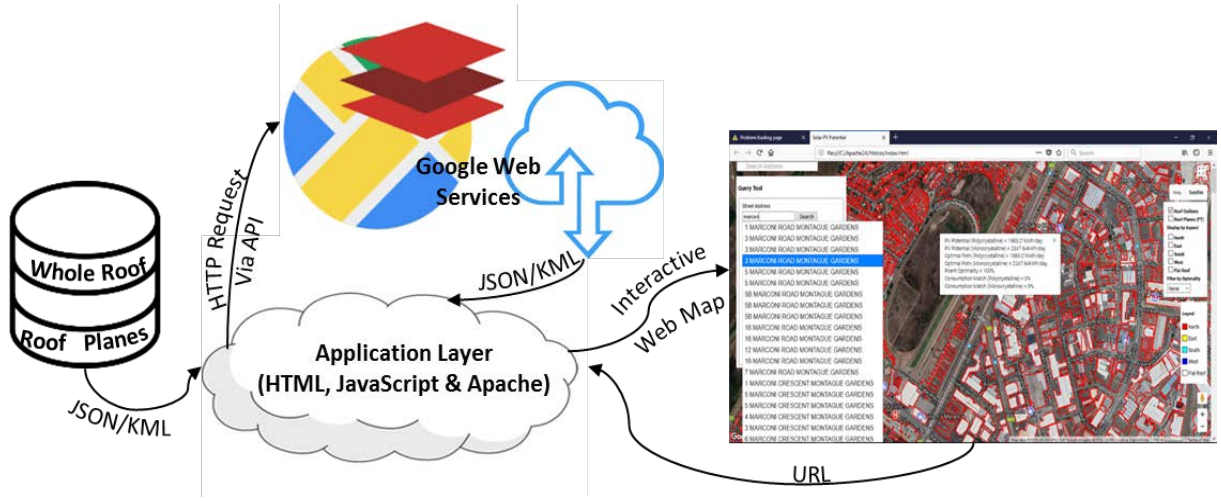

Figure 4.18: Web-based solar PV potential system architecture

Within the HTML document are the CSS scripts which describes the styling on the web-map page. Also contained in the HTML document are the JavaScript libraries and the link to their source codes. With the source-code links declared, the HTML document also contained the JavaScript codes which interacts with the API to manipulate and deliver web services. A single HTML document is written in this study to display the web-based system and it is named “index.html”.

At the beginning of the HTML scripting, the appropriate tags of the root element (<html> </html>) are declared and all subsequent scripts goes inside this root element. Starting with the header of the HTML document, the opening and closing head tags are declared (<head> </head>) and the title of the web page given as “Solar PV Potential” is written within the title tags. Within the style tags, the style of the objects within the division element (div) on the web page is defined using the CSS scripts.

The “div” objects styled include the map, query tool, checkboxes and the legend. The CSS scripts defines the style information such as the feel of the aforementioned “div” objects, its position, colour, font size and type. Position-wise, the map object, which is the Google map tiles, is positioned to fill the entire web page. Other “div” objects are then layered on the map object. The query tool sits on the top-left corner of the web – page, this would allow space for drop down list when searching for street addresses. The checkboxes and the legend on the other hand are placed on the right border of the web page, in between the base map tools. Before the header element is closed, the links to the CSS stylesheet and JavaScript source codes are stated, without which, the JavaScript codes to be written subsequently would not be able to communicate the web services or the data layer.

Next to the header element is the body of the HTML document. After opening the body tag (<body>), a “div” element is created for each “div” object with unique identities given. The identity would allow actions and results from JavaScript calls to be attached to the appropriate “div” object for display and interaction purposes. A look at the web page at this stage is shown in Figure 4.19.

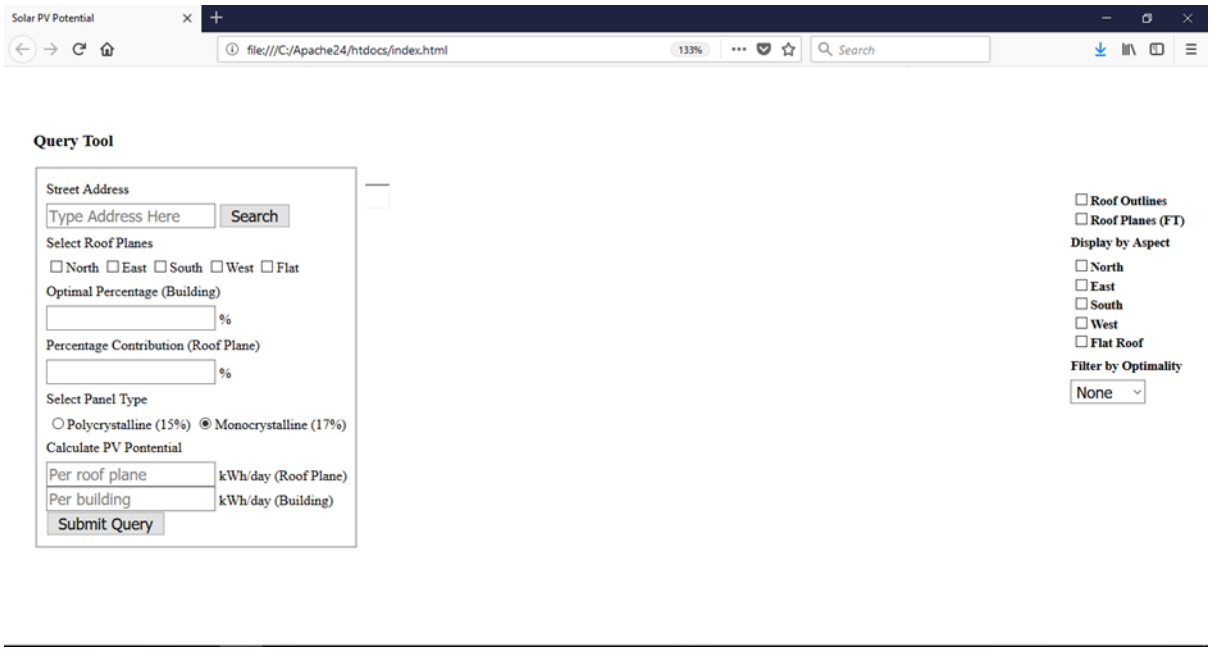

Figure 4.19: Web page view 1

Upon creation of “div” elements for each object, the JavaScript codes to interact with data layer and the web service through the API is written within the script tags. The map object is initially added after the script tag is opened (<script>). A global variable (var map;) is declared outside a function to initialize the map object. This is done so that the map object could be referenced in other places outside the map initialize function. Within the map initialize function, a new map is added and options such as where to centre the map, start zoom and the position of map controls was stated. The map object is the anchored to the “div” element created earlier to house it.

Also within the map initialize function, scripts are written to overlay the data layer, which contains the solar photovoltaic database. An empty array (var layer = [ ];) is declared global variable to house layers to be imported. A layer is declared a map data, subsequently, a jQuery AJAX function is used to request the JSON file of the whole roof and give a response, which is then added as a GeoJSON object to the map. The whole roof layer is then styled to draw only the outline, leaving the fill-space for the roof plane layer to fill. The roof plane layer on the table web service is also added to the map and styled in colour to reflect the direction each roof plane is facing.

At this stage, all the essential objects have been added to the web page, however, it remains mainly static with little or no interaction possible. Therefore, JavaScript

functions are added to make the web page interactive, as the essence of deploying the solution online is to disseminate information to users. To begin with, a toggle function is written to switch between layers using the checkboxes created earlier. This would make it easy and possible to be able to click on each feature and obtain information about it. Afterwards, event functions are created, so that when any feature is clicked on the map, it would popup an information window displaying pre-set attributes of the feature. Likewise, event functions are created to change the style of the layers by highlighting it or increase the outline weight, as the mouse moves the layer feature. Other interactivity function added includes the map zooming into a building roof, when clicked.

To make information extraction more rich and user-friendly, JavaScript functions are written to activate the query toolbox. The first element within the query tool “div” object is the local autocomplete search bar. By typing street addresses into this search bar, and clicking the search button, the building roof of the street address typed is zoomed to and a popup is triggered, which displays pre-set information about the solar photovoltaic potential of that building roof. This is implemented using the jQuery user interface autocomplete function. Again, a jQuery AJAX function is written to request and return the address field of the whole roof database, which is then used as the source of the autocomplete plugin function. Other elements of the query toolbox, such as checkbox and radio button options are all tied to the “Submit Query” button, which when triggered, displays the solar photovoltaic potential of the building selected via the address search bar.

A click function is written and anchored to the “Submit Query” button, using the conditional “if statement”. The function matches the street address typed in by a user with the address value in the street address field of the data layer. If it matches, then it returns requested information about solar photovoltaics potentials of the building roof, such as optimal percentage, percentage contribution of a roof plane to the whole building roof, etc. These information are then displayed on the query dashboard as soon as the “Submit Query” button is triggered. On completion of the query tool design, the closing script tag (</script>) is appended. The body of the web page is completed and this stage and also closed using the appropriate closing tag (“</body>). Likewise, the entire HTML document comprising the styling, “div” elements and objects is closed using the HTML document closing tag (</html>). The complete HTML document, with

JavaScript codes inherent is attached as Appendix 4. Displays of the customised web-based solar photovoltaic system are shown in Figure 4.20(a) and (b).

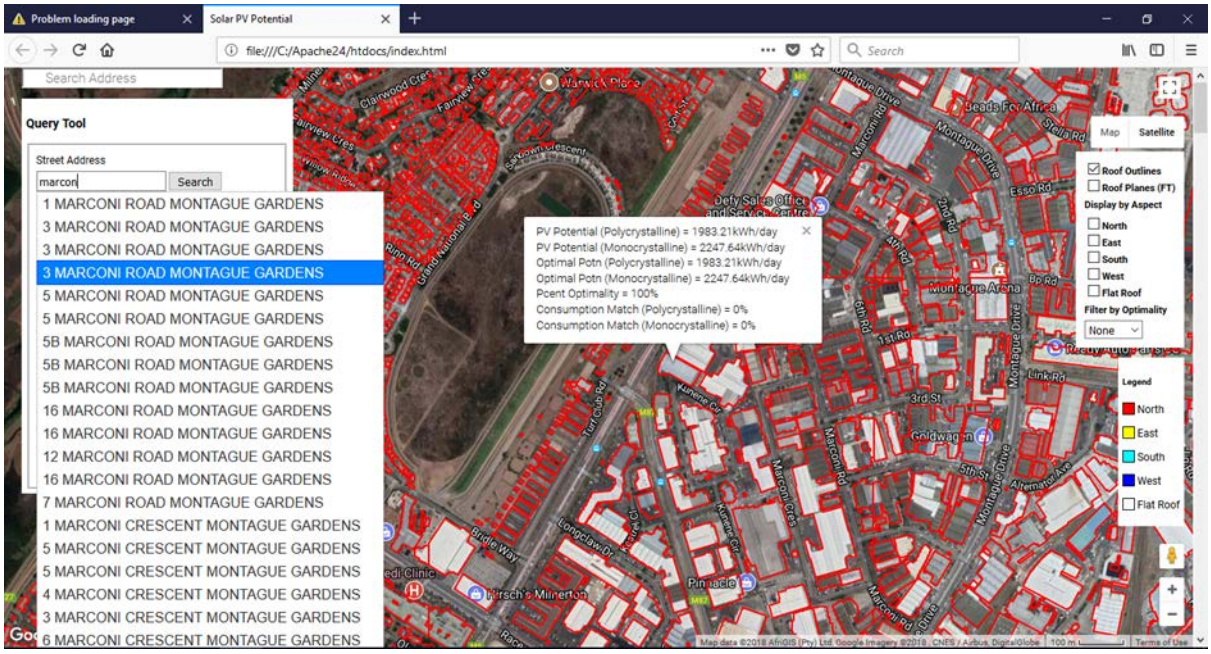

Figure 4.20(a): Web page view 2

Figure 4.20(b): Web page view 3

A sample of the designed system is provided through this link (file:////geoubufsh001.wf.uct.ac.za/adlade005@wf/Demo/index.html), the link is better viewed using the Mozilla Firefox web browser, as the system is not live in the sample

version and other web browsers would require additional settings to access local files via the web.

4.5.3 Discussion of Web Development Analysis and Results

Without a proper and adequate way of disseminating information, efforts and analysis put into generating the information becomes a waste of time and resources. It is as a result of this, that the solar photovoltaic potential information gotten from various phases of analysis in this study are deployed to the web. By deploying the solution of this study to the web, it provides a capacity to reach a large number of users within the targeted area. Although, the processes involved in the analysis carried out to generate the solar photovoltaic potential are remote sensing and GIS based, the information generated are for the general public to utilize. This also informed the decision to deploy the solution from a GIS desktop application to the web, as the bulk of the general public may not have access or understand the workings of a GIS application.

The JavaScript codes housed within the HTML document are utilized in rendering the visualization and querying the published data layers in order to obtain the desired solar photovoltaic potential information from the web-based tool. The HTML and JavaScript codes written can be easily reused on other on other web map APIs that are JavaScript based. Such web map APIs include Leaflet, OpenLayers, MapBox, ArcGIS APIs and Bing Maps. Since these APIs are all JavaScript based, they use similar API code structures, the only focal point of departure would be to replace the JavaScript source code links and the CSS stylesheet links in the HTML header element. This thus provides opportunity to switch between various web map APIs as soon as each present advanced features and capabilities, while using the same code written earlier as base and with little modifications.

The primary aim of this study is to create an awareness about the potentials of building-integrated solar photovoltaic system, which prompted the creation of the web tool. Therefore, interactivity is added to the web page to retrieve solar photovoltaic potentials of each building roof dynamically. Utilizing these information, building property owners or property developers would be able to make an informed decision about the geographic and physical potential of building-integrated solar photovoltaic

system before embarking on its implementation. Information made available through the web tool includes the potential of each roof plane, the accumulative potential of the parent building roof, percentage contribution of each roof plane to the accumulative potential of the parent building roof, consumption match, etc.

This analysis concludes the phases of procedures carried out in creating a web-based solar photovoltaic potential system of building roofs in the City of Cape Town. Before a summary of the analysis is given, it is important to access the accuracy of the results generated form the foregoing analyses. The accuracy assessment of the building roof detection and extraction, solar radiation estimation, as well as that of the solar photovoltaic potential estimate are discussed in the section below.

4.6 Accuracy Assessment

It is important to access the results obtained so far, in order to ascertain their accuracies and validity. The accuracy assessment of results and outputs obtained in this study are considered in three stages, firstly, the accuracy of the building roof extraction process is assessed in Section 4.6.1, followed by the validation of the solar radiation model results in Section 4.6.2. Lastly, the accuracy of the solar photovoltaic potential estimated is also validated in Section 4.6.3

4.6.1 Accuracy Assessment for the Extraction of Building Roofs

The confusion matrix method of thematic accuracy assessment and its derived-metrics such as kappa coefficient, according to Congalton and Green (2009), are a very effective way of assessing a classification accuracy because individual category accuracies are clearly presented alongside both the commission and omission errors. According to Rutzinger et al. (2009), there is however, a general a lack of standardization for accuracy assessment of classification techniques, especially for object-based classification techniques, as different authors has describe accuracy to mean different things. However, popular metrics used in accessing the accuracy of an object-based classification includes completeness and correctness. A derived metrics from the combination of these two, called “Quality” is used to determine the overall accuracy. It has found popular acceptance in accuracy assessment of different object-based classification techniques.

In the context of an object-based classification, a True positive (Tp) refers to a classified object that overlaps its corresponding object label in the reference data. A False positive (Fp) is a classified object that does not overlap its corresponding object label in the reference data. While an object in the reference data wrongly classified or omitted in the classification result is called a False negative (Fn). Using these parameters, an accuracy assessment metrics can be derived for completeness and correctness as follows (Heipke et al., 1997; Rutzinger, Rottensteiner & Pfeifer, 2009);

$$\text{Completeness} = \frac{||Tp||}{||Tp|| + ||Fn||} \quad (4.2)$$

$$\text{Correctness} = \frac{||Tp||}{||Tp|| + ||Fp||} \quad (4.3)$$

$$\text{Quality} = \frac{1}{1 + \frac{||Fn||}{||Tp\ Comp||} + \frac{||Fp||}{||Tp\ Corr||}} \quad (4.4)$$

The completeness accuracy assessment metric can also be referred to as the detection rate or the producer's accuracy, the correctness metrics is also called the users accuracy, while the quality metrics is referred to as the overall accuracy (Foody, 2002; Song & Haithcoat, 2005).

A common problem with the accuracy assessment of the object-based classification techniques is how a Tp is determined. Various methods has come up with its own way of determining what constitute a Tp or otherwise (Rutzinger, Rottensteiner & Pfeifer, 2009). Generally an object is denoted a Tp if it has an overlap greater than 50% (Matikainen, Hyyppä & Hyyppä, 2003; Rottensteiner et al., 2005; Zhan et al., 2005). There are various accuracy assessment method for object-based classification result, and there is no supreme accuracy assessment method, as each has its advantages and disadvantages. Also the accuracy assessment result of a building detection and extraction depends on a number of factors, such as the accuracy and source of the reference data, if it is digitized, how painstakingly and what amount of reference object is required to perform a representative accuracy assessment. Other inherent problems with building roof or building footprint extraction is the disparity, which exist between the extracted building outline and the reference outline. This happens as a result of difference in spatial resolution, misalignment of integrated data utilized in the extraction process, topology mismatch and poor digitization resulting in poor accuracy

of the reference data amongst others. This generally affects the accuracy assessment metrics, especially for smaller buildings (Rutzinger, Rottensteiner & Pfeifer, 2009).

A combination of assessment technique is posited by Rutzinger et al. (2009), and for the purpose of this study, two accuracy assessment method for object-based classification namely, Point-in-Polygon (PIP) method and the Mutual Overlap method are used to access the accuracy of the building roof classification result. The point-in-polygon method computes the centroid coordinates of the classified object (building roof) and the reference object. If the centroid of the classified object is contained in the reference object and vice versa, then the object is designated a Tp. For every classified building roof, the number of centroids belonging to the reference building roof contained in it is counted, and if it is positive, the classified building roof is designated a Tp for correctness, else it is designated as Fp. Similarly, for every building roof in the reference data, the number of centroids belonging to the classified building is counted, and if it is positive, the reference building roof is designated as a Tp for completeness, else a Fn. Since the purpose of the building roof classification in this study is to obtain its area, the completeness and the correctness is also computed as a function of the area, therefore, the numbers of Tps, Fps and Fns are replaced with the sums of the areas for each. There is, however, no equal correspondence between the number of Tps used for completeness and the correctness, making it a setback of this method (Rutzinger, Rottensteiner & Pfeifer, 2009).

The mutual overlap method compares the area of mutual overlap (intersect) between the classified building roof and the reference building roof, forming the correspondence between the two dataset. The mutual overlap for the correctness is determined by finding the percentage of the mutual overlap area divided by the area of the classified building roof. While the mutual overlap for the completeness is determined by finding the percentage of the mutual overlap area divided by the area of the reference building. A threshold for total overlap percentage is chosen, usually between 50% and 70%. This becomes a setback for this method, as author selects the overlap percentage threshold as deemed fit. A classified building roof with its percentage overlap greater than the selected threshold becomes the Tp for correctness, if less than the threshold, it is designated as Fp. Similarly, a reference building roof with overlap greater than the selected threshold becomes the Tp for completeness, else it is designated as Fn.

For the purpose of accuracy assessment in this study, a building footprint data is obtained from the City of Cape Town open data portal to serve as the reference data. The data was obtained from 3D building models generated photogrammetrically, it has a location accuracy of +- 20cm. This data is considered fair enough for comparison purpose, as it covers part of the metropolitan area of the city including residential, commercial and mixed zones. Likewise, it would have been a cumbersome process to digitize a large number of building roofs enough to form a representative area for classification result. Portions of the building roof classification result that correspond to the reference data is extracted, resulting in 14,437 number of building roofs. The reference data have similar topology characteristics with the classification result in some areas, as it was generated photogrammetrically. Other areas where the topology have been resolved for the reference buildings are identified on the classification result and the topology is resolved accordingly. Samples of areas, which cut across the entire reference data, where there are differences in topology and alignment of the reference data and classification result are shown in Figure 4.21(a).

Figure 4.21(a): Topology difference and misalignment error between reference data and classified result

Using the point-in-polygon method, the centroids coordinates of both the classified and reference buildings are computed. Thereafter, the coordinates are plotted to form a point Shapefile and overlaid on each corresponding dataset (classified and reference).

The feature identity resulting from the overlay analysis is then utilized in detecting building roofs that falls into Tp for completeness and correctness, as well as the Fp and the Fn. For completeness, 14,349 classified building roofs have their centroids falling into the corresponding reference building, thereby becoming the number of true positives for completeness, denoted as “Tp.Comp”, while the number of the false negatives denoted as “Fn” are 88. The number of true positives for correctness denoted as “Tp.Corr” are 14,379 and the false positives (Fp) are 58. Using Equations 4.2, 4.3 and 4.4, the completeness, correctness and the quality measure are calculated and shown in Table 4.5(a).

Table 4.5(a): Table showing accuracy analysis using the PIP method

	PIP Method
Completeness	99.3%
Correctness	99.5%
Quality	98.9%

As stated earlier, the completeness also refers to the producer’s accuracy and the correctness refers to the user’s accuracy, while the quality metrics refers to the overall accuracy.

Using the mutual overlap method, an overlay operation is carried out using the intersect method, to determine the mutual overlap area. The percentage mutual overlap for completeness is calculated as follows;

(Mutual Overlap (Area) / Area of Reference Building) * 100

For Correctness;

(Mutual Overlap (Area) / Area of Classified Building) * 100

The evaluation is considered using object counts and as function of the sums of areas for three (3) total overlap thresholds i.e. 60%, 70% and 80%. Number of Tps, Fps and Fns for each of the threshold is shown in Table 4.5(b).

Table 4.5(b): Accuracy metrics count for threshold range

	Tp.Comp	Fn	Tp.Corr	Fp
60%	14,232	205	14,232	20
70%	13,718	719	13,718	12
80%	12,737	1,700	12,737	4

Using the metrics counts in Table 4.5(b) in Equations 4.2, 4.3 and 4.4, the accuracy metrics are given in Table 4.5(c).

Table 4.5(c): Table showing accuracy analysis using the mutual overlap method 1

Mutual Overlap Method (Object Count)			
	60%	70%	80%
Completeness	98.6%	95.0%	88.2%
Correctness	99.8%	99.9%	100%
Quality	98.4%	94.9%	80%

The accuracy metrics is also calculated as a function of area using Equations 4.2, 4.3 and 4.4. Cumulative areas for each metrics (Tp, Fp and Fn) is calculated and the result of the accuracy analysis is presented in Table 4.5(d).

Table 4.5(d): Table showing accuracy analysis using the mutual overlap method 2

Mutual Overlap Method (Cumulative Area)			
	60%	70%	80%
Completeness	93.7%	92%	89.5%
Correctness	85.9%	83.5%	72.6%
Quality	81.2%	77.8%	66.9%

The mutual overlap method provides a more detail accuracy analysis compared to the point-in-polygon method. The results of the accuracy as displayed in the tables above are subjective to the quality and flaws of the reference data as discussed earlier. Notwithstanding the misalignment error from the reference data, the accuracy metrics show that the building roof extraction process is of high accuracy.

An objective approach to accessing the accuracy of the extraction process is to apply the building roof extraction algorithm to one of the publicly available dataset, such as the ISPRS benchmark on urban object detection and compare the results to the other methods documented in the benchmark result. The dataset (colour infrared aerial imagery and ALS point data) for three (3) areas of Vaihingen, Germany are downloaded by requesting the data from the ISPRS website (ISPRS, 2018). The three area describes different urban scenes viz. area 1 depicts the “inner city” area, area 2 depicts the “high riser” i.e. areas with few high-rise buildings surrounded with trees. The third area depicts purely residential area. The dataset have similar spatial resolution to the dataset utilized in this study (8cm colour infrared imagery and 7cm average ALS point spacing). It also include polygon Shapefiles for the building roof outline derived from manual stereo plotting.

Few changes are made to the original building roof extraction algorithm designed in this study, in terms of threshold determination, before being applied to the benchmark dataset. The changes are peculiar to the spectral resolution of the aerial imagery (colour infrared vs real RGB band), this affects the determination of the threshold to detect and classify green vegetation. Likewise, the height threshold and minimum building area threshold are changed from 1.8m to 1m and 25m^2 to 2m^2 respectively, as there are some low and small buildings in the benchmark dataset. Each extraction result and accuracy assessment analysis of the three areas are presented below;

Area 1

As mentioned earlier, area 1 represents the inner city area. Buildings of diverse roof structures exit in this image scene, and having different topological relationships, as shown in Figure 4.21(b).

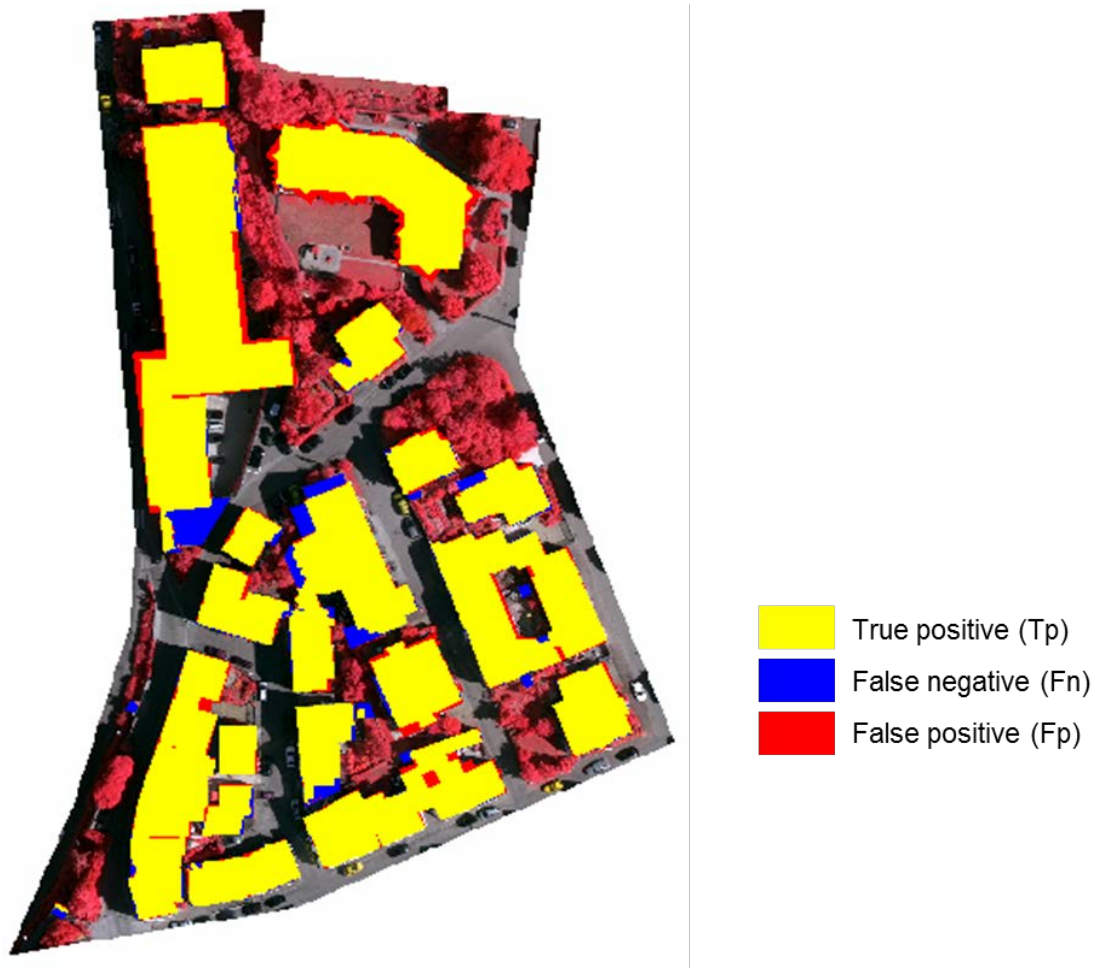

Figure 4.21(b): Comparison of extracted objects vs reference objects for area 1

As previously explained, the Tp depicted as yellow in Figure 4.18(b) represents the area of mutual overlap or correspondence between the extracted object and the reference object. The Fn represents the portion of or an entire object not detected/extracted in the extraction process. While the Fp represents the portion of or an entire object detected and extracted but not available as object in the reference data. The number of objects available in the reference data is 37, the object count for the Tp both for completeness and correctness is 33, the Fn count is 4, while the Fp count is 0. Using the mutual overlap method of accuracy assessment and the metrics counts, the accuracy metrics for area 1 is given below in Table 4.5(e) and Table 4.5(f).

Table 4.5(e): Table showing accuracy metrics per object count for area 1

Object Count	
Completeness	89.2%
Correctness	100%
Quality	89.2%

Table 4.5(f): Table showing accuracy metrics as a function of area for area 1

Cumulative Area	
Completeness	96.5%
Correctness	93.7%
Quality	90.6%

Out of twenty seven (27) methods submitted for the benchmark test, only ten (10) use the integration of aerial imagery and LiDAR-derived DSM to detect and extract building outlines (Rottensteiner et al., 2014). Out of the ten methods, only six (6) used the model based approach, an approach under which the extraction algorithm designed in this study falls into. It is worth noting that this category of method and approach produced results with higher accuracy metrics when compared to other methods and approaches evaluated (Rottensteiner et al., 2014). The method and approach designed in this study compares well and better than the method having the highest accuracy metrics in this category. From the benchmark test result for area 1, the “LJU2” and “ZJU” methods, have the best trade-off between Fps and Fns (Rottensteiner et al., 2014). The accuracy assessments metrics obtained using the method designed in this study (denoted as ADE) is therefore compared with these two (2) methods in Table 4.5(g).

Table 4.5(g): Table showing accuracy metrics comparison for area 1

	Compl (Obj)	Corr (Obj)	Compl (Area)	Corr (Area)
LJU2	91.9%	100%	94.6%	93.1%
ZJU	81.1%	100%	92.1%	95.2%
ADE	89.2%	100%	96.5%	93.7%

Area 2

This area contains high risers, i.e. there are few high-rise buildings, closely surrounded with trees, as shown in Figure 21(c).

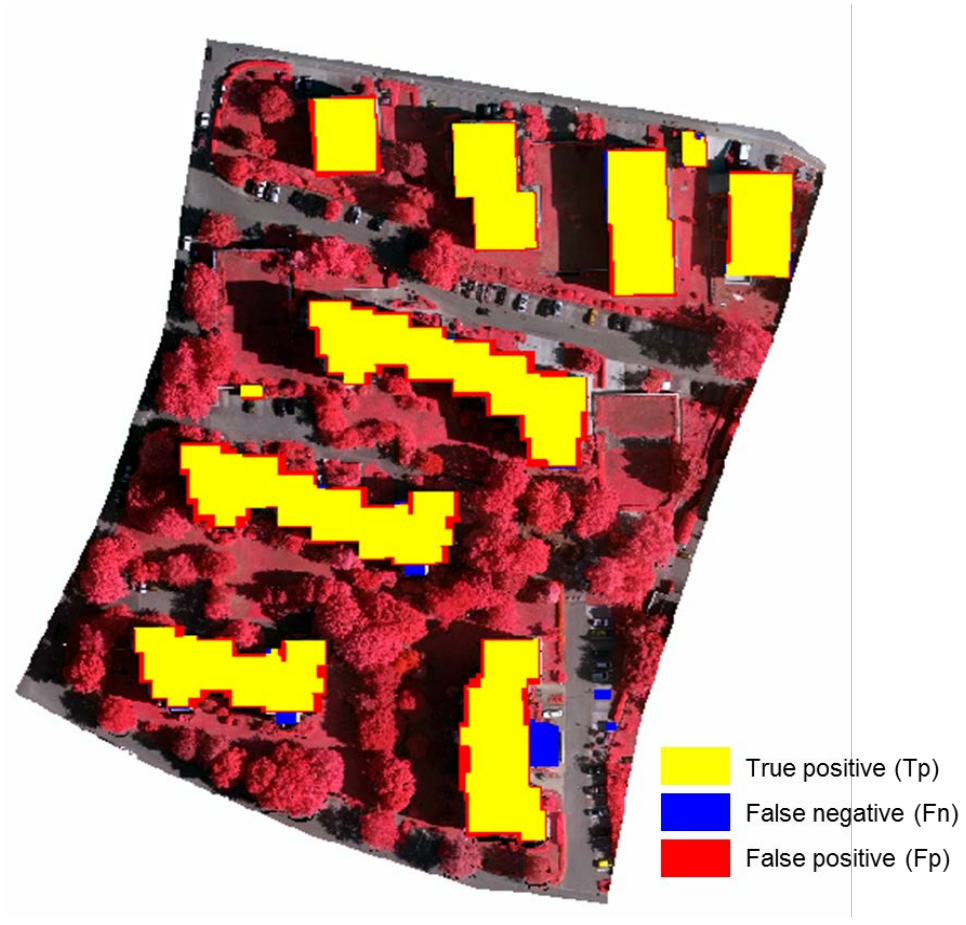

Figure 4.21(c): Comparison of extracted objects vs reference objects for area 2

There are 14 number of objects manually stereo plotted in the reference data, the object count for the Tp both for completeness and correctness is 12, the Fn count sits at 2, while the Fp count is 0. Using the mutual overlap method of accuracy assessment and the metrics counts given above, the accuracy metrics for area 2 in terms of object

count and as a function of the area are given below in Table 4.5(h) and Table 4.5(i) respectively.

Table 4.5(h): Table showing accuracy metrics per object count for area 2

Object Count	
Completeness	85.7%
Correctness	100%
Quality	85.7%

Table 4.5(i): Table showing accuracy metrics as a function of area for area 2

Cumulative Area	
Completeness	97.4%
Correctness	89.9%
Quality	87.8%

The accuracy metrics are also compared with the two leading methods (LJU2 and ZJU), as carried out earlier, and found to compare well. This is presented in Table 4.5(j).

Table 4.5(j): Table showing accuracy metrics comparison for area 2

	Compl (Obj)	Corr (Obj)	Compl (Area)	Corr (Area)
LJU2	85.7%	100%	95.1%	94.3%
ZJU	71.4%	90.9%	94.4%	97.7%
ADE	85.7%	100%	97.4%	89.9%

Area 3

Area 3 as shown in Figure 4.21(d), represents purely residential area, characterized with low lying roof structures.

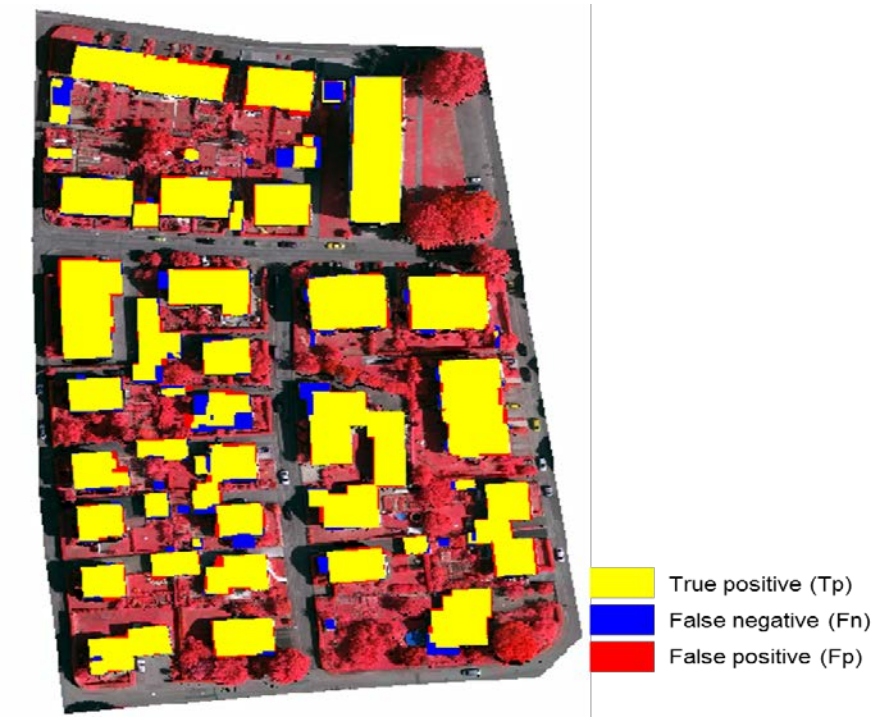

Figure 4.21(d): Comparison of extracted objects vs reference objects for area 3

The same procedure is repeated for area3, as carried for area 1 and area 2. There are 57 number of objects in the reference data, the count of Tp objects both for completeness and correctness is 49, the Fn object count sits at 8, while the count of the Fp count is 0. Again, using the mutual overlap method of accuracy assessment and the metrics counts given above, the accuracy metrics for area 3 in terms of object count and as a function of the cumulative area are given below in Table 4.5(k) and Table 4.5(l) respectively.

Table 4.5(k): Table showing accuracy metrics per object count for area 3

Object Count	
Completeness	86%
Correctness	100%
Quality	86%

Table 4.5(l): Table showing accuracy metrics as a function of area for area 3

Cumulative Area	
Completeness	93.9%
Correctness	93.9%
Quality	88.5%

The accuracy metrics are also compared with the two leading methods (LJU2 and ZJU), as carried out for area 1 and area 2, and found to compare well. This is presented in Table 4.5(m).

Table 4.5(m): Table showing accuracy metrics comparison for area 3

	Compl (Obj)	Corr (Obj)	Compl (Area)	Corr (Area)
LJU2	85.7%	100%	95.1%	94.3%
ZJU	71.4%	90.9%	94.4%	97.7%
ADE	85.7%	100%	97.4%	89.9%

The average accuracy metrics for all the three areas (area 1, area 2 and area 3) are also computed. It is also compared with the averages of the two methods (LJU2 and ZJU) used in the comparison. The total number of reference objects sits at 108, other metrics count and parameter value, as well as the average accuracy metrics is presented in Table 4.5(n) and Table 4.5(o).

Table 4.5(n): Total metrics count and parameter values for all areas

	Compl (Obj)	Corr (Obj)	Compl (Area – m^2)	Corr (Area – m^2)
Tp	94	94	18444.5	18444.5
Fp		0		1431.89
Fn	14		838.52	

Table 4.5(o): Table showing accuracy metrics comparison for all areas

	Compl (Obj)	Corr (Obj)	Compl (Area)	Corr (Area)
LJU2	91.9%	100%	94.6%	93.1%
ZJU	81.1%	100%	92.1%	95.2%
ADE	89.2%	100%	96.5%	93.7%

From the results show in Table 4.5(o), the building roof detection and extraction method designed in this study compares well with the other two methods (LJU2 and ZJU), which have the best metrics trade off in the category of methods and approaches adopted. Largely, objects available in the reference and not detected in the classification process, denoted as Fn are generally small buildings, with area less than 10m^2. Rottensteiner et al. (2014), argued that detection of small buildings is difficult or

yet unattainable for fully automatic detection process, based on the results submitted for the benchmark test. However, this is not a problem of the detection/extraction algorithm, but of the point density of the LiDAR data per square-metre. All the small buildings that are not detected in the test sample areas (area 1, area 2 and area 3) do have a height value of less than 0.5m in the LiDAR-derived DSM. This range of building height value, therefore does not connote a building in the real sense of image interpretation, and are therefore, filtered away by the adopted building height thresholds for different detection algorithm. These smaller buildings, if “ground-truthed” would probably be dog kennels, tool sheds or perforated roofs, which would in essence allow passage of ALS pulse through it.

4.6.2 Accuracy Assessment for Global Solar Radiation Estimate

In order to validate the accuracy of the global solar radiation estimate, it is imperative to compare the estimates gotten from the method or model adopted with the real solar radiation data recorded at weather stations within the study area. In order to achieve this, historic solar radiation data for five years from 2012 to 2016 are sourced from weather data custodians. For this study, the solar radiation data is sourced from Agricultural Research Council. Hourly solar radiation measurements in Watts for each day of the five (2012 – 2016) year for three weather stations within the study area are provided for validation purpose. The weather stations, which the solar radiation data are sourced from include Cape Point Vineyards: Noordhoek AWS, Vergelegen BO and Cape Town: Constantia.

The coordinates of the weather stations are plotted and overlaid on the aerial imagery to ascertain if it indeed falls within the study area. The solar radiation raster for the grid areas the weather stations falls within are retrieved and also overlaid on the aerial imagery, in preparation for comparison. Basic summary statistics such as average, total, highest and lowest solar radiation for each day are included in the sourced weather report. A sample of the weather data report is provided in Appendix 3. Further summary statistics are carried out to determine the mean monthly solar radiation over the period of measurements (2012 – 2016) and this is displayed in Table 4.6.

Table 4.6: Table showing the historic mean monthly solar radiation measured

	Noordhoek AWS (Watts)	VERGELEGEN BO (Watts)	CONSTANTIA (Watts)
Jan	7487.6	5957.61	7208.57
Feb	6637.28	5762.02	6319.8
Mar	5148.94	4724.89	4715.48
Apr	3813.53	3378.38	3393.6
May	2700.88	2347.95	2319.94
Jun	1995.53	1847.21	1756.32
Jul	2104.77	2078.86	1978.71
Aug	2765.71	2770.76	2653.83
Sep	3993.36	3611.84	3814.15
Oct	5169.13	4760.78	5370.04
Nov	6281.37	5111.19	6629.79
Dec	7199.07	5510.47	7260.01

The mean monthly global solar radiation estimates for the locations occupied by the weather stations are also extracted from the data directory of the solar radiation estimation results. The clear-sky insolation index for each month as obtained from the NASA meteorological and solar energy data website are used to obtain the real-sky solar radiation estimate for the location of the weather stations. The calculated real-sky solar radiation estimates alongside the measured solar radiation is displayed in Table 4.7(a, b and c).

Table 4.7(a): Table showing the measured vs the calculated mean monthly solar radiation (1)

NOORDHOEK AWS					
	Measured (Watts)	Estimated Clear Sky (Watts)	Clear Sky Index	Estimated Real Sky (Watts)	Difference (Watts)
Jan	7487.6	8865.76	0.76	6737.98	749.62
Feb	6637.28	8162.46	0.76	6203.47	433.81
Mar	5148.94	6934.12	0.76	5269.93	-120.99
Apr	3813.53	5435.47	0.74	4022.25	-208.72
May	2700.88	4180.76	0.72	3010.14	-309.26
Jun	1995.53	3567.53	0.71	2532.95	-537.42
Jul	2104.77	3840.31	0.72	2765.03	-660.26
Aug	2765.71	4846.11	0.74	3586.12	-820.41
Sep	3993.36	6280.62	0.76	4773.27	-779.91
Oct	5169.13	7635.14	0.77	5879.06	-709.93
Nov	6281.37	8613.38	0.77	6632.30	-350.93
Dec	7199.07	9026.87	0.77	6950.69	248.38
Average	**4608.10**	**6449.05**	**0.75**	**4863.60**	**-255.50**
				RMSE	**547.64**

Table 4.7(b): Table showing the measured vs the calculated mean monthly solar radiation (2)

VERGELEGEN BO					
	Measured (Watts)	Estimated Clear Sky (Watts)	Clear Sky Index	Estimated Real Sky (Watts)	Difference (Watts)
Jan	5957.61	8764.99	0.76	6661.39	-703.78
Feb	5762.02	7740.17	0.76	5882.53	-120.51
Mar	4724.89	6154.36	0.76	4677.31	47.58
Apr	3378.38	4435.21	0.74	3282.05	96.33
May	2347.95	3132.64	0.72	2255.50	92.45
Jun	1847.21	2547.29	0.71	1808.58	38.63
Jul	2078.86	2803.12	0.72	2018.25	60.61
Aug	2770.76	3832.52	0.74	2836.06	-65.30
Sep	3611.84	5398.28	0.76	4102.69	-490.85
Oct	4760.78	7076.30	0.77	5448.75	-687.97
Nov	5111.19	8415.88	0.77	6480.23	-1369.04
Dec	5510.47	9039.61	0.77	6960.50	-1450.03
Average	**3988.50**	**5778.36**	**0.75**	**4367.82**	**-379.32**
				RMSE	**660.20**

Table 4.7(c): Table showing the measured vs the calculated mean monthly solar radiation (3)

CONSTANTIA					
	Measured (Watts)	Estimated Clear Sky (Watts)	Clear Sky Index	Estimated Real Sky (Watts)	Difference (Watts)
Jan	7208.57	8961.67	0.76	6810.87	397.70
Feb	6319.8	7985.28	0.76	6068.81	250.99
Mar	4715.48	6455.25	0.76	4905.99	-190.51
Apr	3393.6	4750.50	0.74	3515.37	-121.77
May	2319.94	3428.48	0.72	2468.50	-148.56
Jun	1756.32	2825.26	0.71	2005.94	-249.62
Jul	1978.71	3086.86	0.72	2222.54	-243.83
Aug	2653.83	4138.23	0.74	3062.29	-408.46
Sep	3814.15	5703.58	0.76	4334.72	-520.57
Oct	5370.04	7345.54	0.77	5656.07	-286.03
Nov	6629.79	8626.02	0.77	6642.04	-12.25
Dec	7260.01	9206.57	0.77	7089.06	170.95
Average	**4451.69**	**6042.77**	**0.75**	**4565.18**	**-113.50**
				RMSE	**283.60**

The difference between measure and calculated solar radiation estimate is shown on the table, as well as the average of each set of observation or estimation. The Root Mean Square Error (RMSE) is calculated by obtaining the summation of the square of the difference between the measured and the estimated solar radiation and finding the square root of the summation divided by the number of observations. Graphical representations of the comparison are shown in Figure 4.22 (a, b and c).

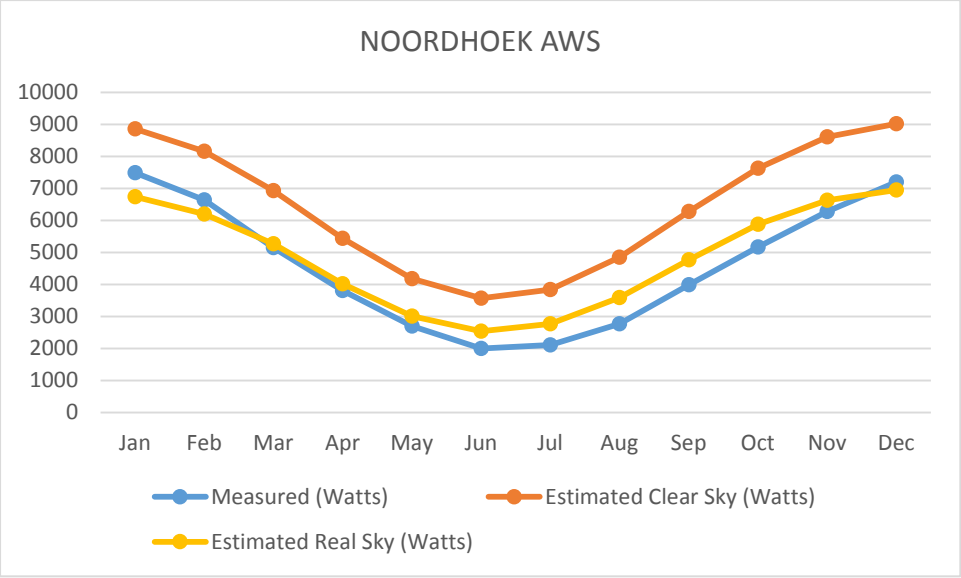

Figure 4.22(a): Mean monthly variation between the observed and the estimated radiation (1)

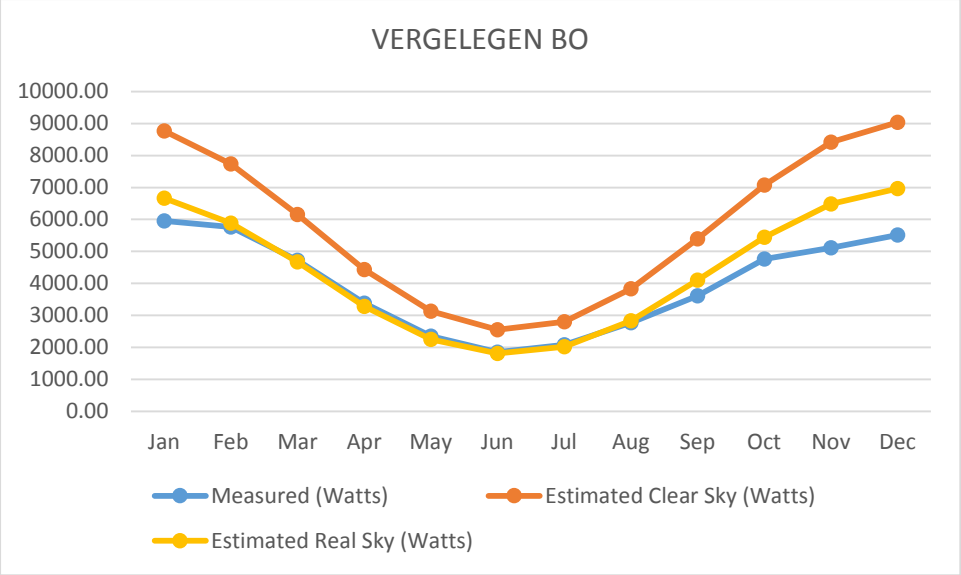

Figure 4.22(b): Mean monthly variation between the observed and the estimated radiation (2)

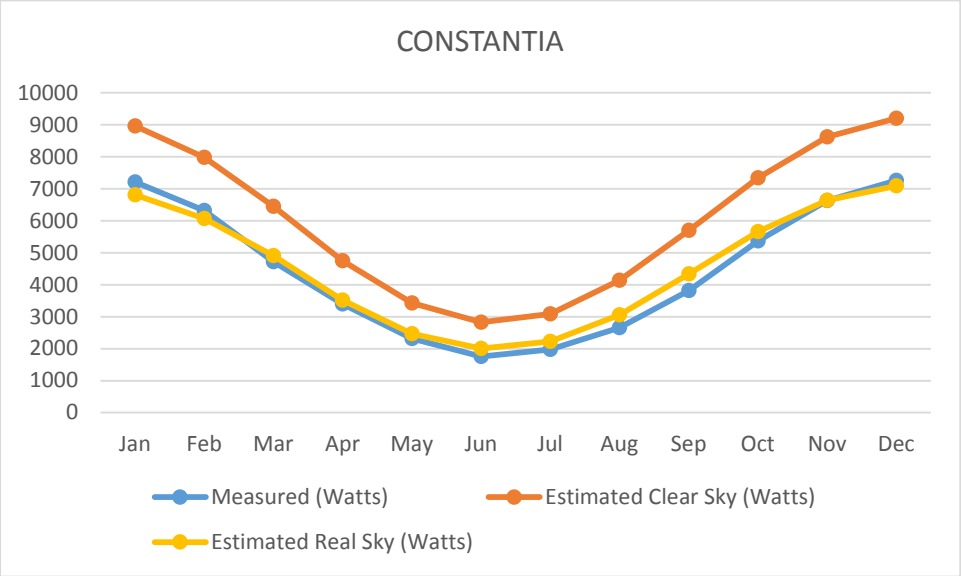

Figure 4.22(c): Mean monthly variation between the observed and the estimated radiation (3)

From the graphical representations for each of the three weather stations, there appear to be a more consistent variation between the clear-sky estimate and the measure solar radiation throughout the year. The variation between the estimated real-sky and measured solar radiation on the other hand is not consistent year-round. This happens as a result of the difficulty inherent in solar radiation estimation, which is the determination of the cloud cover from day to day, as this varies over time. The clear-sky index values as obtained from the NASA meteorological and solar energy data website are historic monthly average of the recorded difference between the extra-terrestrial solar radiation and terrestrial solar radiation.

To better investigate the correlation between the measured and estimated solar radiation values, some days of the year are randomly selected, so as to compare the daily sum of the solar radiation between the measured and the estimated. The comparison is presented in Table 4.8 (a, b and c).

Table 4.8(a): Table showing the measured vs the estimated daily sum of solar radiation (1)

NOORDHOEK AWS					
	Measured (Watts)	Estimated Clear Sky (Watts)	Clear Sky Index	Estimated Real Sky (Watts)	Difference (Watts)
Jan-01	8338.33	9059.66	0.76	6885.34	1452.99
Feb-15	7201.36	8172.11	0.76	6210.80	990.55
Mar-31	4814.74	6318.03	0.76	4801.70	13.04
Apr-15	4112.54	5553.87	0.74	4109.86	2.68
May-01	3644.90	4848.20	0.72	3490.70	154.20
Jun-15	1783.77	3431.80	0.71	2436.58	-652.81
Jul-31	2667.47	4134.61	0.72	2976.92	-309.45
Aug-15	2331.96	4711.38	0.74	3486.42	-1154.46
Sep-01	3562.52	5474.24	0.76	4160.42	-597.91
Oct-15	3642.18	4547.15	0.77	3501.31	140.87
Nov-30	7914.20	8914.71	0.77	6864.33	1049.87
Dec-15	7216.18	9094.13	0.77	7002.48	213.70
Average	**4769.178**	**6188.32**	**0.75**	**4660.57**	**108.61**
				RMSE	**735.77**

Table 4.8(b): Table showing the measured vs the estimated daily sum of solar radiation (2)

VERGELEGEN BO					
	Measured (Watts)	Estimated Clear Sky (Watts)	Clear Sky Index	Estimated Real Sky (Watts)	Difference (Watts)
Jan-01	5653.98	7432.90	0.76	5649.01	4.98
Feb-15	5717.67	7304.79	0.76	5551.64	166.03
Mar-31	3713.99	4603.55	0.76	3498.70	215.29
Apr-15	3093.51	4445.68	0.74	3289.81	-196.29
May-01	2896.64	4175.97	0.72	3006.70	-110.06
Jun-15	1450.20	2050.60	0.71	1455.93	-5.73
Jul-31	2289.54	3225.64	0.72	2322.46	-32.93
Aug-15	2611.91	3767.04	0.74	2787.61	-175.71
Sep-01	3206.35	3922.41	0.76	2981.03	225.33
Oct-15	4470.99	5493.52	0.77	4230.01	240.98
Nov-30	5274.37	6823.71	0.77	5254.25	20.12
Dec-15	5177.11	7079.56	0.77	5451.26	-274.15
Average	**3796.36**	**5027.11**	**0.75**	**3789.87**	**6.49**
				RMSE	**168.57**

Table 4.8(c): Table showing the measured vs the estimated daily sum of solar radiation (3)

CONSTANTIA					
	Measured (Watts)	Estimated Clear Sky (Watts)	Clear Sky Index	Estimated Real Sky (Watts)	Difference (Watts)
Jan-01	7812.42	9212.02	0.76	7001.13	811.29
Feb-15	6774.22	8020.65	0.76	6095.69	678.53
Mar-31	4002.40	5601.92	0.76	4257.46	-255.06
Apr-15	3441.69	4753.14	0.74	3517.32	-75.63
May-01	3142.29	3979.78	0.72	2865.44	276.84
Jun-15	1548.13	2780.40	0.71	1974.08	-425.95
Jul-31	2557.98	3569.92	0.72	2570.34	-12.36
Aug-15	2310.64	3995.08	0.74	2956.36	-645.72
Sep-01	3203.72	4839.14	0.76	3677.74	-474.02
Oct-15	4111.81	7313.76	0.77	5631.59	-1519.78
Nov-30	7808.17	9108.18	0.77	7013.30	794.88
Dec-15	6776.46	9212.39	0.77	7093.54	-317.08
Average	**4457.49**	**6032.20**	**0.75**	**4554.50**	**-97.01**
				RMSE	**653.92**

The graphical representations of the comparison for the daily sum are shown in Figure 4.23 (a, b and c) for better visualization.

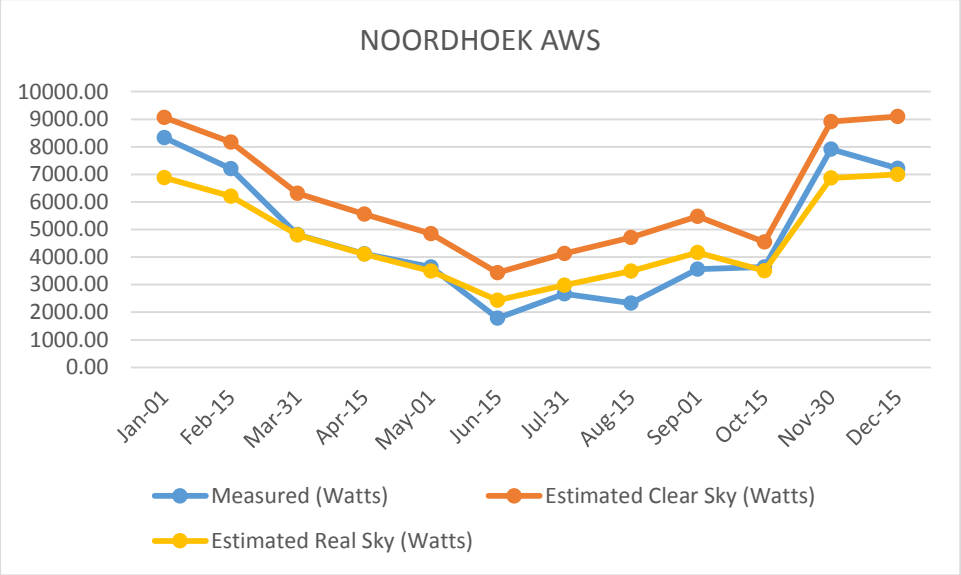

Figure 4.23(a): Daily sum variation between the observed and the estimated radiation (1)

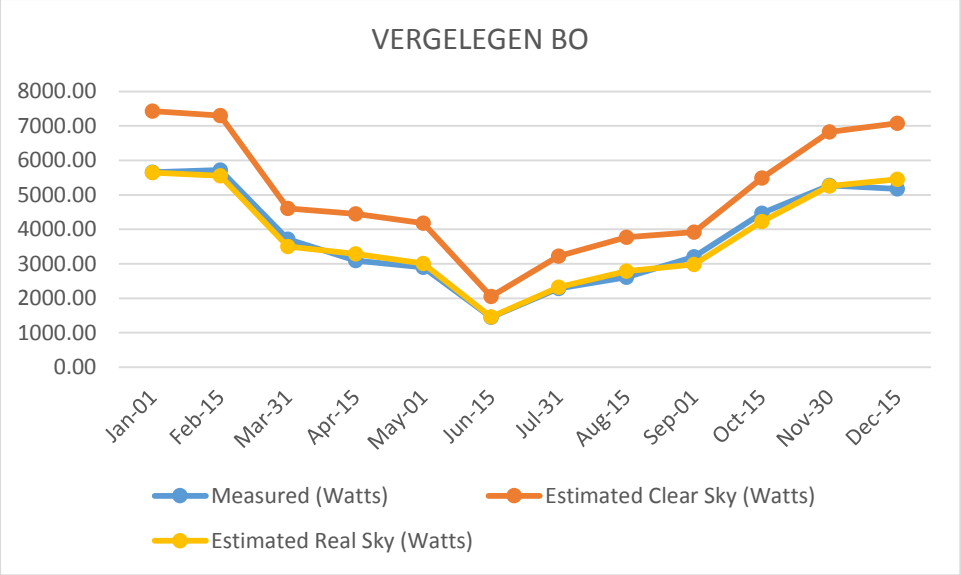

Figure 4.23(b): Daily sum variation between the observed and the estimated radiation (2)

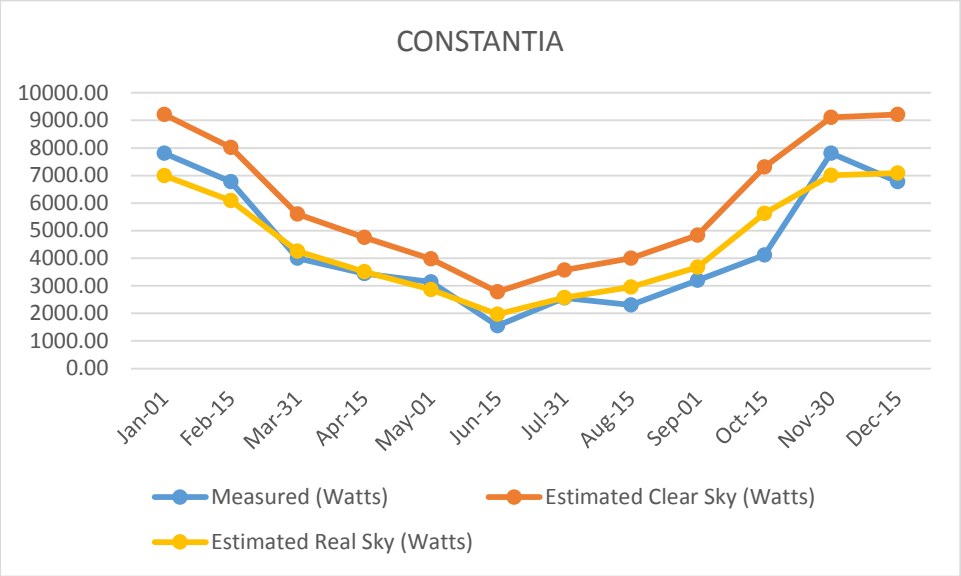

Figure 4.23(c): Daily sum variation between the observed and the estimated radiation (3)

Unlike the trend observed for the monthly mean comparison, the variation appears consistent between the estimated clear-sky and real-sky solar radiation and not with the measured radiation. The averaging of the monthly radiation values brings about the consistency as observed in the comparison between the monthly mean in Figure 4.25 (a, b and c). However, there are more days that have closer radiation values with the measured values, hence the reason for the inconsistent variation. To further investigate the correlation, hourly variation between the measured and estimated solar radiation values for selected three days in the year are compared and presented in

Table 4.9 (a, b and c), Table 4.10 (a, b and c) and Table 4.11 (a, b and c). Each table is followed with its corresponding graphical representation for easy referencing.

Table 4.9(a): Table showing the measured vs the estimated hourly solar radiation (1)

NOORDHOEK AWS					
	Measured (Watts)	Estimated Clear Sky (Watts)	Clear Sky Index	Estimated Real Sky (Watts)	Difference (Watts)
Jan-1-08H	194.79	322.80	0.76	245.33	-50.54
Jan-1-09H	491.81	624.45	0.76	474.58	17.23
Jan-1-10H	692.17	959.75	0.76	729.41	-37.25
Jan-1-11H	806.00	991.02	0.76	753.17	52.82
Jan-1-12H	883.39	1093.60	0.76	831.13	52.26
Jan-1-13H	1025.26	1130.76	0.76	859.38	165.89
Jan-1-14H	1033.82	1126.36	0.76	856.03	177.79
Jan-1-15H	882.32	1100.64	0.76	836.49	45.83
Jan-1-16H	825.62	1020.59	0.76	775.65	49.97
Jan-1-17H	624.05	809.41	0.76	615.15	8.90
Jan-1-18H	391.22	585.52	0.76	445.00	-53.78
Jan-1-19H	278.69	160.64	0.76	122.09	156.60
Average	**677.43**	**827.13**	**0.76**	**628.62**	**48.81**
				RMSE	**91.73**

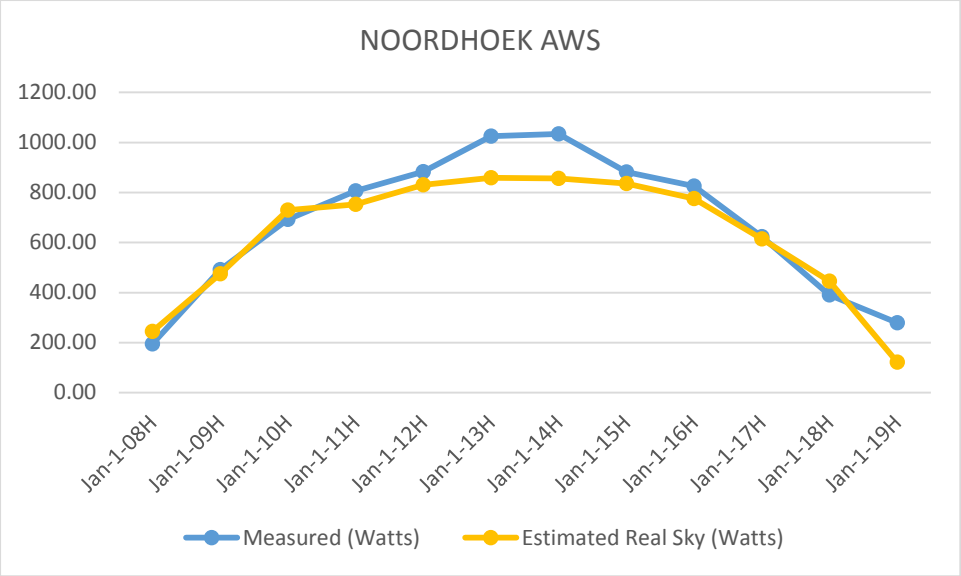

Figure 4.24(a): Hourly variation between the observed and the estimated radiation (1)

Table 4.9(b): Table showing the measured vs the estimated hourly solar radiation (2)

NOORDHOEK AWS					
	Measured (Watts)	Estimated Clear Sky (Watts)	Clear Sky Index	Estimated Real Sky (Watts)	Difference (Watts)
Jun-15-09H	25.94	41.12	0.71	29.19	-3.26
Jun-15-10H	86.14	116.07	0.71	82.41	3.73
Jun-15-11H	198.26	264.40	0.71	187.72	10.54
Jun-15-12H	266.76	385.37	0.71	273.61	-6.85
Jun-15-13H	257.29	301.95	0.71	214.39	42.91
Jun-15-14H	277.22	430.62	0.71	305.74	-28.52
Jun-15-15H	253.17	349.39	0.71	248.06	5.11
Jun-15-16H	166.07	216.04	0.71	153.39	12.68
Jun-15-17H	100.46	0.00	0.71	0.00	100.46
Average	**181.26**	**233.88**	**0.71**	**166.06**	**15.20**
				RMSE	**38.17**

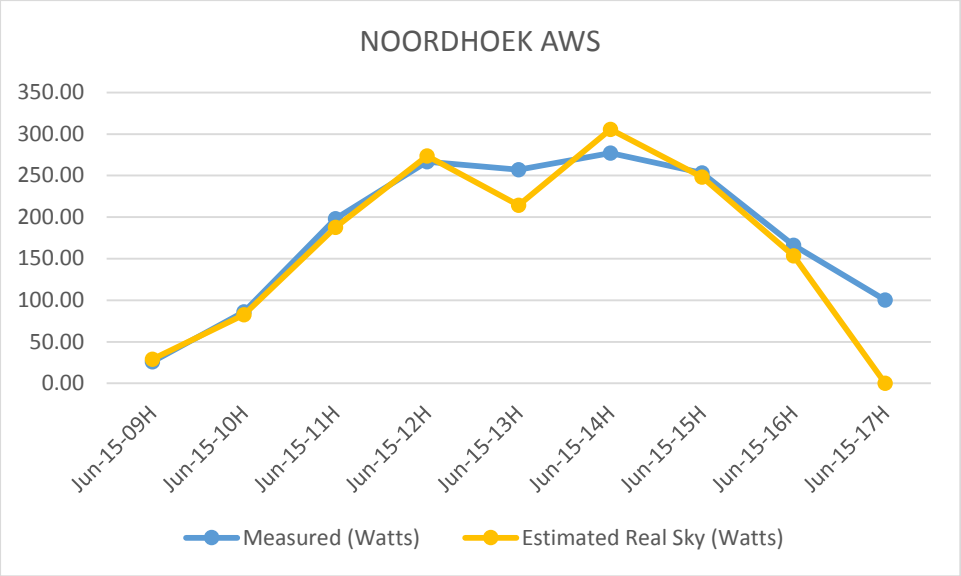

Figure 4.24(b): Hourly variation between the observed and the estimated radiation (2)

Table 4.9(c): Table showing the measured vs the estimated hourly solar radiation (3)

NOORDHOEK AWS					
	Measured (Watts)	Estimated Clear Sky (Watts)	Clear Sky Index	Estimated Real Sky (Watts)	Difference (Watts)
Dec-15-07H	42.68	52.40	0.77	40.35	2.33
Dec-15-08H	178.34	256.24	0.77	197.31	-18.97
Dec-15-09H	310.09	408.46	0.77	314.51	-4.42
Dec-15-10H	488.33	617.08	0.77	475.15	13.17
Dec-15-11H	567.73	716.57	0.77	551.76	15.97
Dec-15-12H	765.47	1008.74	0.77	776.73	-11.26
Dec-15-13H	903.53	1128.99	0.77	869.32	34.21
Dec-15-14H	998.48	1121.54	0.77	863.59	134.89
Dec-15-15H	869.62	1098.73	0.77	846.02	23.60
Dec-15-16H	723.40	924.43	0.77	711.81	11.58
Dec-15-17H	590.88	792.57	0.77	610.28	-19.40
Dec-15-18H	467.49	589.26	0.77	453.73	13.75
Dec-15-19H	242.16	165.43	0.77	127.38	114.78
Average	**549.86**	**683.11**	**0.77**	**526.00**	**23.86**
				RMSE	**51.69**

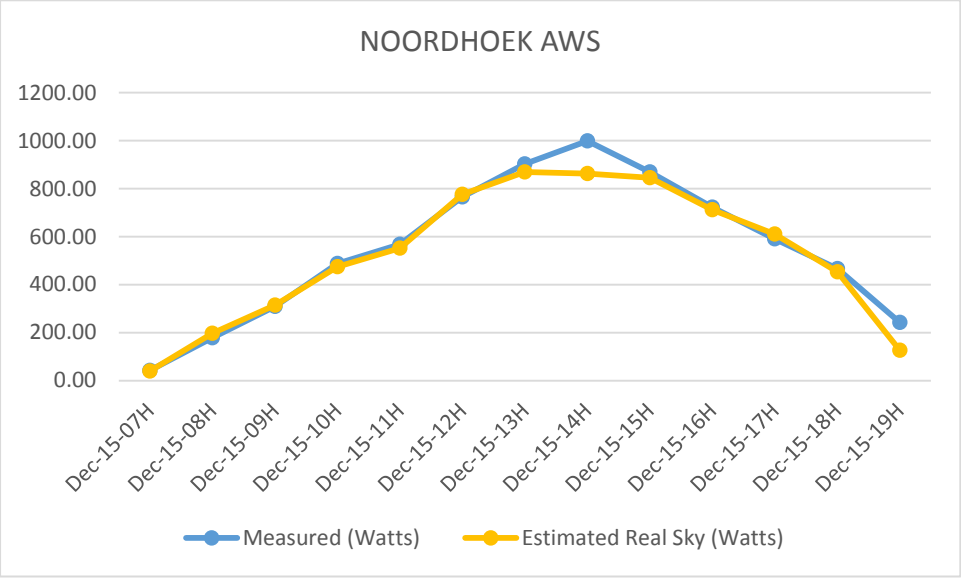

Figure 4.24(c): Hourly variation between the observed and the estimated radiation (3)

Table 4.11(a): Table showing the measured vs the estimated hourly solar radiation (1)

CONSTANTIA					
	Measured (Watts)	Estimated Clear Sky (Watts)	Clear Sky Index	Estimated Real Sky (Watts)	Difference (Watts)
Jan-15-07H	70.66	222.04	0.76	168.75	-98.09
Jan-15-08H	234.25	455.90	0.76	346.48	-112.23
Jan-15-09H	446.46	685.56	0.76	521.03	-74.57
Jan-15-10H	597.49	882.39	0.76	670.62	-73.12
Jan-15-11H	764.96	1027.79	0.76	781.12	-16.16
Jan-15-12H	835.25	1109.81	0.76	843.45	-8.20
Jan-15-13H	999.48	1121.50	0.76	852.34	147.14
Jan-15-14H	963.27	1060.36	0.76	805.87	157.40
Jan-15-15H	808.82	928.54	0.76	705.69	103.13
Jan-15-16H	716.20	820.39	0.76	623.50	92.70
Jan-15-17H	590.76	642.11	0.76	488.00	102.76
Jan-15-18H	416.33	484.78	0.76	368.43	47.90
Jan-15-19H	216.07	12.26	0.76	9.32	206.75
Average	**589.23**	**727.19**	**0.76**	**552.66**	**36.57**
				RMSE	**109.09**

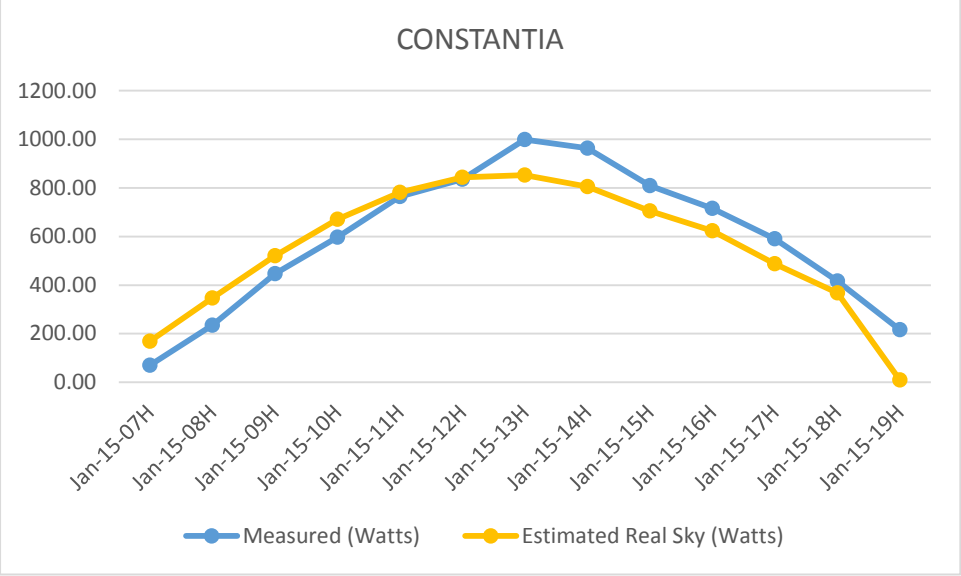

Figure 4.25(a): Hourly variation between the observed and the estimated radiation (1)

Table 4.11(b): Table showing the measured vs the estimated hourly solar radiation (2)

CONSTANTIA					
	Measured (Watts)	Estimated Clear Sky (Watts)	Clear Sky Index	Estimated Real Sky (Watts)	Difference (Watts)
Jun-15-09H	34.10	64.41	0.71	45.73	-11.64
Jun-15-10H	122.95	250.73	0.71	178.02	-55.07
Jun-15-11H	207.10	262.22	0.71	186.18	20.93
Jun-15-12H	241.93	412.87	0.71	293.14	-51.21
Jun-15-13H	262.82	416.61	0.71	295.79	-32.97
Jun-15-14H	241.44	308.21	0.71	218.83	22.61
Jun-15-15H	217.14	376.37	0.71	267.22	-50.08
Jun-15-16H	138.33	203.07	0.71	144.18	-5.85
Jun-15-17H	70.77	0.00	0.71	0.00	70.77
Average	**170.73**	**254.94**	**0.71**	**181.01**	**-10.28**
				RMSE	**41.34**

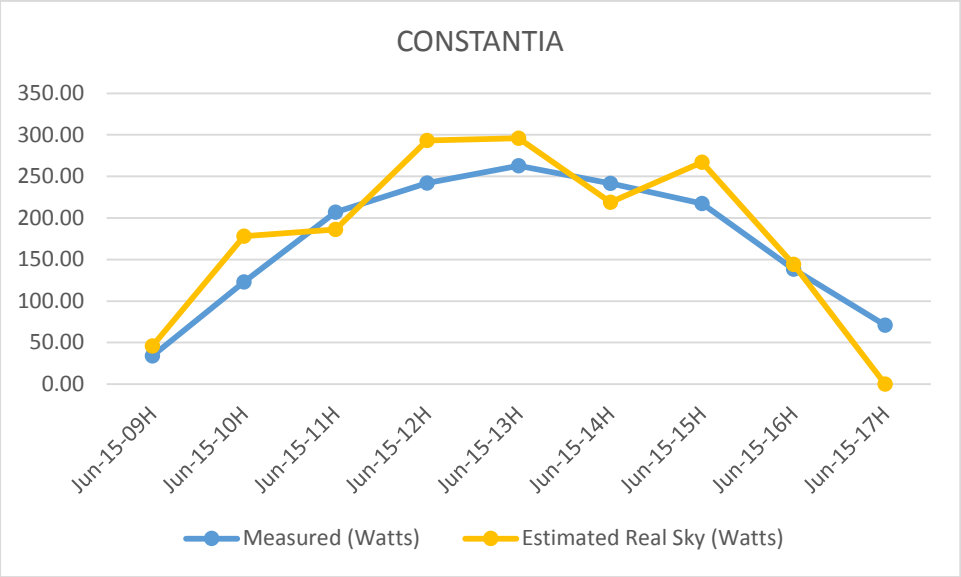

Figure 4.25(b): Hourly variation between the observed and the estimated radiation (2)

Table 4.11(c): Table showing the measured vs the estimated hourly solar radiation (3)

CONSTANTIA					
	Measured (Watts)	Estimated Clear Sky (Watts)	Clear Sky Index	Estimated Real Sky (Watts)	Difference (Watts)
Dec-15-06H	8.41	41.93	0.77	31.28	-23.87
Dec-15-07H	84.17	171.56	0.77	132.10	-47.94
Dec-15-08H	255.60	337.30	0.77	259.72	-4.12
Dec-15-09H	430.72	512.72	0.77	394.80	35.92
Dec-15-10H	544.46	679.02	0.77	522.85	21.61
Dec-15-11H	592.72	821.59	0.77	632.62	-39.90
Dec-15-12H	713.47	928.77	0.77	715.15	-1.68
Dec-15-13H	860.02	1124.89	0.77	866.16	-6.15
Dec-15-14H	806.55	1064.96	0.77	820.02	-13.47
Dec-15-15H	732.71	953.39	0.77	734.11	-1.39
Dec-15-16H	586.30	744.81	0.77	573.50	12.80
Dec-15-17H	579.65	742.36	0.77	571.62	8.03
Dec-15-18H	370.09	467.89	0.77	360.27	9.81
Dec-15-19H	187.24	17.70	0.77	13.63	173.61
Average	**482.29**	**614.92**	**0.77**	**473.49**	**8.80**
				RMSE	**51.35**

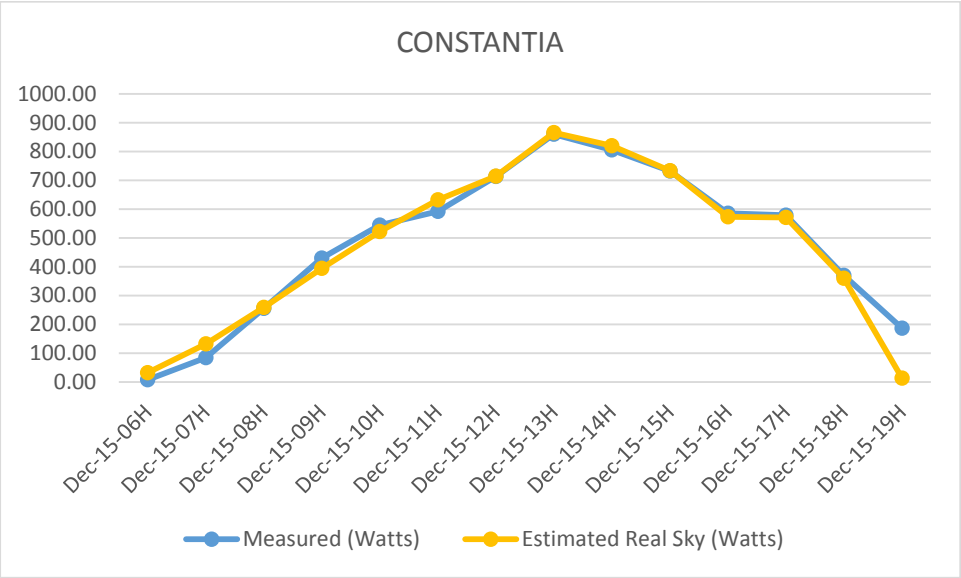

Figure 4.25c): Hourly variation between the observed and the estimated radiation (3)

From the solar radiation validation analysis carried out, there appear to be a better correlation between the measured radiation value and the estimated value of the model adopted in this study, as it moves away from monthly averages to daily and hourly comparisons. This is evident in lower differences between the measured and

the estimated radiation values, as well as in the RMSE value. It is for this reason that the mean annual solar radiation is considered adequate for information display purpose in this study. Applying the same method and approach to daily and hour values would even yield a more accurate result, but would require vast amount of storage and display capacity. From the validation analysis and results obtained, it can be said that the solar radiation model in GRASS GIS adequately estimates the solar radiation to a high degree of accuracy, provided the parameters are properly configured to reflect the climatic condition of the study area.

4.6.3 Accuracy Assessment for Solar Photovoltaic Potential Estimate

In order to assess the accuracy of the solar photovoltaic potential estimate, it is required to compare the estimate arrived at, with the generation output from an existing solar photovoltaic system installation. Therefore, to have an ideal comparison, the existing photovoltaics system should have generated electricity from the solar panels for at least a year (12 months). This is necessary, since the estimate from this study is based on the mean annual solar radiation to yield a mean daily potential output.

The Black River Park, is the first to install a large capacity roof-mounted solar photovoltaic system in Southern Africa, and it is indeed the largest so far, with an installed capacity of 1.2 megawatt. It is rated among the 30 largest roof integrated solar photovoltaic system in the world, and follows closely, that of Google headquarters, USA (1.6 MW), the Rome Trade Fair, Italy (1.4 MW) and Toyota Parts Centre, Belgium at 1.8 MW capacity (SOLA, 2015). The first phase, which is 700 Kw was completed in July 2013 and the second phase (500 Kw) was completed in August 2014.

A 12-month (August 2013 – July 2014) generation output for the first phase is provided by the management of Black River Park and is used in the accuracy assessment of the solar photovoltaic potential estimate of this study. The location is identified from the aerial imagery and the area occupied by the solar panels are digitized in ArcGIS software to obtain its area in square meters as shown in Figure 4.26.

Figure 4.26: Digitized area occupied by Black River Park's solar panels

Using the LiDAR data, a DSM is generated for the area, and the global solar radiation is estimated using the r.sun model as explained previously. Figure 4.27(a) and (b) shows the mean annual global radiation estimate and the aspect map respectively.

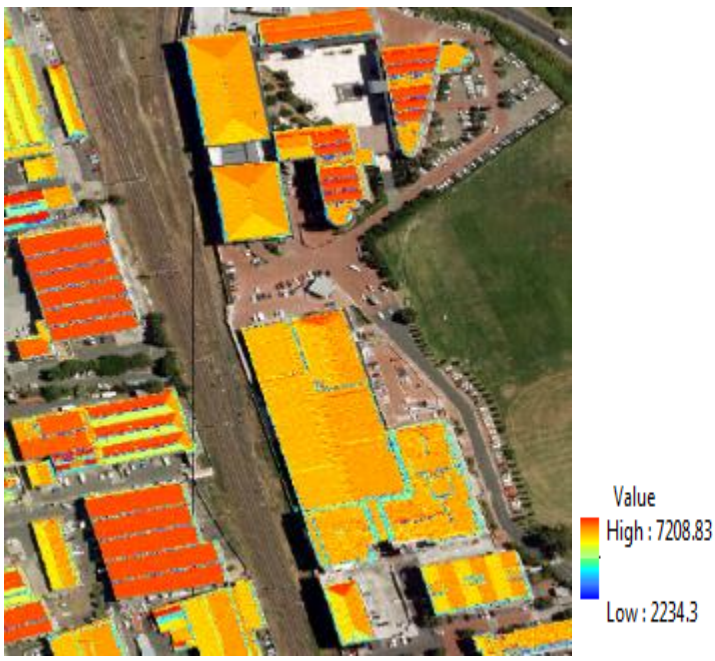

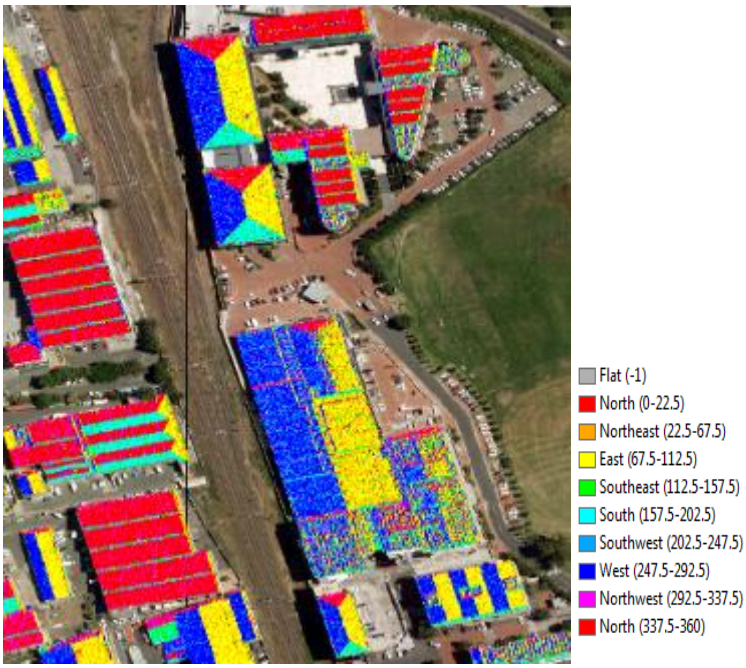

Figure 4.27(a): Mean annual radiation of Black River Park (b): Aspect map of Black River Park

The solar photovoltaic potential is estimated using the same procedure as discussed under Section 4.4. The resulting attribute table of the digitized solar panel area is shown in Table 4.12.

Table 4.12: Table showing the estimated photovoltaic potential of Black River Park

OB_ID	SHAPE_Area	Solar_Radiation_Est.	Panel_Eff.	Performance_Ratio	PV_Potential_Clearsky	ClearSky_Index	PV_Potential_Est_Realsky
1	753.97	6591.518	15	0.76	566.559	0.75	413.588
2	168.23	6291.928	15	0.76	120.668	0.75	88.088
3	106.81	6203.313	15	0.76	75.535	0.75	55.141
4	110.91	6282.787	15	0.76	79.436	0.75	57.989
5	69.11	6227.251	15	0.76	49.061	0.75	35.814
6	60.54	6178.653	15	0.76	42.642	0.75	31.129
7	116.13	6810.816	15	0.76	90.164	0.75	65.820
8	79.73	6862.143	15	0.76	62.373	0.75	45.532
9	111.44	6789.551	15	0.76	86.259	0.75	62.969
10	84.08	6808.847	15	0.76	65.265	0.75	47.644
11	80.768	6805.492	15	0.76	62.662	0.75	45.743
12	585.28	6128.063	15	0.76	408.872	0.75	298.477
13	1183.95	6129.826	15	0.76	827.346	0.73	603.962
14	625.16	6252.380	15	0.76	445.594	0.73	325.284
15	397.22	6264.938	15	0.76	283.693	0.73	207.096
16	347.08	6073.188	15	0.76	240.296	0.73	175.416
	Sum(daily):	**102700.694**			**3506.425**		**2559.690**

The 12-month generation output from the Black River Park is shown in Table 4.13.

Table 4.13: Table showing one year generation output in kWh for Black River Park

Datum	PV South/Central 121 (kWh)	PV NB 181 (kWh)	PV NB 182 (kWh)		
Aug-13	20054.668	23485.944	14171.952		
Sep-13	27941.200	30711.377	18810.532		
Oct-13	36431.329	38414.641	23904.196		
Nov-13	40691.778	39881.321	25321.410		
Dec-13	44895.197	43490.355	27796.965		
Jan-14	43524.082	42313.823	27123.837		
Feb-14	41101.187	42126.338	26547.659		
Mar-14	34881.328	37325.570	23099.078		
Apr-14	25167.590	28794.091	17400.232		
May-14	15759.456	18454.329	11109.829		
Jun-14	13932.838	17005.292	10242.717		
Jul-14	16138.046	19156.966	11721.065		
Sum:	360518.699	381160.047	237249.472	**978928.218**	**Annual production**
				81577.352	**Monthly mean**
				2681.995	**Daily mean**

The mean daily estimate derived from analysis carried out in this study for the area occupied by the solar panels is 2,559.690 kWh, while the recorded mean daily output generation of the photovoltaic system was 2,681.995 kWh. This shows a difference of 122.305 kWh between the estimated solar photovoltaic potential and the actual generation capacity of the installed solar photovoltaic system. The monthly variation between the estimated potential and the installed production is shown in Figure 4.28.

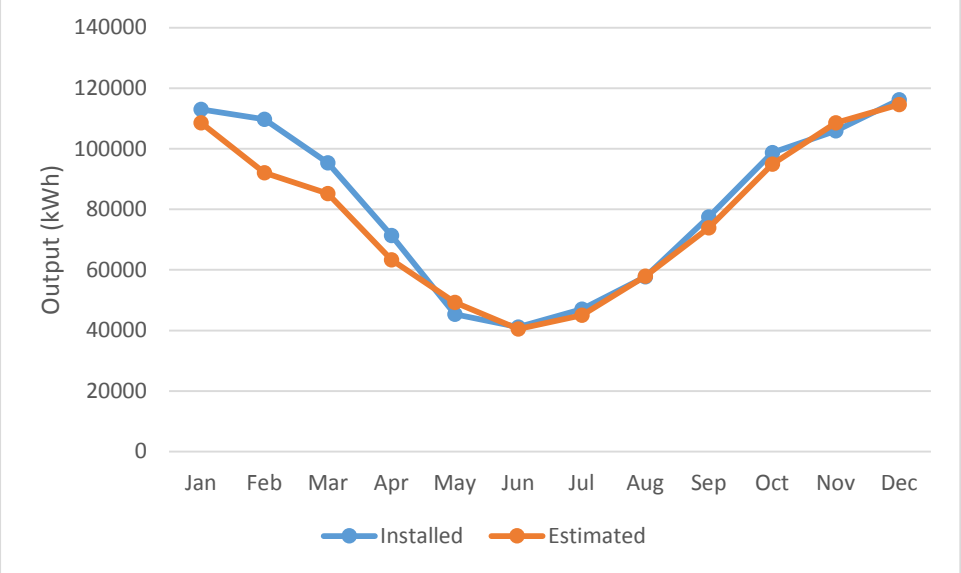

Figure 4.28: Monthly variation between the installed PV system and the estimated potential

The comparison between the installed output and the estimated potential shows that the estimates gotten, using the methods of this study, are good and can be relied upon for planning and decision-making purposes. Having assessed the accuracy of the building roof extraction, the solar radiation estimates and that of the solar photovoltaic potential estimate, a summary of all analyses and results produced is presented in the section below.

4.7 Summary of Analysis and Result

Various analyses are carried out, as discussed above, to create a web-based system, which can be used to evaluate the solar photovoltaic potential of building roofs in the City of Cape Town. These analyses are carried out in sequence of phases, as explained in the preceding sections and sub-sections, starting with the processing of LiDAR and aerial imagery and culminating with a web tool to obtain solar photovoltaic potential of building roofs. Four phases of analysis are involved, the results from the first two phases of analysis serve as input into the third phase and the output of the third phase serves as input into the final phase of the analysis. The first phase deals with extraction of building roof and roof planes, while the second phase has to do with estimating the solar radiation of building roof areas within the study area. The third phase consolidates the results of phase one and phase two to create a solar photovoltaic potential geodatabase for the study area. While in the final phase, data layers from phase three are published via web map API and serve as the information source of the customized web-based system.

A unique two-in-one classification technique to detect and extract building roof span and roof planes is developed. The object-based classification process takes as input, the aerial imagery and three LiDAR-derived surface models, which include nDSM, slope and aspect rasters. The first stage of the workflow generates the building roof outline, which represents the span area of the building roof. While the second stage decomposes the building roof structure into roof planes. The extracted roof plane image objects are vectorised and exported as Shapefile, together with properties of the LiDAR-derived raster (height, slope and aspect) as attributes. These attributes become useful inputs in the third phase of the analysis. About five hundred and forty-five thousand (545,000) building roof outlines are extracted and these are

decomposed to about one million seven hundred thousand (1,700,000) building roof planes. The two-in-one classification technique developed and results obtained from the building roof extraction analysis thus answered the question as to which spatial data analysis method is suitable to effectively extract building roof outline together with each roof plane comprising the whole building roof.

Furthermore, in the second phase of analysis, the global solar radiation analysis shows how the solar radiation over a building could be efficiently estimated. Using a modified a modified Python script, the tool is looped through each day of the year obtaining the daily sums of solar radiation by specifying the parameters that defines the atmospheric conditions of the study area. The python script drafted accepts the LiDAR data as sole input and returns the mean annual solar radiation values in a raster file. The script platform helps reduce crisscrossing of software platforms, to bring about algorithm optimization and reducing processing speed significantly. This thus answered the question of how the global solar radiation over a building could be efficiently estimated.

The third phase of the analysis combine results and outputs from the previous phases together with other ancillary data to build the solar photovoltaic potential database for City of Cape Town. From the solar photovoltaic potential analysis, 74% of the extracted building roofs have optimal percentages of 50% and above. This means that about 74% of buildings in Cape Town poses rooftops that are optimized for solar photovoltaic system. The final phase of the analysis enhances the information sitting in the geodatabase of the solar photovoltaic potential by creating an interactive web-based system to bring about a broad information dissemination platform. This thus answer the question of how a solar photovoltaic estimation tool could be enhanced to provide an efficient solution for web-based building-integrated solar photovoltaic system.

Results and estimates derived from this study are assessed for accuracy, and found to be good and reliable. The solar radiation estimates are validated using measured solar radiation from three weather stations within the study area. The validation results show high correlation and similarities between the measured and estimated solar radiation. Likewise, the solar photovoltaic potential estimation is compared with an installed system and found to compare well. The usefulness and possible areas of

application of results and outputs generated from various analysis carried out in this study are discussed in the following section

4.8 Discussion of Results

Results obtained in each phase of this study can be utilized in diverse areas of application beyond the scope of this study, thereby making the results and outputs in this study a primary or secondary source of data to other various applications. Briefs of such applications are given hereunder.

4.8.1 Building Roof Extraction Applications

There is a lack of large scale building roof inventory in municipality planning departments across Africa, consequently, potentials of building roof data in urban areas are often neglected or under-utilized. Most geometric and physical characteristics of building roofs exist only in single units as part of a building plan. The benefits and impact of building roof extraction data in urban planning cannot be over emphasized, as it has been proven overtime, to be very useful in infrastructural development, city planning suitability analysis, roof deformation analysis, and risk management amongst others.

Having the knowledge of the geometry configuration and surface characteristics of building roofs are quite essential in determining the snow load capacity of building roofs, also roof plane extraction using the aspect raster helps in identifying deformities in building roof planes. Similarly, building roof extraction data is a vital input in various suitability analysis studies. The amount of rainwater a building roof can harvest is determined using the surface area, slope and aspect information from building roof data. A multimedia or telecommunication company looking for high-rise building with flat roof to mount billboards or telecommunication mast can result to a building roof inventory to search for suitable buildings. These would in turn fast-track the rate at which African cities can achieve sustainability. Rainwater harvesting decision, fast-tracked with inputs from building roof extraction data would contribute to meeting goal number six of the United Nations Sustainable Development Goals (UN SDGs), which is to “ensure access to water and sanitation for all”.

The technique designed in this study is capable of generating building roof inventory and database for an entire city within a short period of time, provided the required input datasets are available. The City of Cape Town, as a result of the method it adopted for extracting building footprint and roof outlines, has succeeded in extracting only about 10% of buildings within the city (City of Cape Town, 2017). The building roof inventory could also be deployed on a web portal, with options to digitize and capture the roof of new building developments as soon as it is available on the tile mapping service provider, in a “participatory” GIS context. This amongst others form the basic requirements for attaining a smart city status.

4.8.2 Solar Radiation Database Applications

The need for estimation of solar radiation database exist in a lot of environmental science fields. Solar radiation estimates are utilized in architectural design in determining cooling loads for building structures and directions roof structures could face. It is also utilized in hydrologic models, estimating agriculture crop yields and estimation of evapotranspiration, amongst other vast areas of applications. Unlike precipitation and temperature data, solar radiation data are hard to obtain in South Africa, as only few of the available weather stations has the capability to record the solar radiation. If most of the weather stations does not record solar radiation, then it becomes difficult to obtain spatially continuous solar radiation estimates for areas away from the weather stations.

Estimates from meteorological satellite would have suffice for areas away from where ground solar radiation records are available, however, solar radiation estimates from the satellite are of coarse resolution and are therefore not useful in some applications, such as building-integrated solar photovoltaics. The analysis of the global solar radiation estimation in this study yields a validated medium-scale and high resolution (60cm) solar radiation database for the City of Cape Town municipality. This can then be used in any application requiring solar radiation estimates. The current highest resolution available for the city stands at 1000m, obtainable from GeoSUN Africa in conjunction with SolarGIS (GeoSUN Africa, 2014).

4.8.3 Solar Photovoltaic Potential Applications

The results generated in this study could be utilised as a decision-making tool by public authorities, such as municipalities, as well as by the private sector, in assessing and determining which building roof would be viable for solar photovoltaic installations. The information generated by this study and made available through the web-based solar photovoltaic potential tool, would make it possible to evaluate different types of building, ranging from residential to commercial, in terms of the solar photovoltaics potential of their roof planes. This in turn would contribute immensely in meeting goal number seven of the UN SDGs, which is to “ensure access to affordable, reliable, sustainable and modern energy for all”.

With the solar photovoltaic potential information made available on the web, the general public is able to access information by simply typing the street address of the building of interest, to determine the amount of electricity that could be generated from the building roof. By incorporating other information, such as the consumption match percentage and average cost of equipment and installation, decisions could be made about the possibility of installing solar panels for electricity generation purposes.

The geodatabase created could be updated from time to time by the custodian to reflect changes in structural developments. The information made available from this study would certainly be able to accelerate the decision-making process, either by government authorities or by the private sector, concerning building-integrated solar photovoltaic deployment. This would in turn speed up the processes required to meet government targets for cutting fossil fuel usage and promoting renewable energy development. This would also help a municipality like City of Cape Town to achieve self-sufficiency in terms of energy sustainability and in its drive for a greener city.

4.9 Chapter Summary

In summary, this chapter was able to present the details about all the analyses carried in this study, and their results, starting with the LiDAR data processing and DEMs generation in Section 4.1, through the creation of web-based solar photovoltaic potential system in Section 4.5 and ending with the validation of the results generated

from the analysis carried out. Based on the results generated, some conclusions could now be drawn and recommendations could be given as presented in the next chapter.

CHAPTER 5
CONCLUSIONS AND RECOMMENDATIONS

Having discussed and summarized the analyses carried out, and the results generated, in Chapter 4, this chapter presents the conclusion to this study. This chapter also presents some recommendations, with regards to possible future work, which could be carried out to improve the current study.

5.1 Conclusions

The City of Cape Town is leading the green city initiatives not only in Africa, but across the world. The city was recently ranked among top five global climate-conscious and sustainable cities by the global Carbon Disclosure Project (CDP). The city posited in its 2016 submission to the CDP that it has reduce carbon emissions through initiatives such as waste management at landfill sites and reduction in carbon energy supply generation with about 10% of electricity sourced from renewable energy, amongst others (Steyn, 2017). Notwithstanding the achievement, the city is still poised to attain the status of the greenest city in the world, consequently, building-integrated solar photovoltaic system offers significant contribution in attaining such feat.

However, before embarking on a large-scale process of installing solar photovoltaic systems, it is important to evaluate the viability of such installations by identifying the best locations for installing the panels and estimating the amount of electricity that could actually be generated or harvested. Moreover, the problem of creating awareness about the potentials of building-integrated solar photovoltaic persist. Thereby making the development of a web-based solar potential calculator very important. The results and the information generated from this research offer an effective solution, given the planning intricacies involved in the widespread installation of solar photovoltaic systems. Ignoring or avoiding this necessary stage, of evaluation and assessment, would result in a significant loss of time and resources.

The aim of this research, which is to create awareness about the potentials each building could offer in harvesting solar energy for electricity in the City of Cape Town using photovoltaic technology, is achieved. In achieving the aim, the laid-out objectives

at the beginning of the research are pursued. The pursuit of these objectives lead to development of novel techniques including a unique two-in-one building roof extraction model, thereby answering the research question of which spatial data analysis method is suitable to effectively detect and extract building roof outline together with roof planes comprising the whole building roof. The transferability capability of the designed method and its validation yielding better accuracy metrics, when compared with similar methods, brought to focus its novelty.

Likewise, the development of an algorithm, which accepts LiDAR point data to generate a high resolution and validated solar radiation database for the entire city, being the second objective pursued, helped answered the question of how the global solar radiation over a building could be efficiently estimated. The validation of the solar radiation database, using ground measurements data within the study area yielded a good correlation in monthly, daily and hourly comparison, with better comparison achieved towards the hourly comparison. This therefore ascertains that the solar radiation model adapted in this study is capable of estimating global solar radiation over an area to a high degree of accuracy.

The third objective pursued, which is to estimate the solar photovoltaic potential of building roofs helped answered the question of how solar photovoltaic potential can be estimated using building roof data and solar radiation database. From the methods developed and results generated, the potential of sections or planes of each building roof could be analysed to determine its viability for photovoltaic panel installation. The solar photovoltaic potential estimates derived, using the methodologies developed in this study was also compared with an existing large-scale building integrated solar photovoltaic system. This was found to compare well with that of the installed capacity, thereby making estimates generated from this study reliable and dependable.

Similarly, from the results derived from the analyses carried out in this study, it shows that solar resources are in abundance within the City of Cape Town. These can be harnessed to increase the percentage of electricity the City of Cape Town is sourcing from renewable energy and thereby meeting its set out renewable energy target and reducing its carbon footprint. However, the size of the building roof plays a prominent role in determining the amount of energy, which could be harvested from the building roof. The bigger a building roof, the more the area of the roof, which will be available

to receive the solar radiation. Other Factors such as the roof orientation and the slope play a lesser role in determining the amount of solar radiation compared to the building roof surface area, as roof planes facing the south still receives tangible amount of solar radiation. Likewise, issues with the roof slope could be maneuvered by varying the tilt of the solar panel during installation, except in the cases of near vertical building roofs.

In answering the fourth research question, an objective to build an interactive web-based tool capable of evaluating and assessing the potentials, designs and installation of building-integrated solar photovoltaic system was pursued. This was achieved by combining outputs of the three previous objectives to develop a novel web-based solar photovoltaic potential calculator via JavaScript and HTML scripting. This becomes a universal and dynamic tool, which is capable of helping renewable energy developers as well as regulator in making an informed decision about the viability of a building-integrated solar photovoltaic system before approval or development, as the case may be.

The objectives pursued, methods developed and results generated in this study succeeded in answering all the research questions raised. The methods developed in this study, together with the output results are capable of achieving a pioneering feat in Africa and by extension globally, as it has been designed from scratch to remotely evaluate the solar photovoltaic potential of building roofs at a city-wide scale, without resorting to physical field measurements. Existing methods have only been tested over smaller area, as seen, for instance, in areas delineated in the ISPRS benchmark test project. Various novel applications of results generated using the designed methods have been discussed already in Section 4.8. All these combine to contribute significantly to the technological advancement of existing body of scientific knowledge in the GIS field.

Obviously, the use of remote sensing and GIS has improved the rate at which spatial problems could be solved within a short period. This was also made possible by the fact that data sharing is becoming commonplace in the GIS world. As is evident from this research, GIS is an efficient tool that can and should be used in the utility and renewable energy sector to solve spatially related issues. Finally, results obtained from this research are key in the City of Cape Town’s pursuit of sustainable, smart and green city status.

5.2 Research Limitations

As mentioned in the accuracy assessment section, a major inherent problem with automatic building roof extraction technique is the ability to resolve topological differences between the extracted building roof and the actual building roof in densely built-up areas. This is as a result of the automatic extraction algorithm not been able to detect the demarcation of buildings joined together. The automatic extraction algorithm only separate buildings when there are actually spaces between them. Therefore, a post classification exercise might be required to resolve the differences in the topology.

5.3 Recommendations

As highlighted in the conclusions, the web-based tool developed is capable of becoming a decision-making tool for renewable energy regulators and developers. A city-wide scale system, as designed in this study is more suited for the renewable energy regulator, as they are responsible for the regulation and deployment of solar photovoltaic system with their domain. A renewable energy developer or a homeowner who desires to evaluate the solar photovoltaic potential of few buildings might find it expensive or laborious to setup or purchase the kind of system developed in this study. It is therefore recommended that renewable energy regulators at the municipal level, which have the financial capacity to develop or purchase this kind of system, to go ahead and develop such system. In turn, the regulator or municipality can then give the public (renewable energy developers and homeowners) access to the web-based system and decide if it will be an open or proprietary data.

Furthermore, the building roof data and solar radiation data generated are very important primary data required as inputs in various applications as highlighted in Section 4.8. It is therefore recommended that the municipality acquire results generated in the building roof extraction and solar radiation analysis of this study. This can then be made available to the public as an open or proprietary data. Future works based on the results of the research includes incorporating wind energy potential, rainwater harvesting potential, etc. to the web-based tool, so as to have a synergized sustainability system online. This can also be modified to provide a small-scale web

service, rendering photovoltaic, wind or rainwater harvesting potentials to other web applications via an API.

REFERENCES

Aguayo, P., 2013. *Solar energy potential analysis at building scale using LiDAR and satellite data.* Master's thesis. University of Waterloo. Available: https://uwspace.uwaterloo.ca/handle/10012/7603 [2015, January 13].

Álvarez, J., Mitasova, H. & Allen, H.L. 2011. Estimating monthly solar radiation in south-central Chile. *Chilean Journal of Agricultural Research.* 71(4):601-609.

Amador, J. & Domínguez, J. 2005. Application of geographical information systems to rural electrification with renewable energy sources. *Renewable Energy.* 30(12):1897-1912.

Anderson, E., Thompson, J., Crouse, D. & Austin, R. 2006. Horizontal resolution and data density effects on remotely sensed LIDAR-based DEM. *Geoderma.* 132(3):406-415.

Awrangjeb, M. & Fraser, C. 2013. Rule-based segmentation of LIDAR point cloud for automatic extraction of building roof planes. *ISPRS Ann.Photogramm.Remote Sens.Spat.Inf.Sci.* 2(3/W1):1-6.

Awrangjeb, M., Ravanbakhsh, M. & Fraser, C. 2010. Automatic detection of residential buildings using LIDAR data and multispectral imagery. *ISPRS Journal of Photogrammetry and Remote Sensing.* 65(5):457-467.

Awrangjeb, M., Zhang, C. & Fraser, C.S. 2013. Automatic extraction of building roofs using LIDAR data and multispectral imagery. *ISPRS Journal of Photogrammetry and Remote Sensing.* 83:1-18.

Baatz, M. & Schäpe, A. 2000. Multiresolution segmentation: an optimization approach for high quality multi-scale image segmentation. *Angewandte Geographische Informationsverarbeitung XII.* :12-23.

Baban, S. & Parry, T. 2001. Developing and applying a GIS-assisted approach to locating wind farms in the UK. *Renewable Energy.* 24(1):59-71.

Baillard, C. & Maıtre, H. 1999. 3-D reconstruction of urban scenes from aerial stereo imagery: a focusing strategy. *Computer Vision and Image Understanding.* 76(3):244-258.

Barry, D. 2017. *Service architecture.* Available: https://www.service-architecture.com/articles/web-services/representational_state_transfer_rest.html [12 sept. 2017].

Baumann, P. 2014. *History of remote sensing, aerial photography.* Available: http://www.oneonta.edu/faculty/baumanpr/geosat2/RS%20History%20I/RS-History-Part-1.htm [2015, June 4].

Bergamasco, L. & Asinari, P. 2011. Scalable methodology for the photovoltaic solar energy potential assessment based on available roof surface area: Application to Piedmont Region (Italy). *Solar Energy.* 85(5):1041-1055.

Blaha, S. & Paksoy, M.2006. Parallelized Interpolation: A Quantitative Assessment. *Class of 2007 Senior Conference on Computational Geometry and GIS.* 15.

Bojanowski, J. 2013. Quantifying Solar Radiation at the Earth Surface with Meteorological and Satellite Data. Ph.D Thesis. University of Twente.

Botes, A. 2014. *City of Cape Town launches small scale embedded energy generation guidelines and tariff.* Available: http://urbanearth.co.za/articles/city-cape-town-launches-small-scale-embedded-energy-generation-guidelines-and-tariff [2015, June 19].

Bottaccioli, L., Patti, E., Macii, E. & Acquaviva, A. 2017. GIS-based Software Infrastructure to Model PV Generation in Fine-grained Spatio-temporal Domain. *IEEE Systems Journal.* DOI:10.1109/JSYST.2017.2726350.

Bouziani, M., Goita, K. & He, D. 2010. Rule-based classification of a very high resolution image in an urban environment using multispectral segmentation guided by cartographic data. *Geoscience and Remote Sensing, IEEE Transactions on.* 48(8):3198-3211.

Brewer, J., Ames, D.P., Solan, D., Lee, R. and Carlisle, J., 2015. *Using GIS analytics and social preference data to evaluate utility-scale solar power site suitability*. *Renewable energy*, 81, pp.825-836.

Brito, M., Gomes, N., Santos, T. & Tenedório, J. 2012. Photovoltaic potential in a Lisbon suburb using LiDAR data. *Solar Energy.* 86(1):283-288.

Bronkhorst, S., Raw, B. & Mulcahy, M. 2017. *Utility-Scale Renewable Energy: Market Intelligence Report 2017.* (Report no. GC/2017/01). Cape Town: GreenCape.

Brown, P., Jean, J., O'Sullivan, F. & Miller, R. 2017. *The Future of Solar Now Depends on More Than Just Technology.* Available: https://www.rdmag.com/article/2017/11/future-solar-now-depends-more-just-technology [Nov 11, 2017].

Burger, B. 2017. *The Fraunhofer Institute for Solar Energy Systems ISE.* Available: https://www.energy-charts.de/energy_pie.htm [26 May, 2017].

Burrough, P.A. & McDonnell, R.A. 2011. *Principles of geographical information Systems.* Oxford University Press.

Camargo, L.R., Zink, R., Dorner, W. & Stoeglehner, G. 2015. Spatio-temporal modeling of roof-top photovoltaic panels for improved technical potential assessment and electricity peak load offsetting at the municipal scale. *Computers, Environment and Urban Systems.* 52:58-69.

Canny, J. 1986. A computational approach to edge detection. *Pattern Analysis and Machine Intelligence, IEEE Transactions on.* (6):679-698.

Carl, C. 2014. *Calculating Solar Photovoltaic Potential on Residential Rooftops in Kailua Kona, Hawaii.* Master's Thesis. University of Southern California. Available: https://spatial.usc.edu/wp-content/uploads/2014/03/CarlCarolineThesis.pdf [2015, July 18].

Carleer, A., Debeir, O. & Wolff, E. 2005. Assessment of very high spatial resolution satellite image segmentations. *Photogrammetric Engineering & Remote Sensing.* 71(11):1285-1294.

Chaudhari, M., Frantzis, L. & Hoff, T.E. 2004. PV grid connected market potential under a cost breakthrough scenario. *Navigant Consulting, Inc.Retrieved on September.* 16:2010.

Chauhan, S. 2016. *What is web API and why to use it?* Available: http://www.dotnettricks.com/learn/webapi/what-is-web-api-and-why-to-use-it- [12 Sep. 2016].

Cheng, L., Gong, J., Chen, X. & Han, P. 2008. Building boundary extraction from high resolution imagery and lidar data. *International Archives of the Photogrammetry, Remote Sensing and Spatial Information Sciences.* 37:693-698.

Childs, C. 2004. Interpolating surfaces in ArcGIS spatial analyst. *ArcUser, July-September.* :32-35.

City of Cape Town 2011. *Cape Town 2011: State of energy and energy futures report.* Available: https://www.capetown.gov.za/en/EnvironmentalResourceManagement/publications/Documents/State_of_Energy_+_Energy_Futures_Report_2011_revised_2012-01.pdf [2015, May 25].

City of Cape Town 2012. *Statistics for the City of Cape Town - 2012.* Available: https://www.capetown.gov.za/en/stats/Documents/City_Statistics_2012.pdf [2015, February 22].

City of Cape Town 2014. *State of Cape Town 2014.* Available: https://www.capetown.gov.za/en/stats/CityReports/Documents/SOCT%2014%20report%20complete.pdf [2015, June 17].

City of Cape Town 2015a. *Coct 2040 energy vision.* Available: http://www.savingelectricity.org.za/pdf/2040_energy_vision_cct_brochure.pdf [08/09/2017].

City of Cape Town 2015b. *Guidelines for embedded generation: Application process to become an embedded generator in the City of Cape Town.* Available: https://www.capetown.gov.za/en/electricity/Application%20Forms/CTGuidelinesforEmbeddedGeneration-V28-20-Jan-2015.pdf [2015, June 19].

City of Cape Town 2015c. *Utilities Services – Electricity Services: Consumptive Tariffs.* Available: https://www.capetown.gov.za/en/electricity/Elec%20tariffs%20201415/Schedule%20of%20Consumptive%20Tariffs.pdf [2015, June 20].

City of Cape Town 2017. *City of Cape Town Open Data Portal - Data Set Description.* Available: https://web1.capetown.gov.za/web1/opendataportal/DatasetDetail?DatasetName=Building%20footprints [May 16, 2017].

Congalton, R.G. & Green, K. 2009. *Assessing the accuracy of remotely sensed data: principles and practices.* 2nd ed. Boca Raton: Taylor & Francis Group.

Cord, M., Jordan, M. & Cocquerez, J. 2001. Accurate building structure recovery from high resolution aerial imagery. *Computer Vision and Image Understanding.* 82(2):138-173.

Curren, J., Makhele, L., Jakubowski, A., Goldblatt, M., Langiss, O., Basteck, T. & Schiffner, A. 2009. Regional Regulatory Action Plan for the Western Cape– November 2009. *Western Cape Department of Environmental Affairs and Development Planning and the German Technical Cooperation (GTZ), Cape Town, South Africa.*

De Vries, B.J., Van Vuuren, D.P. & Hoogwijk, M.M. 2007. Renewable energy sources: Their global potential for the first-half of the 21st century at a global level: An integrated approach. *Energy Policy.* 35(4):2590-2610.

DEADP 2010. *White paper on sustainable energy for the Western Cape Province.* Available: http://www.cityenergy.org.za/uploads/resource_186.pdf [2014, March 29].

DEADP 2013. *State of Environment Outlook Report for the Western Cape Province.* Available: http://eadp.westerncape.gov.za/sites/default/files/news/files/2013-05-30/state-of-environment-outlook-report-energy.pdf [2015, May 11].

Dean, J., Kandt, A., Burman, K., Lisell, L. & Helm, C.2009. Analysis of web-based solar photovoltaic mapping tools. *ASME 2009 3rd International Conference on Energy Sustainability Collocated with the Heat Transfer and InterPACK09 Conferences.* American Society of Mechanical Engineers. 85.

Definiens, A. 2007. Definiens developer 7 reference book. *Definiens AG, München.* :21-24.

Demir, N., Poli, D. and Baltsavias, E., 2008. Extraction of buildings and trees using images and LiDAR data. *The International Archives of the Photogrammetry, Remote Sensing and Spatial Information Sciences*, *37*(4), pp.313-318.

Dentlinger, L. 2017. *Load shedding could become a reality.* Available: http://ewn.co.za/2017/05/30/ngubane-load-shedding-could-become-a-reality [05/07/2017].

DongHyuk, L., KyoungMu, L. & SangUk, L. 2008. Fusion of LiDAR and Photogrammetric Imagery for Precise and Automatic Building Extraction. *□□□□□□□ □□ □□□.* :237-242.

Dubayar, R. & Rich, P.M. 1996. GIS-based solar radiation modeling. *GIS and Environmental Modeling: Progress and Research Issues.* :129.

eNCA 2015. *Power Watch.* Available: http://www.enca.com/coverage/power-outages-sa [2015, May 26].

EPIA 2011. *Solar Generation 6: Solar Photovoltaic Electricity Empowering the World.* Available: http://www.greenpeace.org/international/Global/international/publications/climate/2011/Final%20SolarGeneration%20VI%20full%20report%20lr.pdf [2014, September 23].

Eskom 2015a. *Koeberg power station.* Available: http://www.eskom.co.za/Whatweredoing/ElectricityGeneration/KoebergNuclearPowerStation/Pages/Koeberg_Power_Station.aspx [2015, May 11].

Eskom 2015b. *What is load shedding.* Available: http://loadshedding.eskom.co.za/LoadShedding/Description [2015, May 26].

Eskom 2017. *Medupi unit 4 synchronised to the national grid.* Available: http://www.eskom.co.za/news/Pages/Junn1.aspx [14/07/2017].

ESRI 2012a. *How Aspect works.* Available: http://resources.arcgis.com/en/help/main/10.1/index.html#//009z000000vp000000 [2015, May 26].

ESRI 2012b. *Modeling solar radiation.* Available: http://resources.arcgis.com/en/help/main/10.1/index.html#//009z000000t9000000 [2014, November 19].

ESRI 2013. *Creating raster DEMs and DSMs from large lidar point collections.* Available: http://resources.arcgis.com/en/help/main/10.1/index.html#//015w0000004q000000 [2015, March 10].

Euston-Brown, M., Cilliers, Z., Van Rensburg, L. & Ward, S. 2015. *Cape Town state of energy report 2015.* Cape Town: Integrated Strategic Communications, Branding and Marketing Department, City of Cape Town.

Fielding, R.T. 2000. Architectural Styles and the Design of Network-based Software Architectures. Doctoral. University of California, Irvine.

Foody, G.M. 2002. Status of land cover classification accuracy assessment. *Remote Sensing of Environment.* 80(1):185-201.

Fu, P. & Rich, P. 2000. The solar analyst 1.0 user manual. *Helios Environmental Modeling Institute.* 1616.

GeoSUN Africa 2014. *SA Solar Maps.* Available: http://geosun.co.za/downloads/sa-solar-maps/ [May 12, 2016].

Gonzalez, H., Halevy, A., Jensen, C.S., Langen, A., Madhavan, J., Shapley, R. and Shen, W., 2010, June. Google fusion tables: data management, integration and collaboration in the cloud. In *Proceedings of the 1st ACM symposium on Cloud computing* (pp. 175-180). ACM.

Google Developers 2016. *Fusion Tables REST API.* Available: https://developers.google.com/fusiontables/docs/v2/getting_started [Aug 19, 2017].

Google Maps 2017. *Map and Tile Coordinates.* Available: https://developers.google.com/maps/documentation/javascript/coordinates [Nov 06,2017].

Great Britain Dept. for BERR & DTI Sustainable Energy Programme 2006. *Photovoltaics in buildings: guide to the installation of PV systems .* 2nd ed. London: BERR.

Greif, J. 2000. *The European solar radiation atlas.* Presses des MINES.

He, Y., Zhang, C. & Fraser, C.S. 2014. An energy minimization approach to automated extraction of regular building footprints from airborne LiDAR data. *ISPRS Annals of Photogrammetry, Remote Sensing and Spatial Information Sciences.* 1:65-72.

Heipke, C., Mayer, H., Wiedemann, C. & Jamet, O. 1997. Evaluation of automatic road extraction. *International Archives of Photogrammetry and Remote Sensing.* 32(3 SECT 4W2):151-160.

Hill, J.M., Graham, L.A., Henry, R.J., Cotter, D. & Young, D. 2000. Wide-area topographic mapping and applications using airborne light detection and ranging (LIDAR) technology. *Photogrammetric Engineering and Remote Sensing.* 66(8):908-960.

Hockenos, P. 2014. *The social impact of Germany's energy transition.* Available: https://www.cleanenergywire.org/dossiers/social-impact-germanys-energy-transition [Sep 14, 2016].

Hofierka, J., Huld, T., Cebecauer, T. & Šúri, M. 2014. Open source solar radiation tools for environmental and renewable energy applications. *ENVIRONMENTAL SOFTWARE SYSTEMS.* :448.

Hofierka, J. & Kaňuk, J. 2009. Assessment of photovoltaic potential in urban areas using open-source solar radiation tools. *Renewable Energy.* 34(10):2206-2214.

Hofierka, J. and Suri, M., 2002, September. The solar radiation model for Open source GIS: implementation and applications. In *Proceedings of the Open source GIS-GRASS user's conference* (Vol. 2002, pp. 51-70).

Hoogwijk, M.M. 2004. On the global and regional potential of renewable energy sources. Ph.D. Thesis. Utrecht University. Available: https://dspace.library.uu.nl/handle/1874/782 [2015, May 12].

Hulsey, A. 2014. *South Africa: is the future more coal or renewables?* Available: https://sites.utexas.edu/mecc/2014/05/09/south-africa-is-the-future-more-coal-or-renewables/ [2014, July 16].

IEA 2008. *Energy technology perspectives: scenarios and strategy to 2050.* Available: http://www.iea.org/media/etp/etp2008.pdf [2014, April 5].

IEA 2012. *World energy outlook 2012.* Available: http://www.worldenergyoutlook.org/publications/weo-2012/ [2014, April 8].

Inglesi-Lotz, R. & Pouris, A. 2012. Energy efficiency in South Africa: A decomposition exercise. *Energy.* 42(1):113-120.

ISPRS 2018. *ISPRS Test Project on Urban Classification, 3D Building Reconstruction and Semantic Labeling.* Available: www2.isprs.org/commissions/comm3/wg4/tests.html [Jan 11, 2018].

Jabari, S. & Zhang, Y. 2013. Very high resolution satellite image classification using Fuzzy rule-based systems. *Algorithms.* 6(4):762-781.

Jakubiec, J.A. & Reinhart, C.F. 2012. Towards validated urban photovoltaic potential and solar radiation maps based on lidar measurements, GIS data, and hourly daysim simulations. *Proceedings of SimBuild, Madison, Wisconsin.* :1-10.

Jarząbek-Rychard, M. and Maas, H.G., 2017. *Geometric Refinement of ALS-Data Derived Building Models Using Monoscopic Aerial Images. Remote Sensing*, 9(3), p.282.

Jinmei, L. & Guoyu, W.2011. A refined quadtree-based automatic classification method for remote sensing image. *Computer Science and Network Technology (ICCSNT), 2011 International Conference on.* IEEE. 1703.

Jo, J.H. & Otanicar, T.P. 2011. A hierarchical methodology for the mesoscale assessment of building integrated roof solar energy systems. *Renewable Energy.* 36(11):2992-3000.

Johansson, H. 2011. Rich Web Map Applications-An assessment of performance, functionality and implementation of Rich Internet Application techniques in web-based GIS. Chalmers University of Technology.

Karnatak, H. 2012. *Concepts and applications of Web-GIS and Geo-Web services - technology and applications.* Available: https://nrsc.gov.in/sites/all/pdf/SPIE%20APRS%20Tutorial_Geowebservices_HCK.pdf [12 Sept, 2017].

Kim, K. & Shan, J. 2011. Building roof modeling from airborne laser scanning data based on level set approach. *ISPRS Journal of Photogrammetry and Remote Sensing.* 66(4):484-497.

Knier, G. 2002. *How do photovoltics work?* Available: http://science1.nasa.gov/science-news/science-at-nasa/2002/solarcells/ [2014, August 16].

Kodysh, J.B., Omitaomu, O.A., Bhaduri, B.L. & Neish, B.S. 2013. Methodology for estimating solar potential on multiple building rooftops for photovoltaic systems. *Sustainable Cities and Society.* 8:31-41.

Krupa, J. & Burch, S. 2011. A new energy future for South Africa: The political ecology of South African renewable energy. *Energy Policy.* 39(10):6254-6261.

Lafarge, F., Descombes, X., Zerubia, J. & Pierrot-Deseilligny, M. 2008. Automatic building extraction from DEMs using an object approach and application to the 3D-city modeling. *ISPRS Journal of Photogrammetry and Remote Sensing.* 63(3):365-381.

Lalwani, M., Kothari, D. & Singh, M. 2010. Investigation of solar photovoltaic simulation softwares. *International Journal of Applied Engineering Research.* 1(3):585-601.

Lawrence, R.L. & Wright, A. 2001. Rule-based classification systems using classification and regression tree (CART) analysis. *Photogrammetric Engineering and Remote Sensing.* 67(10):1137-1142.

Ledoux, H. & Gold, C. 2005. An efficient natural neighbour interpolation algorithm for geoscientific modelling. In *Developments in Spatial Data Handling.* Springer. 97-108.

Lee, D.H., Lee, K.M. & Lee, S.U. 2008. Fusion of lidar and imagery for reliable building extraction. *Photogrammetric Engineering & Remote Sensing.* 74(2):215-225.

Li, S., Dragićević, S. & Veenendaal, B. 2011. *Advances in web-based GIS, mapping services and applications.* 1st Edition ed. London: CRC Press/Balkema.

Li, S., Xiong, C. & Ou, Z. 2011. A Web GIS for sea ice information and an ice service archive. *Transactions in GIS.* 15(2):189-211.

Li, Y., Wu, H., An, R., Xu, H., He, Q. & Xu, J. 2013. An improved building boundary extraction algorithm based on fusion of optical imagery and LiDAR data. *Optik-International Journal for Light and Electron Optics.* 124(22):5357-5362.

Liu, X. 2008. Airborne LiDAR for DEM generation: some critical issues. *Progress in Physical Geography.* 32(1):31-49. DOI:10.1177/0309133308089496.

Luo, W., Taylor, M. & Parker, S. 2008. A comparison of spatial interpolation methods to estimate continuous wind speed surfaces using irregularly distributed data from England and Wales. *International Journal of Climatology.* 28(7):947-959.

Martín, A.M., Domínguez, J. and Amador, J., 2015. *Applying LIDAR datasets and GIS based model to evaluate solar potential over roofs: a review.* AIMS Energy, 3(3), pp.326-343.

Masó, J., Pomakis, K. & Julià, N. 2010. *Web Map Tile Service Implementation Standard.* (OGC 07-057r7). Wayland, Massachusetts: Open Geospatial Consortium Inc.

Matikainen, L., Hyyppä, J. & Hyyppä, H. 2003. Automatic detection of buildings from laser scanner data for map updating. *International Archives of Photogrammetry, Remote Sensing and Spatial Information Sciences.* 34(3/W13):218-224.

Mayer, H. 1999. Automatic object extraction from aerial imagery—a survey focusing on buildings. *Computer Vision and Image Understanding.* 74(2):138-149.

Miller, D. 2014. *The Web API business layer anti-pattern.* Available: http://bizcoder.com/the-web-api-business-layer-anti-pattern [Jun 16, 2017].

Mitchell, T. Ed. 2008. *Web mapping illustrated*. California: O'Reilly Media, Inc.

Mo, J. 2015. *Solar Roof Tiles - 4 Factors to Consider When Choosing Solar Roofing.* Available:

http://ensav.co.za/ceiling_insulation_solar_roof_tiles_4_factors_to_consider_when_choosing_solar_roofing_article.php [May 19, 2017].

Morgan, M. & Tempfli, K. 2000. Automatic building extraction from airborne laser scanning data. *International Archives of Photogrammetry and Remote Sensing.* 33(B3/2; PART 3):616-623.

Morris, C. & Pehnt, M. Eds. 2016. *Energy transition: The Germany energiewende*. Revised ed. Berlin: Heinrich Böll Foundation.

Muñoz Pujol, X. 2003. *Image segmentation integrating colour, texture and boundary information.* Universitat de Girona.

Myers, D.E. 1994. Spatial interpolation: an overview. *Geoderma.* 62(1):17-28.

NASA 2015. *NASA Surface meteorology and Solar Energy: Data Subset.* Available: https://eosweb.larc.nasa.gov/cgi-bin/sse/subset.cgi?email=skip@larc.nasa.gov [2015, March 14].

NERSA 2016. *Market Overview and Current Levels of Renewable Energy Deployment.* Available: http://www.energy.gov.za/files/renewable-energy-status-report/Market-Overview-and-Current-Levels-of-Renewable-Energy-Deployment-NERSA.pdf [Jun 12, 2017].

Nguyen, H., Pearce, J., Harrap, R. & Barber, G. 2012. The application of LiDAR to assessment of rooftop solar photovoltaic deployment potential in a municipal district unit. *Sensors.* 12(4):4534-4558.

Nguyen, H. & Pearce, J.M. 2010. Estimating potential photovoltaic yield with r. sun and the open source geographical resources analysis support system. *Solar Energy.* 84(5):831-843.

Nield, D.. 2016. *95% of Germany's Energy was Provided by Renewables Last Sunday* [If Germany can do it, so can everyone]. Available: http://www.sciencealert.com/last-sunday-95-percent-of-germany-s-energy-was-provided-by-renewables [23rd May, 2017].

NRCAN 2015. *Table Joining Service (TJS).* Available: http://www.nrcan.gc.ca/earth-sciences/geomatics/canadas-spatial-data-infrastructure/standards-policies/8930 [June 19, 2017].

O'Callaghan, J.. 2015. *Solar Impluse 2 safely lands in Hawaii after completing daring five-day flight across the Pacific Ocean* Available: http://www.dailymail.co.uk/sciencetech/article-3148669/Success-Solar-Impulse-2-safely-lands-Hawaii-completing-daring-five-day-flight-Pacific-Ocean.htm [2015, July 8].

OGC 2017. *FAQs - OGC's Purpose and Structure.* Available: http://www.opengeospatial.org/ogc/faq#2 [Feb 12, 2017].

Ordóñez, J., Jadraque, E., Alegre, J. & Martínez, G. 2010. Analysis of the photovoltaic solar energy capacity of residential rooftops in Andalusia (Spain). *Renewable and Sustainable Energy Reviews.* 14(7):2122-2130.

O'Rourke, C. 2004. A Look at Rich Internet Applications: Lookinq at technoloqies for going beyond the aging HTML standard. *Oracle Magazine.* 18(4):59-60.

Page, J., Albuisson, M. & Wald, L. 2001. The European solar radiation atlas: a valuable digital tool. *Solar Energy.* 71(1):81-83.

Pegels, A. 2010. Renewable energy in South Africa: Potentials, barriers and options for support. *Energy Policy.* 38(9):4945-4954.

Peng, J. & Liu, Y. 2005. Model and context-driven building extraction in dense urban aerial images. *International Journal of Remote Sensing.* 26(7):1289-1307.

Perez, R., Seals, R., Ineichen, P., Stewart, R. & Menicucci, D. 1987. A new simplified version of the Perez diffuse irradiance model for tilted surfaces. *Solar Energy.* 39(3):221-231.

Quinn, S. & Dutton, J. 2017. *The history and importance of web mapping.* Available: https://www.e-education.psu.edu/geog585/node/643 [Aug 17, 2017].

Ramachandra, T. & Shruthi, B. 2007. Spatial mapping of renewable energy potential. *Renewable and Sustainable Energy Reviews.* 11(7):1460-1480.

Ramirez, J.R. 2006. A new approach to relief representation. *Surveying and Land Information Science.* 66(1):19-25.

Ramírez-Rosado, I.J., García-Garrido, E., Fernández-Jiménez, L.A., Zorzano-Santamaría, P.J., Monteiro, C. & Miranda, V. 2008. Promotion of new wind farms based on a decision support system. *Renewable Energy.* 33(4):558-566.

REN21 2013. *Renewables 2013: Global Status Report.* Available: http://www.ren21.net/Portals/0/documents/Resources/GSR/2013/GSR2013_lowres.pdf [2014, October 11].

REN21.2017 2017. *Renewables 2017 Global Status Report.* Paris: REN21 Secretariat.

Resch, B., Sagl, G., Törnros, T., Bachmaier, A., Eggers, J.B., Herkel, S., Narmsara, S. and Gündra, H., 2014. *GIS-based planning and modeling for renewable energy: Challenges and future research avenues. ISPRS International Journal of Geo-Information, 3(2), pp.662-692*.

Rialhe, A.1996. Epure project: Economical potential use of renewable energy. *Renewable Energy Development European Conference and APAS-RENA Contractors Meeting.* EDIFIR, Florence.

Rigollier, C., Bauer, O. & Wald, L. 2000. On the clear sky model of the ESRA—European Solar Radiation Atlas—with respect to the Heliosat method. *Solar Energy.* 68(1):33-48.

Roofing Calculator 2015. *Roof pitch calculator.* Available: http://www.roofcalc.org/roof-pitch-calculator/ [2015, April 22].

Rottensteiner, F., Sohn, G., Gerke, M., Wegner, J.D., Breitkopf, U. & Jung, J. 2014. Results of the ISPRS benchmark on urban object detection and 3D building reconstruction. *ISPRS Journal of Photogrammetry and Remote Sensing.* 93:256-271.

Rottensteiner, F., Trinder, J., Clode, S. & Kubik, K. 2004. Fusing airborne laser scanner data and aerial imagery for the automatic extraction of buildings in

densely built-up areas. *International Archives of Photogrammetry and Remote Sensing.* 35(B3):512-517.

Rottensteiner, F., Trinder, J., Clode, S. & Kubik, K. 2005. Using the Dempster–Shafer method for the fusion of LIDAR data and multi-spectral images for building detection. *Information Fusion.* 6(4):283-300.

Ruiz-Arias, J., Tovar-Pescador, J., Pozo-Vázquez, D. & Alsamamra, H. 2009. A comparative analysis of DEM-based models to estimate the solar radiation in mountainous terrain. *International Journal of Geographical Information Science.* 23(8):1049-1076.

Rutzinger, M., Rottensteiner, F. & Pfeifer, N. 2009. A comparison of evaluation techniques for building extraction from airborne laser scanning. *IEEE Journal of Selected Topics in Applied Earth Observations and Remote Sensing.* 2(1):11-20.

Sadeghi, M. and Karimi, M., 2017. *GIS-BASED SOLAR AND WIND TURBINE SITE SELECTION USING MULTI-CRITERIA ANALYSIS: CASE STUDY TEHRAN, IRAN. ISPRS-International Archives of the Photogrammetry, Remote Sensing and Spatial Information Sciences, pp.469-476.*

SA DME 1998. *White Paper on the Energy Policy of the Republic of South Africa.* Available: http://www.energy.gov.za/files/policies/whitepaper_energypolicy_1998.pdf [2014, April 20].

SA DME 2003. *White Paper on Renewable Energy.* Available: http://www.energy.gov.za/files/policies/whitepaper_renewables_2003.pdf [2014, May 11].

SA DNT 2010. *Reducing greenhouse gas emissions: The carbon tax option.* Available: http://www.treasury.gov.za/public%20comments/Discussion%20Paper%20Carbon%20Taxes%2081210.pdf [2014, May 21].

SA DoE 2010. *Integrated Resource Plan 2010.* Available: http://www.doe-irp.co.za/content/INTEGRATED_RESOURCE_PLAN_ELECTRICITY_2010_v8.pdf [2014, April 28].

SA GCIS 2012. *South Africa year book 2011/12: Energy.* Available: http://www.gcis.gov.za/sites/www.gcis.gov.za/files/docs/resourcecentre/yearbook/2011/13_Energy.pdf [2014, March 13].

SA GCIS 2013. *South Africa year book 2012/13: Energy.* Available: http://www.gcis.gov.za/sites/www.gcis.gov.za/files/docs/resourcecentre/yearbook/2012/08%20Energy%20.pdf [2014, October 11].

Sampath, A. & Shan, J. 2004. Urban modelling based on segmentation and regularization of airborne LIDAR point clouds, *Proc. ISPRS 20th Congress. Comm. III*, pp. 937-941.

Schut, P. 2010. *Georeferenced Table Joining Service (TJS).* (OGC 10-070r2). Wayland, Massachusetts: Open Geospatial Consortium Inc.

Sebitosi, A. & Pillay, P. 2008. Renewable energy and the environment in South Africa: A way forward. *Energy Policy.* 36(9):3312-3316.

Shankleman, J. 2017. *Germany Achieves Milestone – Renewables Supply Nearly 100 Percent Energy for a Day.* Available: http://www.renewableenergyworld.com/articles/2016/05/germany-achieves-milestone-renewables-supply-nearly-100-percent-energy-for-a-day.html [23 May 2017].

Shankleman, J. & Martin, C. 2017. *Solar Could Beat Coal to Become the Cheapest Power on Earth.* Available: https://www.bloomberg.com/news/articles/2017-01-03/for-cheapest-power-on-earth-look-skyward-as-coal-falls-to-solar [May, 2017].

Sibson, R.1980. A vector identity for the Dirichlet tessellation. *Mathematical Proceedings of the Cambridge Philosophical Society.* Cambridge Univ Press. 151.

Simao, A., Densham, P.J. & Haklay, M.M. 2009. Web-based GIS for collaborative planning and public participation: An application to the strategic planning of wind farm sites. *Journal of Environmental Management.* 90(6):2027-2040.

Sithole, G. & Vosselman, G. 2004. Experimental comparison of filter algorithms for bare-Earth extraction from airborne laser scanning point clouds. *ISPRS Journal of Photogrammetry and Remote Sensing.* 59(1):85-101.

SoDa 2004. *Solar energy services for professionals.* Available: http://www.soda-is.com/eng/services/climat_free_eng.php#c5 [2015, January 25].

Sohn, G. & Dowman, I. 2007. Data fusion of high-resolution satellite imagery and LiDAR data for automatic building extraction. *ISPRS Journal of Photogrammetry and Remote Sensing.* 62(1):43-63.

Solangi, K., Islam, M., Saidur, R., Rahim, N. & Fayaz, H. 2011. A review on global solar energy policy. *Renewable and Sustainable Energy Reviews.* 15(4):2149-2163.

Song, W. & Haithcoat, T.L. 2005. Development of comprehensive accuracy assessment indexes for building footprint extraction. *IEEE Transactions on Geoscience and Remote Sensing.* 43(2):402-404.

Sorensen, B. 2000. Renewable Energy: Its Physics, Engineering, Use, Environmental Impact. *Economics, and Planning Aspects.San Diego: Academic Press.*

Sørensen, B. & Meibom, P. 1999. GIS tools for renewable energy modelling. *Renewable Energy.* 16(1):1262-1267.

Steyn, L. 2017. *Going Green: Cape Town named as top 5 global leader for climate disclosure.* Available: http://www.traveller24.com/Explore/Green/going-green-cape-town-named-as-top-5-global-leader-for-climate-disclosure-20170327 [2017-03-27].

Šúri, M. and Cebecauer, T., 2010. SolarGIS: New web-based service offering solar radiation data and PV simulation tools for Europe, North Africa and Middle East. In *Proceedings of the International Conference on Solar Heating, Cooling and Buildings EUROSUN* (Vol. 28).

Suri, M., Cebecauer, T., Skoczek, A. & Betak, J.2012. Solar electricity production from fixed-inclined and sun-tracking C-Si photovoltaic modules in South Africa. South African Solar Energy Conference (SASEC). Stellenbosch, South Africa, Available from: http://www. sasec. org. za/ [Accessed 23/10/2013].

Šúri, M. & Hofierka, J. 2004. A new GIS-based solar radiation model and its application to photovoltaic assessments. *Transactions in GIS.* 8(2):175-190.

Šúri, M., Huld, T.A. & Dunlop, E.D. 2005. PV-GIS: a web-based solar radiation database for the calculation of PV potential in Europe. *International Journal of Sustainable Energy.* 24(2):55-67.

Timilsina, G.R., Kurdgelashvili, L. & Narbel, P.A. 2012. Solar energy: Markets, economics and policies. *Renewable and Sustainable Energy Reviews.* 16(1):449-465.

Tobias, O.J. & Seara, R. 2002. Image segmentation by histogram thresholding using fuzzy sets. *Image Processing, IEEE Transactions on.* 11(12):1457-1465.

Tomljenovic, I., Tiede, D. and Blaschke, T., 2016. *A building extraction approach for Airborne Laser Scanner data utilizing the Object Based Image Analysis paradigm. International Journal of Applied Earth Observation and Geoinformation, 52, pp.137-148.*

Tooke, T.R. 2013. *Opportunities for Mapping Rooftop Solar Energy using LiDAR: An Introduction for BC Local Governments.* Available: http://www2.gov.bc.ca/assets/gov/environment/climate-change/stakeholder-support/ceei/resources/lg_cas-lidar-solar-report.pdf [2015, February 15].

Trimble 2010. *Data GuidedTour3: Advanced Buidling Extraction.* Available: http://www.ecognition.com/document/data-guidedtour3advanced-buidling-extraction [2014, June 17].

Trollip, H., Ward, S. & Walsh, V. 2011. *Moving mountains : Cape Town's action plan for energy and climate change.* First edition ed. Cape Town: Environmental Resource Management Department, City of Cape Town.

Tymvios, F., Jacovides, C., Michaelides, S. & Scouteli, C. 2005. Comparative study of Ångström's and artificial neural networks' methodologies in estimating global solar radiation. *Solar Energy.* 78(6):752-762.

UN Department of Economic and Social Affairs 2013. *World economic and social survey 2013: Sustainable development challenges.* United Nations.

UN General Assembly 2015. *Transforming our world: The 2030 agenda for sustainable development.* New York: A/RES/70/1, 21 October.

UNDP 2016. *UNDP Support to the Implementation of the Sustainable Development Goals.* Available: http://www.undp.org/content/undp/en/home/librarypage/sustainable-development-goals/undp-support-to-the-implementation-of-the-2030-agenda.html [Sep 13, 2017].

UNFCCC 1998. *Kyoto protocol to the United Nations Framework Convention on Climate Change.* Available: http://unfccc.int/resource/docs/convkp/kpeng.pdf [2014, April 20].

UNHABITAT 2014. *The State of Africa Cities 2014: Re-imagining sustainable urban transitions.* Available: http://unhabitat.org/books/state-of-african-cities-2014-re-imagining-sustainable-urban-transitions/ [2015, March 13].

US EIA 2014a. *Solar Explained.* Available: http://www.eia.gov/energyexplained/index.cfm?page=solar_home [2014, December 03].

US EIA 2014b. *South Africa.* Available: www.eia.gov/beta/international/analysis.cfm?iso=ZAF [2014, August 4].

Uzar, M. & Yastikli, N. 2013. Automatic building extraction using LiDAR and aerial photographs. *Boletim De Ciencias Geodesicas.* 19(2):153-171.

Voivontas, D., Assimacopoulos, D., Mourelatos, A. & Corominas, J. 1998. Evaluation of renewable energy potential using a GIS decision support system. *Renewable Energy.* 13(3):333-344.

Vu, T.T., Yamazaki, F. & Matsuoka, M. 2009. Multi-scale solution for building extraction from LiDAR and image data. *International Journal of Applied Earth Observation and Geoinformation.* 11(4):281-289.

Wagner, J. 2015. *Top 10 most mapping APIs.* Available: https://www.programmableweb.com/news/top-10-mapping-apis-google-maps-microsoft-bing-maps-and-mapquest/analysis/2015/02/23 [12 Sept. 2017].

Wang, O., Lodha, S.K. & Helmbold, D.P.2006. A bayesian approach to building footprint extraction from aerial lidar data. *3D Data Processing, Visualization, and Transmission, Third International Symposium on.* IEEE. 192.

WEF 2017. *The world's 10 biggest economies in 2017.* Available: https://www.weforum.org/agenda/2017/03/worlds-biggest-economies-in-2017/ [Sep 10, 2017].

Western Cape Government 2015. *City of Cape Town's energy efficiency drive.* Available: https://www.westerncape.gov.za/110green/news/city-cape-towns-energy-efficiency-drive [04/09/2017].

Wiginton, L., Nguyen, H. & Pearce, J.M. 2010. Quantifying rooftop solar photovoltaic potential for regional renewable energy policy. *Computers, Environment and Urban Systems.* 34(4):345-357. DOI:10.1016/j.compenvurbsys.2010.01.001.

Wilson, J. & Gallant, J. 1998. SRAD: a program for estimating radiation and temperature in complex terrain. (Unpublished).

Yuan, J., 2016. *Automatic building extraction in aerial scenes using convolutional networks. arXiv preprint arXiv:1602.06564.*

Yunfei, B., Guoping, L., Chunxiang, C., Xiaowen, L., Hao, Z., Qisheng, H., Linyan, B. & Chaoyi, C. 2008. Classification of LIDAR point cloud and generation of DTM from LIDAR height and intensity data in forested area. *The International Archives of the Photogrammetry, Remote Sensing and Spatial Information Sciences.* 37(7):313-318.

Zhan, Q., Molenaar, M., Tempfli, K. & Shi, W. 2005. Quality assessment for geo-spatial objects derived from remotely sensed data. *International Journal of Remote Sensing.* 26(14):2953-2974.

Zhang, K., Chen, S., Whitman, D., Shyu, M., Yan, J. & Zhang, C. 2003. A progressive morphological filter for removing nonground measurements from airborne LIDAR data. *Geoscience and Remote Sensing, IEEE Transactions on.* 41(4):872-882.

Zhang, K., Yan, J. & Chen, S. 2006. Automatic construction of building footprints from airborne LIDAR data. *Geoscience and Remote Sensing, IEEE Transactions on.* 44(9):2523-2533.

Zuo, X., Chen, L. & Zhang, Y. 2014. A Region Segmentation Algorithm for Remote Sensing Imaging Combined with Multi-feature and Multi-band. *Journal of Computers.* 9(7):1731-1737.

APPENDICES

Appendix 1: Python algorithm to generate nDSM, slope and aspect

```
import arcpy # Import arcpy module

# Local variables:

Input_Raw_LiDAR = " "

Normalized_Las = " "

Output_Coordinate_System = "PROJCS['WGS_1984_Transverse_Mercator',GEOGCS['GCS_WGS_1984',DATUM['D_WGS_1984',SPHEROID['WGS_1984',6378137.0,298.257223563]],PRIMEM['Greenwich',0.0],UNIT['Degree',0.0174532925199433]],PROJECTION['Transverse_Mercator'],PARAMETER['false_easting',0.0],PARAMETER['false_northing',0.0],PARAMETER['central_meridian',19.0],PARAMETER['scale_factor',1.0],PARAMETER['latitude_of_origin',0.0],UNIT['Meter',1.0]]"

LasDataset_lasd = " "

nDSM_init = " "

Slope_Raster_init = " "

Aspect_Raster_int = " "

nDSM = " "

Slope_Raster = " "

Aspect_Raster = " "

# Process: Las_Height

arcpy.gp.Model12(Input_Raw_LiDAR, Normalized_Las)

# Process: Create LAS Dataset
```

```
arcpy.CreateLasDataset_management(Normalized_Las, LasDataset_lasd, "NO_RECURSION", Output_Coordinate_System, "NO_COMPUTE_STATS", "ABSOLUTE_PATHS", "NO_FILES")

# Process: LAS Dataset to Raster

tempEnvironment0 = arcpy.env.outputCoordinateSystem

arcpy.env.outputCoordinateSystem = Output Coordinate System

arcpy.LasDatasetToRaster_conversion(LasDataset_lasd, nDSM_init, "ELEVATION", "BINNING MAXIMUM NATURAL_NEIGHBOR", "FLOAT", "CELLSIZE", "0.08", "1")

arcpy.env.outputCoordinateSystem = tempEnvironment0

# Process: Copy Raster

arcpy.CopyRaster_management(nDSM_init, nDSM, "", "", "0", "NONE", "NONE", "", "NONE", "NONE", "", "NONE")

# Process: Slope

tempEnvironment0 = arcpy.env.outputCoordinateSystem

arcpy.env.outputCoordinateSystem = ""

tempEnvironment1 = arcpy.env.nodata

arcpy.env.nodata = "NONE"

arcpy.gp.Slope_sa(nDSM_init, Slope_Raster_init, "DEGREE", "1")

arcpy.env.outputCoordinateSystem = tempEnvironment0

arcpy.env.nodata = tempEnvironment1

# Process: Copy Raster (2)

arcpy.CopyRaster_management(Slope_Raster_init, Slope_Raster, "", "", "0", "NONE", "NONE", "", "NONE", "NONE", "", "NONE")

# Process: Aspect
```

```
tempEnvironment0 = arcpy.env.outputCoordinateSystem

arcpy.env.outputCoordinateSystem = ""

tempEnvironment1 = arcpy.env.nodata

arcpy.env.nodata = "NONE"

arcpy.gp.Aspect_sa(nDSM_init, Aspect_Raster_int)

arcpy.env.outputCoordinateSystem = tempEnvironment0

arcpy.env.nodata = tempEnvironment1

# Process: Copy Raster (3)

arcpy.CopyRaster_management(Aspect_Raster_int, Aspect_Raster, "", "", "0", "NONE", "NONE", "", "NONE", "NONE", "", "NONE")
```

Appendix 2: Python algorithm to calculate mean annual radiation

```
#! /usr/bin/python2.7

import os

import sys

import subprocess

import arcpy

# Local variables:

Input_Files = "D:\Adedayo\Raw Data\LiDAR Tiles_2015\grid_1162.las"

Output_LAS_Dataset = "D:\Adedayo\Analysis\Solar_Radiation\DSM_60cm\lasdataset\grid_1162.lasd"

Output_Raster = "D:\Adedayo\Analysis\Solar_Radiation\DSM_60cm\grid_1162"

Output_Coordinate_System = "PROJCS['WGS_1984_Transverse_Mercator',GEOGCS['GCS_WGS_1984',DATUM['D_WGS_1984',SPHEROID['WGS_1984',6378137.0,298.257223563]],PRIMEM['Greenwich',0.0],UNIT['Degree',0.0174532925199433]],PROJECTION['Transverse_Mercator'],PARAMETER['false_easting',0.0],PARAMETER['false_northing',0.0],PARAMETER['central_meridian',19.0],PARAMETER['scale_factor',1.0],PARAMETER['latitude_of_origin',0.0],UNIT['Meter',1.0]]"

NoData = "0"

# Process: Create LAS Dataset

arcpy.CreateLasDataset_management(Input_Files, Output_LAS_Dataset, "NO_RECURSION", "", Output_Coordinate_System, "NO_COMPUTE_STATS", "ABSOLUTE_PATHS", "NO_FILES")

# Process: LAS Dataset to Raster

tempEnvironment0 = arcpy.env.outputCoordinateSystem
```

```
arcpy.env.outputCoordinateSystem = Output_Coordinate_System

tempEnvironment1 = arcpy.env.nodata

arcpy.env.nodata = NoData

arcpy.LasDatasetToRaster_conversion(Output_LAS_Dataset, Output_Raster, "ELEVATION", "BINNING MAXIMUM NATURAL_NEIGHBOR", "FLOAT", "CELLSIZE", "0.6", "1")

arcpy.env.outputCoordinateSystem = tempEnvironment0

arcpy.env.nodata = tempEnvironment1

# The script is used loop the r.sun process in GRASS environment for 365 days and get the

# average using r.series to get the mean annual solar radiation

gisdbss = os.path.join("D:\Adedayo\Analysis\Solar_Radiation")

location = "Radiation_Estimation"

mapset = "grid_33"

grass7bin = r"C:\Program Files\GRASS GIS 7.1.svn\grass71svn.bat"

startcmd = [grass7bin, '--config', 'path']

try:

    p = subprocess.Popen(startcmd, shell=False,

                         stdout=subprocess.PIPE, stderr=subprocess.PIPE)

    out, err = p.communicate()

except OSError as error:

    sys.exit("ERROR: Cannot find GRASS GIS start script"

             " {cmd}: {error}".format(cmd=startcmd[0], error=error))

if p.returncode != 0:
```

```
    sys.exit("ERROR: Issues running GRASS GIS start script"
             " {cmd}: {error}"
            .format(cmd=' '.join(startcmd), error=err))
gisdb = out.strip(os.linesep)
os.environ['GISBASE'] = gisdb
g_pydr = os.path.join(gisdb, "etc", "python")
sys.path.append(g_pydr)
import grass.script as grass
import grass.script.setup as grsetup
rcfile = grsetup.init(gisdb, gisdbss, location, mapset)
# use grass functions here
# Import DSM raster into grassgis
grass.run_command("g.mapset", flags = "c", mapset = "grid_1162a", location = "Radiation_Estimation", dbase = gisdb)
arcpyDSM = "D:\Adedayo\Analysis\Solar_Radiation\DSM_60cm\grid_1162\w001001.adf"
grass.run_command("r.in.gdal", flags = "o", input = arcpyDSM, output="grid_1162", overwrite = True)
#Set computation region
grass.run_command("g.region", raster = "grid_1162@grid_1162a")
# calculate Slope and Aspect Map
slopemap = "SlopeMap"
aspectmap = "AspectMap"
```

```
grass.run_command("r.slope.aspect", elevation = "grid_1162@grid_1162a", slope = slopemap, aspect = aspectmap, overwrite = True)

# Calculate the Horizon to model for shading

grass.run_command("r.horizon", elevation = "grid_1162@grid_1162a", step = 30, bufferzone = 0, maxdistance = 2000, output = "horangle", overwrite = True)

# calculate Lon and Lat

latmap = "LatMap"

longmap = "LongMap"

grass.run_command("r.latlong", input = "grid_1162@grid_1162a", output = latmap, overwrite = True)

grass.run_command("r.latlong", flags = "l", input = "grid_1162@grid_1162a", output = longmap, overwrite = True)

# To calculate Global Solar Radiation"

# specify the range for calculation

doy = range(1, 366)

for i in doy:

        solarRad = "DailyRad_DOY" + str(i)

        # running the global solar radiation model in mode 2

        grass.run_command("r.sun",

                                        flags = "p",

                                        elevation = "grid_1162@grid_1162a",

                                        aspect = "AspectMap",

                                        slope = "SlopeMap",

                                        linke_value = 3.2,
```

```
                                albedo_value = 0.18,

                                lat = "LatMap",

                                long = "LongMap",

                                horizon_basename = "horangle",

                                horizon_step = 30, step = 0.5,

                                glob_rad = solarRad, overwrite = True, day = i)

# Calculating the Mean Annual Global Radiation

year_ave = "MeanAnnual_Rad"

grass.run_command("g.list", flags ="r", type = "raster", pattern ="^Daily", mapset = "grid_1162a", separator = "comma", output = "maplist.txt", overwrite = True)

f = open("maplist.txt", "r")

lst = []

for line in f.readlines():

        lst.append(line.replace("\n", "").split(","))

        grass.run_command("r.series", input = lst, output = year_ave, method = "average", overwrite = True)

f.close()

# export the outputs to Erdas Imagine file format

grass.run_command("r.out.gdal", flags = "c", input = year_ave, output = (year_ave + str (".img")), format = "HFA", type = "Float64", nodata = "0", overwrite = True)

os.remove(rcfile)
```

Appendix 3: Weather data report sample

HOURLY REPORT: Available Data Shown

Comp#	Station Name	Latitude	Longitude	Altitude
30689	VERGELEGEN BO	-34.08989	18.90774	271

Compno	Year	Month	Day	Hour	Rs
30689	2012	1	1	1	0.01053114
30689	2012	1	1	2	0.03588388
30689	2012	1	1	3	0.05031544
30689	2012	1	1	4	0.06318684
30689	2012	1	1	5	0.05870135
30689	2012	1	1	6	1.998771
30689	2012	1	1	7	37.95171
30689	2012	1	1	8	135.8073
30689	2012	1	1	9	337.9156
30689	2012	1	1	10	677.7844
30689	2012	1	1	11	810.8382
30689	2012	1	1	12	905.8948
30689	2012	1	1	13	950.1524
30689	2012	1	1	14	956.5551
30689	2012	1	1	15	720.7613
30689	2012	1	1	16	667.5225
30689	2012	1	1	17	301.2333
30689	2012	1	1	18	209.5305
30689	2012	1	1	19	98.24911
30689	2012	1	1	20	9.267593
30689	2012	1	1	21	0.04446482
30689	2012	1	1	22	0.02047722
30689	2012	1	1	23	0.01969713
30689	2012	1	1	24	0.0175519
30689	2012	1	1	**Average**	284.24
30689	2012	1	1	**Total**	6,821.78
30689	2012	1	1	**Highest**	956.56
30689	2012	1	1	**Lowest**	0.01

ELEMENT	DESCRIPTION	UNIT	STATION TYPE
Rs	Average Hourly Radiation	Watts	AWS

Appendix 4: HTML document script

```
<!DOCTYPE html>

<html>

<head>

<meta name="viewport" content="initial-scale=1.0, user-scalable=no">

<meta charset="utf-8">

<title>Solar PV Potential</title>

<style>html, body {width: 100%;height: 100%;margin: 0;padding: 0;}</style>

<style>#map {position:absolute;top:0;bottom:0;right:0;left:0; z-index: 0;}</style>

<style type="text/css">

#checkboxes {position: absolute;right: 10px;top: 90px;font-family: Roboto;font-size: 11px;font-weight: bold;background-color: #fff;padding: 10px 10px;}

#checkboxes, label {display: block; margin-bottom: 5px; margin-top: 5px;}

#legend {position: absolute; right: 10px;bottom: 100px;background-color: #fff;margin: 10px;padding: 5px;font-size: 12px;font-family: Roboto;}

.color {height: 12px;width: 12px;margin-right: 3px;float: left;border: 1.8px solid;}

.red {background-color: #FF0000;}

.yellow {background-color: #FFFF00;}

.blue {background-color: #0000FF;}

.cyan {background-color: #00FFFF;}

.white {background: #FFFFFF;}

#visualization {position: relative; float: left; background-color: #FFFFFF;}

#description {font-family: Roboto;font-size: 15px;font-weight: 300;}
```

```
#infowindow-content.title {font-weight: bold;}

#infowindow-content {display: none;}

#map #infowindow-content {display: inline;}

.pac-card {margin: 10px 10px 0 0;border-radius: 2px 0 0 2px;box-sizing: border-box;-moz-box-sizing: border-box;outline: none;box-shadow: 0 2px 6px rgba(0, 0, 0, 0.3);background-color: #fff;font-family: Roboto;}

#pac-container {padding-bottom: 12px;margin-right: 12px;}

.pac-controls {display: inline-block;padding: 5px 11px;}

.pac-controls label {font-family: Roboto;font-size: 13px;font-weight: 300;}

#pac-input {background-color: #fff;font-family: Roboto;font-size: 15px;font-weight: 300;margin-left: 20px;padding: 0 20px 0 25px;text-overflow: ellipsis;   width: 150px;position: relative;top: 100px;left: 10px;}

#pac-input:focus {border-color: #4d90fe;}

#title {color: #fff;background-color: #4d90fe;font-size: 25px;font-weight: 500;padding: 6px 12px;}

#target {width: 150px;}

#query-tool {position: absolute; left: 10px; top: 30px;background-color: #fff;margin: 10px;padding: 5px;font-size: 12px;font-family: Roboto; text-overflow: ellipsis;}

#query-tool, label {display: block; margin-bottom: 5px; margin-top: 5px;}

</style>

<script type="text/javascript" src="https://www.google.com/jsapi"></script>

<script
src="https://ajax.googleapis.com/ajax/libs/jquery/3.2.1/jquery.min.js"></script>

<link rel="stylesheet"
href="https://ajax.googleapis.com/ajax/libs/jqueryui/1.12.1/themes/base/jquery-ui.css"/>
```

```
<script src="https://ajax.googleapis.com/ajax/libs/jqueryui/1.12.1/jquery-ui.min.js"></script>

</head>

<body>

<input id="pac-input" class="controls" type="text" placeholder="Search Address">

<div id="map"></div>

<div id="checkboxes">

<input type="checkbox" id="layer1" onclick="toggle(1);"/>Roof Outlines <br />

<input type="checkbox" id="layer3" onclick="toggle(7);"/>Roof Planes (FT)

<label for="north">Display by Aspect </label>

<input type="checkbox" id="north" onclick="toggle(2);"/>North <br />

<input type="checkbox" id="east" onclick="toggle(3);"/>East<br />

<input type="checkbox" id="south" onclick="toggle(4);"/>South<br />

<input type="checkbox" id="west" onclick="toggle(5);"/>West<br />

<input type="checkbox" id="flat" onclick="toggle(6);"/>Flat Roof

<label for="dropdown">Filter by Optimality </label>

<select id="dropdown">

<option>None</option>

<option> < 50% </option>

<option> > 50% </option>

</select>

</div>

<div id="query-tool" >
```

```
<h3>Query Tool</h3>

<fieldset>

<label for="erfsearch">Street Address  </label>

<input type="text" id="addsearch" class="controls" placeholder="Type Address Here">

<button id="search">Search </button>

<form id="qt">

<label for="rpl">Select Roof Planes </label>

<input type="checkbox" name="boxN" onclick="check();" id="rpl-north"/>North

<input type="checkbox" name="boxE" id="rpl-east" />East

<input type="checkbox" name="boxS" id="rpl-south"/>South

<input type="checkbox" name="boxW" id="rpl-west" />West

<input type="checkbox" name="boxF" id="rpl-flat" />Flat

<label for="optm">Optimal Percentage (Building) </label>

<input type="textbox" id="optm"/> %

<label for="optm">Percentage Contribution (Roof Plane) </label>

<input type="textbox" id="contr"/> %

<label for="spanel">Select Panel Type </label>

<input type="radio" name="spanel" id="panel1" value="0.15" />Polycrystalline (15%)

<input type="radio" name="spanel" id="panel2" value="0.17" />Monocrystalline (17%)

<label for="cal">Calculate PV Pontential </label>

</form>
```

<input type="textbox" id="output2" placeholder="Per roof plane"/> kWh/day (Roof Plane)

<input type="textbox" id="output" placeholder="Per building"/> kWh/day (Building)

<button id="querybut">Submit Query</button>

</fieldset>

<script>

var map;

var layers = [];

var infoWindow;

var arry = [];

var arry1 = [];

function initMap() {

var tableid = '1p0ZlD3SvenBwyAF2xWrgo7SNairtFUXVVcuEee_g'

var map_options = {

zoom: 10,

center: {lat: -33.8637733598, lng: 18.5129762863},

mapTypeControl: true,

mapTypeControlOptions: {

style: google.maps.MapTypeControlStyle.HORIZONTAL_BAR,

position: google.maps.ControlPosition.RIGHT_TOP},

scaleControl: true,

```
};
map = new google.maps.Map(document.getElementById('map'), map_options);
var strictBounds = new google.maps.LatLngBounds(
new google.maps.LatLng(-34.404441, 18.348296),
new google.maps.LatLng(-33.376207, 18.990996)
);
map.fitBounds(strictBounds);
// Create the search box and link it to the UI element.
var input = document.getElementById('pac-input');
var searchBox = new google.maps.places.SearchBox(input);
map.controls[google.maps.ControlPosition.LEFT_TOP].push(input);
// Bias the SearchBox results towards current map's viewport.
map.addListener('bounds_changed', function() {
searchBox.setBounds(strictBounds);
});
var markers = [];
// Listen for the event fired when the user selects a prediction and retrieve
// more details for that place.
searchBox.addListener('places_changed', function() {
var places = searchBox.getPlaces();
if (places.length == 0) {
return;
}
```

```
// Clear out the old markers.
markers.forEach(function(marker) {
marker.setMap(null);
});
markers = [];
// For each place, get the icon, name and location.
var bounds = new google.maps.LatLngBounds();
places.forEach(function(place) {
if (!place.geometry) {
console.log("Returned place contains no geometry");
return;
}
var icon = {
url: place.icon,
size: new google.maps.Size(80, 70),
origin: new google.maps.Point(0, 0),
anchor: new google.maps.Point(17, 34),
scaledSize: new google.maps.Size(25, 25)
};
// Create a marker for each place.
markers.push(new google.maps.Marker({
map: map,
icon: icon,
```

```
title: place.name,
position: place.geometry.location
}));
if (place.geometry.viewport) {
// Only geocodes have viewport.
bounds.union(place.geometry.viewport);
} else {
bounds.extend(place.geometry.location);
}
});
map.fitBounds(bounds);
});
layers[1] = new google.maps.Data();
layers[2] = new google.maps.Data();
layers[3] = new google.maps.Data();
layers[4] = new google.maps.Data();
layers[5] = new google.maps.Data();
layers[6] = new google.maps.Data();
$.getJSON("whole_roof_outline.json", function(data){
layers[1].addGeoJson(data);
});
layers[1].setStyle({
fillColor: 'none',
```

```
fillOpacity: 0.0,
strokeColor: 'red',
strokeWeight: 2
});
$.getJSON("roof_plane_N.json", function(data){
layers[2].addGeoJson(data);
});
layers[2].setStyle({
fillColor: '#FF0000',
fillOpacity: 1.0,
strokeWeight: 0.4
});
$.getJSON("roof_plane_E.json", function(data){
layers[3].addGeoJson(data);
});
layers[3].setStyle({
fillColor: '##FFFF00',
fillOpacity: 1.0,
strokeWeight: 0.4
});
$.getJSON("roof_plane_S.json", function(data){
layers[4].addGeoJson(data);
});
```

```
layers[4].setStyle({
fillColor: '#00FFFF',
fillOpacity: 1.0,
strokeWeight: 0.4
});
$.getJSON("roof_plane_W.json", function(data){
layers[5].addGeoJson(data);
});
layers[5].setStyle({
fillColor: '#0000FF',
fillOpacity: 1.0,
strokeWeight: 0.4
});
$.getJSON("roof_plane_FR.json", function(data){
layers[6].addGeoJson(data);
});
layers[6].setStyle({
fillColor: '#FFFFFF',
fillOpacity: 1.0,
strokeWeight: 0.4
});
layers[7] = new google.maps.FusionTablesLayer({
query: {
```

```
select: 'geometry',
from: tableid
},
styles: [{
where: "Class_name = 'North'",
polygonOptions: {
fillColor: '#FF0000',
fillOpacity: 1.0,
strokeWeight: 0.6,
strokeColor: '#000000'
}
}, {
where: "Class_name = 'East'",
polygonOptions: {
fillColor: 'FFFF00',
fillOpacity: 1.0,
strokeWeight: 0.6,
strokeColor: '#000000'
}
}, {
where: "Class_name = 'South'",
polygonOptions: {
fillColor: '#00FFFF',
```

```
fillOpacity: 1.0,
strokeWeight: 0.6,
strokeColor: '#000000'
}
}, {
where: "Class_name = 'West'",
polygonOptions: {
fillColor: '#0000FF',
fillOpacity: 1.0,
strokeWeight: 0.6,
strokeColor: '#000000'
}
}, {
where: "Class_name = 'Flat Roof'",
polygonOptions: {
fillColor: '#FFFFFF',
fillOpacity: 1.0,
strokeWeight: 0.6,
strokeColor: '#000000'
}
}]
});
layers[8] = new google.maps.FusionTablesLayer({
```

```
query: {
select: 'geometry',
from: tableid,
where: "Class_name = 'North'"
}
});
layers[9] = new google.maps.FusionTablesLayer({
query: {
select: 'geometry',
from: tableid,
where: "Class_name = 'East'"
}
});
layers[10] = new google.maps.FusionTablesLayer({
query: {
select: 'geometry',
from: tableid,
where: "Class_name = 'South'"
}
});
layers[11] = new google.maps.FusionTablesLayer({
query: {
select: 'geometry',
```

```
from: tableid,
where: "Class_name = 'West'"
}
});
layers[12] = new google.maps.FusionTablesLayer({
query: {
select: 'geometry',
from: tableid,
where: "Class_name = 'Flat Roof'"
}
});
for (var i = 1; i < layers.length; i++){
layers[i].setMap(null);
}
var legend = document.createElement('div');
legend.id = 'legend';
var content = [];
content.push('<h5>Legend</h5>');
content.push('<p><div class="color red"></div>North</p>');
content.push('<p><div class="color yellow"></div>East</p>');
content.push('<p><div class="color cyan"></div>South</p>');
content.push('<p><div class="color blue"></div>West</p>');
content.push('<p><div class="color white"></div>Flat Roof</p>');
```

```
legend.innerHTML = content.join('');

legend.index = 1;

map.controls[google.maps.ControlPosition.RIGHT_BOTTOM].push(legend);

}

function toggle(i){

if (layers[i].getMap() === null){

layers[i].setMap(map);

}

else {

layers[i].setMap(null);

}

infoWindow = new google.maps.InfoWindow({

content: ""

});

layers[1].addListener('click', function(event) {

infoWindow.setContent('<div style="line-height:1.35;overflow:hidden;white-
space:nowrap;"> PV Potential (Polycrystalline) = '+

event.feature.getProperty("PV_Pontent")+ "kWh/day" + "<br/>PV Potential
(Monocrystalline) = " +

event.feature.getProperty("PV_Ponte_1")+ "kWh/day" + "<br/>Optimal Potn
(Polycrystalline) = " +

event.feature.getProperty("Opt_PV_Pot")+ "kWh/day" + "<br/>Optimal Potn
(Monocrystalline) = " +

event.feature.getProperty("Opt_PV_P_1")+ "kWh/day" + "<br/>Pcent Optimality = " +
```

```
event.feature.getProperty("Opt_Pcent_")+ "%" + "<br/>Consumption Match (Polycrystalline) = " +

event.feature.getProperty("Consmpt_Mt")+ "%" + "<br/>Consumption Match (Monocrystalline) = " +

event.feature.getProperty("Consmpt__1")+ "%" + "</div>");

var anchor = new google.maps.MVCObject();

anchor.set("position",event.latLng);

infoWindow.open(map,anchor);

});

layers[2,3,4,5,6].addListener('click', function(event) {

infoWindow.setContent('<div style="line-height:1.35;overflow:hidden;white-space:nowrap;"> Orientation = '+

event.feature.getProperty("Class_name") +"<br/>Slope = "+

event.feature.getProperty("Mean_slope") +"deg" + "<br/>Mean Elevation = " +

event.feature.getProperty("Mean_nDSM")+"m" + "<br/>PV Potential (Polycrystalline) = " +

event.feature.getProperty("Panel_Pote")+"kWh/day" +"<br/>PV Potential (Monocrystalline) = " +

event.feature.getProperty("Panel_Po_1")+"kWh/day" + "<br/>R_Plane Contribution = " +

event.feature.getProperty("Pcent_Cont")+"%" + "</div>");

var anchor = new google.maps.MVCObject();

anchor.set("position",event.latLng);

infoWindow.open(map,anchor);

});
```

```
layers[1].addListener('mouseover', function(event) {
layers[1].revertStyle();
layers[1].overrideStyle(event.feature, {strokeWeight: 3.5});
});
layers[1].addListener('mouseout', function(event) {
layers[1].revertStyle();
});
layers[2,3,4,5,6].addListener('mouseover', function(event) {
layers[2,3,4,5,6].revertStyle();
layers[2,3,4,5,6].overrideStyle(event.feature, {fillColor: '#00FF00'});
});
layers[2,3,4,5,6].addListener('mouseout', function(event) {
layers[2,3,4,5,6].revertStyle();
});
layers[1].addListener('click', function(e){
var bounds = new google.maps.LatLngBounds();
var feat = processPoints(e.feature.getGeometry(), bounds.extend, bounds);
map.fitBounds(bounds);
});
function processPoints(geometry, callback, thisArg){
if (geometry instanceof google.maps.LatLng){
callback.call(thisArg, geometry);
```

```
}
else if (geometry instanceof google.maps.Data.Point){
callback.call(thisArg, geometry.get());
}
else {geometry.getArray().forEach(function(g){
processPoints(g, callback, thisArg);
});
}
}
}
$(document).ready(function(){
var address = '#addsearch';
$(function(){
$(address).autocomplete({
source: function(request, response){
$.ajax({
url: "whole_roof_outline.json",
dataType: "json",
data: {term: request.term},
success: function(data){
var array = $.map(data.features, function(item){
return{
label: item.properties.ADDDESC,
```

```
value: item.properties.ADDDESC
};
});
response($.ui.autocomplete.filter(array, request.term));
}
});
},
minLength: 1,
select: function(event, ui){
$.each(ui, function(key, element){
$("addsearch").val(element.value);
});
}
});
});
$("#search").click(function(){
var searchString = $(address).val();
layers[1].forEach(function(feat){
if (searchString == feat.getProperty("ADDDESC")){
var bounds = new google.maps.LatLngBounds();
var findFeatGeo = processPoints(feat.getGeometry(), bounds.extend, bounds);
map.fitBounds(bounds);
infoWindow = new google.maps.InfoWindow({
```

```
content: "",

pixelOffset: new google.maps.Size(0, 60)

});

infoWindow.setContent('<div style="line-height:1.35;overflow:hidden;white-space:nowrap;"> PV Potential (Polycrystalline) = '+

feat.getProperty("PV_Pontent")+ "kWh/day" + "<br/>PV Potential (Monocrystalline) = " +

feat.getProperty("PV_Ponte_1")+ "kWh/day" + "<br/>Optimal Potn (Polycrystalline) = " +

feat.getProperty("Opt_PV_Pot")+ "kWh/day" + "<br/>Optimal Potn (Monocrystalline) = " +

feat.getProperty("Opt_PV_P_1")+ "kWh/day" + "<br/>Pcent Optimality = " +

feat.getProperty("Opt_Pcent_")+ "%" + "<br/>Consumption Match (Polycrystalline) = " +

feat.getProperty("Consmpt_Mt")+ "%" + "<br/>Consumption Match (Monocrystalline) = " +

feat.getProperty("Consmpt__1")+ "%" + "</div>");

var anchor = new google.maps.MVCObject();

anchor.set("position",map.getCenter());

infoWindow.open(map,anchor);

google.maps.event.trigger(feat, 'click',{

latLng: bounds

});

}

function processPoints(geometry, callback, thisArg){
```

```
if (geometry instanceof google.maps.LatLng){
callback.call(thisArg, geometry);
}
else if (geometry instanceof google.maps.Data.Point){
callback.call(thisArg, geometry.get());
}
else {geometry.getArray().forEach(function(g){
processPoints(g, callback, thisArg);
});
}
}
});
});
layers[1].addListener("$('#dropdown').change()", function(event){
if (event.feature.getProperty("Gen_Est") < 1000 && $("#dropdown").val() == "<
50%"){
layers[1].revertStyle();
layers[1].overrideStyle(event.feature, {fillColor: '#00FF00'});
}
else if (event.feature.getProperty("Gen_Est") > 1000 && $("#dropdown").val() == ">
50%"){
layers[1].revertStyle();
layers[1].overrideStyle(event.feature, {fillColor: '#00FF00'});
```

```
}
else if ($("#dropdown").val() == "None"){
layers[1].revertStyle();
}
});
$("#querybut").click(function(){
var searchString = $(address).val();
layers[1].forEach(function(f){
var Pv_Potn_P = f.getProperty("PV_Pontent");
var Pv_Potn_M = f.getProperty("PV_Ponte_1");
var Opt_Pcent_P = f.getProperty("Opt_PV_Pot");
var Opt_Pcent_M = f.getProperty("Opt_PV_P_1");
if (searchString == f.getProperty("ADDDESC") && $("input[name
='spanel']:checked").val() == "0.15"){
document.getElementById("output").value = Pv_Potn_P;
document.getElementById("optm").value = Opt_Pcent_P;
}
else if (searchString == f.getProperty("ADDDESC") && $("input[name
='spanel']:checked").val() == "0.17"){
document.getElementById("output").value = Pv_Potn_M;
document.getElementById("optm").value = Opt_Pcent_M;
}
});
```

```
});

$("#querybut").click(function(){

var searchString = $(address).val();

var potnN_P = [];

var potnE_P = [];

var potnS_P = [];

var potnW_P = [];

var potnF_P = [];

var potnN_M = [];

var potnE_M = [];

var potnS_M = [];

var potnW_M = [];

var potnF_M = [];

layers[2,3,4,5,6].forEach(function(f){

if (searchString == f.getProperty("ADDDESC") && f.getProperty("Class_name") ==
"North" && $("input[name ='boxN']:checked").val() && $("input[name
='spanel']:checked").val() == "0.15"){

potnN_P.push(f.getProperty("RPlane_Pon"));

var sumN = potnN_P.reduce(function (a, b){return a + b;}, 0);

document.getElementById("output2").value = sumN;

}

else if (searchString == f.getProperty("ADDDESC") && f.getProperty("Class_name")
== "North" && $("input[name ='boxN']:checked").val() && $("input[name
='spanel']:checked").val() == "0.17"){
```

```
potnN_M.push(f.getProperty("RPlane_Pon"));

var sumN = potnN_M.reduce(function (a, b){return a + b;}, 0);

document.getElementById("output2").value = sumN;

}

else if (searchString == f.getProperty("ADDDESC") && f.getProperty("Class_name")
== "East" && $("input[name ='boxE']:checked").val() && $("input[name
='spanel']:checked").val() == "0.15"){

potnE_P.push(f.getProperty("RPlane_Pon"));

var sumE = potnE_P.reduce(function (a, b){return a + b;}, 0);

document.getElementById("output2").value = sumE;

}

else if (searchString == f.getProperty("ADDDESC") && f.getProperty("Class_name")
== "East" && $("input[name ='boxE']:checked").val() && $("input[name
='spanel']:checked").val() == "0.17"){

potnE_M.push(f.getProperty("RPlane_Pon"));

var sumE = potnE_M.reduce(function (a, b){return a + b;}, 0);

document.getElementById("output2").value = sumE;

}

else if (searchString == f.getProperty("ADDDESC") && f.getProperty("Class_name")
== "South" && $("input[name ='boxS']:checked").val() && $("input[name
='spanel']:checked").val() == "0.15"){

potnS_P.push(f.getProperty("RPlane_Pon"));

var sumS = potnS_P.reduce(function (a, b){return a + b;}, 0);

document.getElementById("output2").value = sumS;

}
```

```
else if (searchString == f.getProperty("ADDDESC") && f.getProperty("Class_name")
== "South" && $("input[name ='boxS']:checked").val() && $("input[name
='spanel']:checked").val() == "0.17"){

potnS_M.push(f.getProperty("RPlane_Pon"));

var sumS = potnS_M.reduce(function (a, b){return a + b;}, 0);

document.getElementById("output2").value = sumS;

}

else if (searchString == f.getProperty("ADDDESC") && f.getProperty("Class_name")
== "West" && $("input[name ='boxW']:checked").val() && $("input[name
='spanel']:checked").val() == "0.15"){

potnW_P.push(f.getProperty("RPlane_Pon"));

var sumW = potnW_P.reduce(function (a, b){return a + b;}, 0);

document.getElementById("output2").value = sumW;

}

else if (searchString == f.getProperty("ADDDESC") && f.getProperty("Class_name")
== "West" && $("input[name ='boxW']:checked").val() && $("input[name
='spanel']:checked").val() == "0.17"){

potnW_M.push(f.getProperty("RPlane_Pon"));

var sumW = potnW_M.reduce(function (a, b){return a + b;}, 0);

document.getElementById("output2").value = sumW;

}

else if (searchString == f.getProperty("ADDDESC") && f.getProperty("Class_name")
== "Flat" && $("input[name ='boxF']:checked").val() && $("input[name
='spanel']:checked").val() == "0.15"){

potnF_P.push(f.getProperty("RPlane_Pon"));
```

```
var sumF = potnF_P.reduce(function (a, b){return a + b;}, 0);

document.getElementById("output2").value = sumF;

}

else if (searchString == f.getProperty("ADDDESC") && f.getProperty("Class_name")
== "Flat" && $("input[name ='boxF']:checked").val() && $("input[name
='spanel']:checked").val() == "0.17"){

potnF_M.push(f.getProperty("RPlane_Pon"));

var sumF = potnF_M.reduce(function (a, b){return a + b;}, 0);

document.getElementById("output2").value = sumF;

}

});

});

});

</script>

<script
src=https://maps.googleapis.com/maps/api/js?key=AIzaSyA_AD7aBB2JfW2RIWLKc
uebXjj6eptUt9U&libraries=places&callback=initMap async defer></script>

</body>

</html>
```